DOE/ER-0045/9

Alloy Development for Irradiation Performance

Semiannual Progress Report
For Period Ending September 30, 1982

U.S. Department of Energy
Office of Fusion Energy

Printed in the United States of America. Available from
National Technical Information Service
U.S. Department of Commerce
5285 Port Royal Road, Springfield, Virginia 22161
NTIS price codes—Printed Copy: A16 Microfiche A01

DOE/ER-0045/9
Distribution
Category
UC-20, 20c

ALLOY DEVELOPMENT FOR IRRADIATION PERFORMANCE SEMIANNUAL PROGRESS REPORT FOR PERIOD ENDING SEPTEMBER 30, 1982

ARGONNE NATIONAL LABORATORY

GENERAL ATOMIC COMPANY

McDONNELL DOUGLAS ASTRONAUTICS COMPANY

MASSACHUSETTS INSTITUTE OF TECHNOLOGY

NAVAL RESEARCH LABORATORY

OAK RIDGE NATIONAL LABORATORY

SANDIA NATIONAL LABORATORIES

WESTINGHOUSE ADVANCED REACTORS DIVISION

WESTINGHOUSE HANFORD COMPANY

Date Published - February 1983

Prepared by
OAK RIDGE NATIONAL LABORATORY
Oak Ridge, Tennessee 37830
operated by
UNION CARBIDE CORPORATION
for the
U. S. DEPARTMENT OF ENERGY
Under Contract No. W-7405-eng-26

Reports previously issued in this series are *as* follows:

DOE/ET-0058/1	Period Ending March 31, 1978
DOE/ET-0058/2	Period Ending June 30, 1978
DOE/ET-0058/3	Period Ending September 30, 1978
DOE/ET-0058/4	Period Ending December 31, 1978
DOE/ET-0058/5	Period Ending March 31, 1979
DOE/ET-0058/6	Period Ending June 30, 1979
DOE/ET-0058/7	Period Ending September 30, 1979
DOE/ER-0045/1	Period Ending December 31, 1979
DOE/ER-0045/2	Period Ending March 31, 1980
DOE/ER-0045/3	Period Ending June 30, 1980
DOE/ER-0045/4	Period Ending September 30, 1980
DOE/ER-0045/5	Period Ending December 31, 1980
DOE/ER-0045/6	Period Ending March 31, 1981
DOE/ER-0045/7	Period Ending September 30, 1981
DOE/ER-0045/8	Period Ending March 31, 1982

FOREWORD

This report is the sixteenth in a series of Technical Progress Reports on *"Alloy Development for Irradiation Performance"* (ADIP), which is one element of the Fusion Reactor Materials Program, conducted in support of the Magnetic Fusion Energy Program of the U.S. Department of Energy. Other elements of the Materials Program are

- *Damage Analysis and Fundamental Studies (DAFS)*
- *Plasma-Materials Intemction (PMI)*
- *Special-Purpose Materials (SPM)*

The first seven reports in this series are numbered DOE/ET-0058/1 through 7. This report is the ninth in a new numbering sequence that begins with DOE/ER-0045/1.

The **ADIP** program element is a national effort composed of contributions from a number of National Laboratories and other government laboratories, universities, and industrial laboratories. It was organized by the Materials and Radiation Effects Branch, Office of Fusion Energy, DOE, and a Task Group on *Alloy Development for Irradiation Performance,* which operates under the auspices of that Branch. The purpose of this series of reports is to provide a working technical record of that effort for the use of the program participants, for the fusion energy program in general, and for the Department of Energy.

This report is organized along topical lines in parallel to a Program Plan of the same title so that activities and accomplishments may be followed readily relative to that Program Plan. Thus, the work of a given laboratory may appear throughout the report. Chapters 1, 2, 8, and 9 review activities on analysis and evaluation, test methods development, status of irradiation experiments, and corrosion testing and hydrogen permeation studies, respectively. These activities relate to each of the alloy development paths. Chapters 3, 4, 5, 6, and 7 present the ongoing work on each alloy development path. The Table of Contents is annotated for the convenience of the reader.

This report has been compiled and edited under the guidance of the Chairman of the Task Group on *Alloy Development for Irmdiation Performance.* E. E. Bloom, Oak Ridge National Laboratory, and his efforts and those of the supporting staff of ORNL and the many persons who made technical contributions are gratefully acknowledged. T. C. Reuther, Materials and Radiation Effects Branch, is the Department of Energy Counterpart to the Task Group Chairman and has responsibility for the **ADIP** Program within WE.

G. M. Haas, Acting Chief
Materials and Radiation Effects Branch
Office of Fusion Energy

CONTENTS

1. **ANALYSIS** AND **EVALUATION** STUDIES

1.1 MATERIALS HANDBOOK FOR FUSION ENERGY SYSTEMS — J. W. Davis (McDonnell Douglas Astronautics Company - St. Louis Division) and T. K. Bierlein (Westinghouse Hanford Company)

1.1.1 ADIP Task

Task Number 1.A.1 - Define material property requirements and make structural life predictions.

1.1.2 Objective

To provide a consistent and authoritative source of material property data for use by the fusion community in concept evaluation, design, safety analysis, and performance/verification studies of various fusion energy systems. A secondary objective is the early identification of areas in the materials data base where insufficient information or voids exist.

1.1.3 Summary

A fourth publication package of data pages has been distributed and a fifth publication package will be released shortly. The fourth publication package contained data sheets covering both the irradiated and unirradiated electrical resistivity of 20% cold worked type 316 stainless steel. The fifth publication package will be much more extensive and contain data sheets on solid tritium breeding materials, magnet case materials, and first wall protection materials. With the release of the fifth publication package, the handbook will contain material information in seven of its nine major chapters. During the remainder of this year the effort will be directed towards expanding the information in these chapters with particular emphasis on ferritic steel data sheets and on liquid lithium data sheets.

1.1.4 Progress and Status

The Materials Handbook for Fusion Energy Systems is now approaching the third anniversary of its authorization and during this time has been transformed from an idea into a document that is both widely recognized and sought. This can be seen in the fact that there are now over 100

copies of the handbook in use today at more than 30 different U.S. organizations consisting of national laboratories, universities, and private industry, and requests for additional copies continue to arrive. While in the beginning the interest in the handbook centered on the promise of things to come rather than content, this situation is beginning to change primarily as a result of the efforts of a few individuals.

A continuing challenge the handbook has had to face is the maintenance of a continuous flow of data pages from the page preparers to the handbook holders. To rectify this situation a number of approaches were tried including the issuance of a programmatic letter by the Materials and Radiation Effects branch of OFE raising the visability of the handbook. While none of these approaches has been singularly successful, taken in total they have helped to increase the flow of data to the handbook. This trend can be seen in a comparison of the number of data pages in 1981 with those submitted in 1982. In 1981 after the publication of the 21 data pages on the glass epoxy laminate G-10CR which were prepared by G. P. Lang of MDAC and R. R. Coltman of ORNL, only 3 additional data pages were submitted for review. These data pages were prepared by R. F. Mattas of ANL and covered the electrical resistivity of 20% cold worked type 316 stainless steel in the irradiated and unirradiated condition. These data pages are contained in the fourth publication package. In 1982 more than 100 data pages have been submitted for review and approval and should be released to the handbook users during 1983. These data pages consist of cryogenic properties of austenitic stainless steel for use in superconducting magnets, which were prepared by N. J. Simon of NBS; properties of lithium ceramic compounds (Li_2O, Li_4SiO_4, Li_2ZrO_3, and $LiAlO_2$) for use in tritium breeding, prepared by G. W. Hollenberg of HEDL; and properties of bulk graphite for use as armor or limiters, prepared by D. J. Suiter of MDAC. The majority of these pages are in the review cycle with roughly 20 approved for release in January. In addition to these data pages approximately *40* more data pages have been received but are not in the review cycle as yet. These data pages cover the irradiated impact strength of ferritic steels, prepared by W. L. Hu of HEDL, melting point of Li_2O prepared by J. Shearer of ANL, tritium permeation of stainless

steel prepared by W. Bauer of SNL, and properties of lithium prepared by W. Brehm of HEDL, and physical sputtering of several materials prepared by J. B. Roberto of ORNL. These data sheets will enter the review cycle later this year. With the publication of these data sheets the handbook will contain information in 7 of its 9 chapters. Even though there are a large number of data pages in the review cycle, the handbook will still need additional data sheets in order to maintain a continuous flow of data. Data sheets that are currently in the planning or preparation stage are: mechanical properties of ferritic steel type HT-9, mechanical properties of graphite type H451, and swelling of austenitic stainless steel type 316.

1.1.5 Future Work

The effort for the handbook over the next 6 months will be directed towards the review of the data sheets and publication of at least half of the data sheets currently in review assuming they are approved by the A&E task group.

2. TEST MATRICES AND METHODS DEVELOPMENT

2.1 NEUTRON SOURCE CHARACTERIZATION FOR MATERIALS EXPERIMENTS - L. R. Greenwood (Argonne National Laboratory)

2.1.1 ADIP/DAFS Tasks

ADIP Task I.A.2 - Define Test Matrices and Procedures
DAFS Task II.A.1 - Fission Reactor Dosimetry

2.1.2 Objective

To characterize neutron irradiation facilities in terms of neutron flux, spectra, and damage parameters (DPA, He, transmutation) and to measure these exposure parameters during fusion materials irradiations.

2.1.3 Summary

Measurements and calculations are presented for the ORR-MFE4A spectral-tailoring experiment after an irradiation of 406 full power days (30 MW) between June 12, 1980 and April 26, 1982. The maximum fluence inside the capsule was 1.76 x 10^{22} n/cm^2 producing 4.67 DPA and 63 appm He in stainless steel (13% Ni). Values outside the sample holders were 1.88 x 10^{22} n/cm^2, 4.94 DPA and 73 appm He in stainless steel. Helium calculations include epithermal effects and the extra displacements from the energetic ^{56}Fe recoils. The status of all other experiments is summarized in Table 2.1.1.

2.1.4 Progress and Status

2.1.4.1 Dosimetry and Analysis for the MFE4A Spectral Tailoring Experiment in ORR

The MFE4A experiment in the Oak Ridge Research Reactor (ORR) was designed to achieve fusion-like helium-to-DPA ratios in stainless steel by altering the neutron spectrum. The irradiation in core position E3

Table 2.1.1. Status of Dosimetry Experiments

	Facility/Experiment	Status/Comments
ORR	- MFE 1	Completed 12/79
	- MFE 2	Completed 06/81
	- MFE 4A1	Completed 12/81
	- MFE 4A2	Completed 11/82
	- MFE 4 B,C	Irradiation in Progress
	- TBC 07	Completed 07/80
	- TRIO-Test	Completed 07/82
	- TRIO-1	Samples Sent 10/82
HFIR	- CTR 32	Completed 04/82
	- CTR 31, 34, 35	Samples Received 09/82
	- CTR 30	Irradiation in Progress
	- T1, T2, T3	Irradiations in Progress
	- RB1, RB2, RB3	Irradiations in Progress
	- CTR 39-45	Samples Sent 10/82
Omega West	- Spectral Analysis	Completed 10/80
	- HEDL1	Completed 05/81
EBR II	- X287	Completed 09/81
IPNS	- Spectral Analysis	Completed 01/82
	- LANL1 (Hurley)	Completed 06/82
	- Hurley/Coltman	Samples Received 11/82

began on June 12, 1980 and was first removed on January 19, 1981 after an exposure of 5481 MWD. Dosimeters were removed at that time and our results were reported previously. [Damage Analysis and Fundamental Studies, Quarterly Progress Report, DOE/ER-0046/6, p. 24, 1981.] The experiment was then further irradiated from March 19, 1981 to September 16, 1981 for 4404 MWD and finally from February 2, 1982 to April 26, 1982 for 2291 MWD. The net exposure was thus 12,176 MWD. Dosimetry capsules for this entire exposure have been analyzed and the results are reported below. The MFE4A experiment is still being irradiated; hence, these interim results are intended to check the progress of the planned exposure.

Four of our original eight stainless steel dosimetry tubes were removed in the present experiment. The other four were left in for

further irradiation along with four new dosimeters to replace those which were removed. Each tube was about 1/16" OD by 2.75" long and contained small quantities of Fe, Co, 80%Mn–Cu, Ti, Nb, Cu, Ni, and helium accumulation monitors. All of the samples were gamma counted by Ge(Li) spectroscopy techniques. The samples were then sent to Rockwell International for helium analyses.

The measured activities are listed in Table 2.1.2. All values have been corrected for burnup; however, self–shielding effects are not

Table 2.1.2. Activation Rates Measured for ORR-MFE4A Dosimeters removed on April 26, 1982 at 12,176 MWD
Values normed to 30 MW; accuracy ±1.5%

Reaction	Height, in.	σφ(atom/atom-s) Inside	σφ(atom/atom-s) Outside
$^{58}Fe(n,\gamma)^{59}Fe$	-0.62	1.72 x 10^{-10}	1.85^{-10}
	–2.47	1.68	1.88
	–3.75	1.72	
	–3.94		1.83
	–4.50		1.82
	–5.78		1.68
	–5.84	1.54	
$^{59}Co(n,\gamma)^{60}Co$	–0.84	5.09 x 10^{-9}	5.65 x 10^{-9}
	–3.97	5.09 x 10^{-9}	
	-4.16		5.48 x 10^{-9}
$^{58}Fe(n,\gamma)^{59}Fe(n,\gamma)^{60}Co$	–0.62	1.59 x 10^{-11}	1.88 x 10^{-11}
	–2.47	1.59	1.92
	–3.75	1.61	
	–3.94		1.87
	–5.78		1.52
	–5.84	1.23	
$^{50}Cr(n,\gamma)^{51}Cr$	–1.19		2.44 x 10^{-9}
$^{54}Fe(n,p)^{54}Mn$	–0.62	1.01 x 10^{-11}	1.05 x 10^{-11}
	–2.47	1.03	1.08
	–3.75	1.02	
	–3.94		1.06
	–4.31	1.00	
	–4.50		1.02
	–5.78		1.01
	–5.84	0.96	

(Cont'd)

Table 2.1.2. (Cont'd)

Reaction	Height, in.	σφ(atom/atom-s) Inside	Outside
$^{46}Ti(n,p)^{46}Sc$	−1.19	1.41×10^{-12}	
	−1.66	1.46	1.56×10^{-12}
	−4.81	1.43	
	−4.97		1.54
	−5.03	1.44	
$^{55}Mn(n,2n)^{54}Mn$	−1.00	3.21×10^{-14}	3.40×10^{-14}
	−4.13	3.23	
	−4.31		3.35
$^{63}Cu(n,\alpha)^{60}Co$	−2.13	7.12×10^{-14}	7.49×10^{-14}
	−5.44		7.07
	−5.50	6.65	
$^{58}Ni(n,p)^{58}Co$+	−2.31	5.68×10^{-12}	5.63×10^{-12}
	−4.56	5.74	
	−4.75		5.55
	−5.63		5.70
	−5.69	5.80	
$^{60}Ni(n,p)^{60}Co$+	−2.31	1.51×10^{-14}	1.74×10^{-14}
	−4.56	1.39	
	−4.75		1.60
	−5.63		1.48
	−5.69	1.20	
$^{58}Ni(n,x)^{57}Co$	−2.31	1.63×10^{-12}	1.73×10^{-12}
	−5.63		1.62
	−5.69	1.52	

+ Burnup correactions are not included but are very high (~50%) for ^{58}Co. The ^{60}Co values are correspondingly too high (~'50%) due to burnin of ^{59}Co.

included since this correction is spectral-dependent and hence must be done concurrently with subsequent spectral adjustment. The values agree quite well with those reported previously, although the previous $^{59}Co(n,\gamma)$ value was altered due to a reanalysis of the Co-V alloy, as reported later. [Damage Analysis and Fundamental Studies, Quarterly Progress Report, WE/ ER-0046/8, p. 21, 1982.1 Furthermore, neutron self-shielding corrections are slightly larger in the present run. The final activity ratios of the Present measurements divided by the earlier measurements are, as follows:

Reaction	Ratio (New/Old)
$^{58}Fe(n,\gamma)$	1.00 ± 0.03
$^{59}Co(n,\gamma)$	0.93 ± 0.06
$^{54}Fe(n,p)$	1.01 ± 0.03
$^{46}Ti(n,p)$	1.05 ± 0.03

Hence, we conclude that there has been no significant change in the spectrum between the two irradiations. The small difference in flux may be due to fuel burnup effects.

The activities in Table 2.1.2 are grouped by their position in the MFE4A assembly. Two tubes were on the inside and two on the outside of an annulus surrounding the experimental samples. The top tubes (0 to −2.5") were irradiated at 400°C and the bottom (−3.9" to −5.8") were at 300°C. All of the activities for a specific reaction fall on smooth curves for the inner and outer positions. At each position the maximum gradient was only about 8% over the entire length (~6") where samples were irradiated. The gradients can all be described quite well by a simple polynomial of form:

$$Ai(h) = Ai(0)(0.9712 - 0.02497\ h - 0.00540\ h^2) \qquad (1)$$

where Ai is the activity for reaction i and Ai(0) is the maximum value which occurs at −2.3" below midplane. This expression was then used to estimate the maximum activation rates for all reactions and these values are listed in Table 2.1.3. The thermal activities are about 8% lower on the inside compared to the outside of the assembly whereas the fast neutron values only decrease by about 5%. Actually, we expect two effects to be operative - a slow flux gradient away from core center and neutron attenuation by the stainless steel sleeve around the inner samples.

Table 2.1.3. Maximum Activation Fates for ORR-MFE4A Values at −2.3" below midplane

Reaction	σφ (atom/atom-s) Inside	σφ (atom/atom-s) Outside	Ratio (In/Out)
$^{58}Fe(n,\gamma)^{59}Fe$[a]	1.75 x 10^{-10}	1.88 x 10^{-10}	0.93
$^{59}Co(n,\gamma)^{60}Co$	5.16 x 10^{-9}	5.65 x 10^{-9}	0.91
$^{54}Fe(n,p)^{54}Mn$	1.03 x 10^{-11}	1.08 x 10^{-11}	0.95
$^{46}Ti(n,p)^{46}Sc$	1.47 x 10^{-12}	1.58 x 10^{-12}	0.93
$^{55}Mn(n,2n)^{54}Mn$	3.26 x 10^{-14}	3.43 x 10^{-14}	0.95
$^{63}Cu(n,\alpha)^{60}Co$	7.10 x 10^{-14}	7.48 x 10^{-14}	0.95

[a] Neutron self-shielding corrections are about 2% for Fe and 10% for the Co(n,γ) reactions.

The maximum activation rates in Table 2.1.3 were used to adjust the flux spectrum calculated by R. A. Lillie, et al.[1] The resultant fluxes are listed in Table 2.1.4 and the spectrum is shown in Figure 2.1.1. The thermal flux was calculated assuming that the neutrons have a Maxwellian distribution centered at 95°C, the temperature of the surrounding moderator. This corresponds to the temperature used in the neutronics

Table 2.1.4. Maximum Flux and Fluence Values for ORR-MFE4A Values at −2.3" below midplane, normalized to 30 MW Fluences calculated for 12,176 MWD

Energy, MeV	Error	Flux (x 10^{14} n/cm^2-s) Inner	Flux (x 10^{14} n/cm^2-s) Outer	Fluence (x 10^{21} n/cm^2) Inner	Fluence (x 10^{21} n/cm^2) Outer
Total	(5%)	5.01	5.37	17.6	18.8
Thermal (<.5 eV)[+]	(5%)	1.70	1.85	5.96	6.51
(2200 m/s)		1.34	1.46	4.71	5.15
0.5 eV - 0.11	(12%)	1.64	1.75	5.77	6.16
>0.11	(10%)	1.66	1.76	5.83	6.19
0.11 - 1	(15%)	0.75	0.80	2.63	2.79
1 - 5	(9%)	0.84	0.88	2.95	3.10
5 - 10	(8%)	0.071	0.075	0.25	0.26
10 - 20	(12%)	0.0021	0.0022	0.0073	0.0077

[+] Maxwellian thermal distribution assumed centered at the moderator temperature of 95°C.

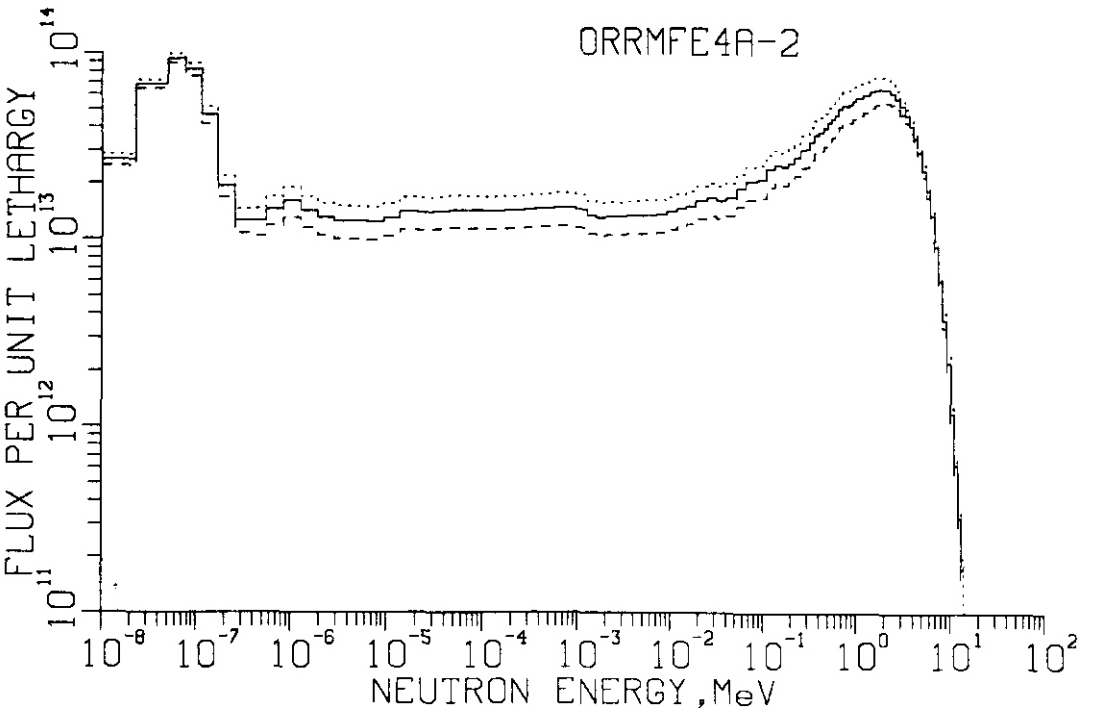

Pig. **2.1.1.** Adjusted neutron flux spectrum for the MFE4A experiment **in** ORR normalized to 30 **MW** after 406 full power days. The dotted and dashed lines represent one standard deviation; however, the flux groups are highly correlated.

calculations at **ORNL. In** any case, the derived 2200 m/s thermal flux **is** independent of the assumed distribution and this value **is** also listed for comparison.

Displacement damage and gas production calculations were performed for both the inner and outer positions and the calculated He and DPA values are listed in Table **2.1.5.**

The He and DPA values at other heights **in** the assembly can be calculated using Eq. **(1)** where **Ai(0) is** taken from Table 2.1.5; however, the Ni values deserve special consideration, as discussed later. The effects of (n,γ) and β-decay are included **in** the table. For nickel-

Table 2.1.5. Damage Parameters for ORR-MFE4A (12,176 MWD)
Maximum exposure at -2.3" below midplane
Fluences were 1.88 x 10^{22} (outer) and 1.76 x 10^{22} (inner)

Element	He(appm)		DPA	
	Inner	Outer	Inner	Outer
Al	3.65	3.86	7.87	5.31
Ti	2.75	2.90	5.04	5.31
V	0.12	0.13	5.59	5.89
Cr	0.90	0.96	5.01	5.28
Mn[a]	0.71	0.75	5.35	5.65
Fe	1.50	1.57	4.45	4.70
Co[a]	0.75	0.79	5.15	5.45
Ni[b]	478.	552.	5.50	5.89
cu	1.31	1.39	4.30	4.53
Zr	0.14	0.15	4.63	4.89
Nb	0.30	0.31	4.27	4.50
Mo	--	--	3.14	3.31
Ta	--	--	2.15	2.27
316 SS[c]	63.4	73.1	4.67	4.94

[a] Self-shielding corrections may be needed for thick samples for the (n,γ) reaction which contributes (5.2%) for Mn and (16.8%) for Co.

[b] Thermal helium and DPA effects included (see text).

[c] Composition assumed: Cr(.18), Mn(.019), Fe(.645), Ni(.13), Mo(0.026).

bearing materials, two effects must be taken into account. First, the helium generation is increased by the two-step process $^{58}Ni(n,\gamma)^{59}Ni(n,\alpha)^{56}Fe$. Secondly, this process increases the DPA in nickel by the ratio of He(appm)/DPA = 567 (see reference 2).

In order to determine the helium generation we need to know the spectral-averaged cross sections for the *two* successive thermal captures. If we start from the usual equations based on the 2200 m/s values (see references 2 and 3), then we must estimate corrections for the epithermal flux. If we knew the cross sections versus energy, then we could simply average over our adjusted spectrum. However, these data are not available

If we assume that resonance contributions are not large, then the epithermal corrections for the two nickel capture reactions should be similar to those for our two dosimetry reactions, namely ^{58}Fe and $^{59}Co(n,\gamma)$. Both of these dosimetry reactions have an epithermal contribution to the reaction rate of about 15%. Hence, the equivalent 2200 m/s fluences to be used to calculate helium production are 5.44 (inner) and 5.90 (outer) x 10^{22} n/cm^2. These values happen to be close to the total thermal fluences (<.5 eV) corrected to room temperature. A simpler way to think about this is to say that the nickel capture rates should be roughly proportional to the Fe and Co rates times the ratios of the appropriate 2200 m/s cross sections.

The nickel damage and helium production values are listed in more detail in Table 2.1.6. The same procedures were used previously to predict a helium value of about 122 appm in nickel at an interim exposure of 5481 MWD. This value was later found to agree quite well with helium measurements at Rockwell International.[4] Of course, helium measurements

Table 2.1.6. Damage and Helium Calculations for Nickel

Reaction	Inner		Outer	
	DPA	He, appm	DPA	He, appm
Fast Neutrons:	4.70	22.5	4.96	23.7
Thermal[a]	0.80	455.6	0.93	528.6
Total	5.50	478.1	5.89	552.3

[a] Thermal calculations use equations in references 2 and 3 with effective thermal fluences of 5.44 and 5.90 x 10^{21} n/cm^2 for the inner and outer positions, respectively.

are now in progress for the present exposure and these values will not only provide the precision needed in the MFE4A experiment, but also can be used to fine tune our calculations if necessary.

2.1.5 Conclusion

The MFE4A experiment is continuing and further measurements will be needed to check the progress, especially to measure the helium-to-DPA rates in stainless steel. Helium measurements are now in progress at Rockwell International and these values will be integrated with our radiometric data.

2.1.6 References

1. T. A. Gabriel, R. A. Lillie, T. Thoms, and R. L. Childs, J. Nucl. Mater. 104, 1445 (1981).
2. L. R. Greenwood, A New Calculation of Thermal Neutron Damage and Helium Production in Nickel, to be published in J. Nucl. Mater.
3. F. W. Wiffen, E. J. Allen, H. Farrar IV, E. E. Bloom, T. A. Gabriel, H. T. Kerr, and F. G. Perey, The Production Rate of Helium During Irradiation of Nickel in Thermal Spectrum Fission Reactors. submitted to J. Nucl. Mater.
4. J. G. Bradley, D. W. Kneff, and H. Farrar IV, Helium Production in ORR MFE4A Nickel, Damage Analysis and Fundamental Studies Quarterly Progress Report, DOE/ER-0046/7, p. 24 (1981).

2.1.6.1 Publications

A paper entitled "A New Calculation of Thermal Neutron Damage and Helium Production in Nickel" was presented by L. R. Greenwood at the

TMS-AIME Symposium on Radiation Damage Analysis for Fusion Reactors in St. Louis, MO on October 25-28, 1982.

2.2 OPERATION OF THE ORR SPECTRAL TAILORING EXPERIMENTS ORR-MFE-4A AND ORR-MFE-4B — J. A. Conlin, I. T. Dudley, and E. M. Lees (Oak Ridge National Laboratory)

2.2.1 ADIP Task

ADIP Task I.A.2. Define Test Matrices and Test Procedures.

2.2.2 Objectives

Experiments ORR-MFE-4A and -4B, which irradiate austenitic stainless steel, use neutron spectral tailoring to achieve the same helium-to-displacement-per-atom (He/dpa) ratio as predicted for fusion reactor first-wall service. Experiment ORR-MFE-4A contains mainly type 316 stainless steel and Path A Prime Candidate Alloy (PCA) at irradiation temperatures of 330 and 400°C. Experiment ORR-MFE-4B contains similar materials at irradiation temperatures of 500 and 600°C.

2.2.3 Summary

The ORR-MFE-4A experiment has operated for an equivalent of 413 d at 30 MW reactor power, with specimen temperatures of 400 and 330°C. It was removed from the reactor on April 26, 1982, because a leak developed in the primary containment. The specimens were transferred to a new capsule, and that assembly has been reinstalled in the ORR for continued irradiation. The ORR-MFE-4B experiment, with specimen temperatures of 500 and 600°C, has operated for 406 d at 30 MW reactor power.

2.2.4 Progress and Status

The details of the Oak Ridge Research Reactor (ORR) Spectral Tailoring Experiments have been described previously.[1-4] On April 16, 1982, the ORR was shut down for refueling and routine reactor maintenance. The control gas flowmeters in the ORR-MFE-4A experiment were removed for calibration. This left the secondary system of the capsule depressurized for a period of approximately 72 h. After the flowmeters were reinstalled and helium flow established in the control gas system, radiation levels inside the experimental facility valve box increased. The increase was found to be

due to traces of slightly radioactive NaK in the control gas line on the outlet side of the capsule. This indicated that a leak had developed in the capsule primary containment and allowed NaK to leak into the control gas system.

The experiment was removed from the reactor and transferred to the ORR hot cell. The in-core section of the capsule assembly was separated from the instrumentation leads and transported to the High Radiation Level Examination Laboratory (HRLEL). The capsule was dismantled and examined to determine the cause of the failures. Metallographic examination of the thermocouples and regions suspected to be associated with the leak established the leak location. The leak had occurred at a silver-solder-sealed tubing penetration through the bulkhead located at the top of the capsule, approximately 10 an (4 in.) above the NaK level. This allowed a few grams of NaK vapor to penetrate the air-filled region above the bulkhead. The condensed vapor had reacted with the air, and the resultant oxides had corroded through the sheath and wires of all six thermocouples and severely attacked the gas tubes that penetrate the bulkhead at this point. An aluminum heat sink in that region was also corroded. The control gas outlet line evidentally had a hole corroded through it, which permitted the NaK that had accumulated above the bulkhead to enter the secondary gas system. The tube was corroded; however, we were unable to locate the actual leak.

All other regions of the capsule were in excellent condition, with no indication of incipient failure. Metallographic mounts were made of two of the thermocouple junctions. The junctions were found to be in excellent condition. There was no evidence of NaK in the secondary gas region surrounding the capsule. The leaked NaK was confined to the secon-dary sweep gas outlet tube only.

The capsule design was modified to eliminate the faults of the first capsule and to incorporate other changes, which should provide an improved, more reliable capsule. The bulkhead penetrations were changed to furnace brazed joints using "Nicrobraze 50," which is resistant to NaK. A number of changes were also made to reduce thermal stress and stress risers in the capsule. The region above the bulkhead, which previously contained

air, will now be sealed with helium to reduce the temperature of the leads in this region and eliminate the possibility of chemical reaction. Although the grounded thermocouple junctions were not, as suspected, the source of the earlier thermocouple failures,[2] all the thermocouples now have insulated junctions. The central thermocouple well was also modified to minimize the temperature difference between the central and NaK thermocouples.

The test specimens were removed early in the disassembly. Some of the pressurized tubes were examined, and the specimens were reloaded in a new holder assembly. The new capsule was placed in a specially designed shielding cask, and the radioactive specimens loaded in the capsule in a hot cell. The capsule assembly was completed while in the cask. The capsule was then removed from the casks under water and inserted into the ORR, and irradiation was begun September 24, 1982. Through September 30, 1982, the ORR-MFE-4A capsule had accumulated an equivalent of 413 d at 30 MW reactor power. Specimen temperatures of 330 and 400°C were again achieved in the reconstituted experiment.

The ORR-MFE-4B capsule continues to operate. Since its installation in the reactor on April 23, 1981, there have been four failures of thermocouples located within the NaK-filled regions, and one central thermocouple located in the central thermocouple well became unreliable. It has been necessary to switch the capsule upper region temperature control from one thermocouple to another on three occasions. In each case historical data was used to establish the temperature relationships for temperature control. The central thermocouple was used for a period to control the capsule upper region temperature. It was observed that the helium:argon ratio used for temperature control of the upper region had changed in relation to the indicated temperature. At that time it was concluded that the central thermocouple had become unreliable. Temperature of the upper capsule region was then controlled by holding a specified helium:argon ratio, which was determined from historical data. It now appears that the upper region of the capsule may have operated for an equivalent 78 d at 30 MW reactor power operation with the temperature as much as 17°C higher than the specified 600°C before it was decided that

the central thermocouple was unreliable. This did not affect the lower capsule region, which operated at the specified temperature of 500°C.

Through September 30, 1982, the MFE-4B capsule has accumulated an equivalent 406 d at 30 MW reactor power operation with a maximum specimen temperature in the upper region of 600°C, except for the equivalent 78 d at 30 MW reactor power operation period mentioned above, and in the lower region of 500°C.

2.2.5 References

1. K. R. Thoms and M. L. Grossbeck, "Operation of the ORR Spectral Tailoring Experiment ORR-MFE-4A," *ADIP Quart. Prog. Rep. Sept. 30, 1980,* DOE/ER-0045/4, pp. 20–24.
2. K. R. Thoms, "Operation of the ORR Spectral Tailoring Experiment ORR-MFE-4A," *ADIP Quart. Prog. Rep. March 31, 1981,* DOE/ER-0045/6, pp. 18–21.
3. I. T. Dudley, "Operation of the ORR Spectral Tailoring Experiments ORR-MFE-4A and ORR-MFE-4B," *ADIP Semiannu. Prog. Rep. Sept. 30, 1981,* DOE/ER-0045/7, pp. 24–29.
4. I. T. Dudley and J. A. Conlin, "Operation of the ORR Spectral Tailoring Experiments ORR-MFE-4A and ORR-MFE-4B," *ADIP Semiannu. Prog. Rep. March 31, 1982,* DOE/ER-0045/8, pp. 10–12.

2.3 HFIR/FFTF IRRADIATION EXPERIMENT – FINAL DESIGN PHASE – A. M. Ermi and D. L. Greenslade (Westinghouse Hanford Company) and J. M. Vitek (Oak Ridge National Laboratory)

2.3.1 ADIP Task

ADIP Task I.A.2, Define Test Matrices and Test Procedures.

2.3.2 Objectives

A combined HFIR/FFTF irradiation experiment is being planned to obtain mechanical properties data of nickel-bearing candidate alloys at high displacement damage levels (100-175 dpa) and the approximate helium concentration levels prototypic of a fusion reactor. By utilizing the HFIR for obtaining high helium production rates and the FFTF for high displacement damage rates, the high displacement damage at the appropriate He/dpa ratio (10-15 appm/dpa) can be achieved more rapidly than by utilizing existing single irradiation facilities.

2.3.3 Summary

The combined HFIR/FFTF experiment on the Path A Prime Candidate Alloy and the Path D Long-Range Ordered Alloys is in the final design stage. A sodium-filled test assembly to be used for the HFIR irradiations has been designed, the main features of which are described. The updated proposed test matrix is also presented.

2.3.4 Progress and Status

2.3.4.1 Introduction

Development of materials for fusion reactor first wall application requires that the material properties be characterized under the hostile first wall environment conditions. Since no high fluence fusion test facility is currently available for the fusion alloy development program, simulation studies must be undertaken in existing irradiation facilities. The HFIR/FFTF experiment is being jointly planned by Westinghouse Hanford Company (WHC) and Oak Ridge National Laboratory (ORNL) to achieve high displacement damage levels with the appropriate average He/dpa ratio for fusion reactors. Using the HFIR for obtaining high helium production

rates (in nickel-bearing alloys), and the FFTF for high displacement damage rates, it will he possible to achieve the desired displacement damage at the appropriate He/dpa ratio for a relatively large irradiation volume. Data from FMIT would then be used to extend this HFIR/FFTF engineering data.

2.3.4.2 Irradiation Plan and Test Matrix

The HFIR/FFTF experiment test plan consists of a series of irradiations alternating between the HFIR and the FFTF. Details of the irradiation scheme and specimen discharges have been described previously.[1]

Upon completion of a thorough space and damage accumulation analysis for the HFIR test capsule, additional specimens were added to the previously reported test matrix.[1] Included in the new matrix are additional specimen variants of the Path A Prime Candidate Alloy (PCA) and some Path D Long-Range Ordered (LRO) Alloys. The updated proposed test matrix is given in Table 2.3.1. There are likely to be no additional changes in the total number of each specimen, although changes are possible in the assignment of a specimen to a different alloy than that specified in the table.

The matrix presently consists of the two alloy classes (PCA and LRO), five specimen types (swelling, creep, tensile, fatigue crack growth and fracture toughness), and three irradiation temperatures *(400,* 500, and 600°C). The exact descriptions of the alloy variants will be specified once the general matrix has been finalized. The final test matrix will be reported in the next semi-annual progress report.

2.3.4.3 Description of Test Hardware

The test vehicle to be used in the FFTF phase of the experiment, the Materials Open Test Assembly (MOTA), has been described elsewhere.[2] An updated and more detailed description of the previously described[1] HFIR test assembly follows.

There are five criteria on which the current design has been based. The capsule design must:

1. Include features for monitoring and controlling specimen temperatures within specified limits.

Table 3.1 Proposed Test Matrix for the HFIR-FFTF Irradiation Experiment

Material	Specimen Type	Irrad. Path[a]	# of Alloy Variants	Duplications	# of Exams	# of Specimens at Each Temperature (°C) 400	500	600	Total # of Spec.
PRIME CANDIDATE ALLOY (PCA)	SWELLING (TEM)	1	7 Prim.	3	3	13	13	13	100
		1	7 2nd	3	3	10	10	10	
		2	7 Prim.	3	2	3	3	3	
	CREEP	1	2	4 Stresses	10	8	8	8	24[b]
	TENSILE	1	6	2	3	60	60	40	220
		2	3	2	2	24	24	12	
	FATIGUE CRACK GROWTH	1	2	3	3	18	18	9	45
	FRACTURE TOUGHNESS	1	1	1	6	6	0	0	6
LONG-RANGE ORDERED ALLOYS (LRO)	SWELLING (TEM)	1	3 Prim.	3	2	81	81	81	432
		1	3 2nd	3	2	27	27	27	
		2	3 Prim.	3	2	36	36	36	
	TENSILE	1	2	2	3	20	20	0	56
		2	2	2	2	3	3	0	

[a] Path 1: Irradiated in HFIR first.
Path 2: Skip first HFIR irradiation: Irradiate in FFTF first.

[b] Ten measurements obtained from each specimen.

2. Efficiently use the test volume that will accommodate the number and types of specimens at helium and dpa damage levels and irradiation temperatures required to meet the test's objectives.

3. Include safety features to minimize the probability of containment vessel failure to reduce the possibility of personnel injury, reactor damage, or destruction of test specimens.

4. Minimize hot cell handling and remote assembly/disassembly operations.

5. Minimize reactor down times for insertion and removal of the test assembly.

The RB1 large removable beryllium facility has been selected as the position for the test assembly in HFIR (Figure 2.3.1). It offers a location which can be instrumented, possesses a relatively large test volume (RB hole diameter = 3.56 cm), and yet retains a reasonable thermal flux for producing helium in nickel-bearing alloys.

The entire RB test assembly, shown in relation to the major HFIR components, is illustrated in Figure 2.3.2. The assembly consists of two main subassemblies: (1) a disposable RB test capsule which will contain the test specimens, and (2) a reusable instrumentation head which will house all instrumentation lines and serve as the interfacing structure. Each subassembly will be discussed in detail below.

2.3.4.3.1 RB Test Capsule. The RB test capsule (~2 m) will be inserted into the shroud flange and reactor core (active length = 51 cm). It will be mounted (with the instrumentation head) to the top of the shroud flange. The test capsule will be composed of two concentric, cylindrical containment vessels. The outer (secondary) containment vessel will be constructed of 6061-T6 aluminum alloy and will have a minimum wall thickness of 2.67 mm. It will be externally subjected to 750 psig coolant water at 55°C. The inner (primary) containment vessel will be constructed of austenitic stainless steel and have a minimum wall thickness of 0.762 mm. It will contain the various specimens located in weeper-type baskets stacked one upon the other. Different temperature zones will be separated by alumina (Al_2O_3) spacers. Sodium has been selected as the heat transfer medium to reduce temperature gradients within the primary vessel. The

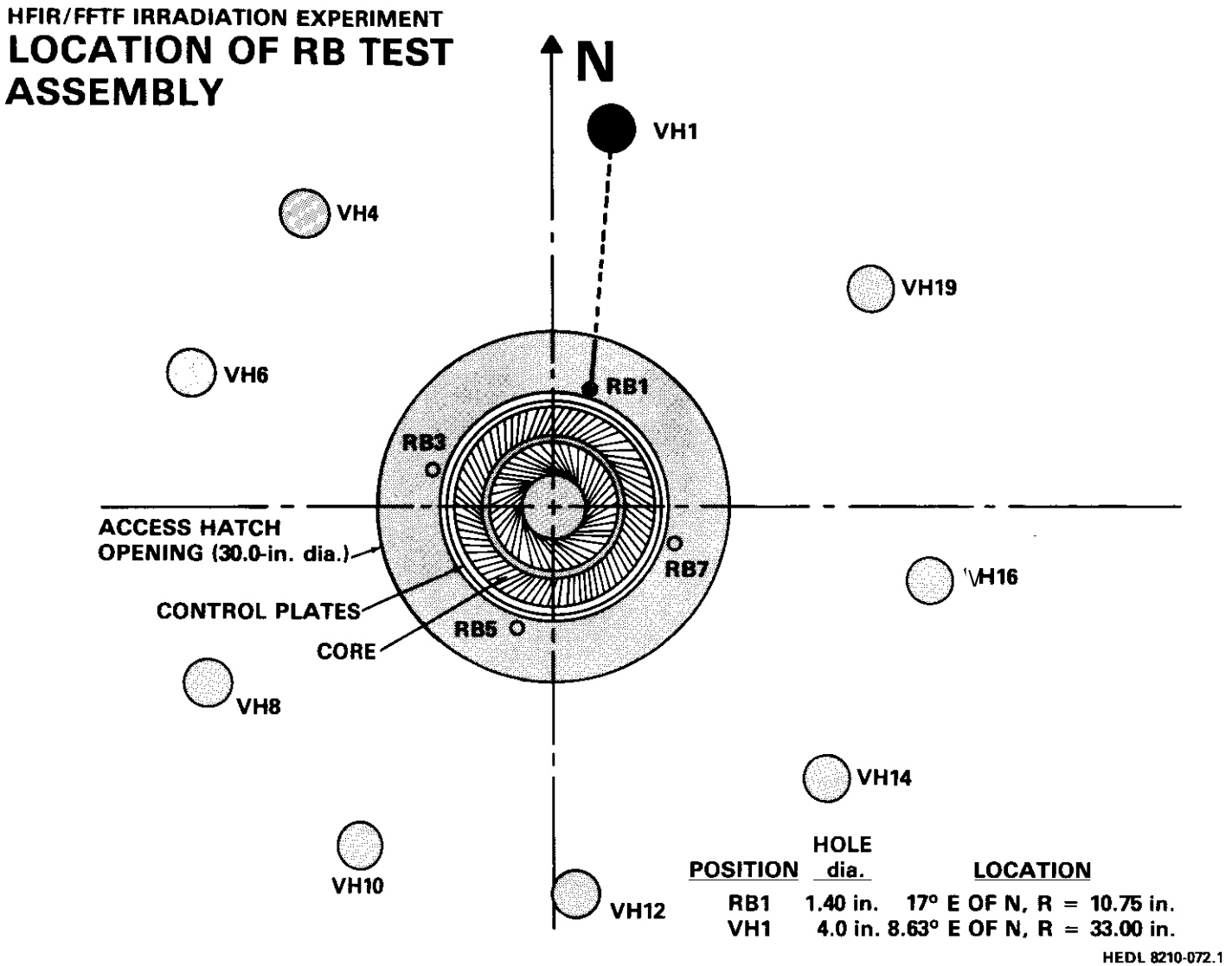

Fig. 2.3.1. Location of RB Test Assembly in HFIR - Horizontal Section.

HFIR/FFTF IRRADIATION EXPERIMENT

RB TEST ASSEMBLY IN HFIR - VERTICAL SECTION

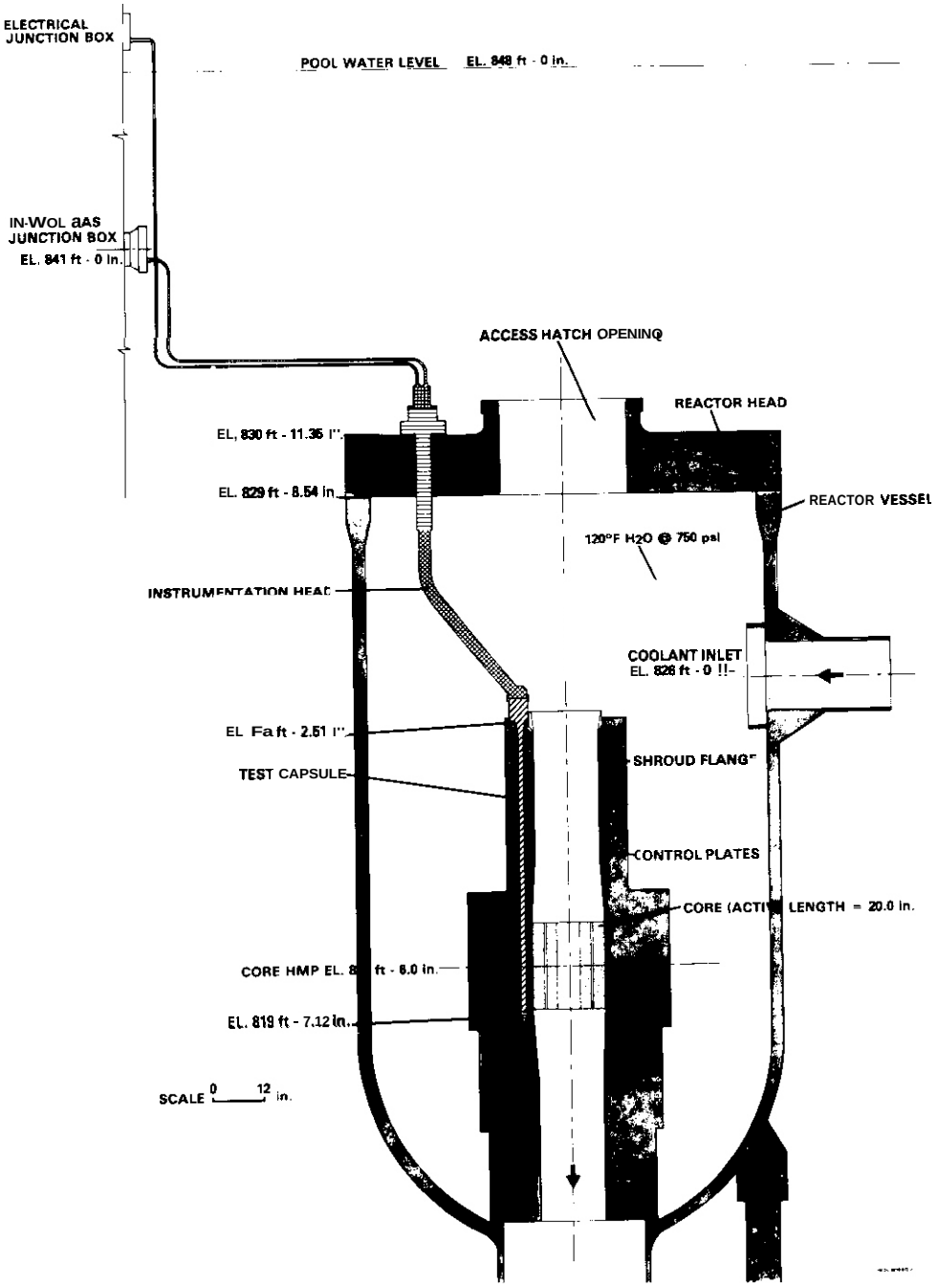

Fig. **2.3.2.** RB **Test Assembly** in HFIR **- Vertical Section.**

internal cover gas (He) pressure will be 5 psig. Irradiation temperatures of 400, 500 and 600°C will be achieved by utilizing an insulating gas (static He/Ne at 100 psig) between the secondary and primary vessel walls. The thermal conductivity of the gas (and thus temperature) will be controlled by varying the He/Ne gas mixture through inlet and outlet gas lines.

The RB test capsule instrumentation will include static gas pressure monitoring for the primary and secondary gases, centerline temperature monitoring at various specimen levels, and gas pressure monitoring of the o-ring sealed plenum at the top of the test capsule (a safety feature). The metal o-ring seals are the means by which the aluminum secondary vessel will be attached to the stainless steel primary vessel. High watt density preheaters will be used during each reactor start-up to prevent possible damage to the primary containment vessel and pressurized tube specimens due to localized melting and thus localized volumetric expansion of the sodium. The preheaters will provide a path for liquid sodium to flow to the free surface. Nine thermocouples, three preheaters and the secondary gas inlet line will be housed in an instrumentation tube located at the centerline of the primary vessel.

There are three above-core components within the primary vessel that are noteworthy. First, directly above the uppermost specimen level is a nickel-plated beryllium cylinder. Its purpose will be to prevent overheating of the above-core test capsule structures. The second component is the sodium reservoir which will facilitate sodium filling of the specimen region in the hot cell. Thirdly, the space above the reservoir is composed essentially of stainless steel to provide a shield to facilitate assembly/disassembly operations of the test assembly once the specimens have become activated. Details of the main features of this subassembly are shown in Figure 2.3.3.

2.3.4.3.2 Instrumentation Head. The instrumentation head will be mounted at both the top of the reactor head and the top of the shroud flange. It is a rigid hollow structure designed to protect all instrumentation lines from the turbulent flow of reactor coolant. Below the reactor head,

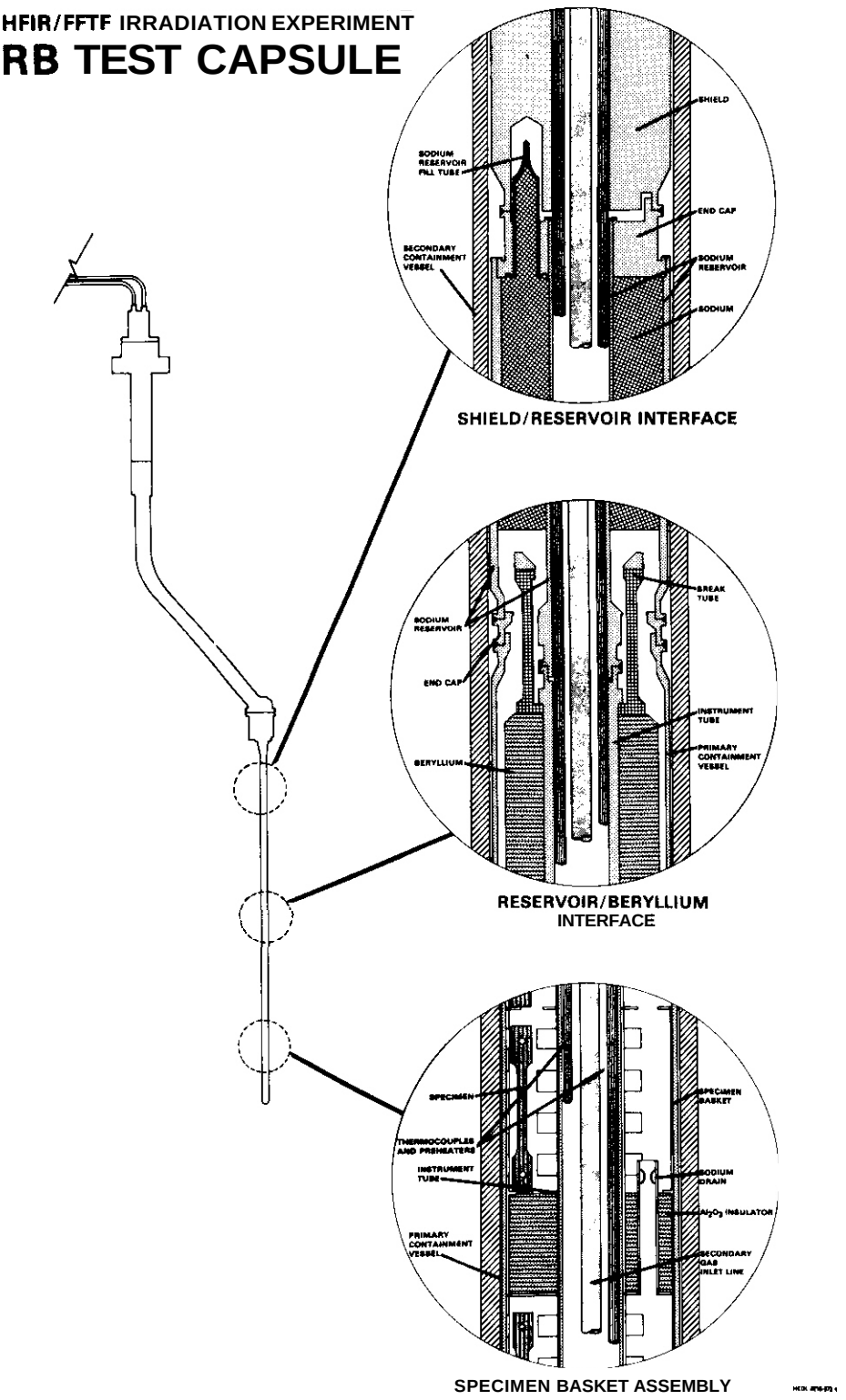

Fig. 2.3.3. RB Test Capsule Details.

the internal gas pressure will be 850 psig; above the reactor head, the internal gas pressure will be 50 psig. Thus, all internal pressures will he well above the local water pressure, which will reduce the probability of water ingress. Each of these pressures will be continuously monitored. Details of the main features of this subassembly are shown in Figure 2.3.4.

2.3.4.4 Specimen and Hardware Handling

A schematic summarizing the cyclical steps required for specimen and hardware handling throughout the experiment is shown in Figure 2.3.5. The RB test capsule will be discarded after each HFIR irradiation. Thus, a total of five capsules will be built. The instrumentation head, however, is planned to be reusable assuming radioactive contamination and activation can be kept at low levels.

2.3.5 Future Work

Once conditional approval of the experiment is given by the Reactcr Experiments Review Committee (RERC) at ORNL, procurement and fabrication of capsule parts can begin. The test matrix will be finalized by the end of CY82 with specimen loading scheduled for approximately July 1983.

2.3.6 References

1. A. M. Ermi and J. M. Vitek, "HFIR/FFTF Irradiation Experiment - Conceptual Plan," *ADIP Semi-Annual Progress Report, March 1982*, DOE/ER-0045/8.
2. R. E. Bauer, "Materials Open Test Assembly in the Fast Flux Test Facility," *Proceedings of the Conference on Fast, Thermal and Fusion Reactor Experiments*, Vol. II, Salt Lake City, Utah (April 1982

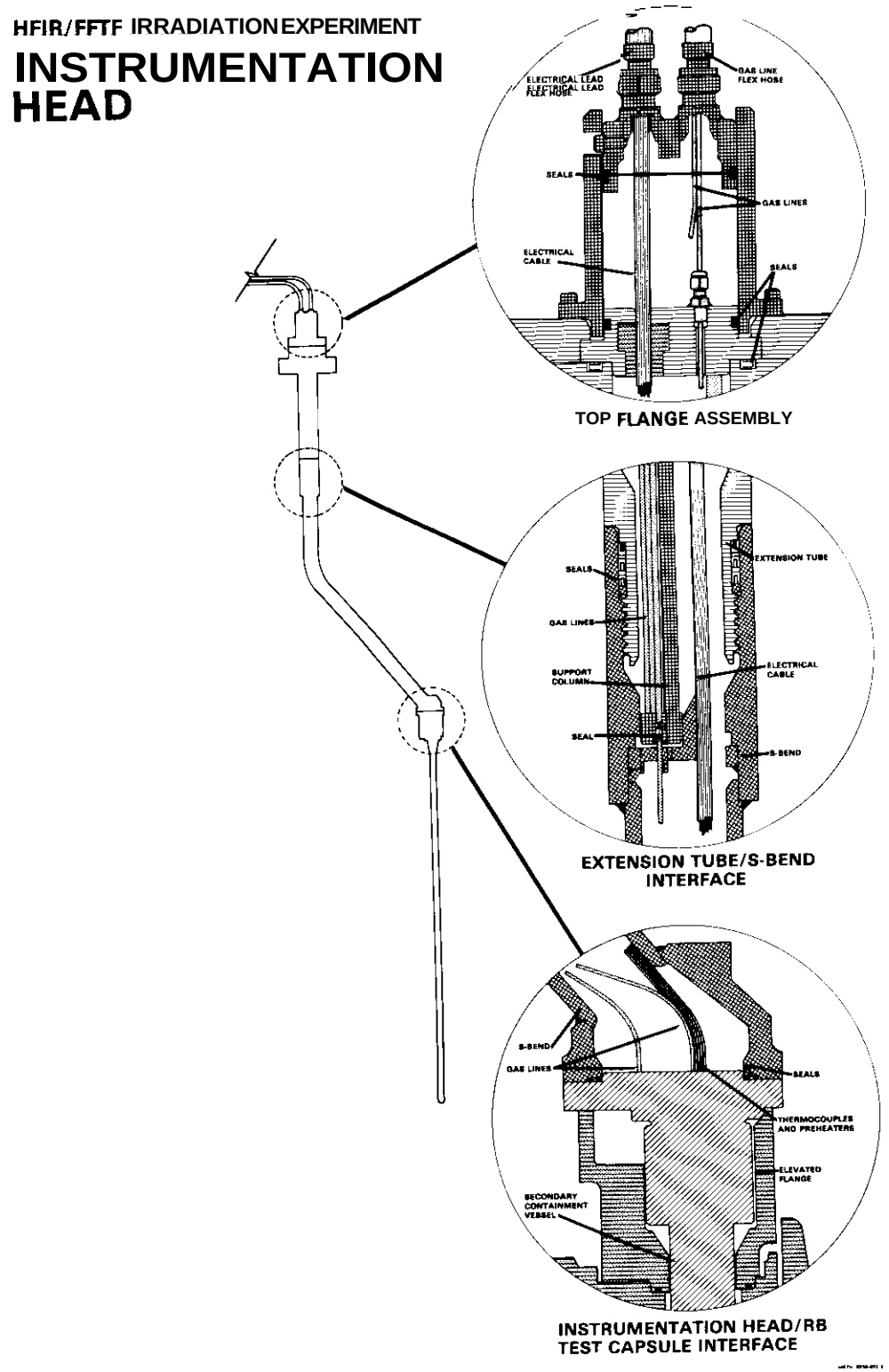

Fig. *2.3.4.* **Instrumentation Head Details.**

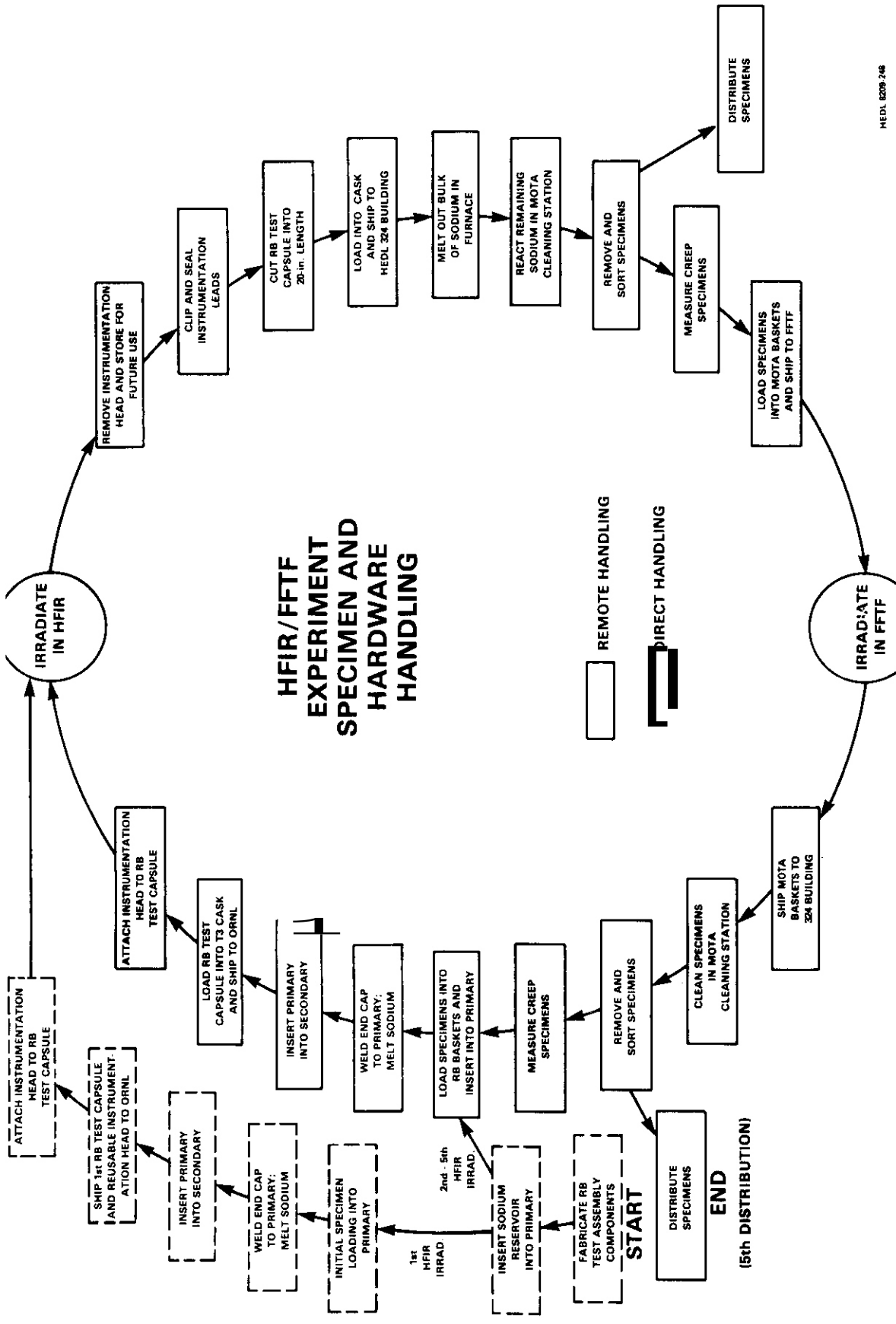

Fig. 2.3.5. Schematic of the Steps Required for Specimen and Hardware Handling.

2.4 NEUTRONICS CALCULATIONS IN SUPPORT OF THE ORR-WE-4 SPECTRAL TAILORING EXPERIMENTS — R. A. Lillie, T. A. Gabriel, and R. L. Childs (Oak Ridge National Laboratory)

2.4.1 ADIP Task

ADIP Task I.A.2, Define Test Matrices and Test Procedures.

2.4.2 Objective

The objective of this work is to provide the neutronic design for materials irradiation experiments in the Oak Ridge Research Reactor (ORR). Spectral tailoring to control the fast and thermal fluxes is required to provide the desired displacement and helium production rates in alloys containing nickel.

2.4.3 Summary

The calculated fluences from the ongoing three-dimensional neutronics calculations are being scaled to agree with experimental data. As of October 11, 1982, this treatment yields 46.25 at. ppm He (not including 2.0 at. ppm He from ^{10}B) and 4.97 dpa for type 316 stainless steel in ORR-MFE-4A and 40.18 at. ppm He and 4.55 dpa in ORR-MFE-4B.

2.4.4 Progress and Status

The operating and current calculated data for the ORR-MFE-4A and -4B experiments are given in Table 2.4.1. Fluences have been scaled by 0.76 to agree with the experimentally measured fluences' and helium production.'

The real-time projections of the helium-to-displacement ratios based on current calculated data as of October 11, 1982 are given in Figs. 2.4.1 and 2.4.2 for the ORR-MFE-4A and -4B experiments, respectively. The projected dates were obtained by assuming an ORR duty factor of *0.86.* Based on current data, the core piece change dates for the ORR-MFE-4A experiments are June 11, 1983 (to a solid aluminum core piece) and September 11, 1984 (to the first hafnium core piece). For the ORR-MFE-4B experiment, these dates are August 11, 1983 and September 11, 1984,

respectively. These corepiece changes will ensure proper helium production to displacement level ratios over the anticipated lifetimes of the experiments[3] (i.e., to greater than 50 dpa).

2.4.5 Future Work

The three-dimensional neutronics calculations that monitor the radiation environment of the ORR-MFE-4 experiments will continue with each ORR reactor cycle. The fluences from these ongoing calculations will continue to be scaled by 0.76 until the scale factor can be updated as new experimental fluences become available.

Table 2.4.1. Operating and Calculated Data for Experiments ORR-MFE-4A and -4B as of October 11, 1982

	ORR-MFE-4A	ORR-MFE-4B
ORR cycles	38	31
Power (MWh)	304,498	299,379
Equivalent full-power days[a]	422.9	415.8
Thermal fluence (neutrons/m^2)	6.25×10^{25}	5.79×10^{25}
Total fluence (neutrons/m^2)	1.96×10^{26}	1.81×10^{26}
Helium (at. ppm)[b]	46.25	40.18
dpa[b]	4.97	4.55

[a] Full power for ORR is 30 MW.

[b] Helium and dpa values are for type 316 stainless steel.

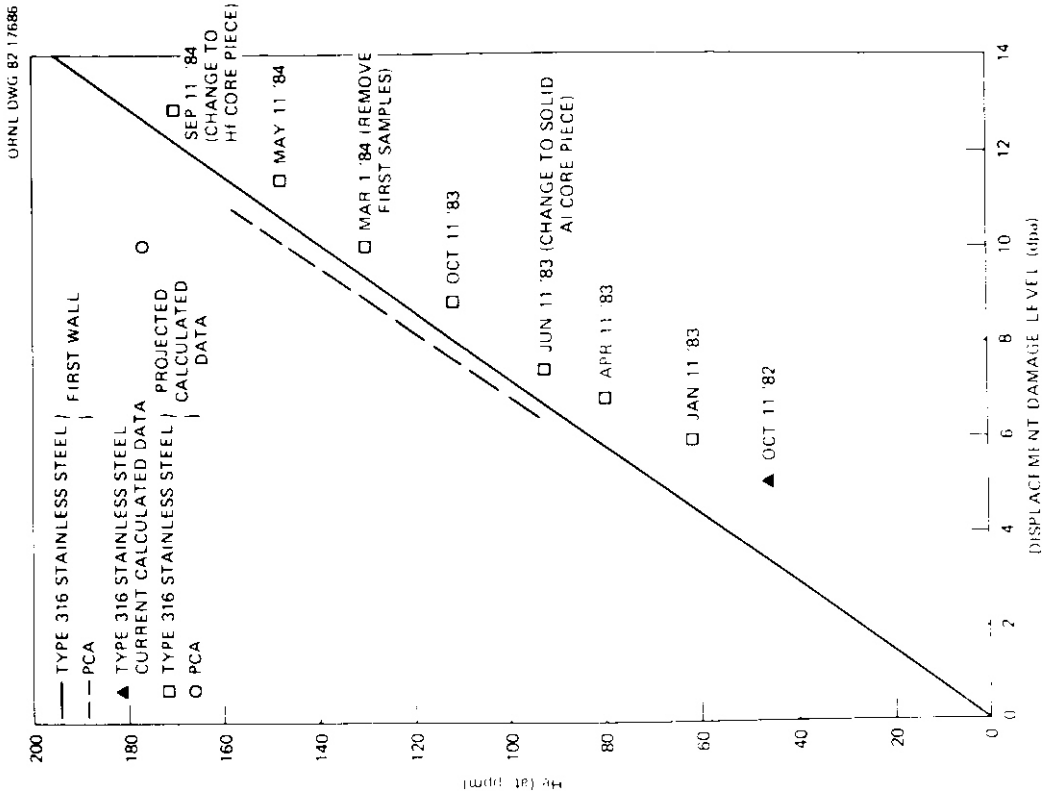

Fig. 2.4.1. Current and Projected Helium and Displacement Damage Levels in the ORR-MFE-4A Experiment.

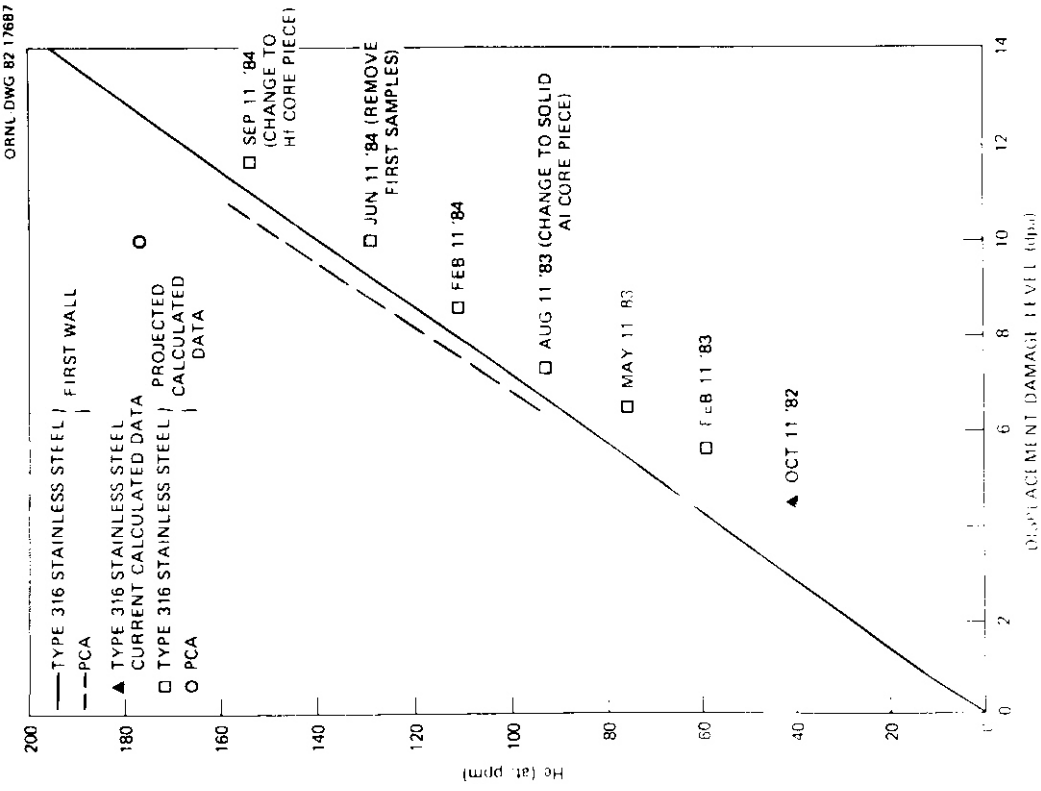

Fig. 2.4.2. Current and Projected Helium and Displacement Damage Levels in the ORR-MFE-4B Experiment.

2.4.6 References

1. L. R. Greenwood, "Neutron Source Characterization for Materials Experiments," *ADIP Semiannu. Prog. Rep. Sept. 30, 1981,* DOE/ER-0045/7, pp. 8–19.
2. J. G. Bradley, *Helium in Nickel and Stainless Steel Irradiated in the ORR-MFE-4A Experimental Assembly,* 82E5G-211, Rockwell International, Canoga Park, Calif. (Jan. 19, 1982).
3. T. A. Gabriel, R. A. Lillie, B. L. Bishop, and R. L. Childs, "Neutronics Calculations in Support of the ORR-MFE-4A Spectral Tailoring Experiment," *ADIP Quart. Prog. Rep. June 30, 1980,* DOE/ER-0045/3, pp. 7–9.

3. PATH A ALLOY DEVELOPMENT – AUSTENITIC STAINLESS STEELS

3.1 IRRADIATION CREEP IN PATH A ALLOYS IRRADIATED TO 5 dpa IN THE ORR-MFE-4A SPECTRAL TAILORING EXPERIMENT — M. L. Grossbeck (Oak Ridge National Laboratory)

3.1.1 ADIP Task

ADIP Task I.C.6, Irradiation Creep in Austenitic Alloys.

3.1.2 Objective

The experiment will measure irradiation creep in an environment that produces helium with the He:dpa ratio characteristic of a fusion reactor.

3.1.3 Summary

Pressurized tubes have been irradiated to 4.8 dpa at 330 and 400°C in the ORR-MFE-4A spectral tailoring experiment. At 330°C, 20%-cold-worked type 316 stainless steel (CW 316) and path A PCA demonstrated irradiation creep similar to predictions of the irradiation creep equation developed in the Fast Breeder Reactor Program. The creep rate for path A PCA was approximately 25% higher than that of type 316 stainless steel.

3.1.4 Progress and Status

3.1.4.1 Introduction

The ORR-MFE-4 spectral tailoring experiment has been designed to irradiate path A alloys under conditions producing an He:dpa ratio characteristic of a fusion reactor first wall. This is achieved by tailoring the neutron spectrum by changing the immediate environment of the irradiation capsule as irradiation proceeds. The surrounding region is changed from water to aluminum to hafnium in order to progressively decrease the thermal component of the flux as ^{59}Ni is produced from ^{58}Ni. The nickel produces helium through the reaction sequence

$$^{58}Ni(n,\gamma)^{59}Ni$$

and

$$^{59}Ni(n,\alpha)^{56}Fe \ .$$

At intervals of approximately 10 dpa the capsule is removed from the reactor; the specimens are recovered and either destructively examined or examined and returned to the reconstituted irradiation vehicle. The irradiation creep experiment employs specimens that are measured at each removal interval and then returned for continued fluence accumulation. It will provide data on neutron irradiation creep with internal helium generation and displacement damage production in the proportion characteristic of the fusion environment. No previous data of this nature exist.

3.1.4.2 Experimental Procedure

Commercially drawn tubing of 4.57-mm (0.180-in.) outside diameter, with 0.25-mm (0.010-in.) wall thickness, was prepared from the fusion program reference type 316 stainless steel, heat X15893, and path A PCA, heat K 280, in the 20- and 25%-cold-worked conditions, respectively. Specimens of the type shown in Fig. 3.1.1 were prepared and pressurized to the stress levels indicated in Table 3.1.1.

The specimens were irradiated in the Oak Ridge Research Reactor (ORR) in the ORR-MFE-4A experiment. The tubes were contained in NaK at controlled temperatures of 330 and 400°C. The specimens were removed for examination at a fluence level of 0.62×10^{26} neutrons/m^2 ($E > 0.1$ MeV), which had produced 4.8 dpa in both alloys and helium levels of 43 at. ppm in type 316 stainless steel and 56 at. ppm in path A PCA.

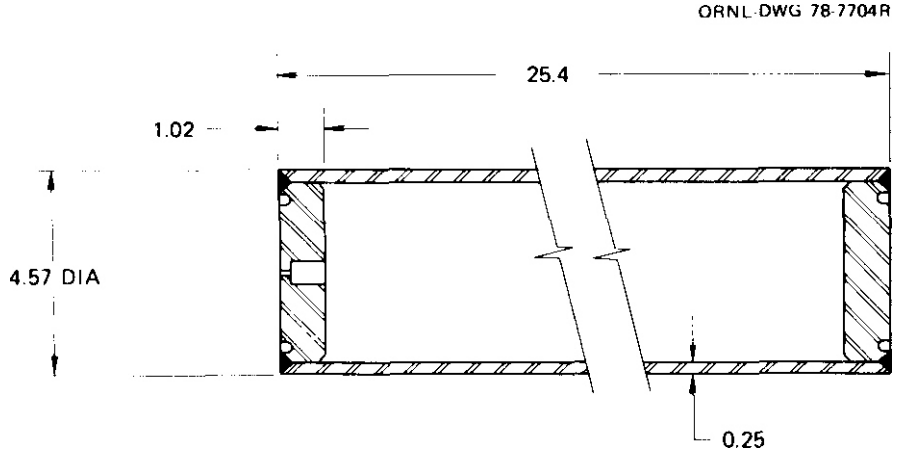

Fig. 3.1.1. Pressurized Tube Specimen Used in Irradiation Creep Experiments in the ORR Spectral Tailoring Experiment. Dimensions in mm.

Table 3.1.1. Irradiation Creep Measurements for Two Path A Alloys Irradiated in ORR-MFE-4A to 4.8 dpa

Specimen	Hoop Stress (MPa)	Effective Stress (MPa)	Irradiation Temperature (°C)	Diametral Strain, $\Delta D/D$ (%)	Effective Strain (%)
20%-Cold-Worked Type 316 stainless Steel *(Heat X15893)*					
AC60	103	89.5	330	0.0049	0.0065
AC53	188	163	330	0.031	0.041
AC91	209	181	330	0.088	0.12
AC85	261	227	330	0.077	0.10
AC84	314	272	330	0.13	0.17
AC82	419	363	330	0.23	0.31
AC80	472	409	330	0.19	0.25
AC55	100	86.6	400	-0.0066	−0.0088
AC61	150	130	400	0.057	0.076
AC45	150	130	400	0.078	0.10
AC62	200	173	400	0.0060	0.0080
AC70	250	217	400	0.11	0.15
AC71	300	260	400	0.053	0.071
AC75	450	390	400	0.080	0.11
25%-Cold-Worked PCA (Heat *K 280*)					
EB61	103	89.5	330	0.035	0.047
EB44	209	181	330	0.029	0.039
EB14	261	227	330	0.163	0.217
EB73	314	272	330	0.194	0.258
EB43	366	317	330	0.184	0.245
EB33	419	363	330	−0.098	−0.13[a]
EB23	472	409	330	0.337	0.448
EB62	100	86.6	400	0.026	0.035
EB65	150	130	400	0.045	0.060
EB74	200	173	400	0.086	0.11
EB24	250	217	400	-0.065	−0.087
EB72	300	260	400	0.088	0.12
EB93	350	303	400	−0.017	−0.023
EB53	400	346	400	0.094	0.13

[a]This tube had apparently developed a leak.

Profilometry measurements were made by a computer-controlled stylus-type laser interferometer. A total of 800 diameter measurements on each tube were used to calculate an average diameter for the central three-fifths of the tube. The instrument is capable of a precision of ±250 nm (±1 x 10^{-5} in.).

3.1.4.3 Results

Results of the diametral measurements appear in Table 3.1.1 and are plotted in Fig. 3.1.2. The strain values have not been corrected for swelling because density measurements indicate no measurable swelling at this low fluence. No correction has been made for thermal creep, because it too is expected to be negligible at these temperatures.

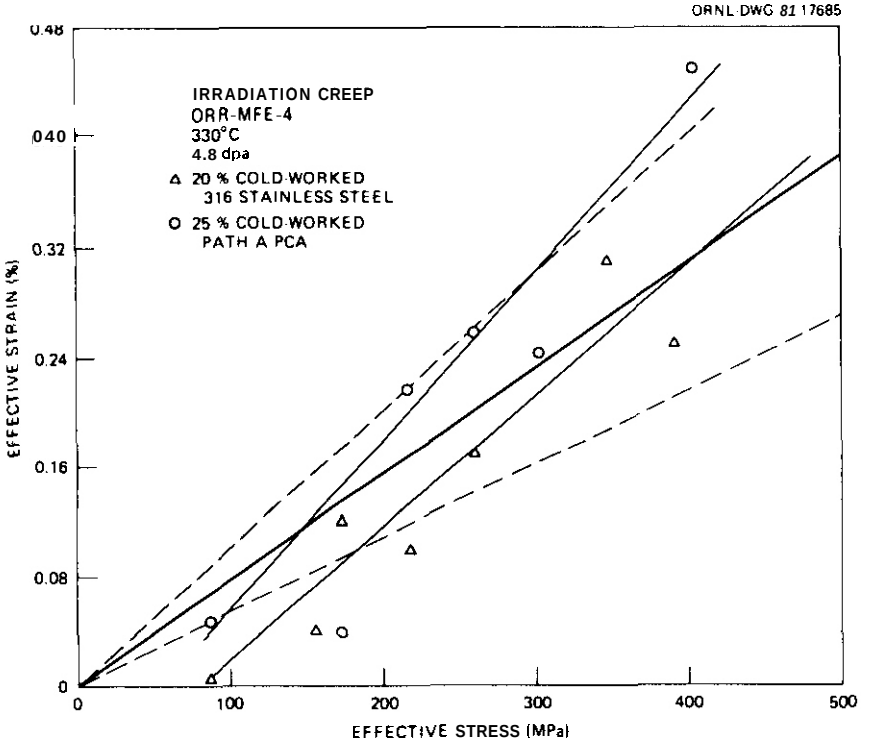

Fig. 3.1.2. Effective Strain as a Function of Effective Stress for Cold-Worked Type 316 Stainless Steel and Path A PCA Irradiated to 4.8 dpa at 330°C. The light lines are approximate trend lines for the data. The equation for EBR-11-irradiated type 316 stainless steel is plotted as the bold line with its ±30% uncertainty limits shown by dashed lines. B. J. high, E. R. Gilbert, and B. A. Chin, "An In-Reactor Creep Correlation for 20% Cold Worked AISI 316 Stainless Steel," p. 108 in *Effects of Radiation on Materials*, ASTM-STP-782, American Society for Testing and Materials, Philadelphia, 1982.

The creep strain at 330°C appears to be a linear function of stress for both alloys investigated. The stress coefficients of creep are 9.2×10^{-6}/MPa and 1.2×10^{-5}/MPa for type 316 stainless steel and path A PCA, respectively. Both alloys exhibited a threshold stress for creep, but this is not understood at the present. One possible explanation is that the threshold results from densification. By use of an expression for densification of austenitic stainless steels,' the entire shift can be accounted for. This phenomenon will be considered further, and a more complete analysis of the data will be given when higher fluence measurements are available.

3.1.4.4 Discussion

Figure 3.1.2 shows the dependence of the irradiation creep strain on stress at 330°C. Also plotted is an expression for irradiation creep of CW 316 FFTF first-core heat based on EBR-II irradiation.[2] The dashed lines show the associated recommended limits of error. The plot is based on dpa, rather than fluence, in order to better correlate results from the two reactors (EBR-II and ORR). Most of the data fall within this limit of error. If the apparent threshold stress for irradiation creep is due to a systematic error, it could be corrected by shifting the data until the trend curve passes through the origin. This treatment would improve the fit to the EBR-II relation for the type 316 stainless steel data, although the PCA will still appear to have a high creep rate. Because the He:dpa value is still lower than desired,[3] the creep behavior may still be shown to be affected by the presence of high helium levels. Higher fluence data will be required to address this possibility.

No significance can be attributed to higher values of creep observed in path A PCA. Only when higher values of fluence are attained can conclusions be drawn. If the higher creep rate is in fact real, then irradiation creep may help relieve stress induced by swelling. Because the swelling rate of PCA appears lower than that of type 316 stainless steel,[4] the PCA might experience lower levels of swelling-induced stresses.

A relation for irradiation creep in a fusion environment, incorporating fast breeder and thermal reactor data, has been formulated by Gilbert and Garner.[5] This relation overpredicts the data for type 316 stainless by a factor of about 2.7. However, better agreement might be obtained when higher fluences and helium levels are attained.

There appears to be significant densification of both alloys during irradiation at 400°C. As a result, no trend in irradiation creep behavior could be determined from these low-fluence data.

3.1.5 Conclusions

Irradiation creep in CW 316 and 25%-cold-worked Path A PCA irradiated at 330°C in ORR to a fluence producing 5 dpa and 43 to 56 at. ppm He is similar to predictions based on data generated in EBR-II. Similar exposure at 400°C resulted in very small net strain. The pressurized tubes have been returned to the ORR-MFE-4A experiment for continued fluence accumulation.

3.1.6 References

1. F. A. Garner, private communication, Hanford Engineering Development Laboratory, 1980.
2. B. J. Puigh, E. R. Gilbert, and B. A. Chin, "An In-Reactor Creep Correlation for 20% Cold Worked AISI 316 Stainless Steel," p. 108 in Effects of Radiation on *Materials,* ASTM-STP-782, American Society for Testing and Materials. Philadelphia, 1982.
3. R. A. Lillie, R. L. Childs, and T. A. Gabriel, "Neutronic Calculations in Support of the ORR-MFE-4 Spectral Tailoring Experiment," *ADIP Quart. Prog. Rep. Dec. 31, 1980,* DOE/ER-0045/5, pp. 15–18.
4. P. J. Maziasz and D. N. Braski, "Swelling and Microstructural Development of Path A PCA and Type 316 Stainless Steel Irradiated in HFIR to ~22 dpa," Sect. 3.2 of this report.
5. E. R. Gilbert and F. A. Garner, "Development of an Irradiation Creep Correlation for 20% Cold-Worked AISI 316 in Fusion Environments," *DAFS Quart. Prog. Rep. Sept. 30, 1980,* DOE/ER-0046/3, p. 190.

3.2 SWELLING AND MICROSTRUCTURAL DEVELOPMENT IN PATH A PCA AND TYPE 316 STAINLESS STEEL IRRADIATED IN HFIR TO ABOUT 22 dpa — P. J. Maziasz and D. N. Braski (Oak Ridge National Laboratory)

3.2.1 ADIP Task

ADIP Task I.C.2, Microstructure and Swelling in Austenitic Alloys.

3.2.2 Objective

This work is intended to evaluate the effect of preirradiation microstructural variation on swelling of path A PCA irradiated in the High Flux Isotope Reactor (HFIR). The results will be compared with results on several heats of types 316 and 316 + Ti stainless steel similarly irradiated.

3.2.3 Summary

Irradiation of several microstructural variants of PCA and 20%-cold-worked N-lot type 316 stainless steel (CW 316) in HFIR to about 10 dpa produced no visible cavities at 300°C, bubbles at 400°C, and varying distributions of bubbles and voids at 500 and 600°C. The PCA-B1 swells the most and CW 316 (N-lot) the least at 600°C. Irradiations have been extended to about 22 dpa. The PCA-A1 swells 0.06%/dpa at 600°C but at a much lower rate at 500°C. The PCA-A3 shows the lowest swelling at 600°C, about half the swelling rate of type 316 stainless steel.

3.2.4 Progress and Status

This work continues the evaluation of swelling in various preirradiation microstructural conditions of the Path A Prime Candidate Alloy (PCA) begun previously.[1] The details and experimental plan for the series of experiments HFIR-CTR-30, -31, and -32 have also been presented elsewhere.[2] The last report presented results on material irradiated to about 10 dpa over the irradiation temperature range 300 to 600°C. This work includes results on specimens irradiated to about 22 dpa in the same temperature range.

3.2.4.1 Experimental

Specimens of various thermallnechanical pretreatments of path A PCA as well as CW 316 (N-lot) were irradiated in HFIR-CTR-31 and -32 in the form of 3-mm-diam, 0.25-mm-thick disks. The compositions of path A PCA, N-lot type 316 stainless steel, and several other relevant alloys are given in Table 3.2.1. The thermal-mechanical treatments necessary to produce microstructural variants of PCA are summarized in Table 3.2.2 and have been described previously.[3]

Table 3.2.1. Compositions of Several Austenitic Stainless Steels

Alloy	Alloy Composition (wt %)										
	Fe	Cr	Ni	Mo	Mn	Si	C	Ti	P	S	N
Path A PCA	Bal	14.0	16.2	2.3	1.8	0.4	0.05	0.24	0.01	0.003	0.01
316 + Ti (R1-heat)	Bal	17.0	12.0	2.5	0.5	0.4	0.06	0.23	0.01	0.013	0.006
316 (DO-heat)	Bal	18.0	13.0	2.6	1.9	0.8	0.05	0.05	0.01	0.016	0.05
316 (N-lot)	Bal	16.5	13.5	2.5	1.6	0.5	0.05		0.09	0.006	0.006

Neutron dosimetry for HFIR-CTR-32 has been reported by Greenwood.[4] The values of thermal and fast neutron fluences are used to calculate the dpa and helium values that were approximated in the last report.[1] These include the important correction to the dpa for the recoil of nickel atoms from helium production, as pointed out by Greenwood.[4]

The irradiation temperatures for HFIR-CTR-30, -31, and -32 were calculated from higher nuclear heating values than those used for earlier HFIR-CTR experiments. These values were based on the same information that led us to suspect that previously calculated temperatures were lower by about 50 to 75°C than the actual irradiation temperatures, and the use of these values led to an upward revision of these temperatures.[1] That revision is not necessary for HFIR-CTR-30, -31, and -32. Early indications from temperature monitors suggest good agreement (±25°C) between

Table 3 Z Z Prei<<adiation Microstructures of the Path A Prime Candidate Allo> (PCA)

Designation		Description of Microstructure	Thermal-Mechanical Treatment
A		Simple microstructures resulting from	
	A1	solution annealing,	25% cold worked plus 15 min at 1175°C
	A2	5 to 10% cold working, or	15 min at 1175°C (A1) plus 10% cold worked
	A3	20 to 25% cold working.	15 min at 1175°C (A1) plus 25% cold worked
B		Microstructures with both coarse grain boundar> MC precipitation and intragraoula< MC precipitation consistinz of	
	B1	coa<se particles or particle clus⊂ers, o<	Solution annealed (A1) plus ∃ h at 800°C plus 8 h at 900°C
	B2	fine mat<ix <eci<itatio~	Solution annealed (A1) plus ∃ h at 800°C plus 25% cold worked plus 2 h at 750°C
C		Microstructures with both fine grain boundary MC precipitation and fine intragranular MC matrix precipitation	Solution annealed (A1) plus Z∃% cold worked plus 2 h at 750°C
		Microstructures with both fine grain boundary MC precipitation and fine intragranular MC matrix precipitati⊏ plus increased dislocation density.	Solution annealed (A1) plus 10% cold worked plus 2 h at 750°C plus 10% cold worked

calculated and actual irradiation temperatures. A report on these same experiments (HFIR-CTR-30 to -32) by the MIT group was confused on this point.[6]

3.2.4.2 Temperature and Fluence Dependence of Swelling

Cavity volume fraction (cvf) swelling values for the several microstructural conditions of PCA and for CW 316 (N-lot) irradiated at 300 to 600°C to 9.6 to 10.6 dpa (375–555 at. ppm He) are given in Table 3.2.3. The results on PCA-A1, -A2, and -C were reported previously,[1] but the results on PCA-B1 and -B2 and CW 316 (N-lot) are completed in this report. The swelling as a function of irradiation temperature at about 10 dpa is plotted for PCA variants and N-lot type 316 stainless steel in Fig. 3.2.1 and at about 22 dpa in Fig. 3.2.2. Comparable results for previously determined[7,8] swelling of CW 316 (DO-heat) and CW 316 + Ti (R1-heat) are also included in these figures.

Each PCA variant and N-lot CW 316 irradiated to 10 dpa showed monotonically increasing swelling with increasing irradiation temperature over the range 300 to 600°C. No cavity swelling was found in any of these specimens at 300°C. The PCA-A1, -A2, and -B2 irradiated at 400°C did not contain any cavities, but PCA-B1 and -C and CW 316 (N-lot) show measurable cavity swelling. For irradiation at 500 and 600°C, swelling tends to increase with increasing temperature for any given alloy-pretreatment combination. After irradiation at 500°C, PCA-A2 and -B1 show the highest swelling (0.33–0.36%) and PCA-A1 and CW 316 (N-lot) show the lowest (0.05%). For 600°C irradiation, PCA-A2 and -B1 are again the highest swelling (1.1–1.2%), PCA-A1 begins to swell significantly, and CW 316 (N-lot) is again the lowest swelling alloy (0.2%).

Samples of CW 316 (N-lot) were examined after irradiation in HFIR at 500 and 600°C to 21.8 dpa (1438–1474 at. ppm He). Samples of PCA-A1 and -A3 irradiated at 600°C to 22.3 dpa (1757 at. ppm He) were also examined. Swelling values (cvf) are given in Table 3.2.3 and their temperature dependence can be seen in Fig. 3.2.2. The temperature dependence of CW 316 (N-lot) seems parallel to that observed at the lower fluence. As

Table 3.2.3. Swelling for 20%-Cold-Worked N-lot Type 316 Stainless Steel and Various Pretreatments of Prime Candidate Alloy Irradiated in HFIR

Alloy and Microstructural Condition[a]	Irradiation Temperature (°C)	Neutron Fluence >0.1 MeV (neutrons/m^2)	Displacement Damage Level[b] (dpa)	Helium Content (at. ppm)	Cavity Volume Fraction Swelling (%)
N-lot 316	300	1.21 x 10^{26}[c]	9.6	375	n.d.[d]
	400	1.26	10.4	435	0.06
	500	1.26	10.4	435	0.05
	600	1.25	10.4	465	0.2
	500	2.52[e]	-21.8	1438	0.26
	600	2.50	-21.8	1474	0.4–0.5
PCA-A3	600	2.50	-22.3	1757	0.20–0.25
PCA-A1	300	1.21	9.7	450	n.d.
	400	1.26	10.5	520	n.d.
	500	1.26	10.5	520	0.05
	600	1.25	10.6	555	0.66
	600	2.50	-22.3	1757	1.2
PCA-B1	300	1.21	10.5	510	n.d.
	400	1.26	10.5	510	0.04
	500	1.26	10.6	550	0.33
	600	1.25	10.6	550	1.2
PCA-B2	300	1.21	10.5	510	n.d.
	400	1.26	10.5	510	n.d.
	500	1.26	10.6	550	0.16
	600	1.25	10.6	550	0.4
PCA-A2	300	1.21	10.5	510	n.d.
	400	1.26	10.5	510	n.d.
	500	1.26	10.6	550	0.36
	600	1.25	10.6	550	1.1
PCA-C	300	1.21	10.5	510	n.d.
	400	1.26	10.5	510	0.25
	500	1.26	10.6	550	0.32
	600	1.25	10.6	550	0.7

[a] See Table 3.2.2.

[b] The contribution produced by recoils during helium production is included. See ref. 4.

[c] Dosimetry from Greenwood.

[d] Not detectable by transmission electron microscopy.

[e] Assuming double the fluence of HFIR-CTR-32; dosimetry is still in progress.

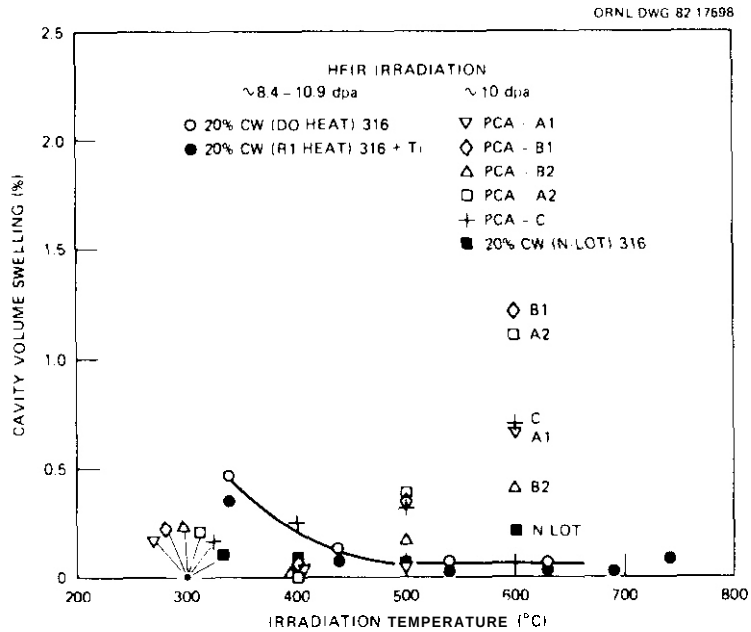

Fig. 3.2.1. Cavity Volume Fraction Swelling as a Function of HFIR Irradiation Temperature for Fluences Producing About 10 dpa. Several microstructural variants of PCA, two heats of type 316 stainless steel and one titanium-modified heat of type 316 stainless steel are included.

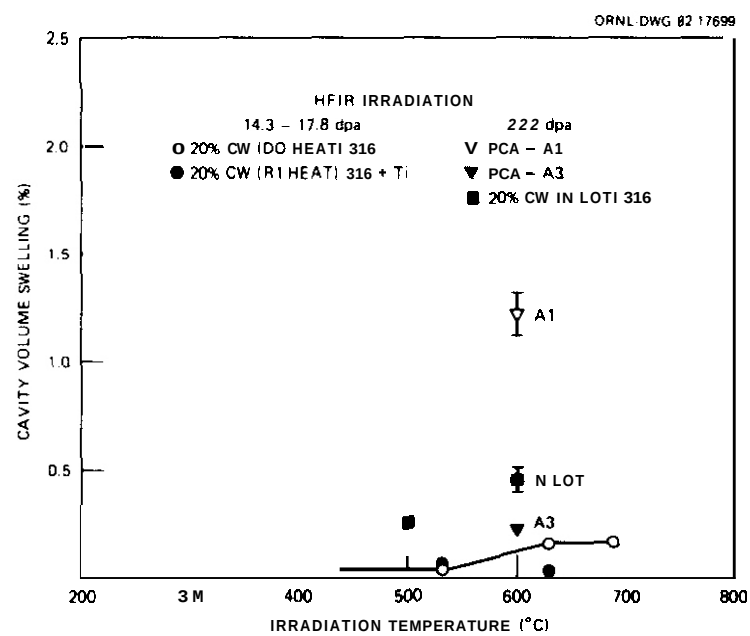

Fig. 3.2.2. Cavity Swelling as a Function of HFIR Irradiation Temperature for PCA-A1, -A3, and Several Heats of Type 316 Stainless Steel. Irradiations were for fluences producing 14 to 22 dpa.

at the lower fluences, Fig. 3.2.2 shows that in the 500 to 600°C range R1- and Do-heats have cavity swelling values of 0.15% or less, much less than PCA-A1 or (N-lot) type 316 stainless steel.

The temperature dependence of swelling for CW 316 (DO-heat) and CW 316 + Ti (R1-heat) at 8 to 18 dpa is opposite to that described above for the various E A pretreatments and CW 316 (N-lot) (see Figs. 3.2.1 and 3.2.2). Instead of swelling increasing with irradiation temperature, maximum swelling (0.35-0.5%) of the DO- and R1-heats of steel occurred at the lower temperature of 325 to 350°C and decreased with increasing temperature of irradiation.

The values of swelling at 500 and 600°C for CW 316 (N-lot) and at 600°C for EA-A1 increase almost linearly with increasing fluence, shown in the plot of swelling as a function of fluence in Fig. 3.2.3. The PCA-A3, examined for the first time here, shows lower swelling than CW 316 (N-lot) at 600°C. The swelling values of various PCA pretreatments and CW 316 (N-lot) are compared with both Do- and R1-heats of steel in Fig. 3.2.3. The R1-heat exhibits the lowest swelling values and the

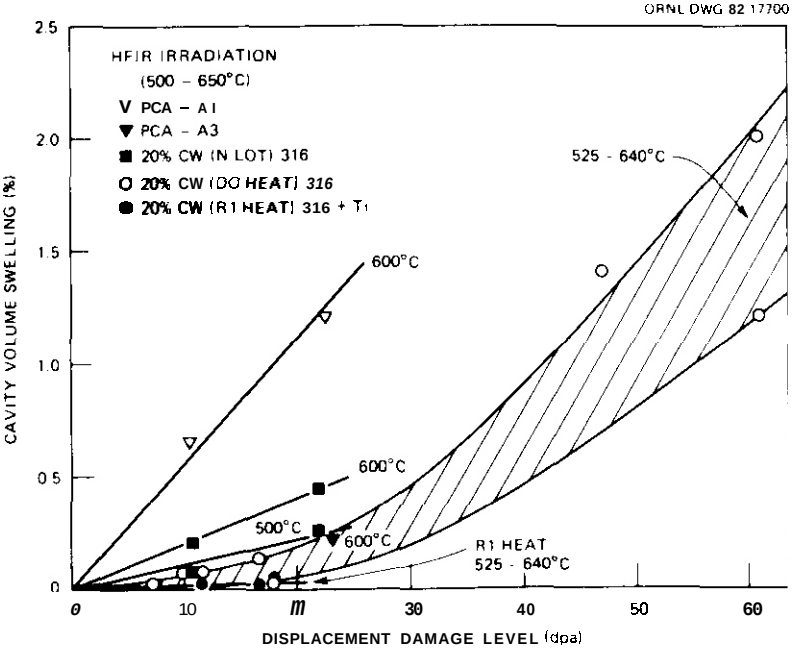

Fig. 3.2.3. Swelling as a Function of Fluence for PCA-A1 Irradiated in HFIR at 600°C and CW 316 (N-lot) at 500 and 600°C. Previous data on CW 316 (DO-heat) and CW 316 + Ti (R1-heat) irradiated at 525 to 640°C are included for comparison.

lowest fluence dependence of the steels, falling on the low side of the scatter band for CW *316* (DO-heat). This scatter band is used as a reference because it extends to fairly high fluences (-61 dpa). Relative to DO-heat, N-lot type *316* stainless steel exhibits a parallel but higher level of swelling with fluence. The EA-A1 is the highest swelling of the group, and PCA-A3 falls within the DO-heat type *316* stainless steel scatter band. These two FCA pretreatment variants demonstrate the amount of swelling variation that can be obtained by preirradiation microstructural manipulation.

3.2.4.3 Microstructural Development

The fluence dependence of microstructural development at *500* and 600°C in CW *316* (N-lot) is illustrated at two magnifications in Figs. 3.2.4 and *3.2.5.* These indicate at least bimodal cavity size distributions in several samples, with a trimodal distribution in the N-lot type *316* stainless steel sample irradiated to about *22* dpa at *600°C.* Previous work by Maziasz[9] suggests that the largest matrix cavities, and certainly the large cavities associated with coarse precipitate particles, are voids. The smallest cavities (shown in Fig. 3.2.5) are probably near-equilibrium helium bubbles. Independent experimental and theoretical work by Spitznagel et al.[10] and Townsend[11] supports this classification scheme. Figure *3.2.4* shows that the number of larger cavities (voids) increases at either 500 or 600°C as fluence increases. At both temperatures, void size increases with fluence for the N-lot type 316 stainless steel, with the largest increase at 600°C due to the appearance of precipitate-associated voids. At either fluence, there is also a considerable increase in both void size and concentration as the temperature is increased from *500* to 600°C. The higher magnification micrographs of Fig. *3.2.5* show that the concentration of visible fine bubbles increases with increasing fluence at *500°C* but decreases for the same fluence comparison at 600°C. At 500°C growth of a previously nucleated "invisible" (below the resolution limit of the microscope) distribution of bubbles is a possible explanation. By contrast, the number of fine bubbles clearly decreases as the sizes of those that remain increase with increasing fluence at *600°C.*

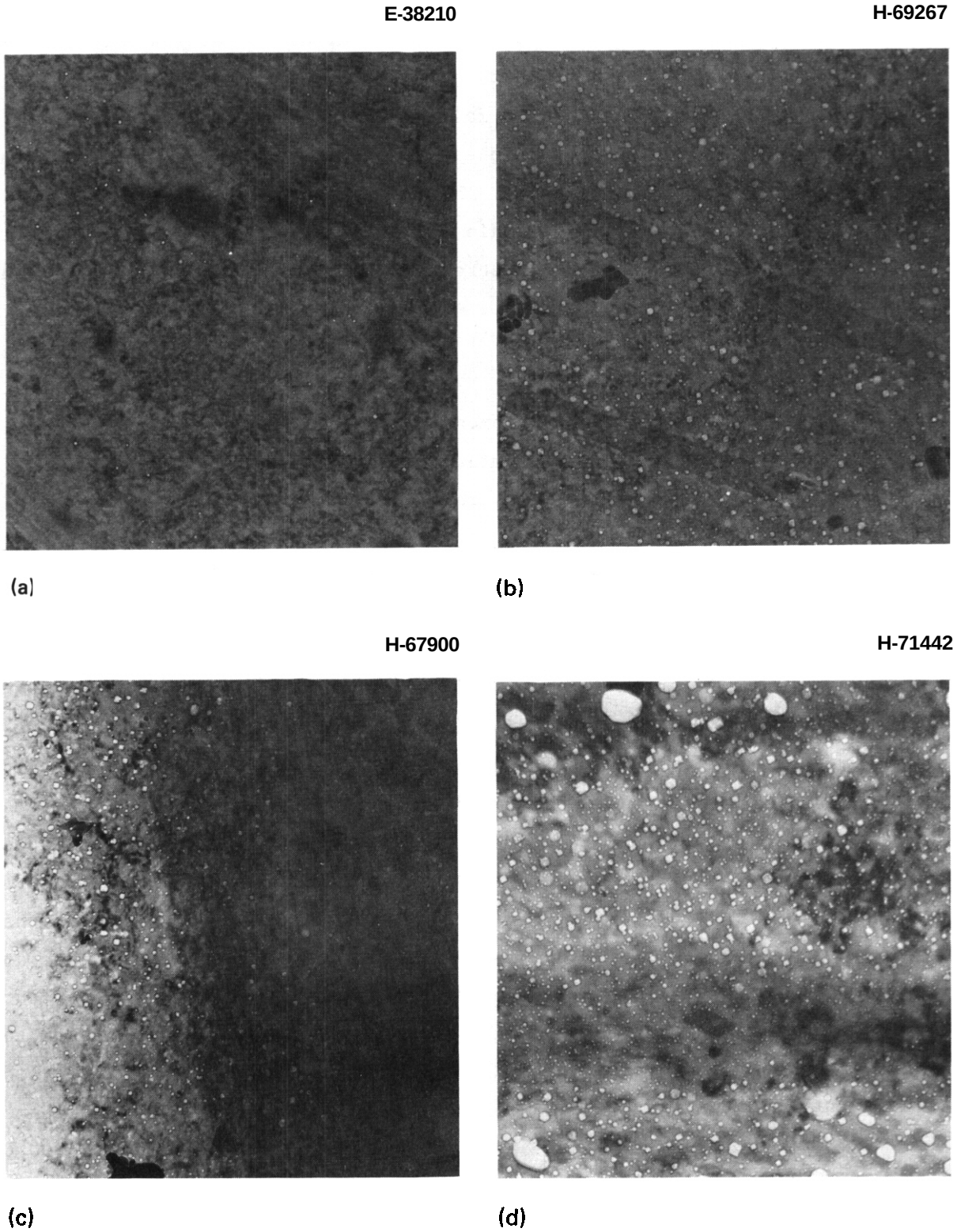

Fig. 3.2.4. Low-Magnification Microstructures of CW 316 (N-lot) to Show Voids and Bubbles Produced by HFIR Irradiation. (a) and (b) Irradiated at 500°C, (c) and (d) at 600°C. The damage level is *10.4* dpa in (a) and (c) and 21.8 dpa in (b) and (d).

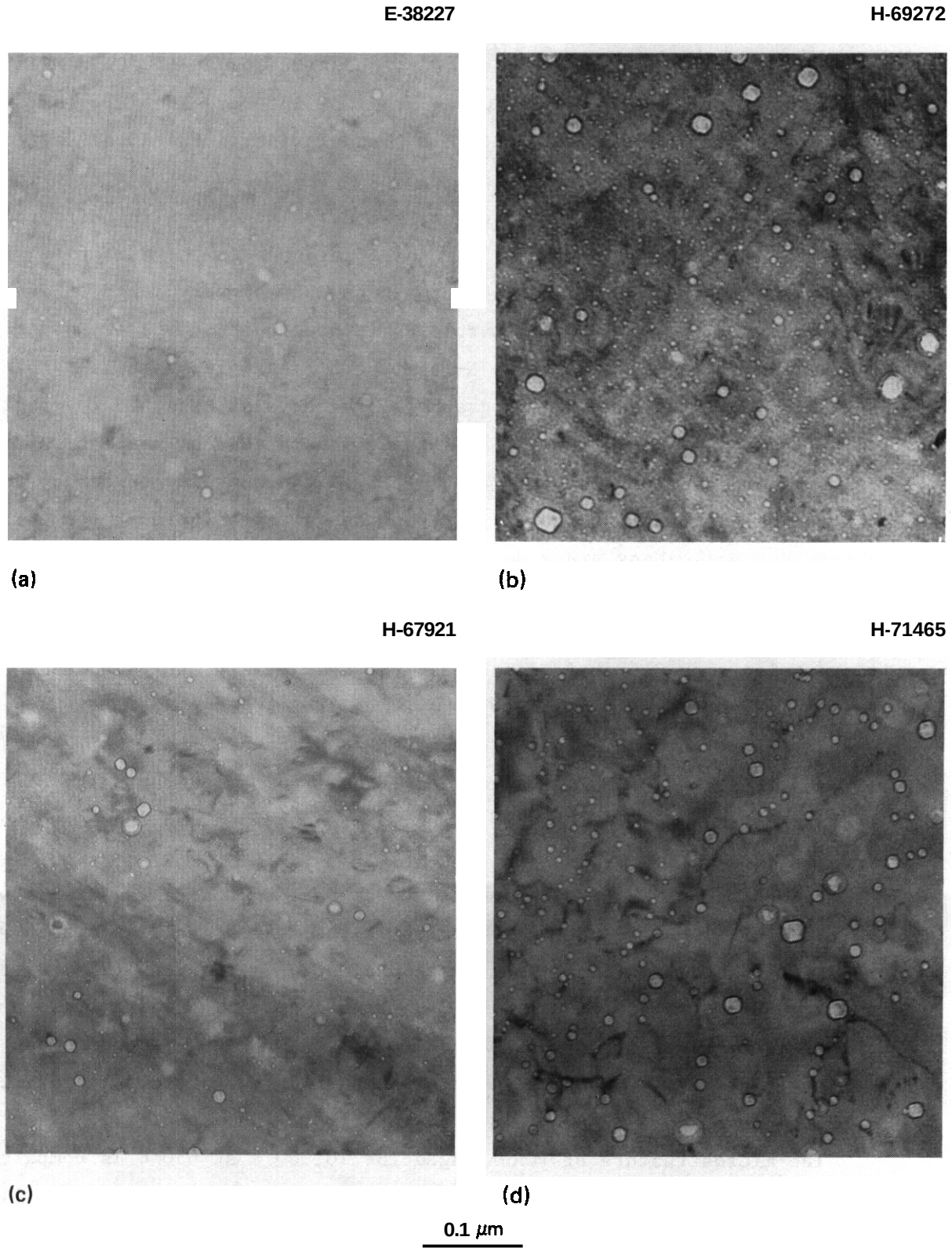

Fig. 3.2.5. Higher Magnification Microstructures of CW 316 (N-lot) to Show Bubbles and Voids Produced by HFIR Irradiation. (a) and (b) Irradiated at 500°C, (c) and (d) at 600°C. The damage level is 10.4 dpa in (a) and (b) and 21.8 dpa in (b) and (d).

The microstructures of EA-A1 and -A3 are compared with CW 316 (N-lot) in Fig. 3.2.6 for irradiation to about 22 dpa at 600°C in HFIR. The swelling is the highest in PCA-A1 at 1.2%, intermediate in N-lot type 316 stainless steel at 0.4 to 0.5%, and lowest in PCA-A3 at 0.2 to 0.25% (see Table 3.2.3). All micrographs in Fig. 3.2.6 show a distribution of fine matrix bubbles. However, the calculated swelling differences among these samples is primarily due to differences in the number of larger matrix voids, and especially to the number of very large voids attached to coarse precipitate particles [probably eta (M_6C) or possibly G-phase]. Figure 3.2.6(a) shows N-lot type 316 stainless steel (a thicker foil than in the other two micrographs). Large voids attached to precipitate along stacking fault bands are mixed with patches of smaller matrix voids and areas containing only small bubbles. Compared with either PCA sample, the swelling is spatially inhomogeneous in the N-lot type 316 stainless steel. Many areas do not show large voids on coarse precipitate particles. The number of large voids attached to coarse precipitate particles is greater and they are more uniformly distributed in EA-A1 than in the N-lot type 316 stainless steel; the result is greatly increased swelling in the former. Finally, the PCA-A3 shows about 80% of its volume containing a high concentration of uniformly dispersed fine bubbles and only small patches of larger matrix cavities. No coarse particles of precipitate phases, like G-phase or eta, were observed, so there are no large voids.

Fine dispersions of titanium-rich MC were found to be associated with the rafts of fine, high-density bubbles in the PCA-A3 irradiated at 600°C. Bright-field and dark-field transmission electron microscopy (TEM) of the same area illustrates this in Fig. 3.2.7. Conversely, areas containing coarser matrix cavities appear denuded of fine MC. This is consistent with the beneficial effects of fine titanium-rich MC particles identified in previous work[12,13] and anticipated for the PCA-A3 material.[1,14]

The microstructure of PCA-A3 aged for 10,000 h at 650°C is compared with the PCA irradiated at 600°C to about 22 dpa (~5240 h) in Fig. 3.2.8. General dislocation concentration and faulted band structures are similar

H-71442

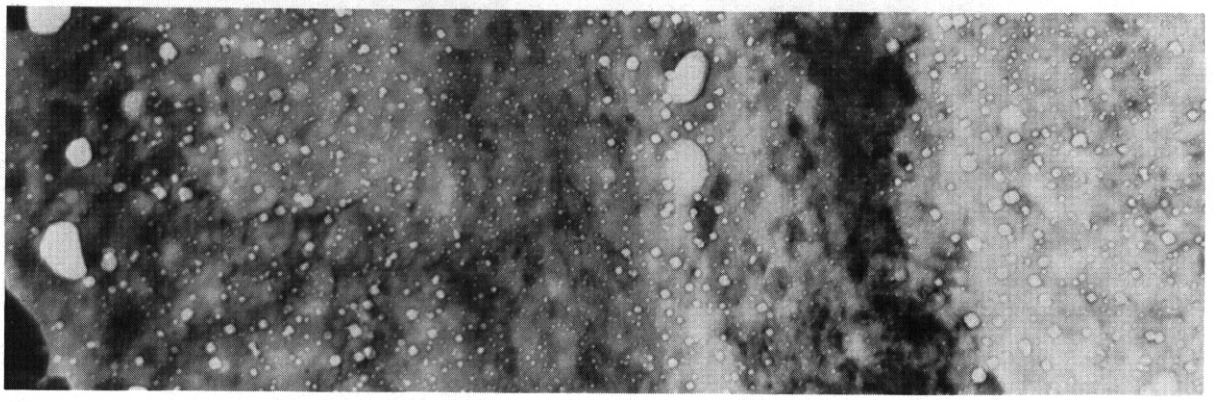

(a) 0.25 μm

E-38664

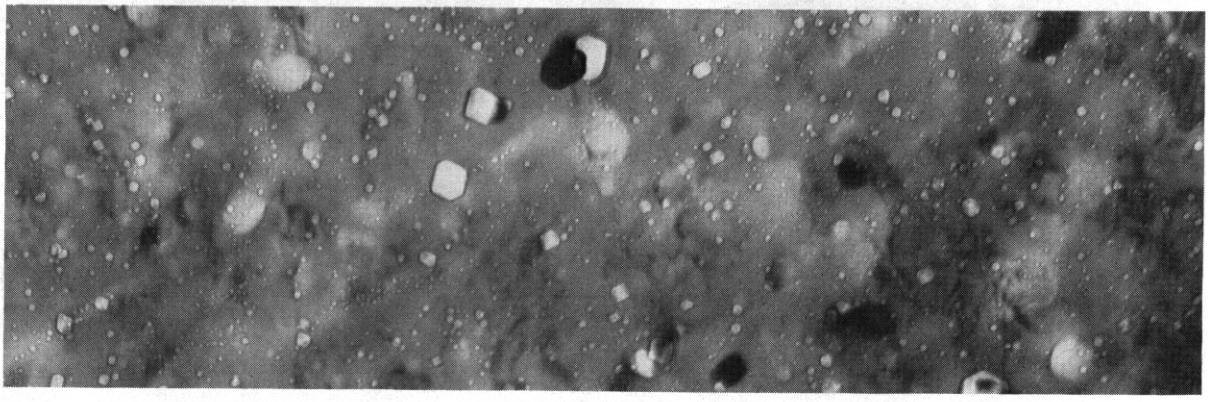

(b) 0.25 μm

H-69230

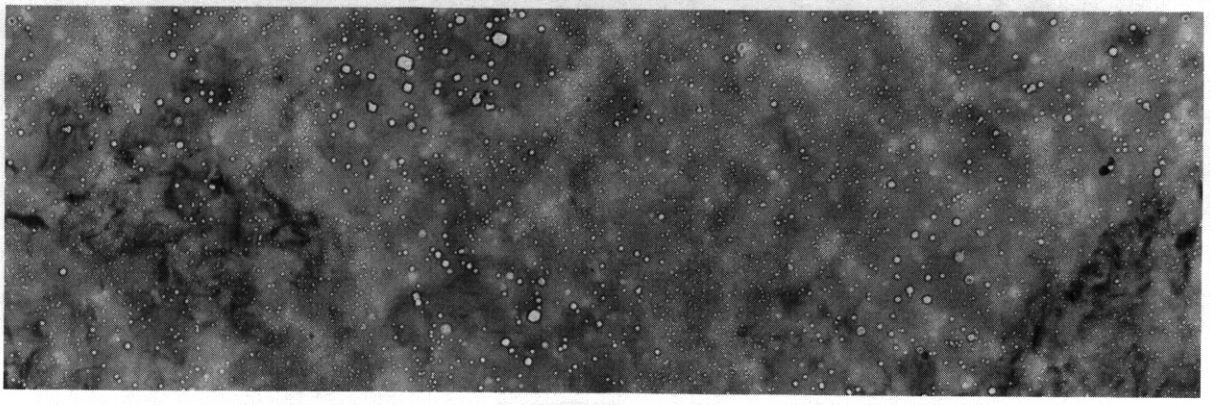

(c) 0.25 μm

Fig. 3.2.6. Comparison of Void and Bubble Microstructures Produced by HFIR Irradiation at 600°C to 21.8 to 22.3 dpa. (a) CW 316 (N-lot). (b) PCA-A1. (c) PCA-A3.

H-69244

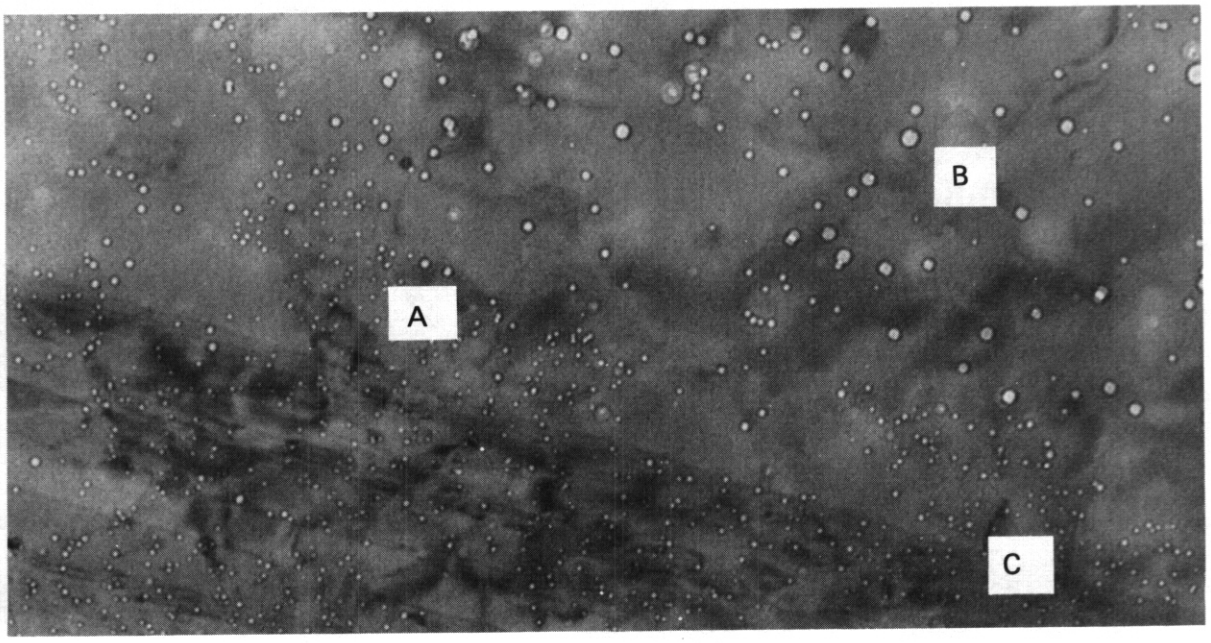

(a)

H-69243

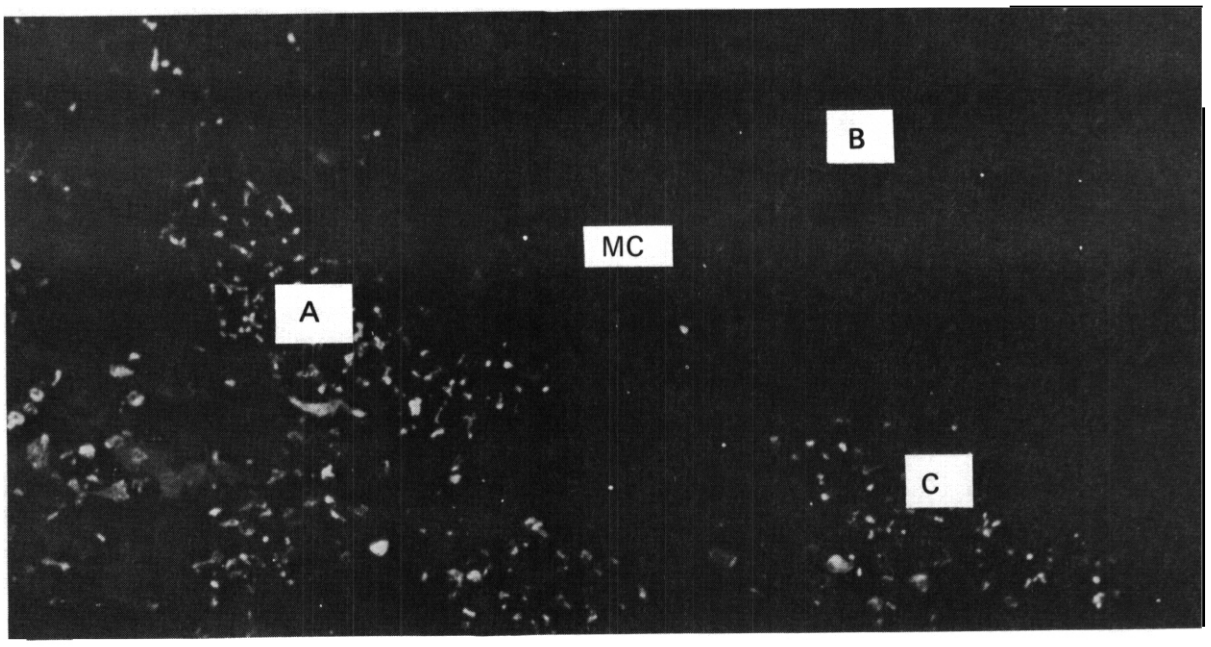

(b)

Fig. 3.2.7. Spatial Correlation of Regions of (a) Pine Bubbles with (b) Fine MC (Imaged in Dark Field) to Illustrate the One-to-one Correspondence Between These Features in PCA-A3 Irradiated in HFIR at 600°C to 22.3 dpa (1757 at. ppm He).

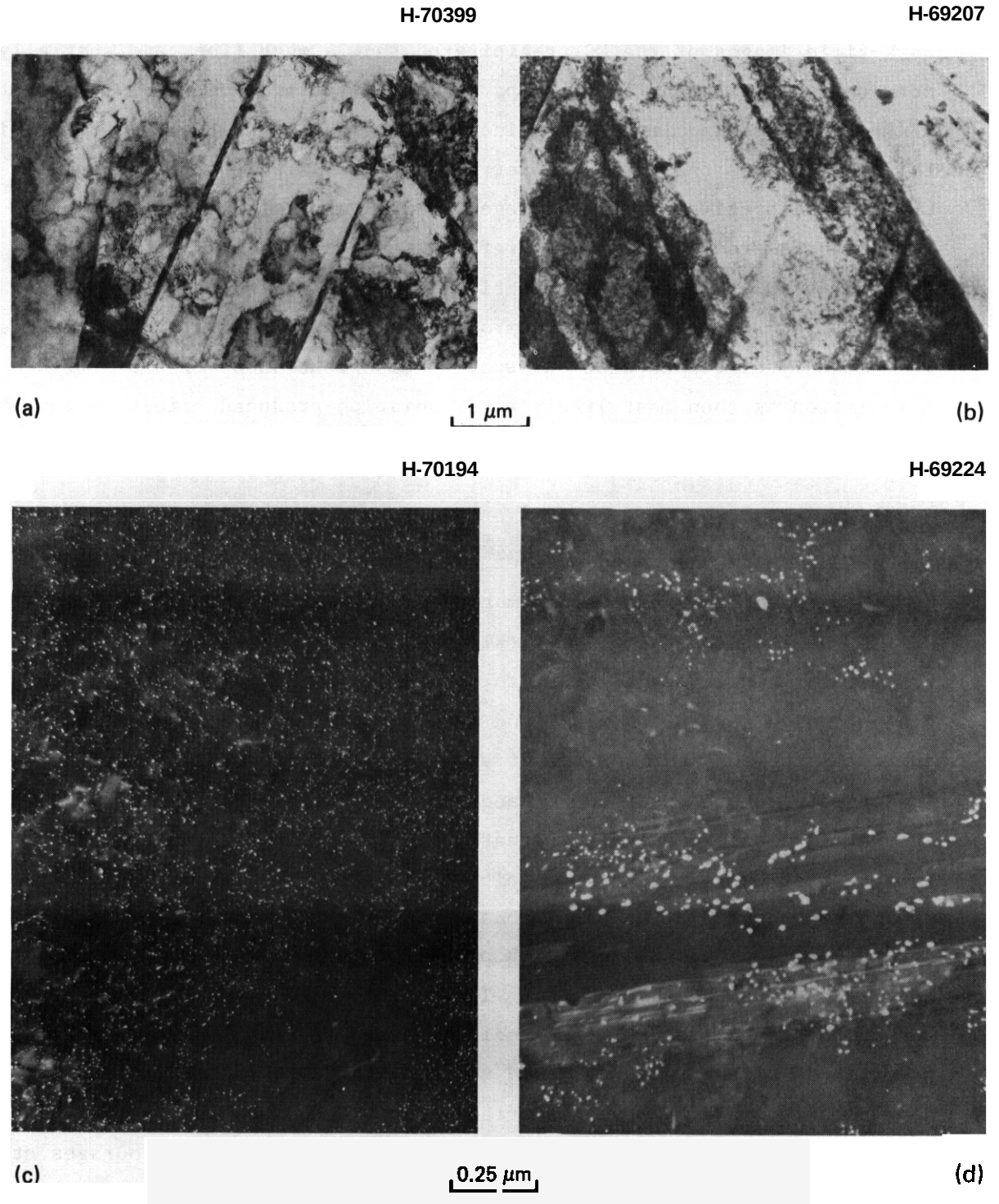

Fig. 3.2.8. Comparison of Dislocation Structure and Fine MC Precipitation (Imaged in Dark Field) for 20%-Cold-Worked Prime Candidate Alloy Aged for 10,000 h at 650°C (a and c) and PCA-A3 (25% Cold Worked) Irradiated in HFIR to 22.3 dpa at 600°C (b and d).

at low magnification [Fig. 3.2.8(a) and (b)], but higher magnification dark-field images of the MC precipitated show a much finer and spatially more uniform distribution of MC particles in the aged material than in the RFIR-irradiated specimen. The fine MC distribution in the aged PCA-A3 in Fig. 3.2.8(c) is the same as observed in other samples of PCA-A3 and in CW 316 + Ti specimens (R1-heat) aged from several minutes to 4400 h at temperatures from 560 to 750°C (refs. 13 and 15). The MC distribution in aged, heavily cold-worked material is virtually independent of time, temperature, and slight alloy compositional variation, within this range. The markedly different size and spatial distribution of MC after HFIR irradiation is then most likely an irradiation-produced effect, although its nature is not completely understood at this time.

3.2.4.4 Discussion

The temperature dependence of swelling for the various PCA pretreatments and for CW 316 (N-lot) is markedly different from that observed in CW 316 (DO-heat) or CW 316 + Ti (R1-heat) for HFIR irradiation at 300 to 650°C for fluences producing up to about 22 dpa. Swelling of the former group is high at 500 and 600°C and very low at lower temperatures. In contrast, the DO- and R1-heats of steel show maximum swelling at the lowest temperature (near 300°C) and very low swelling at 500 to 600°C. The cavity swelling values of greater than 0.2 to 0.3% are due to formation of matrix and/or precipitate-assisted voids. The very low swelling observed in PCA-A3, DO-heat type 316 stainless steel, or R1-heat type 316 + Ti is due to formation of helium bubbles without significant conversion of these to voids.[7-9] These differences in the cavity microstructure also correlate with specific features of the dislocation and precipitate microstructure. Void swelling tends to coincide with the development of a high level of irradiation-induced solute segregation (RISS), which induces phases like $\gamma'(Ni_3Si)$ or G-phase or encourages eta (M_6C) formation (particularly coarse particles of the latter two). Void swelling may also accompany the presence of many Frank faulted loops in the dislocation microstructure.[1,9] Conversely. void swelling resistance appears to coincide with minimum or no RISS, the development of fine

dispersions of tau ($M_{23}C_6$) or especially titanium-rich MC precipitate, and development of dislocation networks with few or no Frank loops.[9,14] These trends are consistently met for HFIR irradiation of all samples of the five heats of steels discussed in this work.

The limited fluence dependent data bears out these same general features. Steels like CW 316 (DO-heat) and CW 316 + Ti (R1-heat), which resist void formation, demonstrate very low swelling rates that are virtually temperature independent, at least in the temperature range of 500 to 650°C, for fluences producing up to about 20 dpa. In the CW 316 (DO-heat), the continuous helium generation gives significant bubble swelling (1—2%) for irradiation producing up to 60 dpa. The average swelling rate in the scatter band for DO-heat type 316 stainless steel (Fig. 3.2.3) is 0.04 to 0.05%/dpa at higher fluences. In contrast, easy void development in CW 316 (N-lot) or PCA-A1 at 500 to 600°C leads to almost linear swelling with no "incubation" period and greater temperature sensitivity of the fluence dependence. The CW 316 (N-lot) swells at a rate of about 0.02%/dpa over the limited fluence range observed at 600°C and at half that rate at 500°C. The PCA-A1 at 600°C exhibits the most rapid swelling at 0.055%/dpa.

3.2.5 Conclusions

1. After irradiation in the HFIR to fluences producing 9.6 to 10.6 dpa (375—550 at. ppm He), PCA-B1, -B2, and CW 316 (N-lot) samples have voids and bubbles present for irradiation at 500 or 600°C, have some fine bubbles at 400°C (except PCA-B2), and have no resolvable cavities for irradiation at 300°C. Voids become more numerous and larger in all these samples as irradiation temperature increases. At 600°C, PCA-Bl swells the most (1.2%), CW 316 (N-lot) the least (0.2%), and PCA-B2 at an intermediate value (0.4%).

2. There is considerable variation in the fluence dependence of swelling of CW 316 (N-lot) at 500 and 600°C and PCA-A1 at 600°C for HFIR irradiation up to about 22 dpa. Swelling increases nearly linearly with increasing fluence, and the "incubation" fluence is virtually nil. The PCA-A1 irradiated at 600°C exhibits the most rapid swelling, 0.055%/dpa.

The CW 316 (N-lot) swells less and the rate is temperature dependent: 0.02%/dpa at *600°C* and about half that at 500°C. The swelling increases as temperature increases, because of increased conversion of bubbles to voids as well as continued growth of voids already present.

3. The PCA-A3 irradiated to 22.3 dpa at 600°C was the lowest swelling among the (N-lot) type 316 stainless steel and PCA pretreatment variants. It had about half the swelling (0.20—0.25%) of that observed in CW 316 (N-lot) irradiated under similar conditions. The PCA-A3 swelling is comparable to that of CW 316 (DO-heat), but slightly greater than that of CW 316 + Ti (R1-heat). The swelling is low in PCA-A3 because there is very little coarsening of the bubble structure or conversion of these bubbles to voids.

4. The temperature dependence of swelling in the PCA pretreatment variants or CW 316 (N-lot) is opposite to that of CW 316 (DO-heat) and CW 316 + Ti (R1-heat). The latter two steels swell most at lower temperatures and least at temperatures from 450 to 700°C.

5. The spatial nonuniformity of the MC precipitate in PCA-A3, even though the material is initially homogeneous, is a concern. This appears to be an effect of irradiation since the distribution of MC is homogeneous in thermal control specimens.

6. Good swelling resistance correlates with the following microstructural features: (a) a sink structure dominated by a fine dispersion of cavities, (b) a low saturation density of network dislocations, (c) minimal RISS effects (i.e., limited development of radiation-induced and/or coarse precipitation), and (d) maximum MC stability (in the titanium-modified steels).

7. This work narrows the desirable PCA pretreatment variants to A1, B2, and A3. The PCA-A3 demonstrates the best swelling resistance of the variants at 600°C and 22.3 dpa. The PCA-B2 remains to be examined at this higher fluence. The PCA-A1 shows considerable swelling at *600°C* but would remain a contender at 300 and 400°C if swelling resistance at those temperatures persists with increasing fluence. The simpler microstructure may also be easier to weld than PCA-A3 or -B2.

8. Future work should consider possible strategies for compositional design to minimize RISS and the formation of undesirable phases as well as to maximize MC stability.

3.2.6 References

1. P. J. Maziasz and D. N. Braski, "Swelling of Path A PCA Irradiated to 10 dpa in HFIR," *ADIP* ***Semiannu.*** *Prog. Rep. Mar. 31, 1982,* DOE/ER-0045/8, pp. 98–116.
2. M. L. Grossbeck, J. W. Woods, and G. A. Potter, "Experiments HFIR-CTR-30, -31, and -32 for Irradiation of Transmission Electron Microscopy Disk Specimens," *ADIP Quart. Prog. Rep. Sept. 30, 1980,* DOE/ER-0045/4, pp. 36–44.
3. P. J. Maziasz and T. K. Roche, "Design and Fabrication of Preirradiation Microstructures in Path A Prime Candidate Alloy," *ADIP Quart. Prog. Rep. Dec. 31, 1980,* DOE/ER-0045/5, pp. 25–42.
4. L. R. Greenwood, "Neutron Source Characteristics for Materials Experiments," *ADIP* ***Semiannu.*** *Prog. Rep. Mar. 31, 1982,* DOE/ER-0045/8, pp. 66–86.
5. P. J. Maziasz, "Microstructural Development of 20%-Cold-Worked Types 316 and 316 + Ti Stainless Steels Irradiated in HFIR: Temperature and Fluence Dependence of the Dislocation Microstructure," *ADIP Quart. Prog. Rep. Sept. 30, 1981,* DOE/ER-0045/7, pp. 54–97.
6. D. Imeson et al., "Irradiation Response of Rapidly Solidified Path **A Type** Prime Candidate **Alloys,**" *ADIP Semiannu. Prog.* ***Rep.*** *Mar. 31, 1982,* DOE/ER-0045/8, pp. 141–68.
7. P. J. Maziasz and M. L. Grossbeck, "Swelling and Microstructure of HFIR-Irradiated 20%-Cold-Worked Types 316 Stainless Steel and 316 + 0.23 wt % Ti," *ADIP Quart. Prog. Rep. Dec. 31, 1980,* DOE/ER-0045/5, pp. 43–69.
8. P. J. Maziasz and M. L. Grossbeck, "Microstructural Development in 20%-Cold-Worked Type 316 Stainless Steel and Titanium-Modified Type 316 Stainless Steel Irradiated in the HFIR: Fluence Dependence of the Cavity Component," *ADIP Quart. Prog. Rep. Mar. 31, 1981,* DOE/ER-0045/6, pp. 28-56.

9. P. J. Maziasz, "Some Effects of Increased Helium Content on Void Formation and Solute Segregation in Neutron-Irradiated Type 316 Stainless Steel," *ADIP Semiannu. Prog. Rep. Mar. 31, 1982,* DOE/ER-0045/8, pp. 169-216; also *J. NucZ. Mater.* 108&109: 359–384 (1982).

10. J. A. Spitznagel et al., "Critical Cavity Sizes in Dual-Ion Bombarded 304 SS. Part I: Experimental," *J. NucZ. Mater.* 108&109: 537–43 (1982).

11. J. R. Townsend, "Critical Cavity Size in Dual Ion-Irradiated 304 SS. Part II: Theoretical," *J. Nucl. Mater.* 108&109: 544-49 (1982).

12. P. J. Maziasz, "Helium Trapping at Ti-Rich MC Particles in Ti-Modified Austenitic Stainless Steel," pp. 477–92 in *Phase Stability During Irradiation,* ed. J. R. Holland, L. K. Mansur, and D. I. Potter, The Metallurgical Society of AIME, Warrendale, Pa., 1981.

13. P. J. Maziasz, J. A. Horak, and B. L. Cox, "The Influence of Both Helium and Neutron Irradiation on Precipitation in 20%-Cold-Worked Austenitic Stainless Steel," pp. 271–92 in *Phase Stability During Irradiation,* ed. J. R. Holland, L. K. Mansur, and D. I. Potter, The Metallurgical Society of AIME, Warrendale, Pa., 1981.

14. P. J. Maziasz and T. K. Roche, "Pre-Irradiation Microstructural Development Designed to Minimize Properties Degradation During Irradiation in Austenitic Alloys," *J. NucZ. Mater.* 103&104: 797–802 (1981).

15. P. J. Maziasz, B. L. Cox, T. K. Roche, and E. E. Bloom, "Time-Temperature Precipitation Curve Determination of the Path A Prime Candidate Alloy for Microstructural Design," *ADIP Quart. Prog. Reo. Sept. 30, 1979,* DOE/ER-0058/7, pp. 103–27.

3.3 THE TENSILE PROPERTIES OF UNIRRADIATED PATH A PCA — D. N. Braski and P. J. Maziasz (Oak Ridge National Laboratory)

3.3.1 ADIP Task

ADIP Task I.B.13, Tensile Properties of Austenitic Alloys.

3.3.2 Objective

The objective of this research is to determine the tensile properties of unirradiated PCA in the temperature range room temperature to 700°C.

3.3.3 Summary

The tensile properties of PCA in the A1 (solution annealed), A3 (25%-cold worked); and B2 (aged, cold worked, and reaged) conditions were determined from room temperature to 600°C. The tensile behavior of PCA-A1 and -A3 was generally similar to that of titanium-modified type 316 stainless steel with similar microstructures. The PCA-B2 was weaker than PCA-A3, especially above 500°C, but demonstrated slightly better ductility.

3.3.4 Progress and Status

3.3.4.1 Introduction

Tensile tests in the temperature range room temperature to 600°C have been run on the path A PCA alloy in three different conditions; Al, A3, and B2. Previous High Flux Isotope Reactor (HFIR) irradiation results for PCA-A1 and -B2 (ref. 1) as well as results for PCA-A3 (elsewhere in this report) have shown that these three treatments provide better resistance to swelling than those producing other micrestructures in PCA.

3.3.4.2 Experimental

The composition of PCA is (wt %) Cr, 14.0; Ni, 16.2; Mo, 2.3; Mn, 1.8; Si, 0.4; Ti, 0.24; C, 0.05; P, 0.01; S, 0.003; N, 0.01; B, 0.0005; Fe, balance. The following thermomechanical treatments were used to produce the three microstructures: Al, 25% cold worked plus 30 min at 1100°C; A3, 30 min at 1100°C plus 25% cold worked; B2, 30 min at 1100°C,

8 h at 800°C, 25% cold worked plus 2 h at 750°C. Small tensile specimens of the SS-1 design[2] were machined from 0.76-mm-thick sheet of PCA in each condition. The gage section is 20.3 mm long with a cross section of 1.52 by 0.76 mm. The specimens were tested in air in an Instron tensile testing machine fitted with a wireround resistance furnace. The crosshead speed was 0.5 mm/min (0.02 in./min, strain rate = 4.2 x 10^{-4}/s). The untested microstructures were characterized by transmission electron microscopy (TEM). Samples for TEM were prepared by electropolishing in a solution of 12.5 vol % H_2SO_4 in methanol at −10°C.

3.3.4.3 Results

The microstructures of PCA in the Al, A3, and B2 conditions are shown in Figs. 3.3.1 and 3.3.2. The PCA-A1 [Pig. 3.3.1(a)] had a low dislocation

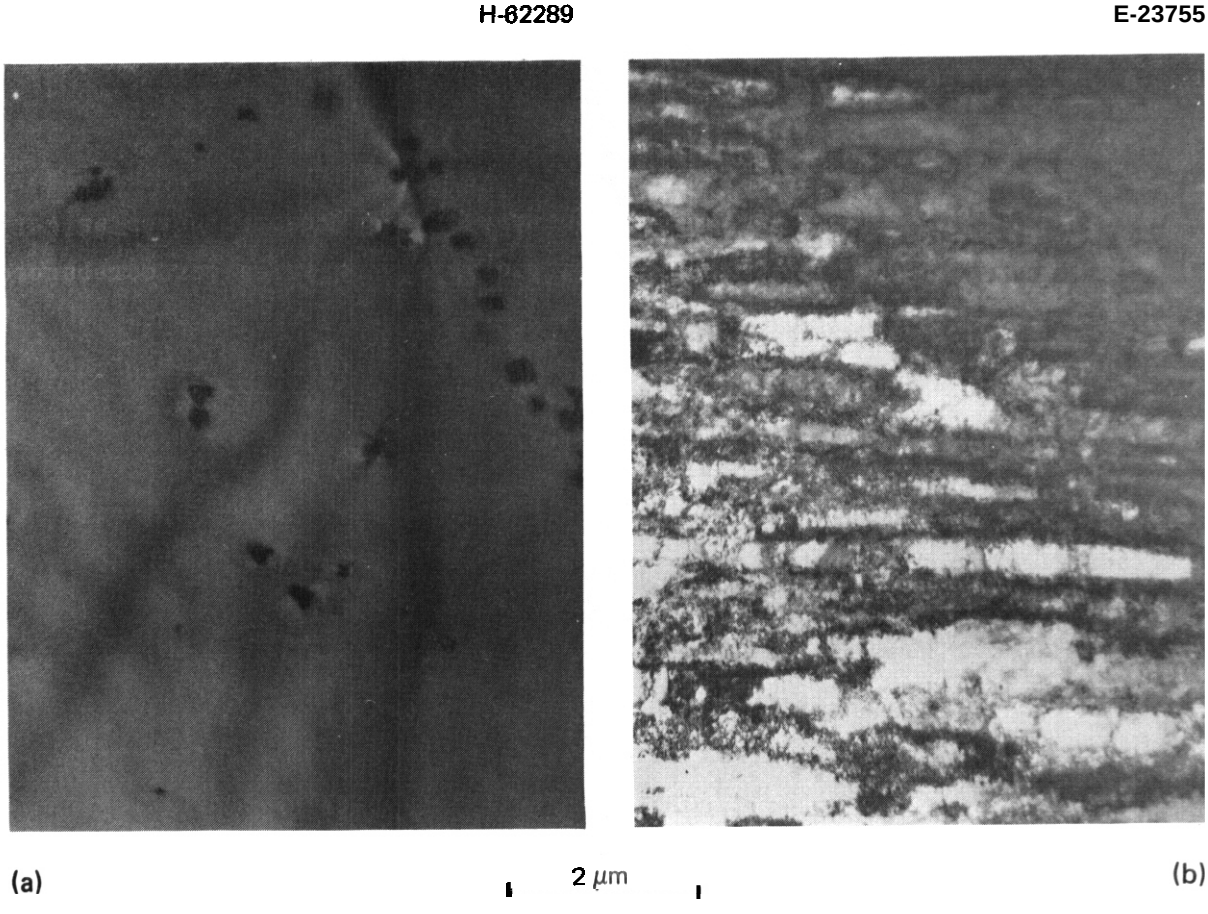

Pig. 3.3.1. Microstructures of Path A PCA Solution Annealed for 30 min at 1100°C (Al). (a) AS annealed. (b) Followed by 25% cold work (A3).

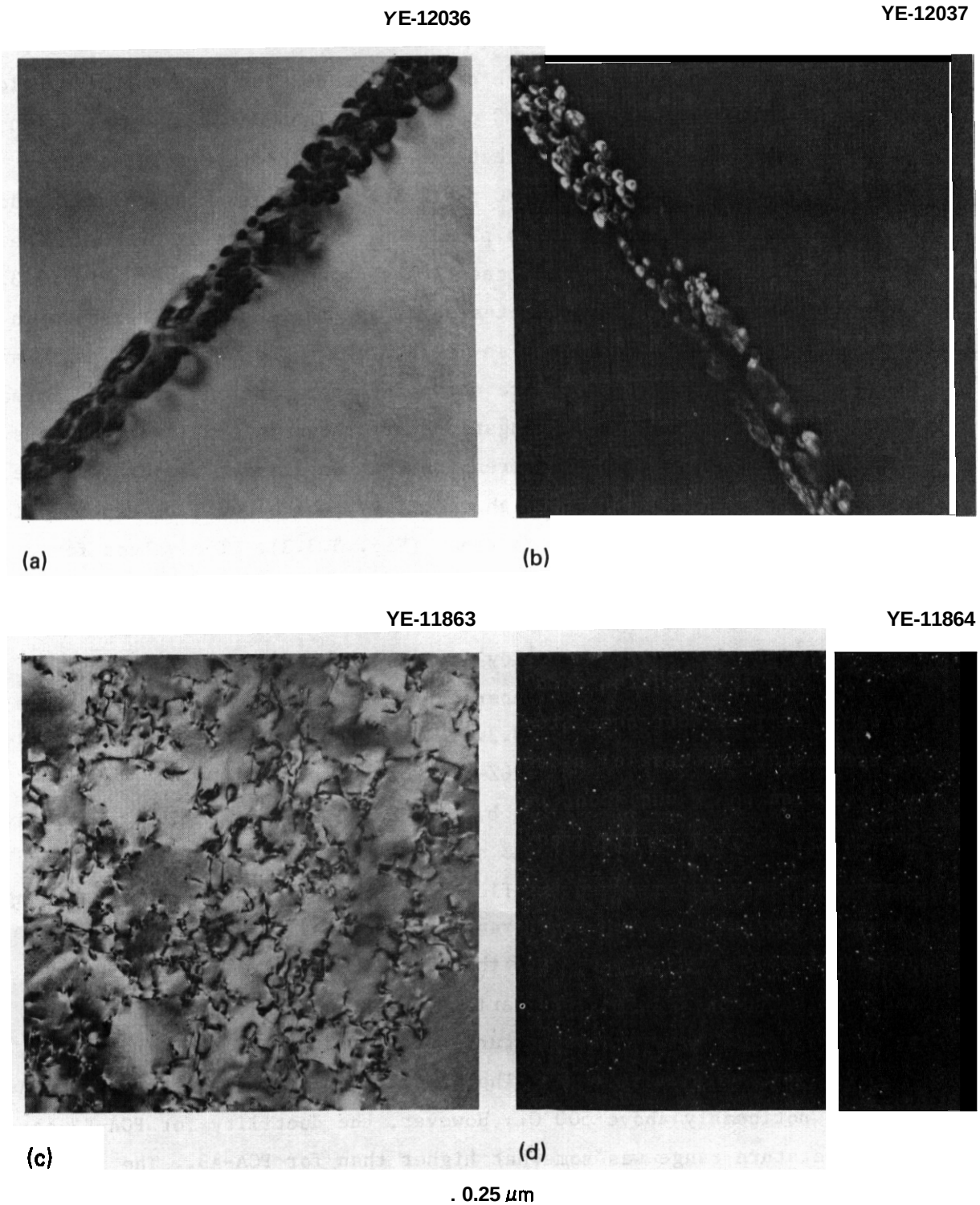

Fig. 3.3.2. Components of the Microstructure of the Path A PCA Condition B2. The grain boundary precipitate produced by the first aging, for 8 h at 800°C, is shown in bright field (a) and dark field (b). The dislocation structure and matrix precipitate after the 25% cold work and reaging for 2 h at 750°C is shown in bright field (c) and precipitate dark field (d).

density and was virtually free of any titanium-rich MC particles. The PCA-A3 [Fig. 3.3.1(b)] had a high dislocation density, typical of a cold-worked material and, again, no MC particles. The PCA-B2 alloy is essentially a cold-worked PCA alloy that has been aged before cold work to produce a coarse dispersion of MC particles in the grain boundaries, and then aged after the cold work to produce a fine dispersion of MC in the matrix. The microstructure components are shown separately in Pig. 3.3.2.

The results of the tensile tests for the three alloys are shown in Figs. 3.3.3 to 3.3.5 and listed in Table 3.3.1. The ultimate tensile and yield strengths (0.2% offset) are shown in upper portions of the figures, while the uniform and total elongations are shown in the lower portions. The EA-A1 demonstrated yield strengths that were about one-half of the ultimate strengths and rather high ductility, which would be expected for this solution-annealed stainless steel (Pig. 3.3.3). The values for strength and ductility are nearly the same (Table 3.3.1) as those reported for solution-annealed type 316 stainless steel with a 0.23 wt % Ti addition.[3] Cold working the alloy increased the yield and ultimate tensile strengths across the temperature range and decreased the elongation to values below 15% (Fig. 3.3.4). However, the PCA-A3 was slightly weaker (and more ductile) than 20%-cold-worked type 316 + Ti (CW 316 + Ti) at the two temperatures reported by Wiffen and Maziasz.[3] The relatively low uniform elongation for PCA-A3 at 300°C is common for cold-worked stainless steels and probably reflects the reduction in strain hardening that occurs in that temperature range. The tensile behavior of EA-A1 and -A3 was generally similar to that for CW 316 + Ti with similar microstructures. The PCA-B2 material was strengthened by the MC particles present in its microstructure but did not reach the strength levels of PCA-A3 (Fig. 3.3.5). The yield and ultimate strengths of PCA-B2 drop off noticeably above 500°C. However, the ductility for PCA-B2 across the temperature range was somewhat higher than for PCA-A3. The yield strength curve for PCA-B2 has been drawn from the average value of two points at room temperature and is shown to increase slightly up to 300°C. We do not believe that this reflects the true behavior of the material but rather that it is a victim of the scatter of yield strength values at room

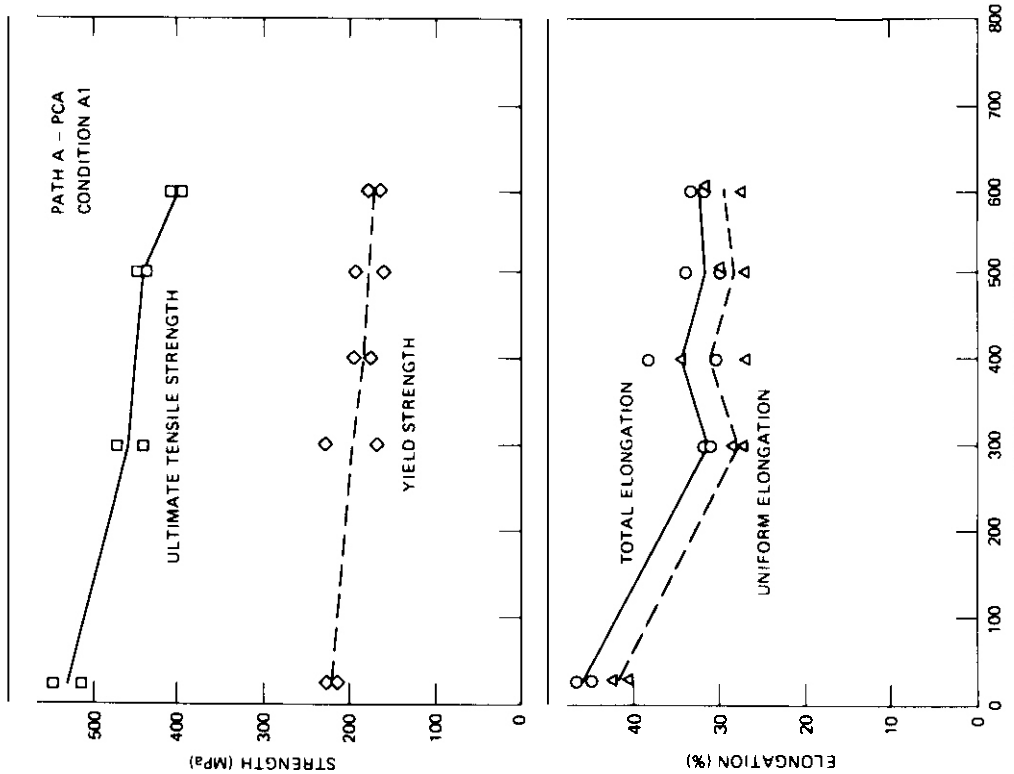

Fig. 3.3.3. Tensile Properties of PCA-A1 (Solution Annealed) as a Function of Temperature.

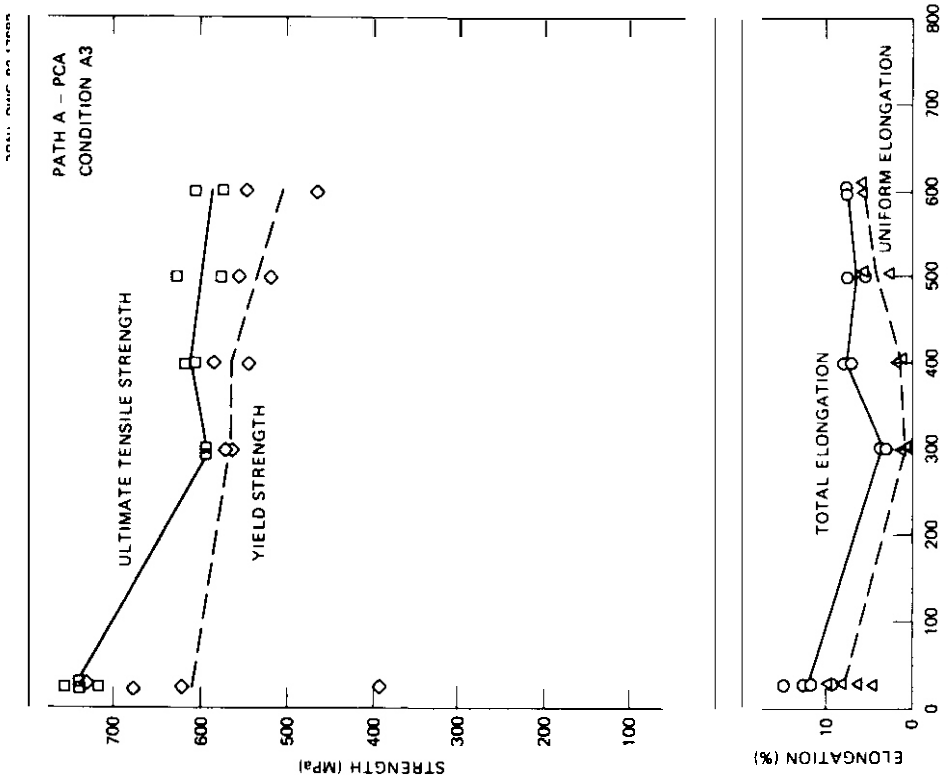

Fig. 3.3.4. Tensile Properties of PCA-A3 (25% Cold Worked) as a Function of Temperature.

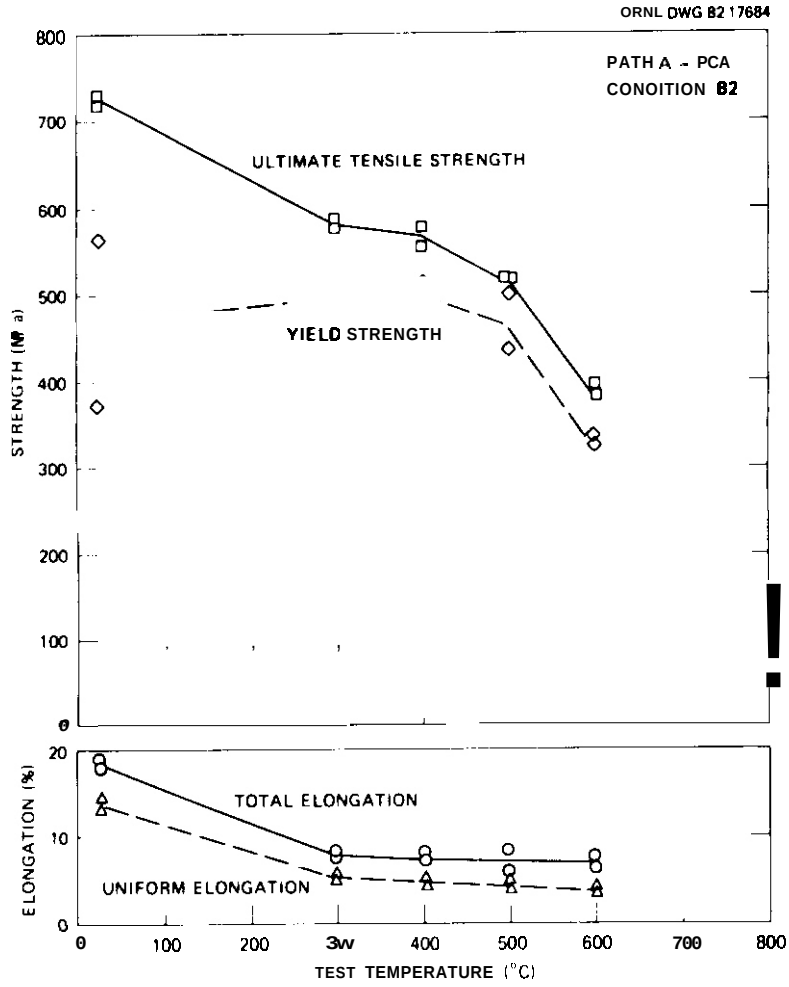

Fig. 3.3.5. Tensile Properties of PCA-B2 (Aged, 25% Cold Worked, and Reaged 15 min at 750°C) as a Function of Temperature.

temperature. A similar situation developed with PCA-A3, and two additional specimens were tested (Fig. *3.3.4);* the results raised the average value of the yield strength at room temperature to one more consistent with those at the elevated temperatures.

It should be noted that rapid solidification techniques have been used to increase the strength levels of PCA without sacrificing ductility,[4] through control of grain size, dislocation distribution, and MC precipitation.

Table 3.3.1. Tensile Data for the Path A PCA Alloy

Test Temperature (°C)	Yield Strength (MPa)	Ultimate Tensile Strength (MPa)	Uniform Elongation (%)	Total Elongation (%)
Condition A1 — Solution Annealed				
22	226.8	513.1	40.3	44.9
22	212.8	545.2	42.1	46.7
300	229.5	470.6	27.7	31.3
300	168.7	440.6	28.0	31.0
400	173.3	437.0	34.0	38.0
400	195.9	444.6	26.6	30.0
500	157.8	446.9	29.6	33.8
500	190.1	437.7	27.8	29.8
600	164.7	396.8	31.3	32.5
600	175.3	402.9	27.5	31.3
Condition A3 — 25% Cold Worked				
22	392.2	740.0	4.9	9.6
22	621.4	717.7	6.8	12.1
22	734.5	757.7	8.0	12.0
22	674.0	734.5	9.7	15.0
300	565.1	592.5	1.3	3.7
300	572.5	592.8	0.9	3.0
400	541.7	609.4	3.3	7.0
400	586.8	613.1	2.1	7.5
500	558.7	629.5	2.9	5.6
500	520.8	575.0	5.4	7.3
600	544.7	604.4	5.8	7.3
600	466.4	574.6	5.8	7.4
Condition B2 — Aged, Cold Worked, and Reaged				
22	371.2	727.8	14.6	18.3
22	553.1	718.3	13.6	17.4
300	492.9	578.1	5.9	8.4
300	499.9	589.4	5.5	7.5
400	487.0	570.8	5.2	8.1
400	517.5	551.7	4.6	7.4
500	435.3	517.6	5.6	8.5
500	503.0	519.7	3.9	6.5
600	437.0	497.3	4.3	7.5
600	430.2	479.3	3.8	6.4

3.3.5 Conclusions and Future Work

The path A PCA alloy in the Al, A3, and B2 conditions was tensile tested in air from room temperature to 600°C. It was concluded that

1. Under comparable conditions, PCA-A1 and -A3 had generally the same tensile behavior as titanium-modified type 316 stainless steel in comparable conditions.

2. The PCA-B2 was somewhat weaker than PCA-A3, especially at 500 and 600°C, but had slightly better ductility.

Future work will include the testing of all three PCA microstructures at 200 and 700°C and the examination of selected fracture surfaces. The tensile data will serve as a baseline with which irradiated PCA may be compared.

3.3.6 References

1. P. J. Maziasz and D. N. Braski, "Swelling of Path A PCA Irradiated to 10 dpa in HFIR," *ADIP Quart. Prog. Rep. Mar. 31, 1982,* DOE/ER-0045/8, p. 101.
2. M. L. Grossbeck and K. R. Thoms, "ORR-MFE-4: A Spectral Tailoring Experiment to Simulate the He/dpa Ratio of a Fusion Reactor in Austenitic Stainless Steel," *ADIP Quart. Prog. Rep.* June *30, 1980,* DOE/ER-0045/3, p. 10.
3. F. W. Wiffen and P. J. Maziasz, "The Influence of Neutron Irradiation at 55°C on the Properties of Austenitic Stainless Steel," *J. Nucl. Mater.* 104: 821–26 (1981).
4. J. Megusar, L. Arnberg, J. B. Vander Sande, and N. J. Grant, "Optimization of Structure and Properties of Path A Prime Candidate Alloy (PCA) by Rapid Solidification," *J. Nucl. Mater.* 99: 190–202 (1981).

3.4 TENSILE PROPERTIES AND SWELLING OF 20%-COLD-WORKED TYPE 316 STAINLESS STEEL IRRADIATED IN HFIR — R. L. Klueh and M. L. Grossbeck (Oak Ridge National Laboratory)

3.4.1 ADIP Tasks

ADIP Task I.B.13, Tensile Properties of Austenitic Alloys, and I.C.2, Microstructure and Swelling in Austenitic Alloys.

3.4.2 Objective

The primary goal of the series of experiments HFIR-CTR-26 through -29 is to expand the mechanical property, microstructure, and swelling data base on irradiated 20%-cold-worked type 316 stainless steel. Previous irradiation experiments HFIR-CTR-9 through -13 provided an initial, lower-fluence data base for an understanding of the behavior of the material. Earlier experiments (HFIR-SS-2 through -8) had also provided high-fluence data. However, the previous work was on specimens from an experimental heat of steel. In the present experiment series, the magnetic fusion energy (MFE) reference heat of type 316 stainless steel (heat X15893) was used. Sufficient overlap with previous irradiation conditions should enable a correlation to be made between the irradiation response of the two heats of steel.

3.4.3 Summary

Immersion density and elevated-temperature tensile properties were determined on 20%-cold-worked type 316 stainless steel irradiated in the HFIR to fluences of 3.5 to 6.3 $\times 10^{26}$ neutrons/m^2 (>0.1 MeV), which resulted in 26 to 49 dpa and 1650 to 3100 at. ppm He. These data were combined with the data previously obtained after irradiation to lower fluences (<4.0 $\times 10^{26}$ neutrons/m^2).

3.4.4 Progress and Status

We previously reported on tensile and immersion density results determined on the MFE reference heat (heat X15893) of type 316 stainless steel irradiated in experiment HFIR-CTR-26 to a maximum fluence of 3.9 $\times 10^{26}$ neutrons/m^2 (>0.1 MeV).[1] This exposure resulted in a maximum

displacement-damage level of 29 dpa and about 1900 at. ppm He. Irradiation temperatures ranged from 284 to 620°C. This experiment was one of a series of four irradiation experiments, HFIR-CTR-26 through -29. In this report, we will present the results from HFIR-CTR-27, which was irradiated to 6.5 x 10^{26} neutrons/m^2 (>0.1 MeV) to give a maximum of 49 dpa and approximately 3100 at. ppm He.

3.4.4.1 Experimental Procedure

Details on the material and test procedure were previously given when results from HFIR-CTR-26 were discussed.'

Experiment HFIR-CTR-27, like HFIR-CTR-26, was irradiated in a HFIR peripheral target position with a peak thermal neutron flux of 2.5 × 10^{19} neutrons/(m^2·s) and fast flux of 1.3 × 10^{19} neutrons/(m^2·s) (>0.1 MeV). Irradiation temperatures were approximately 284, 370, 470, 560, and 620°C. The displacement damage and helium production were calculated by the procedures described by Gabriel, Bishop, and Wiffen.' Fluences ranged from 3.5 to 6.3 x 10^{26} neutrons/m^2 (>0.1 MeV). The calculated displacement damage levels ranged from 26 to 49 dpa, and helium concentrations from 1600 to 3100 at. ppm He.

3.4.4.2 Results and Discussion

The results of immersion density measurements, given in Table 3.4.1, showed measurable swelling at all but the lowest irradiation temperature. These data, along with those previously reported,' will be discussed in detail when all experiments in this series are completed.

Tensile test results are also tabulated in Table 3.4.1. In Fig. 3.4.1 the 0.2%-offset yield strength is plotted against fluence (and displacement damage) for the test temperatures of 350, 450, and 575°C. The curves in this figure are those previously presented for the low-fluence data. Although the low-fluence portion of the curves will undoubtedly need to be altered, we have chosen not to extend the curves until the data from HFIR-CTR-28 are available. Also shown in Fig. 3.4.1 are the data of Grossbeck and Mazlasz[3] for tests on low-fluence irradiations on another heat of steel; these data were also presented and discussed earlier.

Table 3.4.1. Swelling Behavior and Tensile Properties of HFIR-Irradiated 20%-Cold-Worked Type 316 Stainless Steel

Temperature, °C		Fluence[b] >0.1 MeV (neutrons/m^2)	Displacement Damage (dpa)	Helium Content[c] (at. ppm)	Swelling[d] (%)	Strength MPa		Elongation,[f] %	
Test	Irradiation[a]					Yield[e]	Ultimate	Uniform	Total
500	484	3.5 × 10^{26}	26	1640	0.0	851	1064	1.2	5.8
350	370	3.5	26	1670	0.2	940	977	1.5	5.1
350	370	5.2	39	2540	1.3	890	965	5.2	6.9
350	370	5.2	39	2520	0.8	770	869	5.9	8.0
450	470	4.4	33	2130	1.5	500	654	6.5	7.7
450	470	6.3	48	3060	1.1	470	635	9.0	10.9
450	470	6.3	48	3050	1.0	470	634	10.2	12.2
575	560	4.4	33	2180	1.0	362	535	9.8	11.0
575	560	5.8	44	2850		344	512	6.1	6.0
575	560	5.9	44	2880	1.2	338	503	7.2	7.3
600	620	6.5	48	3130	2.1	358	543	7.4	8.0

[a] Irradiation temperatures are calculated, ±50°C.

[b] Calculated from dosimetry of previous experiments.

[c] Calculated from empirical relationship.

[d] Based on immersion density values.

[e] 0.2% offset.

[f] Based on an 18.3-mm gage length.

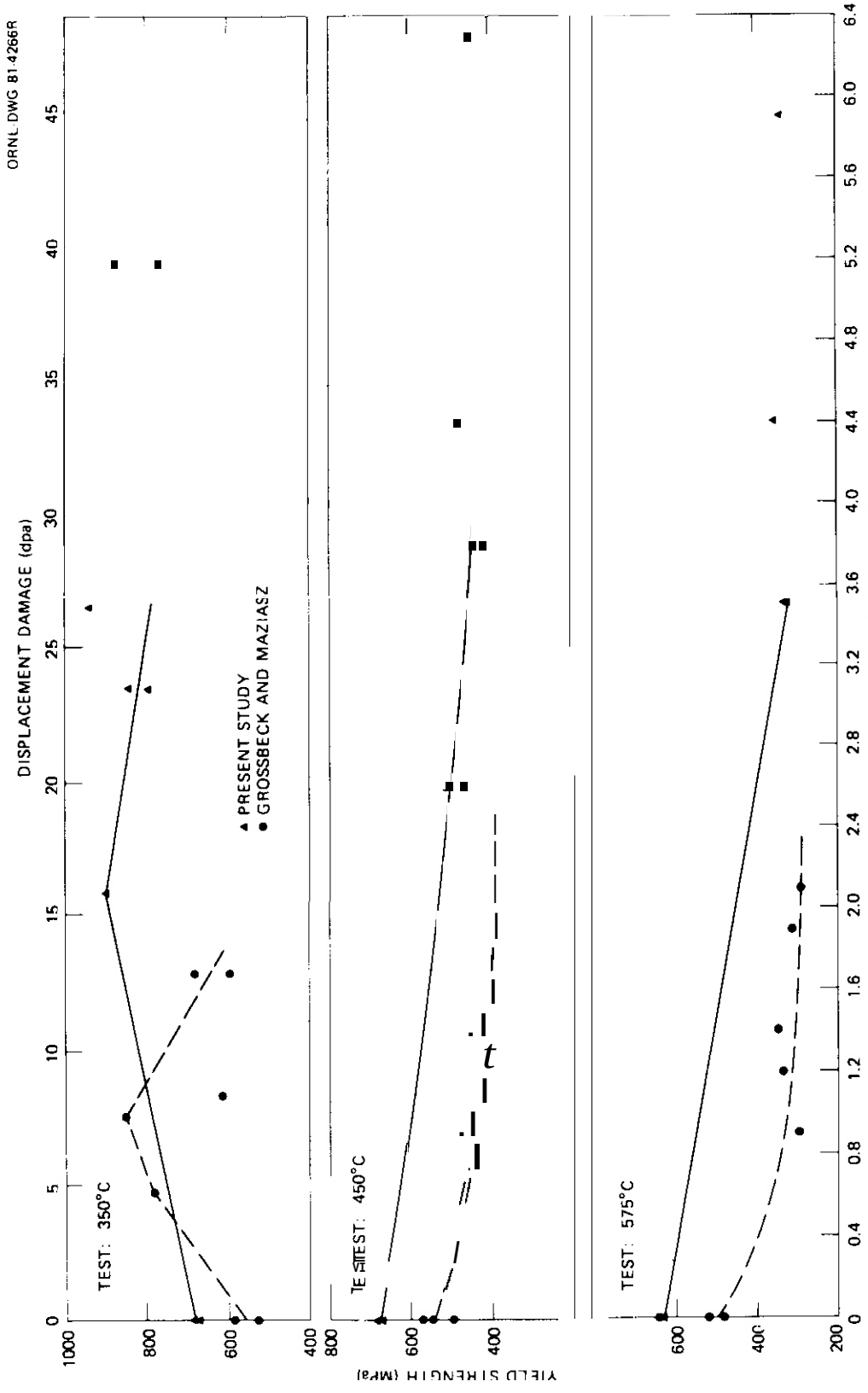

Fig. 3.4.1. The 0.2%-Offset Yield Strength as a Function of Fluence and Displacement Damage for Irradiated 20%-Cold-Worked Type 316 Stainless Steel for Test Temperatures of 350, 450, and 575°C. Irradiation temperatures were near test temperatures.

We previously stated that the trends for our low-fluence yield strength data were in general agreement with those of Grossbeck and Maziasz. The new data alter that conclusion slightly at 350°C, where the peak in yield strength that appears to be present in the Grossbeck and Maziasz data and in our earlier data (as presented by the curve) is no longer as prominent. In fact, the higher fluence data suggest that the yield strength may approach a plateau value. At the other two temperatures, the trends for the two sets of data still appear to be similar.

The total elongation as a function of fluence or displacement damage (Fig. 3.4.2) is generally the inverse of the strength results (i.e., an increase in strength results in a decrease in ductility and vice versa). The only exception to this is at 575°C, where both the yield strength and the total elongation decreased slightly. The uniform elongation values generally follow those for the total elongation (Table 3.4.1). Again, the curves in Fig. 3.4.2 are those previously presented;[1] the new data generally fall along the trends indicated by the low-fluence data.

In addition to comparing our results with the Grossbeck and Maziasz[3] results in the previous report,[1] at 350 and 575°C we also compared them with high-fluence data of Bloom and Wiffen.[4] The latter results extended to about 7×10^{26} neutrons/m^2 (~55 dpa) at 350°C and to about 8.7×10^{26} neutrons/m^2 (~65 dpa) at 575°C. Bloom and Wiffen used the same experimental heat of steel used by Grossbeck and Maziasz. We concluded that the effects of irradiation on the yield strengths show similar trends for all three experiments. The major difference between the Bloom and Wiffen results and the other two experiments was found in the ductility, especially at 575°C. Bloom and Wiffen reported that at 575°C the total elongation approached quite low values at the highest fluences (~0.5%). No such rapid decrease in ductility was indicated in the other two studies at lower fluences.[1,3] That conclusion still applies in light of the new data presented in this report.

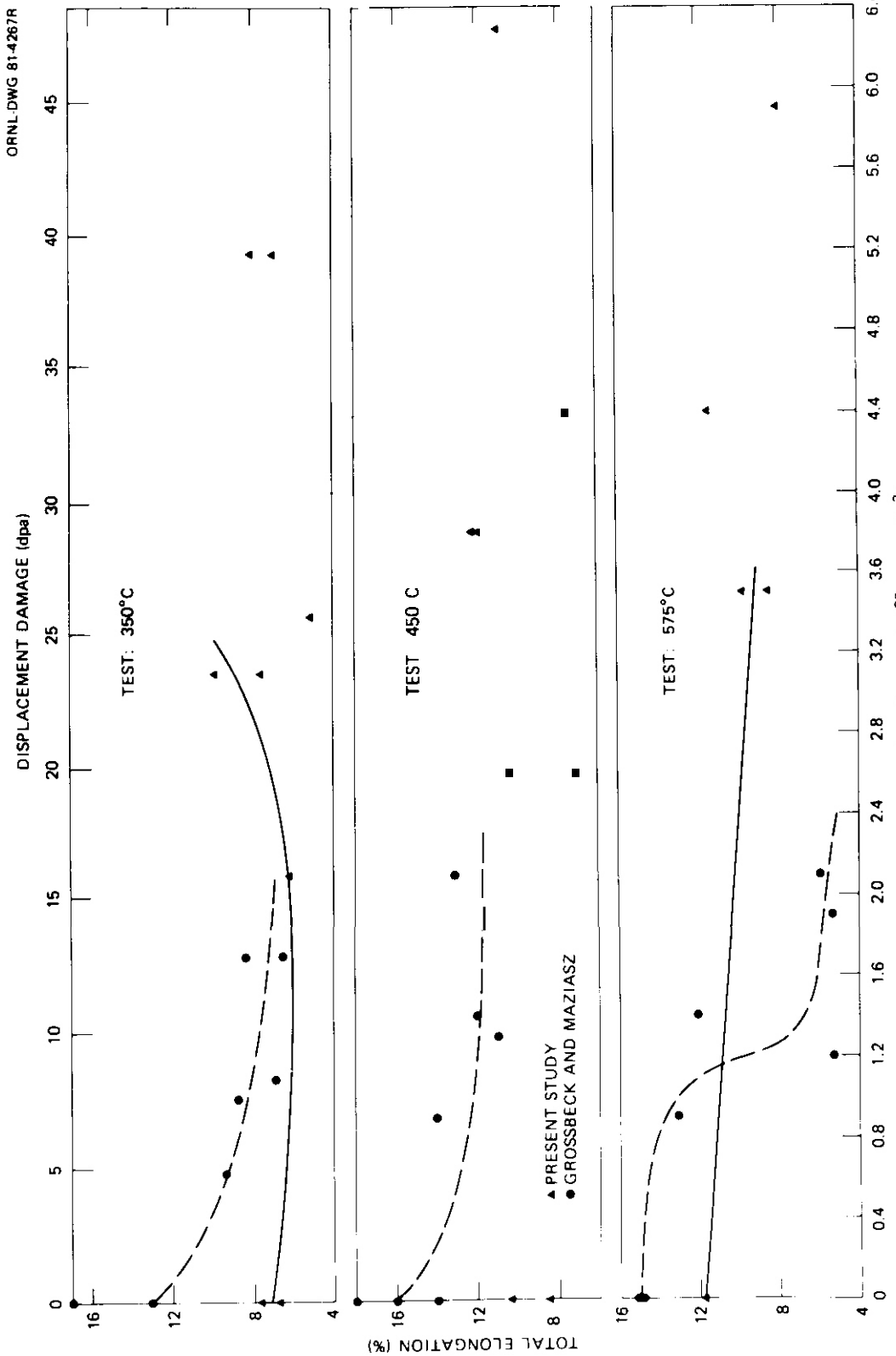

Fig. 3.4.2. Total Elongation as a Function of Fluence and Displacement Damage for 20%-Cold-Worked Type 316 Stainless Steel for Test Temperatures of 350, 450, and 575°C. Irradiation temperatures were near the test temperatures.

3.4.5 Future Work

The HFIR-CTR-28 experiment has been removed from the reactor after 15 cycles (this is the companion experiment to HFIR-CTR-26 reported previously'). Density measurements and tensile test results for this experiment will be reported in the next ADIP progress report.

3.4.6 References

1. R. L. Klueh and M. L. Grossbeck, "Tensile Properties and Swelling of 20%-Cold-Worked Type 316 Stainless Steel Irradiated in HFIR," *ADIP Quart. Prog. Rep. Mar. 31, 1981*, DOE/ER-0045/6, pp. 58–69.
2. T. A. Gabriel, B. L. Bishop, and F. W. Wiffen, *Calculated Irradiation Response of Materials Using Fission Reactor (HFIR, ORR, and EBR-II) Neutron Spectra*, ORNL/TM-6361 (August 1979).
3. M. L. Grossbeck and P. J. Maziasz, "Tensile Properties of Type 316 Stainless Steel Irradiated in a Simulated Fusion Reactor Environment," *J. Nucl. Mater.* 85&86: 883–87 (1979).
4. E. E. Bloom and F. W. Wiffen, "The Effects of Large Concentrations of Helium on the Mechanical Properties of Neutron-Irradiated Stainless Steel," *J. Nucl. Mater.* 58: 171–84 (1975).

3.5 MICROSTRUCTURAL DEVELOPMENT OF 20%-COLD-WORKED TYPE 316 STAINLESS STEEL IRRADIATED IN ORR AT 250 TO 500°C — P. J. Maziasz (Oak Ridge National Laboratory)

3.5.1 ADIP Task

ADIP Tasks I.C.l, Microstructural Stability, and I.C.2, Microstructure and Swelling in Austenitic Alloys.

3.5.2 Objective

These experiments are designed to characterize the microstructural development in austenitic stainless steels irradiated in the Oak Ridge Research Reactor (ORR) and to compare the results with similar data from Experimental Breeder Reactor (EBR)-II and High Flux Isotope Reactor (HFIR).

3.5.3 Summary

No voids, bubbles, or precipitation are observed in 20%-cold-worked (ref.-heat) type 316 stainless steel irradiated in ORR at 250 to 500°C to produce 5 dpa and 38.7 at. ppm He. There is some recovery of the cold-worked structure at 500°C, but not at 250 to 450°C. The total dislocation structure is quite dense from 250 to 450°C due to the presence of many Frank loops and a high concentration of fine loops ("black dots"). No significant effect of helium could be determined, but bubble formation appears retarded in ORR compared with that in HFIR.

3.5.4 Status and Progress

Helium can have pronounced effects on the mechanisms of void swelling, precipitation, and radiation-induced solute segregation in austenitic stainless steels under either ion or neutron irradiation.[1-3] Helium effects for fusion have been inferred from comparison of the results of EBR-II and HFIR irradiation of the same heat of steel. However, neither of these reactor irradiations produces helium and displacement damage in type 316 stainless steel at the ratio to match fusion first-wall service (10—15 at. ppm He/dpa); HFIR produces far too much helium (20—70 at. ppm He/dpa) and EBR-II far too little (0.5—1 at. ppm He/dpa). The ORR has a lower flux, but gives a better match to the helium/dpa generation ratio of a fusion first wall. This report presents microstructural data obtained for type 316 stainless steel irradiated in the ORR.

3.5.4.1 Experimental

Sheet specimens (0.76 mm thick) of the path A reference heat (X-15893) (hereafter referred to as ref.-heat) type 316 stainless steel were irradiated in the 20%-cold-worked (CW) condition. The composition is given in Table 3.5.1 with several other well-known heats of steel for comparison. Specimens were irradiated in the ORR-MFE-2 experiment, in position E-7 of the ORR core. Details of the experimental subassembly are given elsewhere.[4] Design temperatures were 250, 350, 450, and 550°C, but the experiments actually ran at 250, 290, 450, and 500°C. A description of operating history and dosimetry for ORR-MFE-2 is provided by Greenwood.[5] Displacement damage and helium production were calculated from the neutron fluence as recommended by Gabriel et al.,[6] including the recent correction to displacement damage due to nickel atom recoil pointed out by Greenwood.[7] The neutron fluence of 6.8×10^{25} neutrons/m^2 (>0.1 MeV) produced 5 dpa and 38.7 at. ppm He in these samples at all temperatures.

Table 3.5.1. Composition of Several Heats of Type 316 Stainless Steel

Heat Designation	Alloy Composition, wt %												
	Fe	Cr	Ni	Mo	Mn	Si	C	Ti	P	S	N	B	Co
Ref.-heat 316 (X-15893)	Bal	17.3	12.4	2.2	1.7	0.7	0.05		*0.03*	0.015		0.0004	0.35
DO-heat 316	Bal	18.0	13.0	2.6	1.9	0.8	0.05	0.05	0.01	0.016	0.05	0.0005	0.004
N-lot 316	Bal	16.5	13.5	2.5	1.6	0.5	0.05		0.09	0.006	0.006	0.0008	0.05

Disks about 3 mm in diameter were electro-discharge machined from the shoulders of the tensile specimens that had been postirradiation tensile tested. Previous work has established that the tensile testing does not disturb the as-irradiated microstructure in the shoulder region,' contrary to earlier criticism.[9] These samples were examined with the transmission electron microscopy (TEM) techniques described previously.[8,10] The relatively high cobalt content of this alloy resulted in high levels of radioactivity after the ORR irradiation and made specimen handling difficult.

3.5.4.2 Results

There are no bubbles or voids observed in the microstructure of CW 316 (ref.-heat) irradiated in ORR to 5 dpa at temperatures from 250 to 500°C. Figure 3.5.1 shows the microstructure in contrast conditions appropriate for best resolution of small cavities (kinematical diffraction, underfocused), and none can be seen. There is no evidence of precipitation for any of these irradiation conditions. There is, however, an effect of the irradiation on the dislocation structure.

E-34523

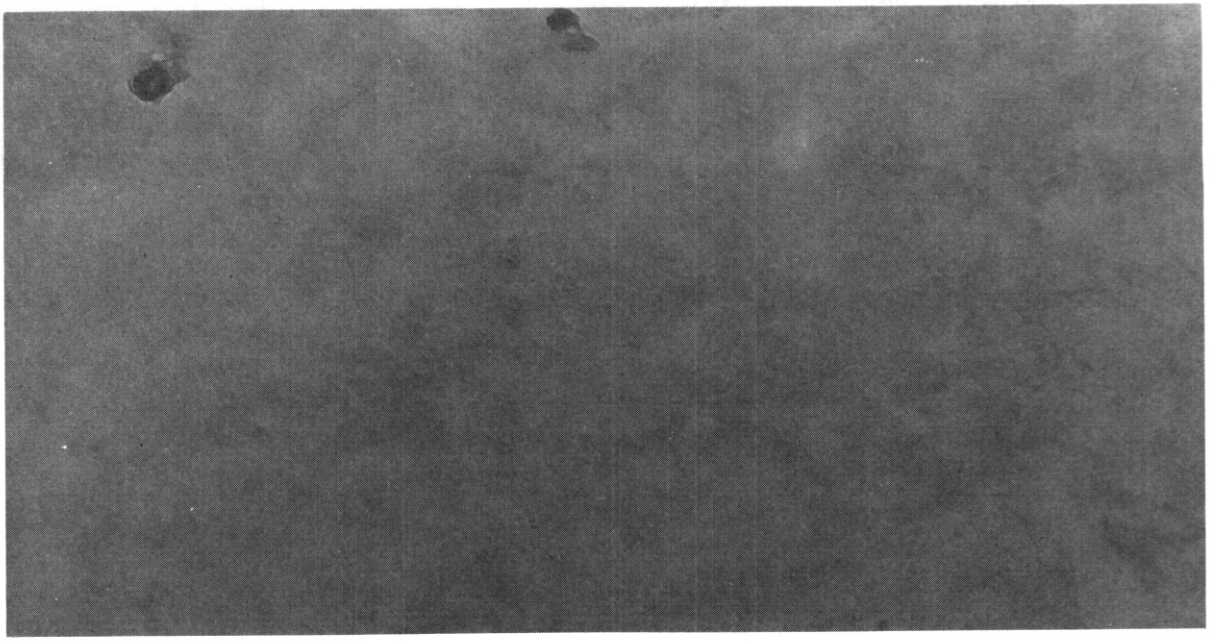

Fig. 3.5.1. CW 316 (Ref.-Heat) Irradiated in ORR at 500°C to 5 dpa (38.7 at. ppm He) and Imaged in the Underfocus, Kinematical Contrast Condition to Demonstrate that No Cavities (Voids or Bubbles) Are Visible.

The overall dislocation concentration is high and quite temperature independent from 250 to 450°C, but, by comparison, appears much less concentrated at 500°C. This can be seen in Fig. 3.5.2. Frank loops (assumed to be interstitial) are a significant portion of the overall dislocation microstructure at all temperatures. The loop component at the various temperatures is shown in Fig. 3.5.3 for one set of (111) planes

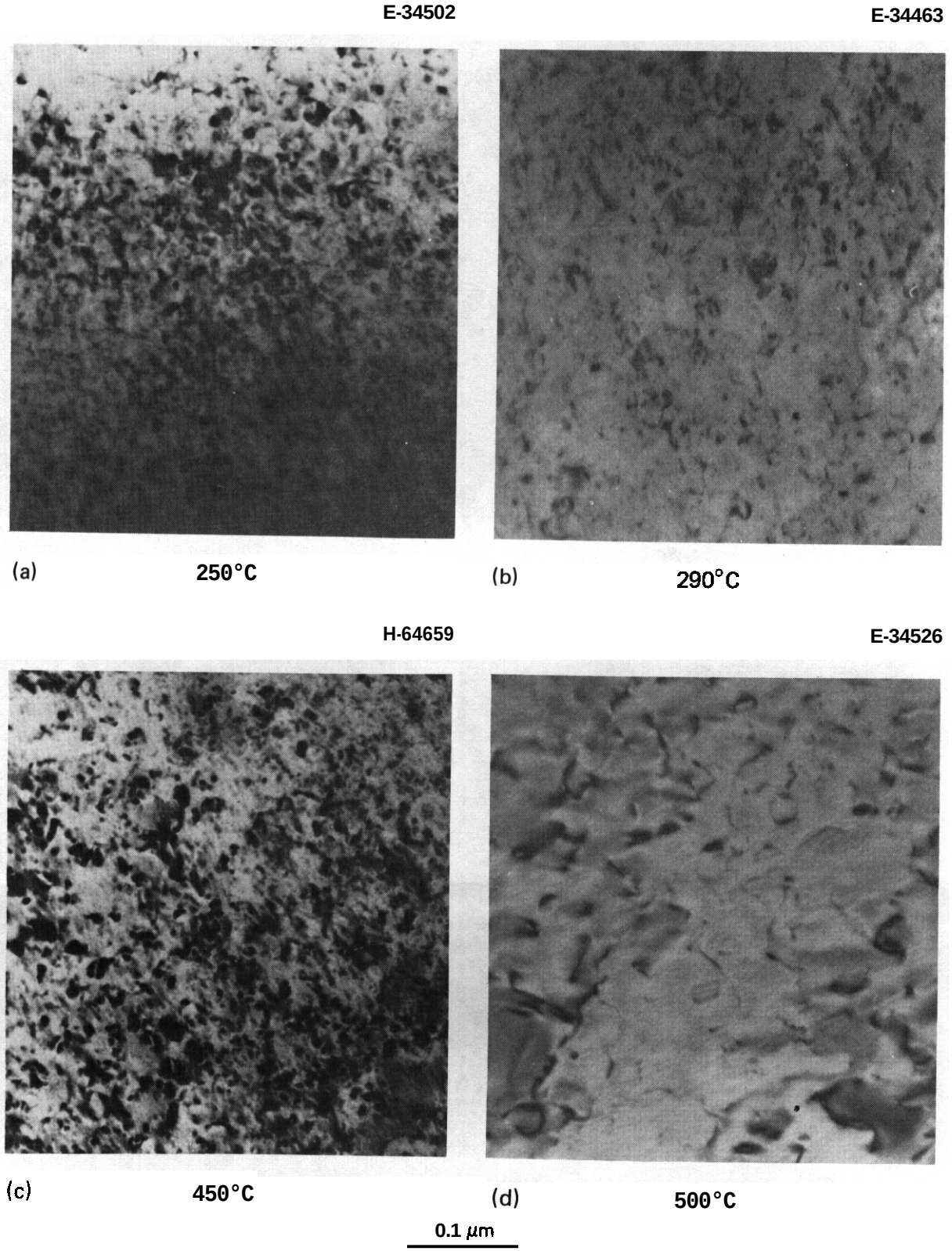

Fig. 3.5.2. Dislocation Microstructures of CW 316 (Ref.-Heat) Irradiated in ORR to 5 dpa (38.7 at. ppm He) at the Temperatures Indicated. All are imaged using g_{200} with $s > 0$. Note the more relaxed structure at 500°C (d).

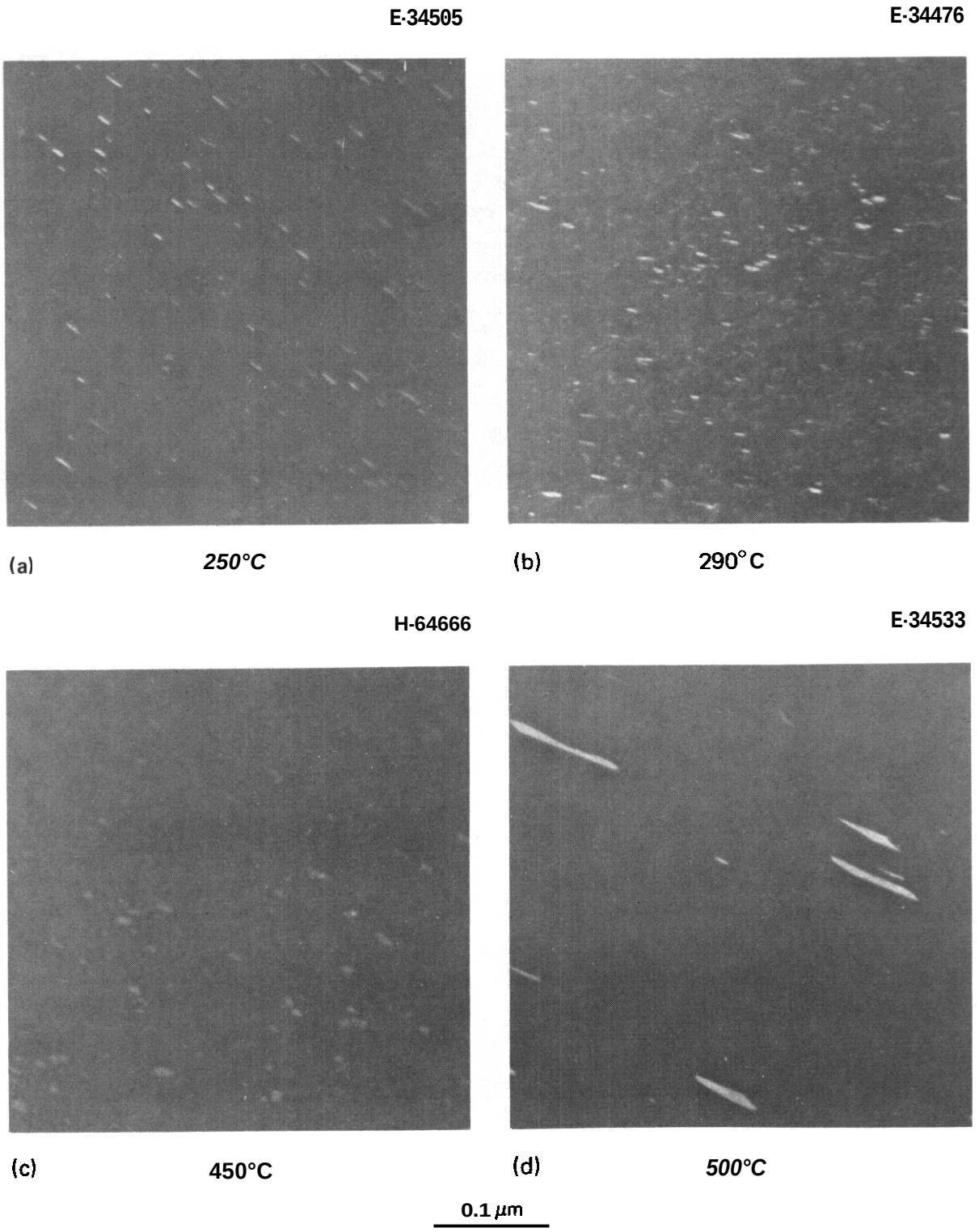

Fig. 3.5.3. Larger Frank Loop Component of the Dislocation Microstructure of CW 316 (Ref.-Heat) Irradiated in ORR to 5 dpa (38.7 at. ppm He) at the Temperatures Indicated. All are imaged in dark field using <111> satellite streaks around g_{200} reflections. Note the large increase in size and decreased density of loops at 500°C, compared with the three lower temperatures.

(hence one-fourth of a total isotropic population) imaged in dark field via <111> satellite streaks around g_{200} matrix reflections. A high concentration of loops ranging from 8 to 25 nm in diameter is observed from 250 to 450°C. Fewer, much larger (17 to 100 nm in diameter) loops are observed at 500°C. The microstructures at 250 to 450°C appear similar to or denser than the network normally found in CW 316 (ref. 8), but the dislocation structure at 500°C is somewhat recovered. Finally, high concentration of "black dots" (<5 nm in diameter) can be seen in Fig. 3.5.2(a) and (b). These features, seen at 250 to 450°C when these samples are imaged in a weak beam-dark field condition (g_{200}, $+g/+3g$), may also be small loops. These "black dots" are not present at 500°C.

3.5.4.3 Discussion

We can compare these microstructural observations with results obtained on austenitic stainless steels irradiated in ORR (refs. 11 and 12), HFIR (refs. 8, 10, 13, and 14), and EBR-II (refs. 3, 15, and 16). Key features of the present results and the literature data are summarized in Figs. 3.5.4 and 3.5.5.

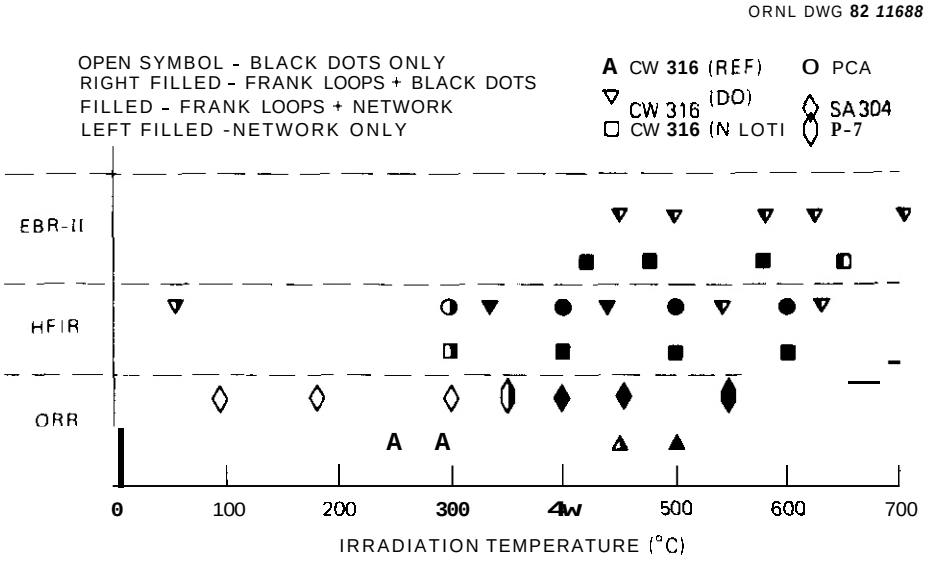

Fig. 3.5.4. Temperature Boundaries Between the Various Components of the Dislocation Microstructure Observed in Austenitic Stainless Steels Irradiated to Fluences Producing 12 dpa or Lower.

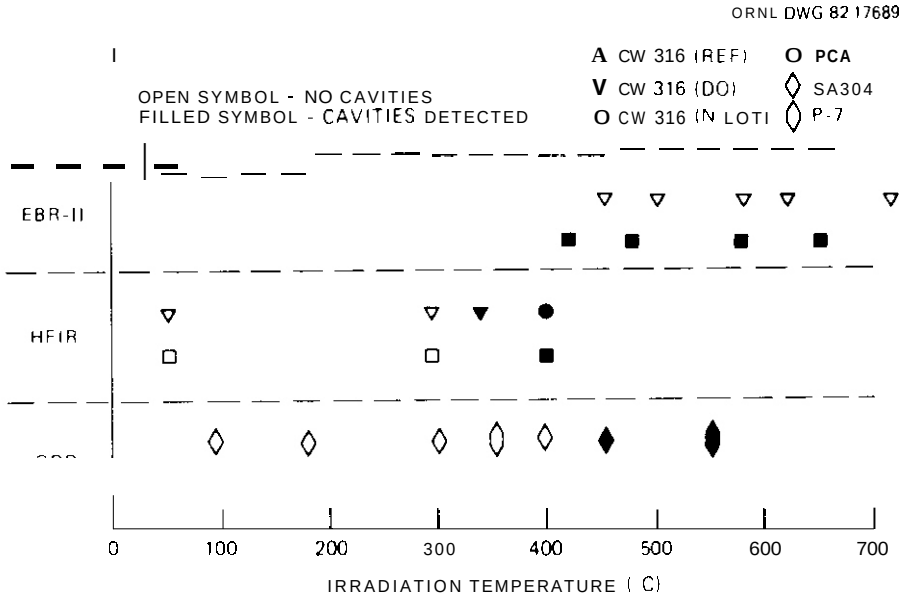

Fig. *3.5.5.* Observations at Fluences Producing 12 dpa or Lower that Define the Lower Temperature Limit for Cavity Formation in Austenitic Stainless Steel.

Bloom et al.[11] irradiated solution-annealed (SA) type *304* stainless steel in the ORR to fluences producing less than *0.5* dpa and less than about *5* at. ppm He at temperatures of *93* to *454°C.* They observed a high density of fine "black-dot'' structures, believed to be loops (of unknown nature), at *93°C.* With only small changes in size and density, this structure persisted at *177* and *300°C.* At 371°C, the "black-dot'' density decreased by several orders of magnitude and disappeared at *398°C.* The features characteristic of higher temperature irradiation damage structures — larger loops and precipitates – began to appear, and small helium bubbles were found at *454°C.* Figures *3.5.4* and *3.5.5* define the temperature limits of these observations. Brager and Garner[''] also observe only Frank loops, networks and "small defect clusters" (≤3 nm in diameter) in SA and CW *316* high-purity austenitic stainless steel (P7) irradiated in ORR–MFE–2 to *3* dpa at *350°C.* They find voids and bubbles in P7 after *4* dpa *(33* at. ppm He) at *550°C.* Data in their work is qualitatively consistent with the present results in that a fairly constant low-temperature microstructure is observed over a range of temperatures before

a transition occurs to a higher-temperature-type microstructure (Figs. 3.5.4 and 3.5.5). The transition (judging from loop and "black-dot" structures) occurs about 100 to 150°C higher for CW 316 (ref.-heat) than for the SA 304 of Bloom et al.

The microstructural results on CW 316 (ref.-heat) irradiated in ORR are consistent with microstructural data on several heats of steel [347, DO-heat and N-lot 316s, Path A Prime Candidate Alloy (PCA)] irradiated in HFIR in several preirradiation microstructural conditions','' [13,14,17,18] as seen in Figs. 3.5.4 and 3.5.5. No voids, bubbles, or irradiation-induced or -enhanced precipitates are observed after HFIR irradiation at 55 to 300°C, for fluences producing up to approximately 11 dpa. Regardless of material or pretreatment, the HFIR microstructures consist of similar-sized Frank loops (~10--30 nm in diameter) and a high concentration of the "black-dot'' defects (~35 nm in diameter) (Fig. 3.5.4). However, dislocation network concentration varies widely and depends strongly on pretreatment. Bubbles are found after HFIR irradiation at 400°C for some of the PCA pretreatments and for CW 316 N-lot. The very fine "black dots" are not observed when these materials contain bubbles.[18] These "black dots" are also absent when voids appear in CW 316 (DO-heat) irradiated in HFIR at 325 to 350°C to 8.4 dpa. Again, this transition from characteristic lower temperature to higher temperature microstructure occurs at about 300 to 350°C in HFIR (Fig. 3.5.4), 100 to 150°C lower than for CW 316 (ref.-heat) irradiated in ORR.

Fast breeder reactor data do not extend below 300 to 350°C. However, the limited data are also mapped with temperatures in Figs. 3.5.4 and 3.5.5. Voids are not observed by Bramman et al.[19] in type 316 stainless steel irradiated below 350°C to 30 to 40 dpa in the Dounreay Fast Reactor (DFR). Voids are also not observed by Bloom and Stiegler[15] for CW 316 (DO-heat) irradiated in EBR-II at 450°C to 10 dpa or at 510°C to 6.4 dpa. Maziasz[3] found no voids or fine bubbles in the same material irradiated in EBR-II to 8.4 dpa at 500°C but did find both voids and bubbles after 36 dpa at 525°C. Brager,[16] however, does observe voids in another heat of CW 316 after EBR-II irradiation to 12.2 dpa at 420 and 475°C (Fig. 3.5.5). The early stages of void formation for type 316 stainless steel in EBR-II

are extremely variable from heat to heat of steel. Within this scatter, however, the ORR results are consistent with EBR-II results (Fig. 3.5.5), and it is not clear whether or not voids should be expected after only 5 dpa in the ORR at 450 to 500°C. Higher fluence data will be required before confident statements about retardation (or acceleration) of void or bubble formation in ORR can be made. Certainly comparison with the HFIR data suggests that bubble swelling at 500°C is retarded in ORR.

3.5.5 Conclusions and Future Work

1. Formation of bubbles, voids, or precipitate phases is not observed in CW 316 (ref.-heat) after irradiation in ORR to 5 dpa (38.7 at. ppm He) at 250 to 500°C.

2. Frank loops are observed at all irradiation temperatures. The dislocation network appears similar to the as-cold-worked structure for irradiation at 250 to 450°C, but some recovery occurs at 500°C. The overall dislocation concentration is similar at 250 to 450°C but is considerably relaxed at 500°C. Frank loop concentrations are high, and the diameters range approximately 8 to 25 nm for irradiation between 250 and 450°C. There are far fewer and much larger loops at 500°C (17–100 nm in diameter).

3. A high concentration of very fine "black dots" (3–5 nm in diameter) are present in the dislocation structure after irradiation at 250 to 450°C but are absent as the network lessens and large loops coarsen at 500°C.

4. Bubble formation may be retarded in ORR compared with similar HFIR irradiation, particularly at 500°C. However, 5 dpa in ORR is too low a fluence to detect any effect on void formation relative to EBR-II or HFIR irradiation.

Future work will include more detailed comparison with EBR-II and HFIR irradiated steels. Work is in progress to identify the "black-dot'' component of the microstructure and to confirm the interstitial nature of the larger Frank loops.

3.5.6 References

1. G. R. Odette, P. J. Maziasz, and J. A. Spitznagel, "Fission-Fusion Correlations for Swelling and Microstructure in Stainless Steels: Effect of the Helium to Displacement per Atom Ratio," *J. Nucl. Mater.* 103&104: 1289–1304 (1981).
2. E. H. Lee, A. F. Rowcliffe, and L. K. Mansur, "Precipitation and Cavity Formation in Austenitic Stainless Steels During Irradiation," *J. Nucl. Mater.* 103&104: 1475–80 (1981).
3. P. J. Maziasz, "Some Effects of Increased Helium Content on Void Formation and Solute Segregation in Neutron Irradiated Type 316 Stainless Steel," *J. Nucl. Muter.* 108&109: 359–84 (1982).
4. J. W. Woods, A. F. Zulliger, and E. E. Bloom, "Status of ORR-MFE-1 and -2 Irradiation Experiments," *ADIP Quart. Prog. Rep. Mar. 31, 1978,* DOE/ET-0058/1, pp. 164–75.
5. L. R. Greenwood, "Fission Reactor Dosimetry," *DAFS Quart. Prog. Rep. June 30, 1981,* DOE/ER-0046/6, pp. 17–28.
6. T. A. Gabriel, B. L. Bishop, and F. W. Wiffen, *Calculated Irmdiation Response of Materials Using Fission Reactor (HFIR, ORR, and EBR-II) Neutron Spectra,* ORNL/TM-6361 (August 1979).
7. L. R. Greenwood, "Neutron Source Characterization for Materials Experiments," *ADIP Quart. Prog. Rep. Mar. 31, 1982,* DOE/ER-0045/8, pp. 66–86.
8. P. J. Maziasz, "Microstructural Development on 20%-Cold-Worked Types 316 and 316 + Ti Stainless Steels Irradiated in HFIR: Temperature and Fluence Dependence of the Dislocation Component," *ADIP Quart. Prog. Rep. Sept. 30, 1981,* DOE/ER-0045/7, pp. 54–97.
9. H. R. Brager and F. A. Garner, "Comparison of the Swelling and Microstructural/Microchemical Evolution of AISI 316 Irradiated in EBR-II and HFIR," *J. Nucl. Mater.* 103&104: 993–98 (1981).
10. P. J. Maziasz and M. L. Grossbeck, "Swelling and Microstructure of HFIR-Irradiated 20%-Cold-Worked Types 316 Stainless Steel and 316 + 0.23 wt % Ti," *ADIP Quart. Prog. Rep. Dec. 31, 1980,* DOE/ER-0045/5, pp. 43–69.

11. E. E. Bloom, W. R. Martin, J. O. Stiegler, and J. R. Weir, "The Effect of Irradiation Temperature on Strength and Microstructure of Stainless Steel," *J. Nucl. Water.* 22: 68–76 (1967).

12. H. R. Brager and F. A. Garner, "The Influence of Cold Work Level, Solute and Helium Content on the Swelling of 'Pure' AISI 316, (Fe–17 Cr–16.7 Ni–2.5 Mo)," *Effects of Radiation on Materials,* ed. H. R. Brager and J. S. Perrin, ASTM-STP-782 (1982), pp. 152–65.

13. F. W. Wiffen and P. J. Maziasz, "The Influence of Neutron Irradiation at 55°C on the Properties of Austenitic Stainless Steels," *J. Nucl. Water.* 103&104: 821–26 (1981).

14. P. J. Maziasz, "Microstructures Developed in Austenitic Stainless Steels Irradiated in HFIR at 55°C," *Trans. Am. Nucl. Soc.* 39: 433–35 (1981).

15. E. E. Bloom and J. O. Stiegler, "Effect of Irradiation on the Microstructure and Creep-Rupture Properties of Type 316 Stainless Steel," *Effects of Radiation on Substructure and Mechanical Properties of Metals and Alloys,* ed. J. Moteff, ASTM-STP-529 (1973), pp. 360–82.

16. H. R. Brager, "The Effects of Cold Work and Pre-Irradiation Heat Treatment on Void Formation in Neutron Irradiated Type 316 Stainless Steel," *J. Nucl. 'dater.* 57: 103–18 (1975).

17. P. J. Maziasz and D. N. Braski, "Swelling of Path A PCA Irradiated to 10 dpa in HFIR," *ADIP Quart. Prog. Rep. Mar. 31, 1982,* DOE/ER-0045/8, pp. 98–116.

18. P. J. Maziasz and D. N. Braski, "Swelling and Microstructural Development of Path A PCA and Type 316 Stainless Steel Irradiated in HFIR to 25 dpa," Sect. 3.2 in this report.

19. J. I. Bramman et al., "Void Swelling and Microstructural Changes in Fuel Pin Cladding and Unstressed Specimens Irradiated in DFR," *Radiation Effects in Rreeder Reactor Structural Materials,* ed. M. L. Bleiberg and J. W. Bennett, TMS-AIME (1977), pp. 479–508.

4. PATH B ALLOY DEVELOPMENT — HIGHER STRENGTH Fe–Ni–Cr ALLOYS

4.1 THE DUCTILITY BEHAVIOR OF IRRADIATED PATH B ALLOYS - W. J. S. Yang and M. L. Hamilton (Westinghouse Hanford Company)

4.1.1 ADIP Task

Task B Alloy Development - Precipitation Hardened Alloys.

4.1.2 Objective

The objective of this study was to assess the practicality of using five Path B alloys in their current form as structural materials in the Fusion First-Wall/Blanket by evaluating both their postirradiation ductility and the corresponding microstructures.

4.1.3 Summary

At test temperatures above 500°C, the postirradiation ductility of the Path B alloys was less than 1% for all alloy conditions studied. The postirradiation ductility was shown to be dependent on preirradiation thermomechanical treatment. Specimens in a cold worked and aged condition exhibited a smaller ductility drop as test temperatures increased above 500°C than specimens in either a cold worked or a solution treated and aged condition. The ductility of the high Ni alloy B6, in a cold worked and aged condition, dropped to a constant and finite level, 0.5-1%, over the test temperature range (300-700°C).

Microstructural studies indicated several possible causes for the low ductility observed in the Path B alloys. Precipitation of helium bubbles at grain boundaries was observed for all alloy conditions. Helium bubbles at grain boundaries could cause a reduction of the grain boundary cohesive energy and could also serve as potential crack nucleation sites during deformation. Other precipitates, which are known to cause a reduction in grain boundary strength were also observed. For example, cavities formed at precipitate/grain-boundary interfaces in cold worked and aged alloy B1; a layer of γ' completely coated grain boundaries in cold worked alloy B1; and n-phase plates were aligned in the grain boundary region in cold worked and aged alloy B4. These features weaken the grain boundaries and diminish their ability to deform. Relative to the weakened boundary, the matrix is quite strong, being

strengthened by the formation of γ' or γ'/γ'' precipitates, radiation-induced faulted loops, and a high density of helium bubbles. Due to the limited deformation tolerance of the grain boundaries, failure will be initiated there before matrix deformation can relax local stress concentrations at high temperatures. A single principal mechanism to explain the low ductility phenomena observed cannot be selected on the basis of the results of the microstructural studies.

Path B alloys in their current form will not provide adequate ductility for first wall applications at high temperatures.

4.1.4 Progress and Status

4.1.4.1 Introduction

Precipitation-hardenable alloys were considered for possible structural applications in the fusion first-wall/blanket, based on their excellent high temperature strength and creep resistance. They also retain good swelling resistance and in-reactor creep resistance as shown in studies performed under the breeder alloy development program.' The Path B alloys are nickel-base precipitation hardening alloys, with matrix hardening arising from the formation of γ' or γ'/γ''. Alloy B1 is a molybdenum-modified γ'-strengthened alloy. Alloy B2 is also a molybdenum-modified γ'-strengthened alloy similar to Nimonic PE16. Alloy B3 is a niobium-modified γ'-strengthened alloy. Alloy B4 is a γ'/γ''-strengthened alloy similar to Inconel 706. Alloy B6 is a high nickel γ'-strengthened alloy.

The Path B alloys were irradiated in HFIR in various thermomechanical conditions including the cold-worked (CW), cold-worked-and-aged (CWA) and solution-treated-and-aged (STA) conditions.' It was anticipated that the high helium levels produced during HFIR irradiation would significantly affect the microstructure and the ductility of the Path B alloys. This study evaluated the postirradiation ductility of the Path B alloys by the disk bend technique. A detailed microstructural examination was also performed to determine the mechanism(s) responsible for the reduction in ductility.

4.1.4.2 Experimental Procedure

The chemical compositions and the various thermomechanical treatments (TMT) of the Path B alloys are listed in Tables 4.1.1 and 4.1.2. Specimens of the Path B alloys were irradiated in HFIR in the form of TEM disks to a goal fluence of 10 dpa. The doses actually accumulated by each specimen at different temperatures are compiled in Table 4.1.3. Disk bend tests were performed according to procedures described elsewhere.[3] Tests were conducted at either the irradiation temperature or at 110°C above the irradiation temperature. All of the tests were conducted at a strain rate on the order of 10^{-4}/sec.

The specimens selected for microstructural study are listed in Table 4.1.4. Included in the examination were CW B1 (L4), CWA B1 (L5), CWA B2 (LA), CWA B4 (LK), and CWA B6 (LP). Alloy B3 was not examined. The disk specimens were electrolytically thinned and subsequently examined in a JEM 100 CX microscope operated at 100 KV. Grain boundary structure and precipitation were also studied by examining the etched specimen surfaces in a scanning electron microscope. The carbide extraction replicas taken from the specimen surface were examined in a transmission electron microscope.

4.1.4.3 Results

4.1.4.3.1 Ductility. All of the Path B alloys exhibited low ductility in their current form at temperatures ranging from 300 to 700°C. The data obtained are given in Table 4.1.5. The reported values of ductility were calculated at the point of maximum load, which provides an indication of the point at which crack propagation begins. At temperatures above ~500°C, a significant decrease in ductility was observed. This "ductility trough'' phenomenon, shown in Figure 4.1.1 for alloys B1 and B3, is common in nickel-base alloys. Specimens in the CWA condition showed the smallest ductility drop in the ductility trough region, while near zero ductility was observed in CW and STA specimens (Figure 4.1.2). For some CWA specimens, essentially a constant level of ductility was maintained across the range of test temperatures. For example, more than 1% ductility was maintained in CWA alloy B2, identified as LA, and more than 0.5% ductility was maintained in both CWA alloy B4, identified

Table C 1 1 Composition of the Path B Alloys

(Wt. %)

	Alloy Designation	Ni	Cr	Mo	Nb	Ti	Al	C	Si	Mn	B	Zr
γ' Strengthen∃ϖ Mo Modified	B1	2⊐.0	1○.0	1.0	---	3.°	1.5	0.03	0.∃	1.○	0.001	○.05
	B2	4○.0	1z.0	3.0	---	1.∃	1.5	0.03	0.∃	0.z	0.001	○.05
γ' Strengthene ϖ Mo Modified	∃3	30 0	1z 0	---	2 0	≥ 0	0 5	0 03	0 ∃	1 ○	○ 001	0 05
γ'/γ" Strengtheo∃ϖ	∃4	C0 0	1z ○	---	3 0	1 8	0 3	0 ○∃	0 ∃	0 z	0 001	○ 05
Nickel Base	B6	75 0	15 ○	---	1 0	z 5	1 ∃	0 ○∃	0 ∃	○ z	0 ○01	○ 05

Table 4.1.2. Thermomechanical Treatments of the Path B Alloys

Alloy	Alloy Code	TMT
B-1	L4	1025°C/5 min./AC + 30% CW
	L5	1025°C/5 min./AC + 30% CW + 750°C/8 hr./AC
	L6	1025°C/5 min./AC + 30% CW + 700°C/8 hr./AC
B-2	L7	1025°C/5 min./AC + 30% CW
	LA	1025°C/5 min./AC + 30% CW + 800°C/8 hr./AC
	LB	1025°C/5 min./AC + 30% CW + 750°C/8 hr./AC
B-3	LE	1025°C/5 min./AC + 30% CW
	LF	1025°C/5 min./AC + 30% CW + 750°C/8 hr./AC
	LH	1025°C/5 min./AC + 30% CW + 700°C/8 hr./AC
B-4	LJ	1025°C/5 min./AC + 30% CW
	LK	1025°C/5 min./AC + 30% CW + 750°C/8 hr./AC
	LL	1025°C/5 min./AC + 30% CW + 700°C/8 hr./AC
B-6	LN	1025°C/5 min./AC + 40% CW
	LP	1025°C/5 min./AC + 40% CW + 800°C/8 hr./AC
	LR	1025°C/5 min./AC + 40% CW + 750°C/8 hr./AC

Table 4.1.3 Dose and Helium Accumulation of the Path B Alloys

	300°C	400°C	500°C	600°C
B-1	7.6 dpa 596 ppm	7.6 dpa 596 ppm	9.2 dpa 852 ppm	8.5 dpa 723 ppm
B-2	4.4 dpa 455 ppm	4.4 dpa 455 ppm	9.2 dpa 1363 ppm	--- ---
B-4	4.4 dpa 455 ppm	4.4 dpa 455 ppm	9.2 dpa 1363 ppm	9.2 dpa 1363 ppm
B-6	4.4 dpa 853 ppm	4.4 dpa 853 ppm	9.2 dpa 2553 ppm	9.2 dpa 2553 ppm

Table 4.1.4. Specimen Matrix for TEM Examinations

Alloy-Code (TMT)	Irradiation Temperature (°C)			
B1-L4 (CW)	300	400		600
B1-L5 (CWA)				600
B2-LA (CWA)		400	500	
B4-LK (CWA)		400	500	
B6-LP (CWA)		400	500	

as LK and LL, and CWA alloy B6, identified as LP and LR. Figures 4.1.1 and 4.1.2 illustrate the severe drop in ductility observed in not only the CW condition of all of the Path B alloys but also in the CWA condition of alloys B1 and B3. A similar trend is observed in the data of CWA B2. There are insufficient data for CWA B4 at high temperature to determine whether it, too, will exhibit a ductility trough at higher temperatures. The high Ni alloy B6 in the CWA condition was the only Path B alloy which did not show a severe drop in ductility in the temperature range of the ductility trough (Figure 4.1.3), although B6 was expected to accumulate the most helium during irradiation due to its higher nickel content.

4.1.4.3.2 Microstructure. Alloy B1: Gamma prime formed during irradiation in CW alloy B1. The size of the γ' changed from 2-3 nm at 300°C to 10 nm at 600°C. A thin layer of γ' which coated grain boundaries was also detected. The grain boundary γ' film in CW alloy B1 is illustrated in Figure 4.1.4. This figure consists of an SEM micrograph showing a γ' layer partially etched from the grain boundaries and a bright-field micrograph of a γ' extraction replica with a γ' dark-field insert. The matrix contained heavily tangled dislocations as well as helium bubbles, the latter being observed in the matrix as well as at the grain boundaries for irradiation temperatures as low as 300°C. The size of the helium bubbles varied from 1.7 nm at 300°C to 3 nm at 600°C

Table 4.1.5. Disk Bend Results for the Path B Alloys

	Irradiation Temperature: / Test Temperature: (2)		Ductility (%) (1) 300°C / T_i+110	400°C / T_i+110	500°C / T_i+110	600°C / T_i+110
B-1	30% CW	(L4)	1.5	0.13	0.55	0.16 / 0.24
	30% CW +750°C/8 hr./AC	(L5)				0.07
	30% CW +700°C/8 hr./AC	(L6)	>1.3/	0.53/	0.33/	0.20
	STA	(LX)	>2.3/	0.35/	0.03/	0.15
B-2	30% CW	(L7)		0.1-0.6	0.5	
	30% CW + 800°C/8 hr./AC	(LA)		1.7	1.2	
	30% CW + 750°C/8 hr./AC	(LB)		1.7	0.28	
	STA	(LT)			0.23	
B-3	30% CW	(LE)	>3.3/>2.0	/0.15	/0.06	0.09/0.19
	30% CW +750°C 3 hr AC	(LF)	>1.3/	1.4/	0.27/	0.06/
B-4	30% CW	(LJ)	>2.6	1.9/1.1	0.71 0.62	0.15 0.53
	30% CW +750°C/8 hr./AC	(LK)		3.4/	0.48	
	30% CW +700°C/8 hr./AC	(LL)		2.6/	0.71	
	STA	(LV)	>2.5	1.6/		
B-6	40% CW	(LN)		1.2/0.93	0.14	0.26
	40% CW +800°C/3 hr./AC	(LP)	>1.3	0.46/	0.84 0.52	0.75
	40% CW +730°C/3 hr./AC	(LR)		0.95/	0.78	

(1) Reported values of ">" some percentage are the strains at which the tests were halted, with no indication of crack propagation.

(2) Data obtained at one or two test conditions, separated by slash (/):

T_i indicates tests performed at the irradiation temperature.

T_i + 110 indicates tests performed at 110°C above the irradiation temperature.

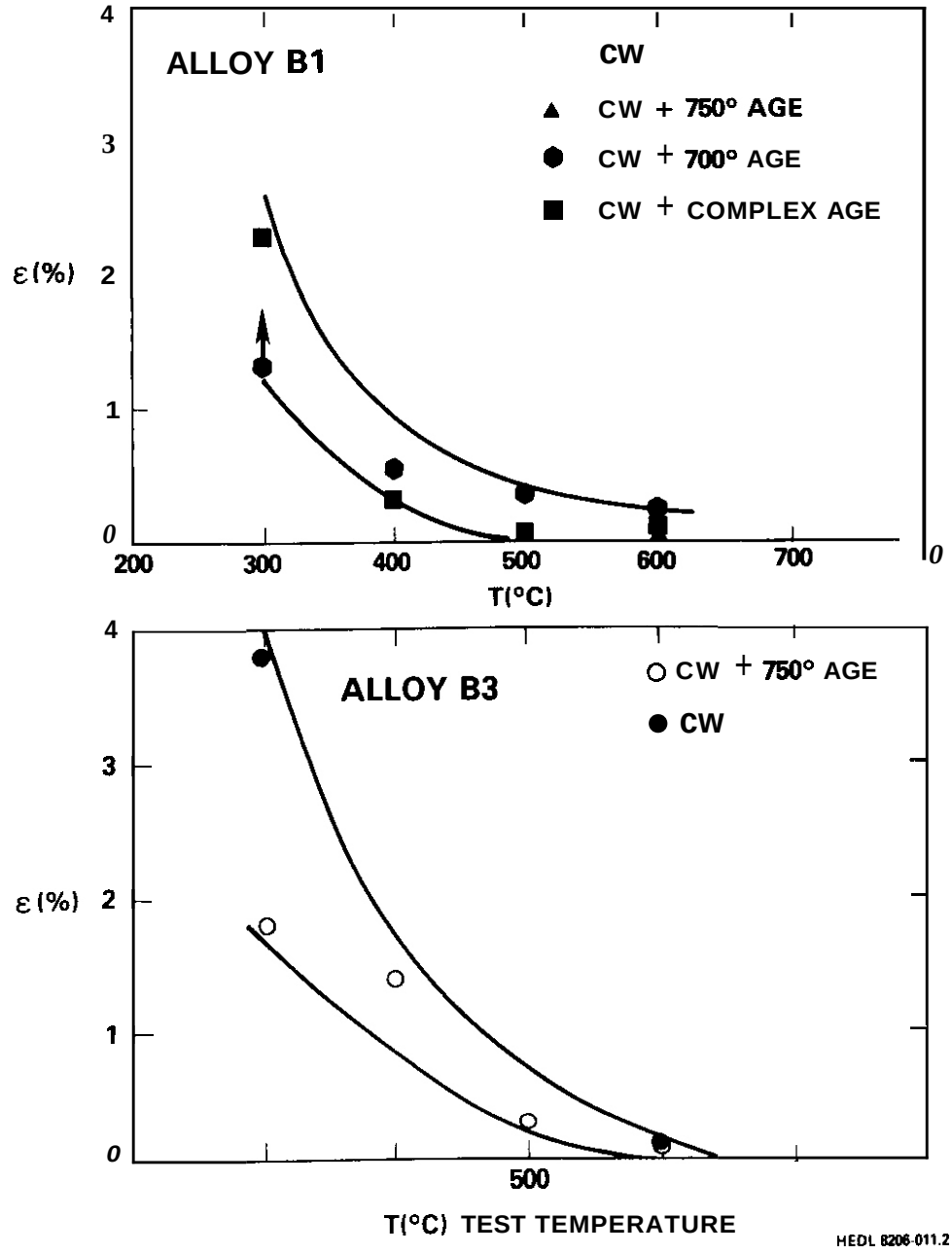

Fig. 4.1.1 The Effect of Thermomechanical Treatment on the Ductility of Alloys B1 and B3 Tested at the Irradiation Temperature.

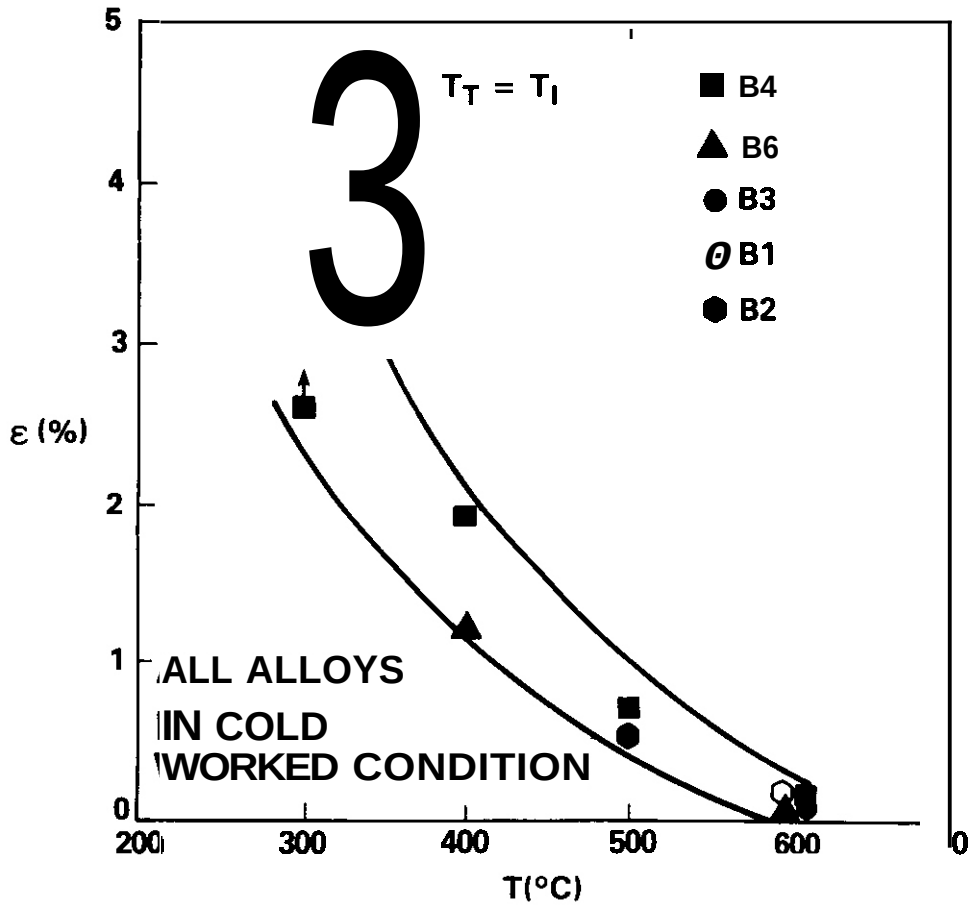

Fig. 4.1.2 The Ductility Trough for Cold Worked Path B Alloys Tested at the Irradiation Temperature.

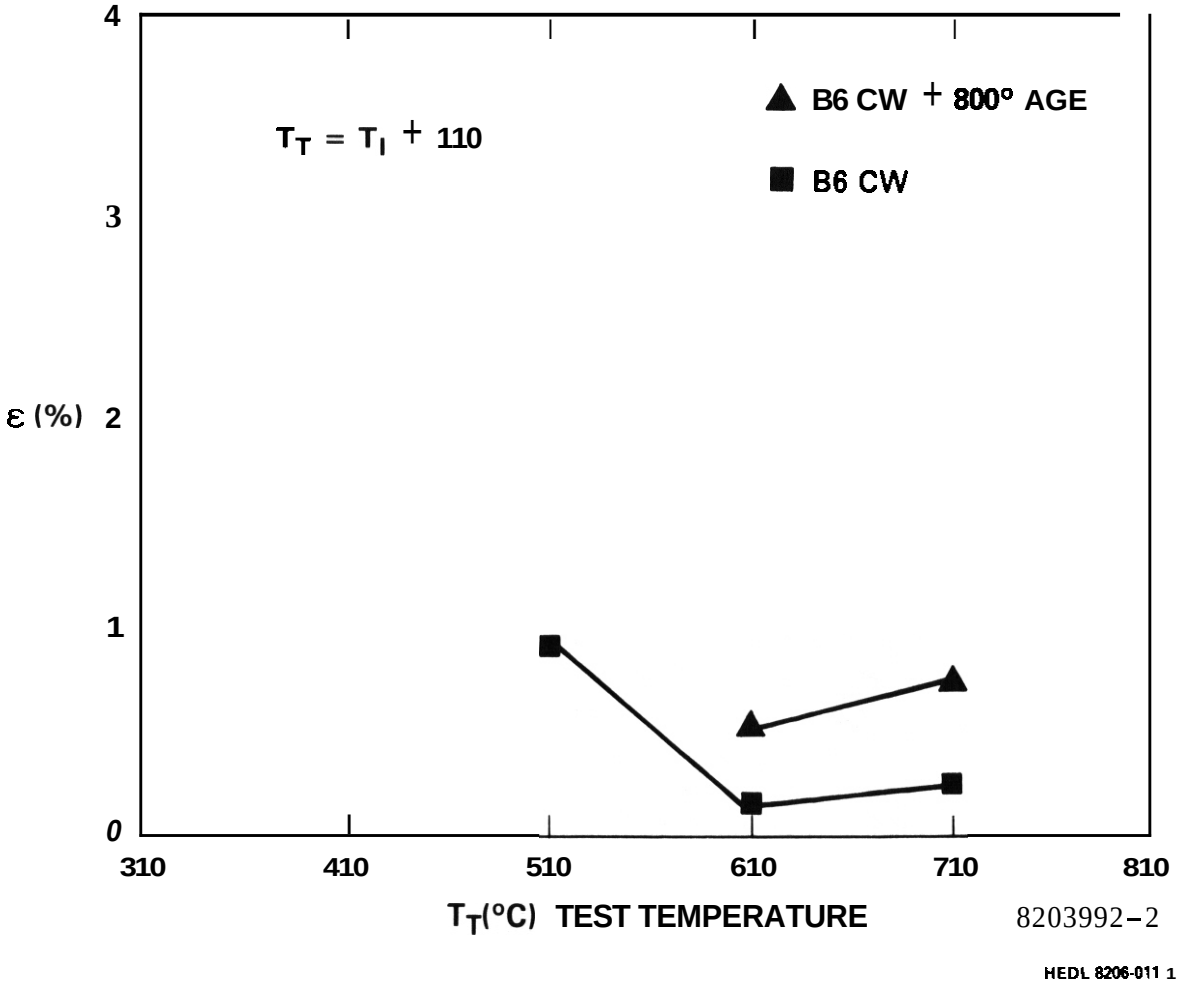

Fig. 4.1.3 The Effect of Thermomechanical Treatment on the Ductility of Alloy B6.

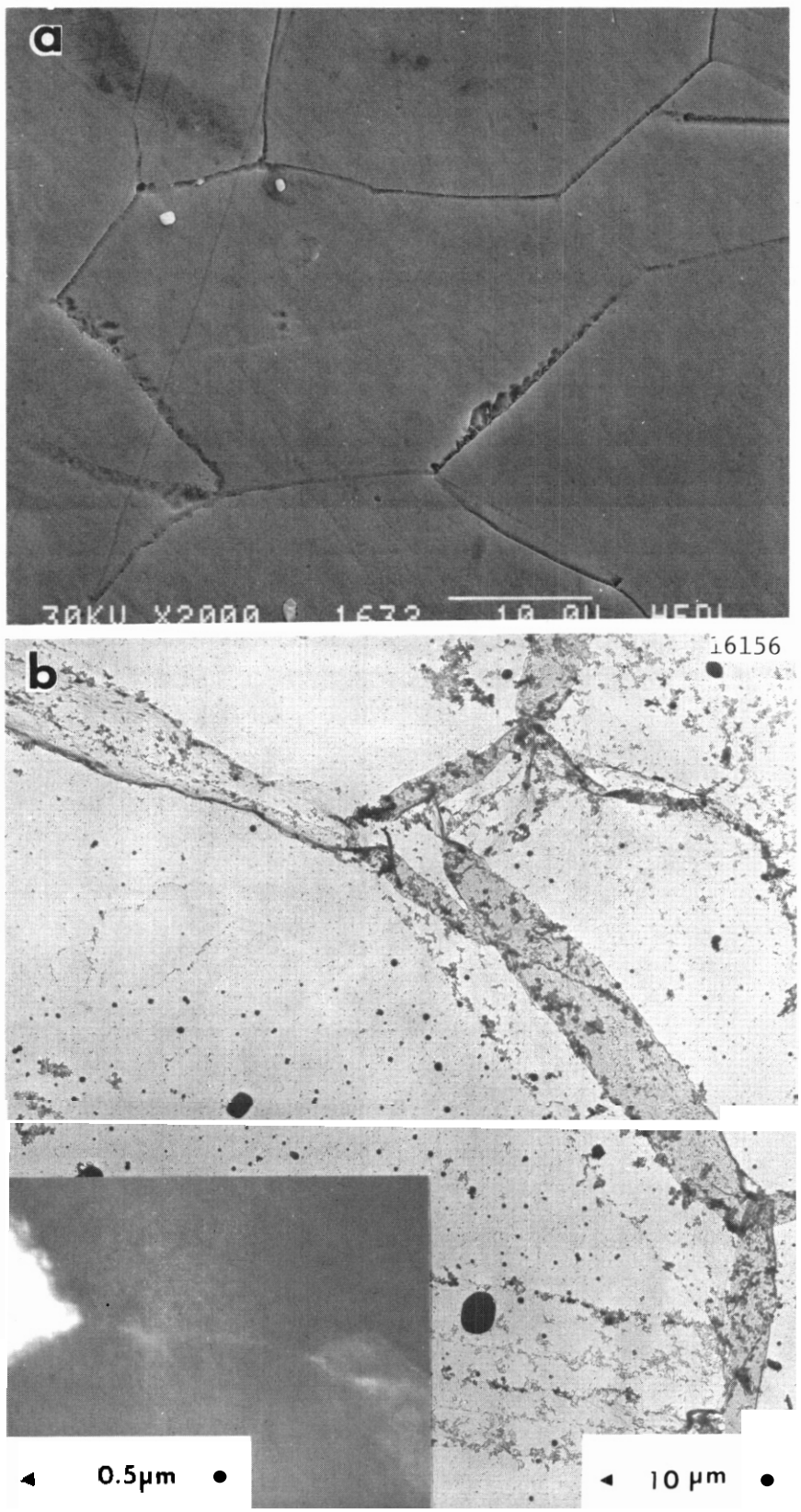

Fig. 4.1.4 The Development of a γ' Layer at the Boundaries in a CW B1 Specimen Irradiated to a Fluence of 8.5 dpa at 600°C. (a) A SEM Micrograph Showing the γ' Layer Partially Etched Away from the Grain Boundaries. (b) A Bright-Field and a γ' Dark-Field Image Taken at a Grain Boundary Region of an Extraction Replica.

with a matrix density of 3 x $10^{16}/cm^3$. Bubbles at grain boundaries were the same size as helium bubbles in the matrix. Figure 4.1.5 shows examples of the helium bubbles observed in CW alloy B1. No cavities large enough to be attributed to void swelling were observed in the matrix. The formation of both the γ' and the helium bubbles during irradiation caused the matrix to harden by more than *40%.* The microhardness of a cold worked specimen increased from 323 DPH in the unirradiated condition to 474 DPH following irradiation at 300°C, and to 463 DPH following irradiation at 600°C. The deformation of these alloys is expected to be affected by the hardened matrix, particularly at high temperatures where grain boundary deformation plays an important role in the total deformation. Early failure is expected whenever a substantial difference in strength exists between the matrix and the grain boundary (i.e., a strong matrix coupled with weak grain boundaries). In CW alloy B1, both the helium accumulation and the γ' segregation at grain boundaries contributed to the relative weakening of the grain boundary.

Uniform void swelling was observed in CWA alloy B1 irradiated at 600°C to a dose of 8.5 dpa. The void swelling value was <0.01%, with void diameters varying from 3 to 20 nm. Void swelling in CWA alloy B1 is illustrated in Figure 4.1.6. Cavities 3 nm in diameter observed in the matrix and at the grain boundaries were thought to be helium bubbles. The CWA treatment introduced uniform γ' precipitates (30 nm in diameter) in the matrix and a complex grain boundary structure consisting of discrete, blocky, Ti-rich G phase, blocky MC and cellular γ'. Figure 4.1.7 shows such complex grain boundary structures. Cavities which form at the precipitate/grain boundary interface during irradiation serve as crack nucleation sites during deformation and enhance the intergranular fracture tendencies of this alloy. Only minor increases in the matrix hardness were observed. An average microhardness value of 372 DPH was obtained on an unirradiated specimen, increasing to 385 DPH on a specimen irradiated at 600°C.

Alloy B2: Uniform void swelling was also observed in irradiated CW alloy B2. Void swelling measured in specimens irradiated at 500°C to 9.2 dpa was <0.01%, with an average void size of 17 nm. Void swelling

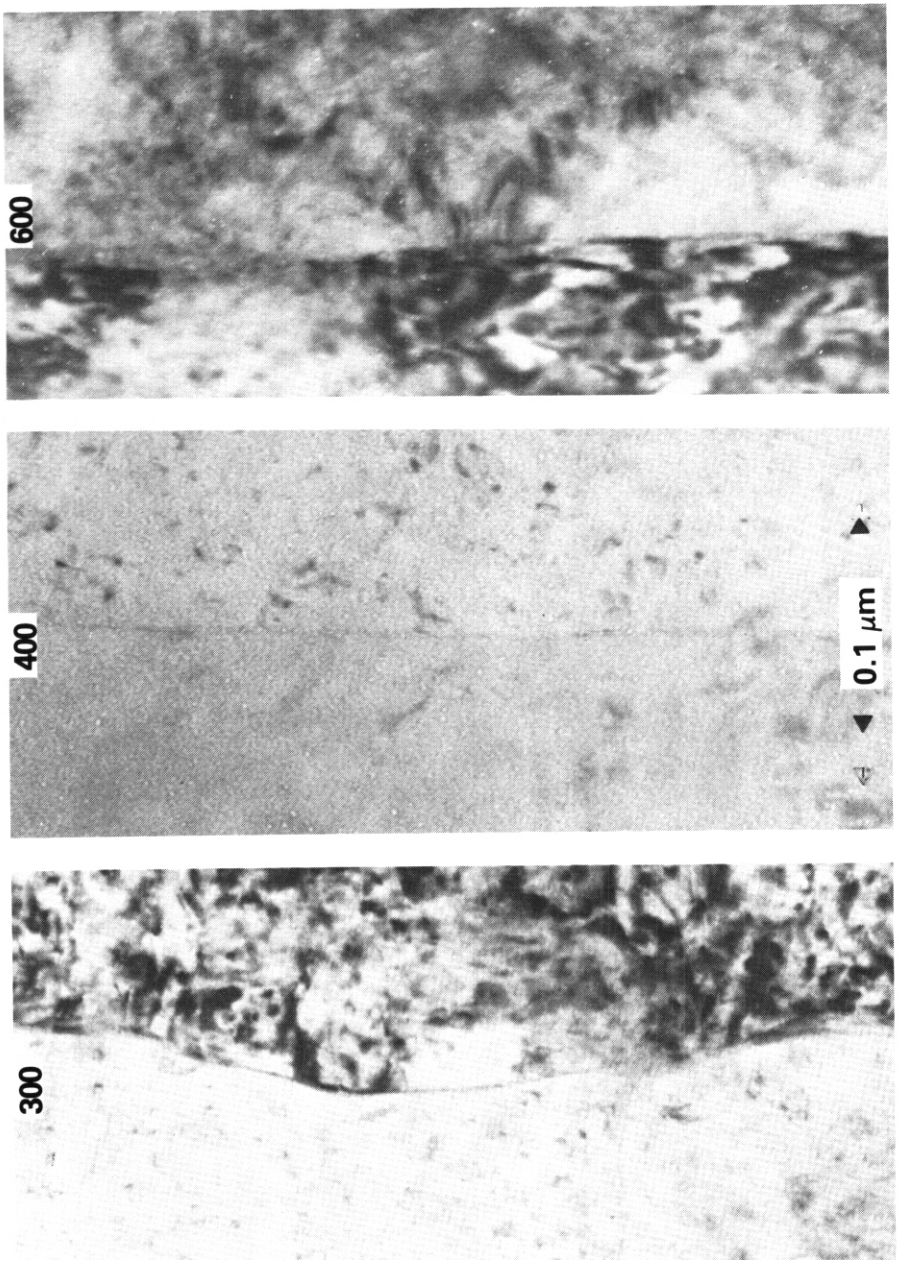

Fig. 4.1.5 Helium Bubbles at Grain Boundaries in 30% CW Alloy B1 Irradiated at (a) 300°C, (b) 400°C and (c) 600°C.

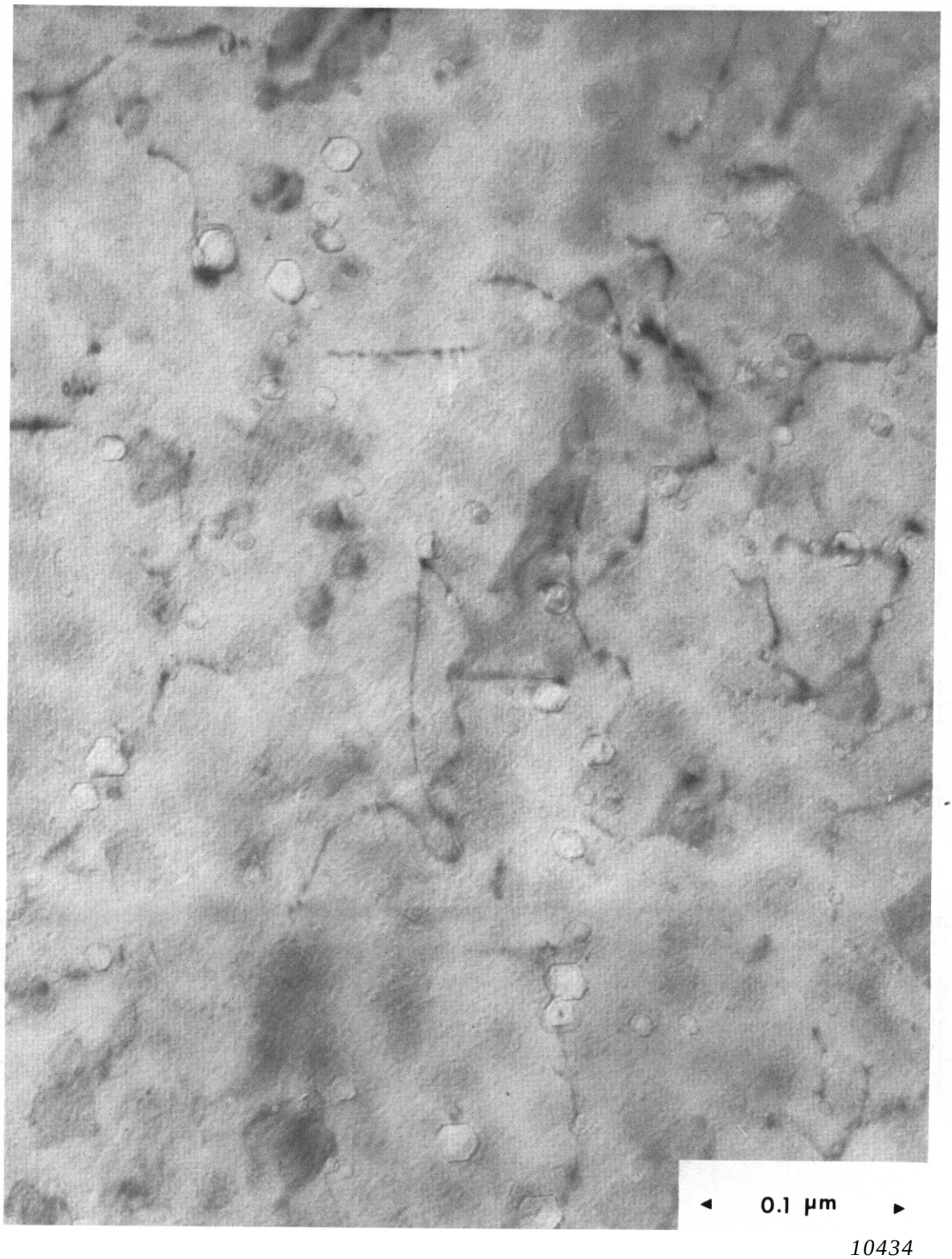

Fig. 4.1.6 Void Swelling in CWA **Alloy** B1 Irradiated at 600°C to a Fluence of 8.5 dpa.

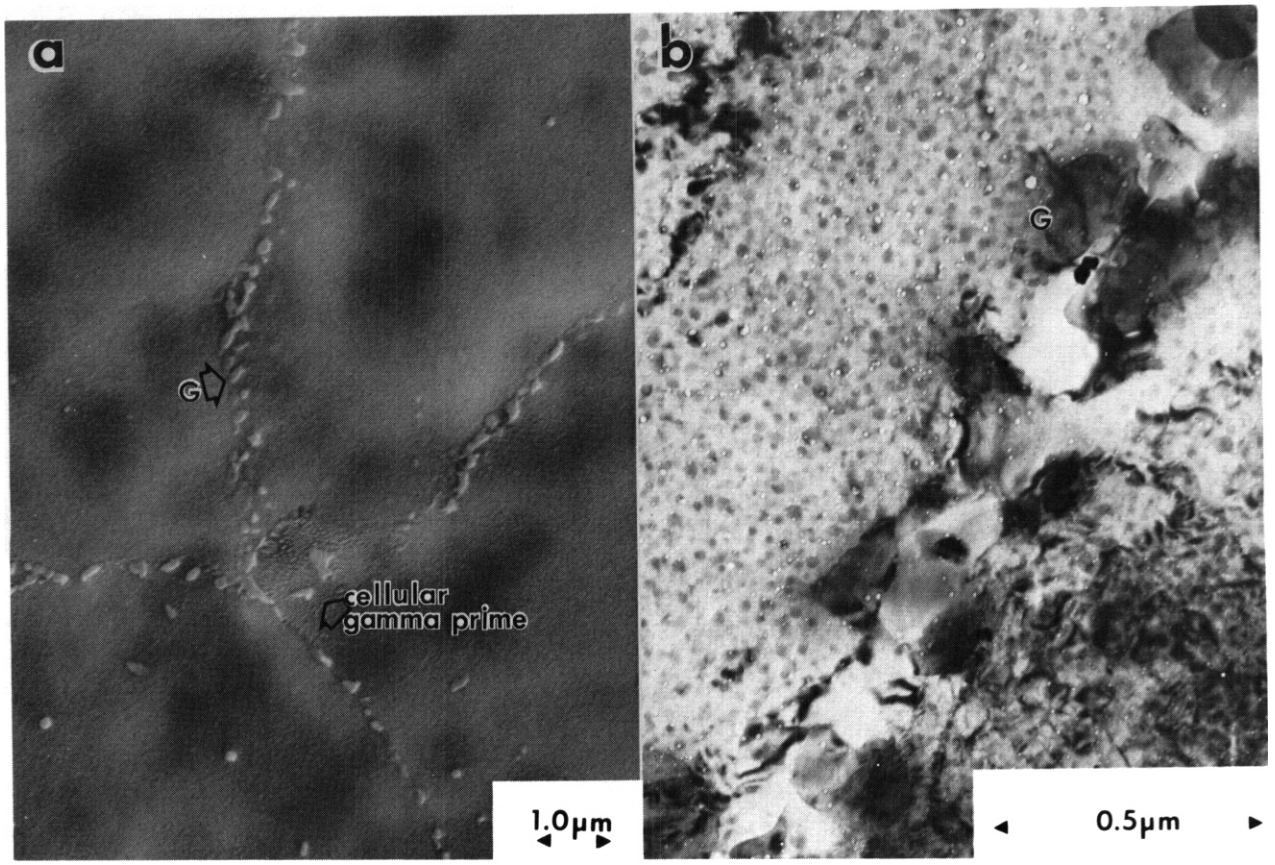

Fig. 4.1.7 Grain Boundary Structure in CWA B1, Consisting of Discrete, Blocky, Ti-rich G-phase, Blocky MC and Cellular γ'. (a) A SEM Micrograph Taken From an Etched Surface; (b) A Transmission Micrograph Showing the Cavities and Precipitates at a Grain Boundary.

in this alloy is illustrated in Figure *4.1.8.* Helium bubbles ***2.7*** nm in diameter were uniformly distributed in the matrix and at grain boundaries (Figure ***4.1.9)*** with a bubble density in the matrix of ***3.6*** x $10^{16}/cm^3$. The size distribution of γ' in irradiated CWA **B2** had two peaks, at diameters of ***7*** and ***40*** nm. The finer γ' was formed during irradiation. The grain boundary structure of CWA **B2** consisted of $M_{23}C_6$ and MC particles. The γ' distribution in the irradiated CWA **B2** is shown in Figure ***4.1.10.*** Figure ***4.1.11*** shows the grain boundary $M_{23}C_6$ and MC precipitates in the irradiated CWA **B2.** The role of the fine precipitates at grain boundaries is uncertain. If these precipitates existed before the cold-work treatment, however, the cold-work-and-age treatment could introduce microcracks at the tips of the precipitates[4-10] with subsequent degradation in alloy mechanical properties.

Alloy *B4*: The γ'/γ''-strengthened alloy ***B4*** exhibited an insignificant amount of void swelling (<<0.01%) and this was located mainly at the grain boundary regions. Helium bubbles 2.7 nm in diameter formed both in the matrix and at the grain boundaries, as shown in Figure 4.1.12. The bubble density in the matrix was 5 x $10^{16}/cm^3$. The CWA treatment produced y', γ'', and η in the matrix and n-plates, blocky G phase and $M_{23}C_6$ at the grain boundaries. The γ'' in CWA alloy ***B4*** dissolved completely during irradiation below 500°C. No γ'' was observed in either of the two specimens examined which had been irradiated at *400* and 500°C. This is consistent with observations on irradiated Inconel 706.[11] Figure ***4.1.13*** shows the γ' in CWA B4 irradiated at 500°C to 9.2 dpa. The n-plates which formed during the CWA treatment remained stable during irradiation. Figure ***4.1.14*** shows the n-plates at grain boundaries together with G and $M_{23}C_6$ particles. The existence of n-plates at grain boundaries may create a plane of weakness in this region along the {111} slip planes, since n-plates have a {111} habit.

Alloy ***B6*:** No void swelling was observed in the high Ni alloy **B6,** although helium bubbles at a density of ***5.4*** x $10^{16}/cm^3$ were observed in the matrix. They had also nucleated at grain boundaries, as had been observed in the other Path B alloys. Figure ***4.1.15*** shows the helium bubbles observed in CWA ***B6*** irradiated at 500°C to ***9.2*** dpa. The γ' size distribution in irradiated CWA ***B6*** had two peaks at diameters of ***4*** and ***60*** nm as revealed in Figure ***4.1.16.*** The finer γ' was formed during

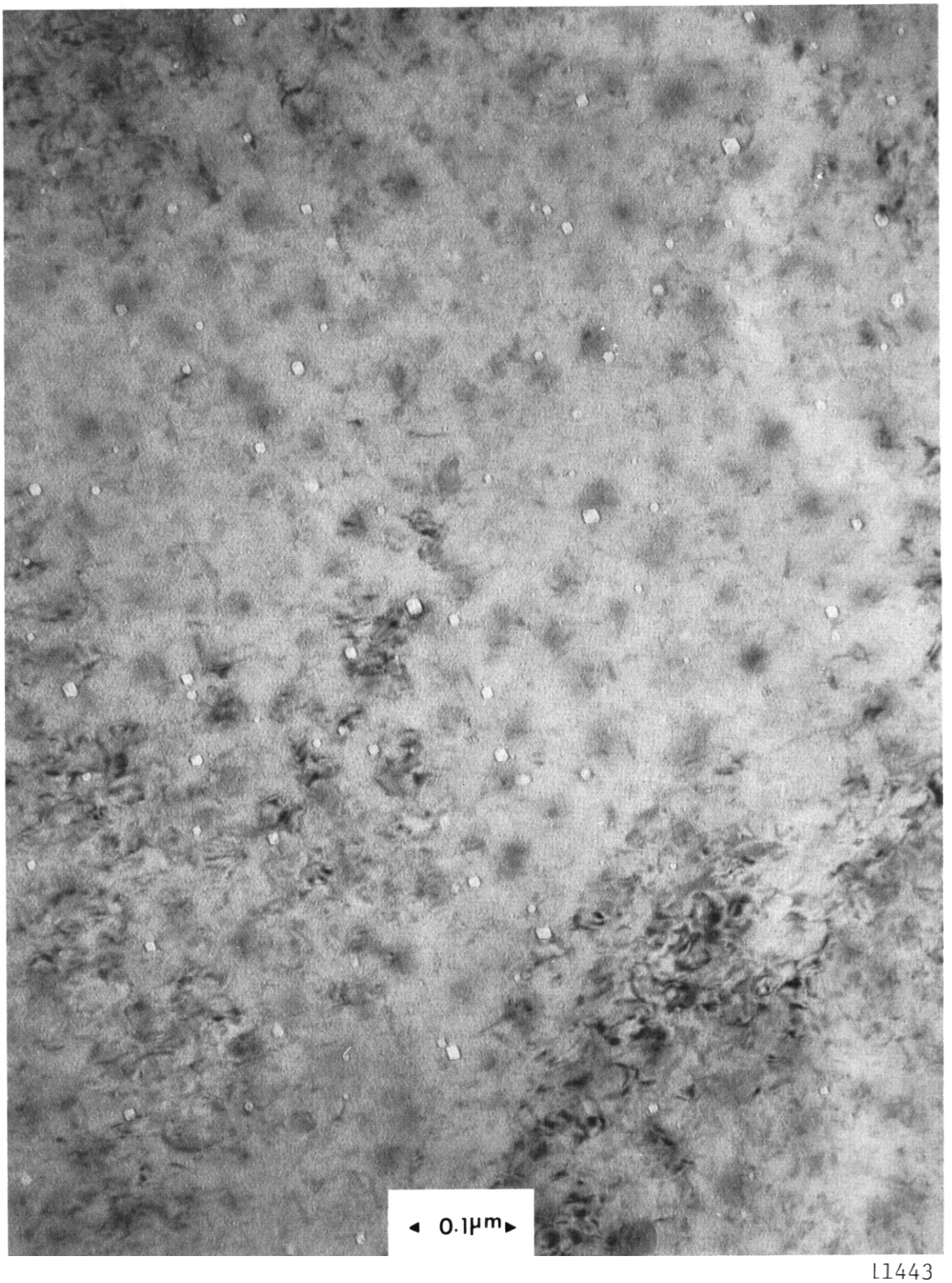

Fig. *4.1.8* Void **Swelling** in **CWA** Alloy **B2 Irradiated at 500°C to a Fluence** of **9.2** dpa.

11441

Fig. 4.1.9 Helium Bubbles in CWA Alloy B2 Irradiated at 500°C to a Fluence of 9.2 dpa.

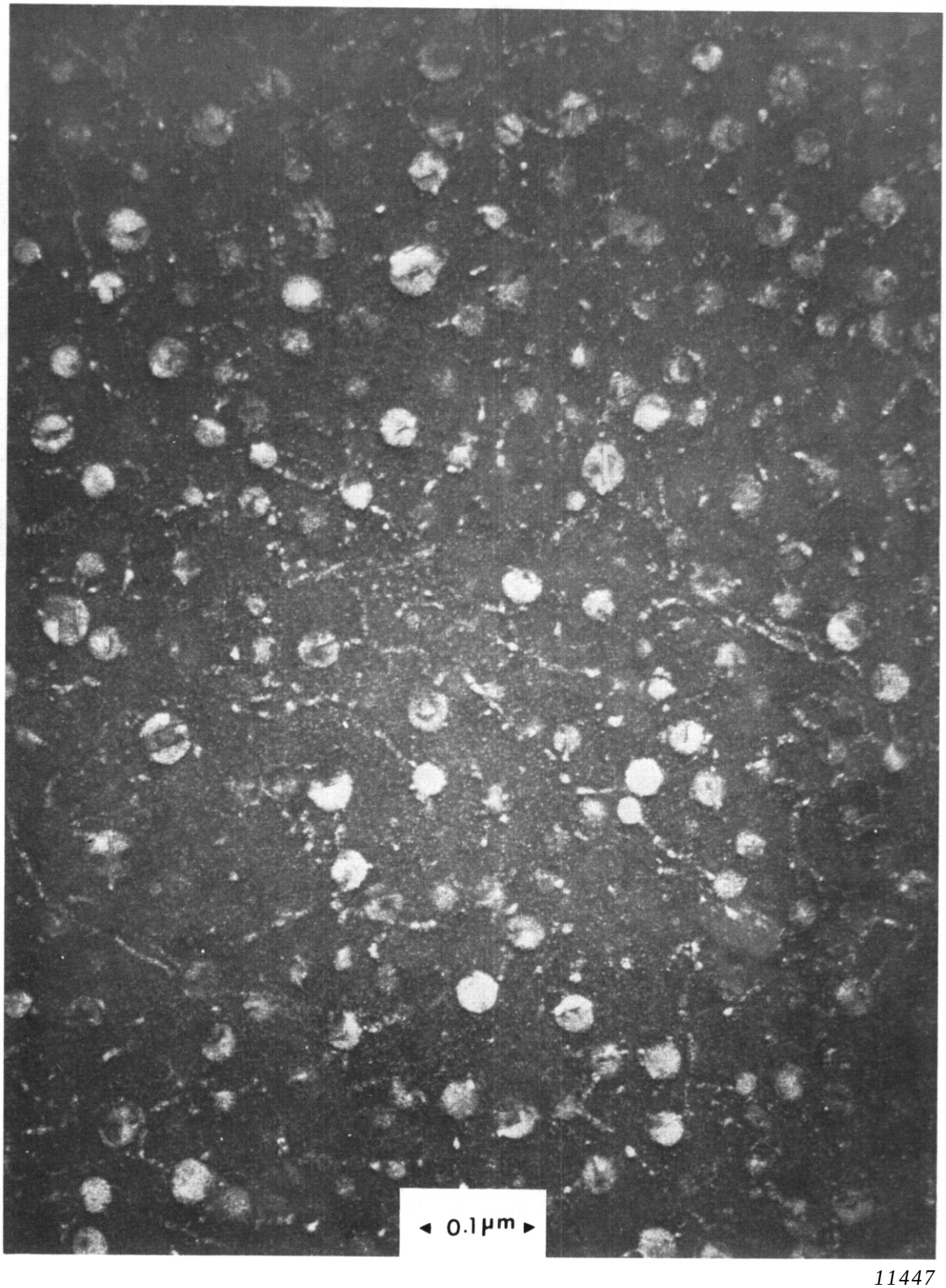

11447

Fig. 4.1.10 Double-Peaked γ' Particle Size Distribution for the Irradiated CWA Alloy B2.

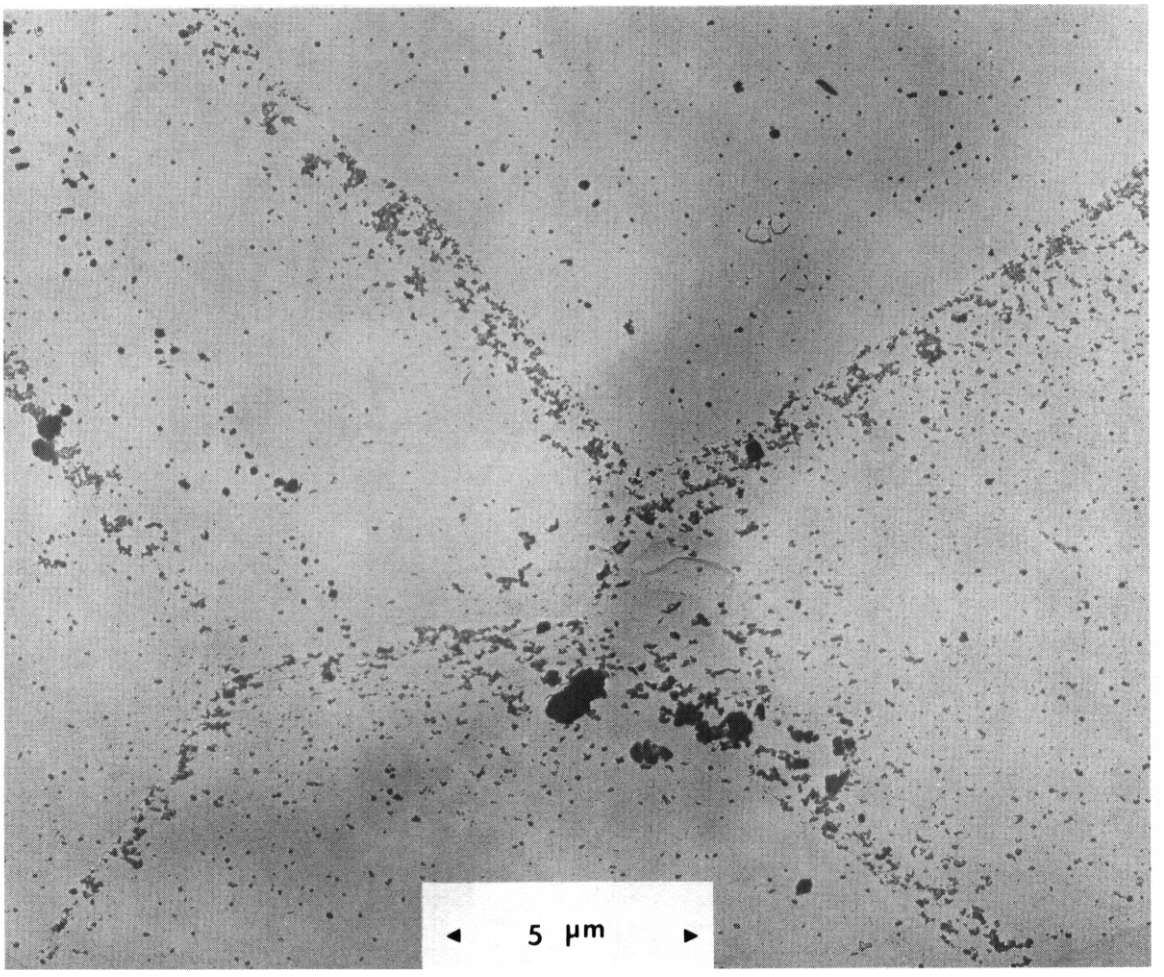

16579

Fig. 4.1.11 Grain Boundary Structure in CWA Alloy B2, Consisting of Fine $M_{23}C_6$ and MC Particles.

11463

Fig. 4.1.12 **Helium** Bubbles **in** CWA Alloy **B4 Irradiated at 500°C to** a **Fluence of 9.2 dpa.**

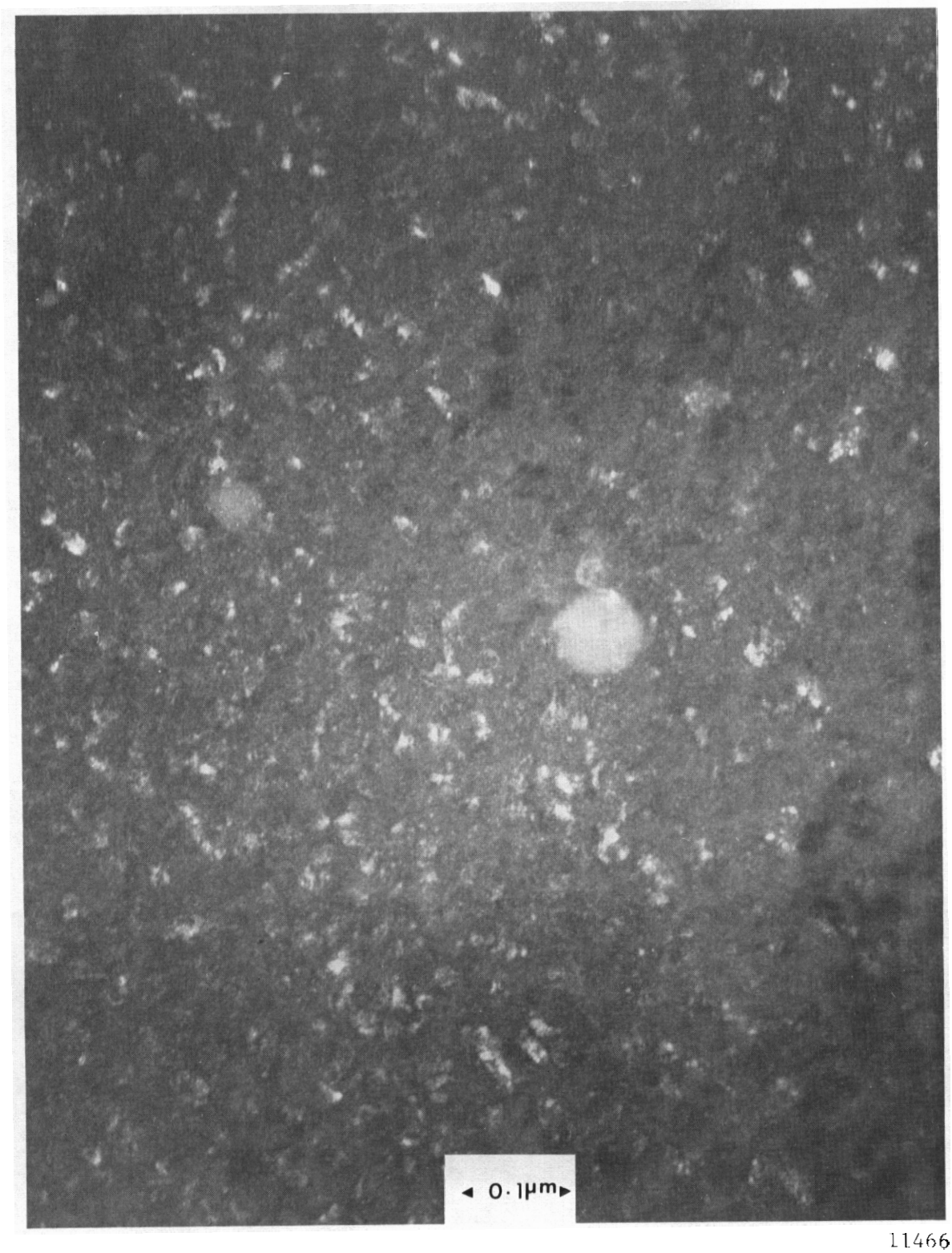

Fig. 4.1.13 Gamma Prime in CWA B4 Irradiated at 500°C to a Fluence of 9.2 dpa.

16587

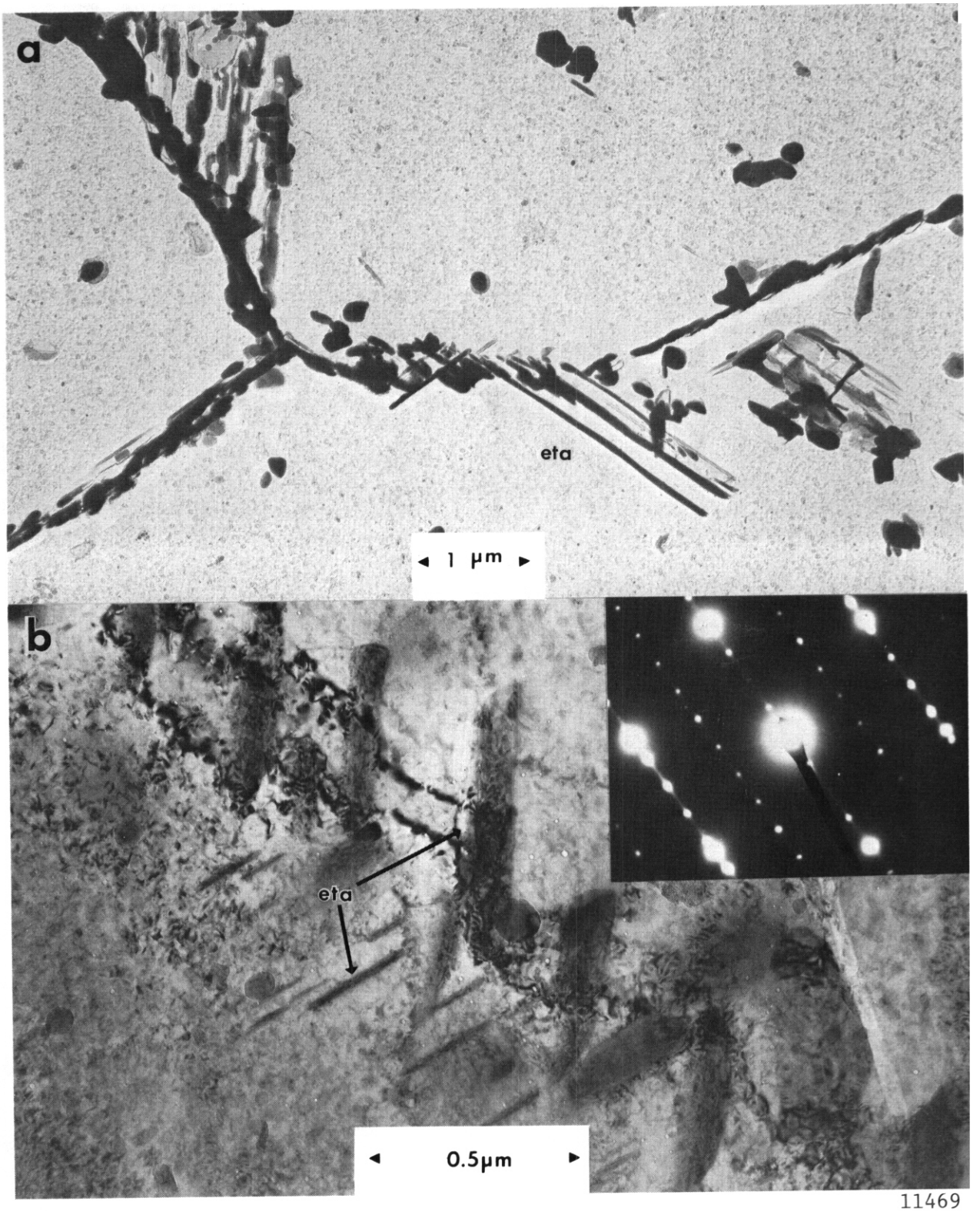

Fig. 4.1.14 Grain Boundary Structure in CWA Alloy B4, Consisting of η-phase Plates and G Phase. (a) Micrograph of the Extraction Replica, (b) Dark-Field Transmission Micrograph of the Specimen.

Fig. 4.1.15 **Helium Bubbles in CWA Alloy B6 Irradiated at** *500°C* to **a Fluence** of **9.2 dpa.**

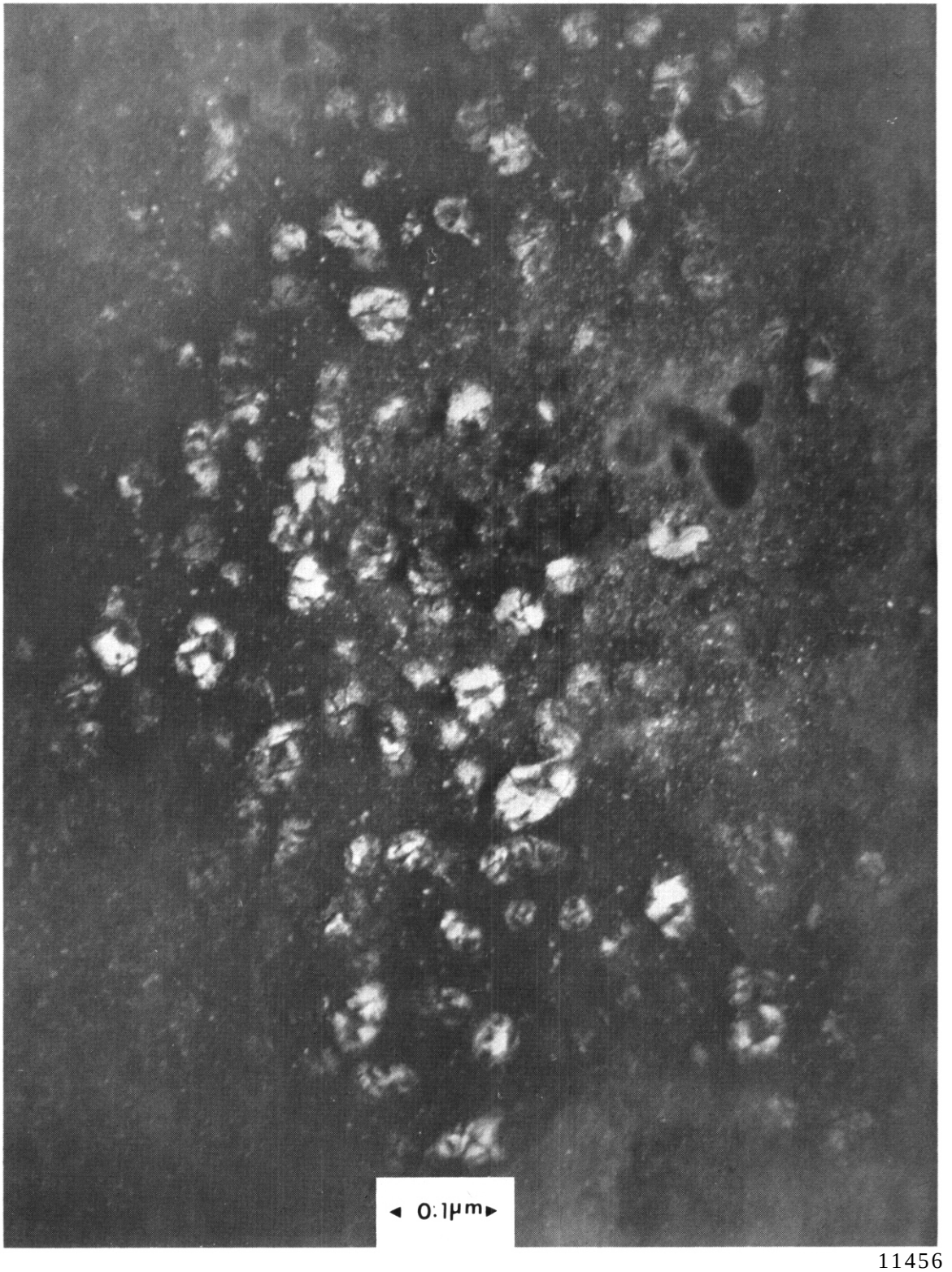

11456

Fig. 4.1.16 Double-Peaked γ' Particle Size Distribution in Irradiated CWA Alloy B6.

irradiation. Only $M_{23}C_6$ formed as discrete particles at grain boundaries during the CWA treatment (Figure 4.1.17). Alloy B6 exhibited the simplest grain boundary structure of all the Path B alloys examined.

A summary of the microstructures observed in Path B alloys is given in Table 4.1.6.

Table *4.1.6* Microstructural Results

Alloy-Code (TMT)	Matrix Features	Grain Boundary Features
B1-L4 (CW)	γ', He bubbles, dislocation tangles	He bubbles, γ' film
B1-L5 (CWA)	γ', He bubbles, voids	He bubbles, discrete G and MC particles, cellular γ'
B2-LA (CWA)	γ', He bubbles, voids	He bubbles, $M_{23}C_6$ and MC
B4-LK (CWA)	γ', η, He bubbles, voids	He bubbles, η, G and $M_{23}C_6$
B6-LP (CWA)	γ', He bubbles	He bubbles, discrete $M_{23}C_6$ particles

4.1.4.4 Discussion

Helium-induced loss of ductility has been the subject of numerous experimental and theoretical studies. The loss of ductility has been ascribed to stress-induced growth of helium-filled cavities on grain boundaries.[12,13] The high density of helium bubbles in the matrix and at the grain boundaries shows that the concentration of helium in irradiated Path B alloys is high. The implication, however, that this helium is responsible for the irradiation-induced loss of ductility is tenuous and perhaps incorrect. Although alloy B6 has the highest helium content of the Path B alloys, in the CWA condition it did not show a dramatic drop in ducility, nor did it possess zero ductility in the temperature range of the ductility trough like some of the low Ni alloys. In fact, the residual ductility in alloy B6 remained fairly constant at *0.5* to 1%. It is suspected that the CWA treatment applied to alloy B6 is not a TMT which would provide a substantial amount of ductility even

16573

16574

Fig. 4.1.17 Grain Boundary Structure in CWA Alloy B6, Consisting of Discrete $M_{23}C_6$ Particles.

in the unirradiated alloy. The residual ductility of the irradiated material may very well be equal to the uniform elongation of the alloy in the unirradiated condition. The helium bubbles at the grain boundaries are expected to affect the alloy primarily at high temperatures where grain boundary sliding plays an important role in deformation (the necking portion of the total elongation).

Several potential mechanisms have been identified to account for the low ductility observed in the Path B alloys. The matrices of the alloys were generally hardened by γ' or γ'/γ'' precipitates formed either during irradiation or during preirradiation TMTs. In addition, faulted loops and helium bubbles produced during irradiation further increased the matrix strength. In relation to the strong matrix, the grain boundaries were weakened by unfavorable precipitates. For instance, helium bubbles at gain boundaries and cavities at precipitate/grain boundary interfaces would be expected to reduce the grain boundary cohesive energy and serve as potential crack nucleation sites during deformation at high temperatures. The γ' film decorating grain boundaries would also decrease the grain boundary cohesive energy. It would also limit the deformation tolerance of the grain boundary[14] since the γ' film exhibits a brittle cleavage failure itself. The η-phase plates at grain boundaries would create planes of weakness, thereby increasing the likelihood of early grain-boundary failure. In general, the low ductility of the Path B alloys is attributed to a combination of the effects of strengthening of the matrix and weakening of the grain boundaries.

Two questions remain unanswered. First, the role of high helium contents in these alloys is uncertain since helium bubbles at the grain boundaries were not determined to be the primary mechanism of the ductility loss. Postirradiation ductility loss in γ'- and γ'/γ''-strengthened alloys has also been observed in EBR-II irradiations[14-17] for which the helium content of the alloys was less than 10 ppm. A recent study by Bennetch and Jesser[18] indicates that no direct correlation can be found between the brittlefracture of austenitic stainless steels and the major microstructural parameters used in theoretical treatments of helium embrittlement (i.e., bubble spacing, bubble diameter, bubble pressure and the areal coverage of grain boundaries by bubbles). In fact, they recommend that the current definition of "helium embrittlement" be re-evaluated.

The second question has to do with the TMT appropriate for this type of alloy. It is evident that the alloy ductility can be improved to some extent by preirradiation thermomechanical treatment, since the postirradiation ductility was dependent on the preirradiation TMT. A better understanding of this phenomenon would require a small scale program of TMT development and mechanical property testing.

4.1.4.5 Conclusions

The disk bend technique was a useful technique for characterizing the ductility of Path B alloys irradiated in HFIR to a dose of ~10 dpa. At test temperatures above 500°C, the postirradiation ductility is less than 1% for all alloy conditions tested. Microstructural studies indicate that in their current form, all the Path B alloys exhibit weakened grain boundaries. Helium bubbles form at the grain boundaries in all alloy conditions. Cavities at precipitate/grain boundary interfaces develop in irradiated **CWA** alloy B1. **A** thin layer **of** γ' film forms on the grain boundary of CW alloy B1. Eta-phase plates form in the grain boundary region in **CWA** alloy B4. The matrix on the other hand is strengthened in each of the alloys examined by the formation of γ' or γ'/γ'' precipitates, radiation-induced faulted loops and helium bubbles. The low ductility behavior of the Path B alloys results from the simultaneous existence of the strong matrix and the weak grain boundaries.

Path B alloys in their current form do not offer adequate ductility for first wall applications at high temperatures.

4.1.5 Future Work

This report completes the examination of the Path B alloys irradiated in the ADIP Program.

4.1.6 References

1. B. A. Chin, R. J. Neuhold and J. L. Straalsund, *Nucl. Tech.*, 57 (1982), p. 426.
2. D. T. Peterson and R. W. Powell, *DAFS Quarterly*, DOE/CR-0046/2 (1980), p. 113.

3. F. H. Huang, M. L. Hamilton and G. L. Wire, *Nucl. Tech.*, 57 (1982) p. 234.
4. B. F. Dyson and D. F. Henn, *J. of Micros.*, 97 (1973), p. 165.
5. B. F. Dyson and M. J. Rogers, *Metal Sci. J.*, (1974), p. 261.
6. B. F. Dyson, M. S. Loveday and M. L. Rodgers, *Proc. Roy. Soc. London* (A) 349, (1976), p. 245.
7. T. Saegura, M. Uemura and J. R. Weertman, *Met. Trans.*, 11A, (1980), p. 1453.
8. M. Kikachi and J. R. Weertman, *Script. Met.*, 14, (1980), p. 797.
9. K. Shiozawa and J. R. Weertman, *Script. Met.*, 15, (1981), p. 1241.
10. M. Kikuchi, K. Shiozawa and J. R. Weertman, *Act. Met.*, 29, (1981), p. 1747.
11. L. E. Thomas, *Proceedings on Phase Stability During Irradiation*, AIME Symposium, J. R. Holland, L. K. Mansur and D. I. Potter, Eds., Pittsburgh, PA, October 5-9 (1980), p. 237.
12. D. R. Harries, *J. Nucl. Mat.*, 82 (1979), p. 2.
13. J. S. Waddington, *Metal Sci. J.*, 1 (1967), p. 156.
14. W. J. S. Yang, *J. Nucl. Mat.*, 108 and 109, (1982), p. 339.
15. R. Bajaj, R. P. Shogan, C. DeFlitch, R. L. Fish, M. M. Paxton and M. L. Bleiberg, *Proceedings, 10th International Symposium on Effects of Radiation on Metals*, Savannah, GA, June 3-5 (1980), p. 326.
16. A. F. Rowcliffe and J. A. Horak, *Trans. ANS*, 38 (1981), p. 266.
17. S. Vaidyanathan, W. C. Bell and T. Lauritzen, Proceedings, *11th International Symposium on the Effects of Radiation on Metals*, Scottsdale, AZ, June 28-30, (1982), p. 619.
18. J. I. Bennetch and W. A. Jesser, *J. Nucl. Mat.*, 103 and 104 (1982), p. 809.

5. PATH C ALLOY DEVELOPMENT — REACTIVE AND REFRACTORY ALLOYS

5.1 MECHANICAL PROPERTY EVALUATIONS OF PATH C VANADIUM SCOPING ALLOYS

- R. E. Gold and R. Bajaj (Westinghouse Electric Corporation)

5.1.1 ADIP Tasks

I.B.ll. Stress-Rupture Properties of Reactive/Refractory Metal Alloys (Path C)

I.B.15 Tensile Properties of Reactive/Refractory Metal Alloys (Path C)

5.1.2 Objective

The objective of this program was to develop creep/stress rupture data for the unirradiated Path C Vanadium Scoping Alloys doped with controlled amounts of nonmetallic impurity, namely oxygen.

5.1.3 Summary

Creep/stress-rupture tests were performed on sheet specimens of the three Path C vanadium Scoping Alloys in the temperature range 650 to 800°C. These specimens had been intentionally contaminated with nominal additions of 600 and 1200 wppm oxygen by controlled gas-metal reactions. The effects of oxygen additions on the creep behavior of the vanadium alloys, over the limited range of stress-temperature conditions examined, did not appear to be significant. Creep strengths and ductilities appeared to be affected very little compared to tests at similar conditions on noncontaminated specimens of the vanadium alloys. These results are different in that regard from similar comparisons of tensile properties of contaminated and noncontaminated vanadium alloy specimens where a partial change in the fracture behavior was observed for the oxygen-contaminated specimens.

This difference may reflect the fact that the creep specimens were tested for longer times at higher temperatures, perhaps facilitating more uniform distribution of the oxygen within the sheet specimens.

5.1.4 Progress and Status

The Path C Vanadium-Base Scoping Alloys, which were prepared for the ETM Research Materials Inventory, sited at the Oak Ridge National Laboratory, are the subject of this evaluation. These include: (compositions in weight percent)

V-20Ti
V-15Cr-5Ti
VANSTAR-7 (V-9Cr-3.3Fe-1.2Zr-0.054C)

Efforts during the preceding fiscal year (FY 81) focused on establishing the tensile and stress-rupture behavior for the unirradiated alloys. In addition, because nonmetallic impurities are known to have significant effects on the mechanical behavior of refractory metal alloys, a procedure was developed for introducing controlled levels of oxygen into mechanical property specimens. The results of these efforts were reported previously.[1-2] Evaluations for the current fiscal year are focused on determination of the tensile and stress rupture properties of intentionally contaminated specimens.

Tasks associated with the FY'82 efforts are:

Task 1. Material Procurement
Task 2. Initial Specimen Preparation and Heat Treatments
Task 3. Contamination Exposures for Mechanical Test Specimens
Task 4. Tensile Evaluations
Task 5. Creep/Stress-Rupture Testing
Task 6. Chemical and Microstructural Characterizations

Tasks 1 through 4 have been completed and reported previously. Task 6, fractography of tensile specimens, has also been reported. Task 5, for the stress-rupture specimens, and Task 6, chemical characterization and fractography of the creep specimens, are the subjects of the present report.

5.1.4.1 Material Identification and Condition

The chemical analysis of the three Path C Vanadium Scoping Alloys and the heat treatments, contamination exposures, and specimen designations have been reported previously. Some of the specimens containing nominal levels of 600 and 1200 wppm oxygen were analyzed by neutron activation analysis at the Oak Ridge National Laboratory. The results of these analyses are listed in Table 5.1.1. For reasons which are not clear at the present time, the measured (analyzed) oxygen pickup values were consistently lower than those deduced by in-situ weight gain measurements.

5.1.4.2 Creep/Stress-Rupture Evaluations

Creep/stress-rupture tests on sheet specimens of the three alloys, each containing two levels of oxygen, were conducted in high vacuum ($<10^{-8}$ torr) with a dead-weight load system. The temperature and stress levels for the experiments were chosen, based on the creep/stress rupture data of noncontaminated alloys, to cause fracture in 1000-2000 hours. The results of these tests are presented below for each of the three alloys.

V-20Ti. The results of creep/stress-rupture tests on V-20Ti specimens are presented in Table 5.1.2 along with those of noncontaminated specimens (from Reference 2). At 650°C, the rupture time increased with increasing oxygen content with a suggestion of a saturation tendency with oxygen. No conclusions

TABLE 5.1.1 Oxygen Analysis (in weight ppm) of Representative Specimens

Alloy	Specimen Designation	Nominal Additional Oxygen Content	Measured Additional Oxygen Content*
V-20Ti	VT–82–1A	600	486
	VT–82–4A	1200	1098
V-15Cr-5Ti	VCT–82–2A	1200	890
	VCT–82–3A	600	591
	VCT-82-3B	600	222
VANSTAR–7	VS–82–1A	600	390
	VS–82–1B	600	332
	VS–82–4A	1200	993

*Due to counting statistics the calculated result is considered to have a precision of ±10%.

TABLE 5 1 ≥ Creep/Stress-Rupture Test Data for V-20Ti

Specimen Ident. No.	Nominal[(a)] O_2 Content (wppm)	Test Temp. (°C)	Stress (MPa)	Stress (ksi)	Time (hrs)	Cumul. Strain (%)	Comment
15	0	650	148	21.5	1158	(0.02)	No Rupture
15 (C t'ø)	0	650	218	31.5	2968	50.7	
16	0	650	276	40	800	34.5	
∃≥-1∃	600	650	276	40	1007 7	24.9[+]	
∃≥-≥B	1200	650	276	40	1158. 4	28.5	
∃≥-3∃	600	700	207	30	14		Controller Malfunction
82-4B	1≥00	700	≥07	30	73≥ 3	43.7	

(a) Additional oxygen content; i.e. above the initial concentration of 450 wppm.

[+] Last strain measurement; fracture strain not presently available

can be drawn for the 700°C tests because of a lack of data. The creep strain versus time curves are shown in Figure 5.1.1.

V-15Cr-5Ti. Table 5.1.3 presents the results of creepfstress-rupture tests of V-15Cr-5Ti specimens. The results of tests on noncontaminated specimens (from Reference 2) are also included for the purposes of comparison. The strain versus time curves for these specimens are shown in Figure 5.1.2. At 750°C, the 600 wppm additional oxygen caused an increase in rupture time and a decrease in strain, compared to noncontaminated specimens. However, increasing the oxygen to 1200 wppm did not further increase the rupture time. At 800°C, the specimen containing 600 wppm of additional oxygen showed no increase in rupture time compared to the noncontaminated material (in fact a slight decrease was observed in rupture time). A further increase to 1200 wppm additional oxygen resulted in a significant improvement in rupture life (by a factor of 2.5) compared to the noncontaminated material.

VANSTAR-7. The results of the creepfstress-rupture tests are presented in Table 5.1.4 and the creep strain-time plots are shown in Figure 5.1.3. At 750°C, oxygen appears to be deleterious to stress-rupture life. No definite conclusion can be drawn, at this time, regarding the role of oxygen at 700°C since one test is still continuing.

5.1.4.3 Fractography of Contaminated Creep Specimens

Reference to Tables 5.1.2 through 5.1.4 and Figures 5.1.1 through 5.1.3 indicates that, despite the presence of up to 1200 wppm oxygen, the strain values at rupture were consistently high for all specimens, ranging from a low value of 13.1% to over 43%. Three specimens each of V-20Ti and V-15Cr-5Ti and two VANSTAR-7 specimens were examined by scanning electron microscopy in order to characterize the fracture

TABLE 5.1.3 Creep/Stress-Rupture Test Data for V-15Cr-5Ti

Specimen Ident. No	Nominal[(a)] O_2 Content (wppm)	Test Temp. (°C)	Stress (MPa)	Stress (ksi)	Time (hrs)	Cumul. Strain (%)	Comment
1B	0	650	414	60	1055	(0.5)	No Rupture
BZ-5B	600	700	414	60	17.7		
17	0	750	368	53.5	115	13.8	
1B	0	750	345	50	327	22.4	
B2-1B	600	750	345	50	791.9	17.4	
B2-2B	1200	750	345	50	780.0	14.6	
16	0	800	276	40	629.0	22.5	
8Z-3B	600	800	276	40	547.8	13.1	
8Z-4B	1200	800	276	40	1543.3	15.2	

(a) Additional oxygen i.e. the of 230 wppm.

TABLE 5 1 C Cre≡ϖ/Stre55-Ruϖture Test D≡t≡ fϴr VANSTA∩–¬

Sp≡cimen Id–nt. No	Nominal O_2 Content (wppm) [a]	Test Temp. (°C)	Str≡55 (MPa)	Time (hrs)	Cumul. Strain (%)	Comment
15	0	650	z76	1261	(0 11)	Nϴ Ruϖture
15 (Cϴϴt'ϖ)	0	6≡0	≡≡1	1671	(0 52)	Nϴ Ruϖture
17	0	700	z76	1z00	(0 1z)	No Ruϖture
17 (Cϴϴt'ϖ)	0	¬≡0	z76	1¬3≡	1C ≡	
≡z-≡B	600	700	z76	≡57≡ ≡	z ≡6+	In Proϴ≷re5 5
≡Z-4ϖ	1Z00	¬00	z76	z≡zz 5	0 1≡	In Pro≷ress
16	0	7≡0	z07	21≡z 0	(1 0z)	Nϴ Ruϖture
16 (C t'd)	0	750	Z41	2Cz≡	19 ≡	
≡Z-1B	600	750	276	1≡≡ 6	1¬ 4	
≡z-zB	1z00	750	z76	10 z	16 7	Controlle< Malfunction
≡z-6B	1z00	750	z76	4≡≡ 8	z 57+	Repe≡t of Previous Te5t

[a] Adϖitiϴnal ϴxy≷en conteϴt, i.e aϴove the iϴitial concentr≡tion ϴf 280 wppm.

+ Las.t strain measurement; fr≡cture 5traiϴ ϴϴt ϖre5eϴtly av≡il≡ϴle

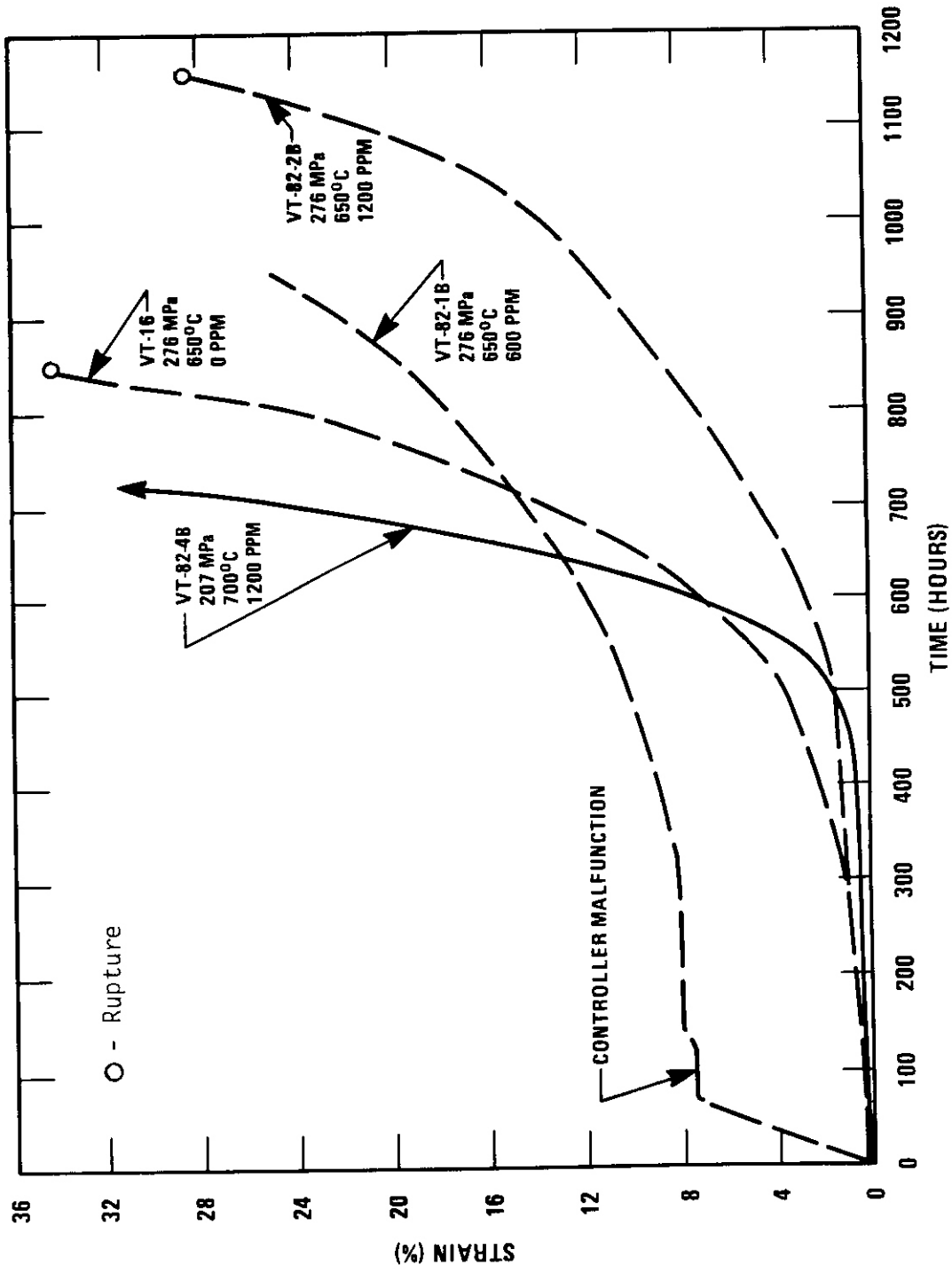

Figure 5.1.1 ωf on the ωf V at 650°C and

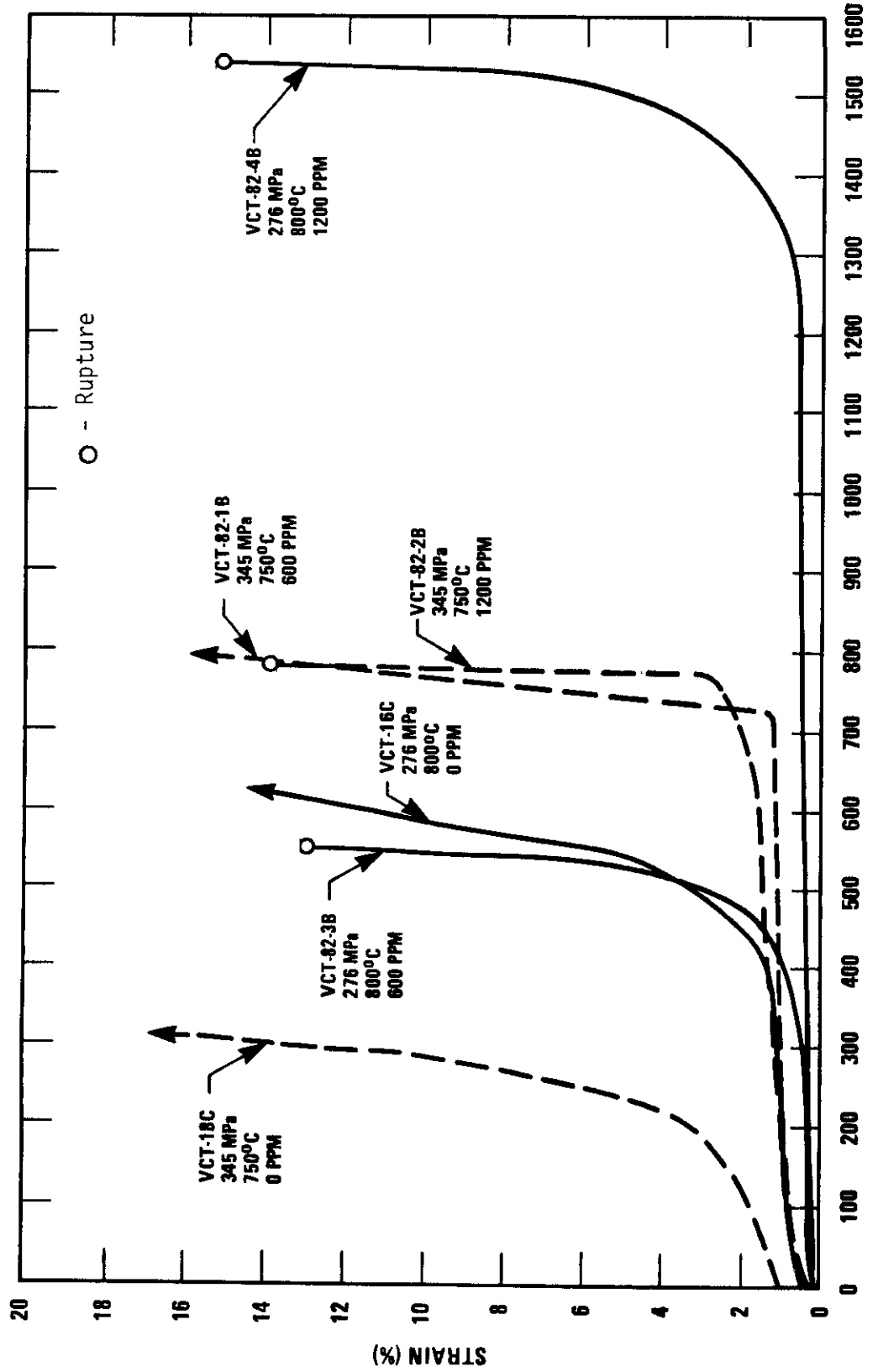

5 1 2 of Oxygen on of V-15Cr-5Ti at 800 C

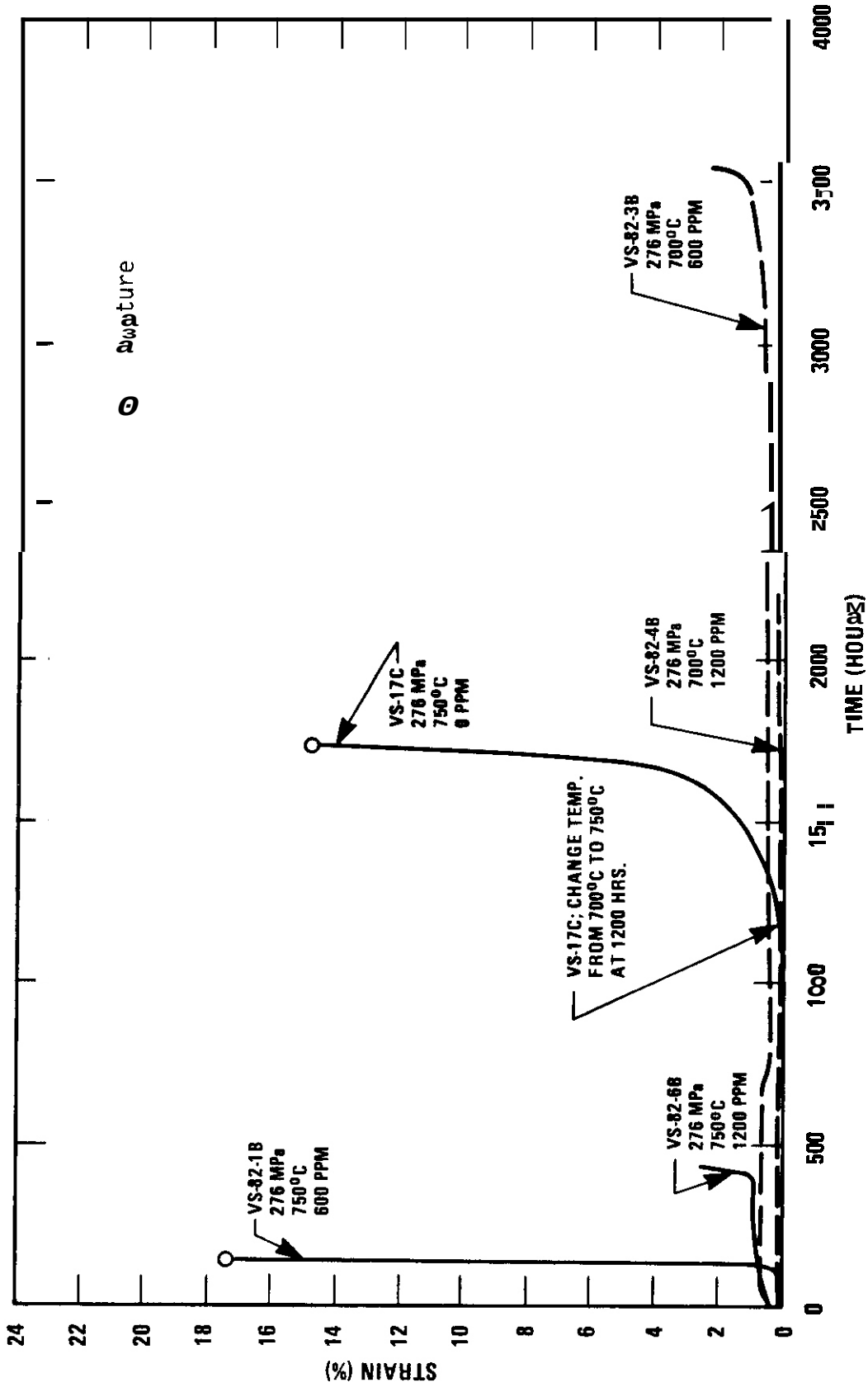

Figure 5 1 3 Effect of Oxygen on the Creep Properties of VANSTAR-7 at 700°C and 750°C

surfaces. Representative micrographs are presented in Figures 5.1.4 through 5.1.9. With the single exception of a small area of one of the V-15Cr-5Ti specimens where mixed intergranular and cleavage fracture was observed, Figure 5.1.6, all fracture surfaces displayed only ductile, dimpled rupture.

These results are different from those observed and reported previously ,for identical specimens which had been tensile tested at room temperature, 500, and 700°C (Reference 2). For the tensile specimens, cleavage and intergranular separation were found to be dominant fracture modes in the near-surface regions where the oxygen concentrations were likely to be the highest. The central regions of the tensile specimens were still quite 'tough' and final specimen fracture had occurred by ductile shear at high values of total elongation.

5.1.5 Discussion of Results

From the limited data base developed in this program, a general conclusion regarding the role of oxygen in creep/stress rupture cannot be made for all the vanadium base alloys. It is clear that the effects of oxygen vary from alloy to alloy and from one temperature to another. For example, in V-15Cr-5Ti, a saturation tendency is observed at oxygen concentrations above 600 wppm (additional) at 750°C and no such tendency is evident at 800°C. Also, at 800°C, an addition of 600 wppm did not contribute to improved rupture life but 1200 wppm improved the rupture life significantly without a negative effect on the creep ductility. It is also possible that the response of creep/stress rupture to oxygen content is stress dependent. This issue cannot be resolved at present from the existing data. As can be seen from a comparison of Tables 5.1.2 and 5.1.3, the effects of oxygen are different for different alloys (V-20Ti vs V-15Cr-5Ti).

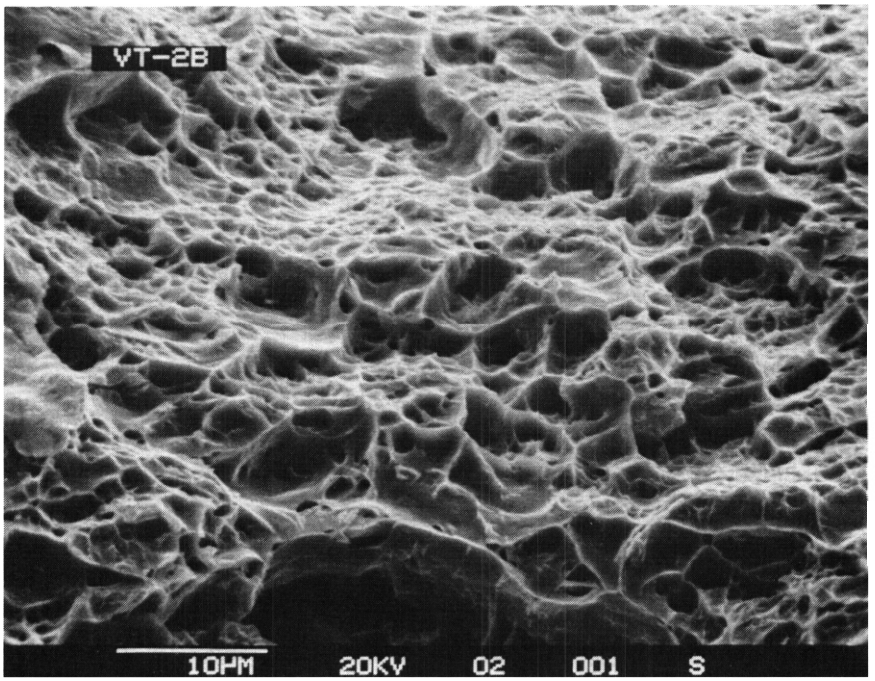

Figure *5.1.4.* Scanning Electron Micrograph of V-20Ti Creep Tested at 650°C, 276 MPa.

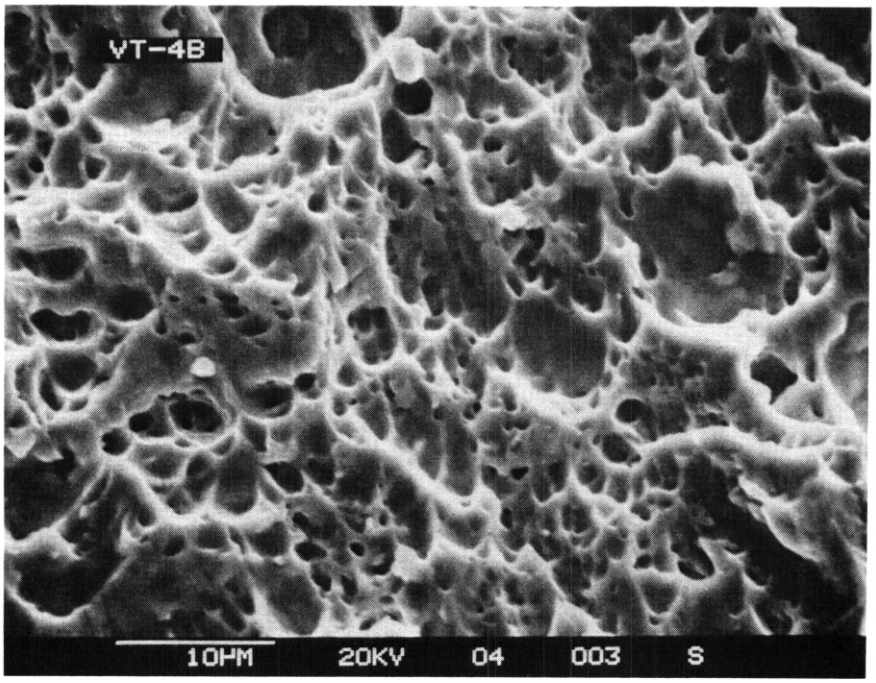

Figure 5.1.5 Scanning Electron Micrograph of V-20Ti Creep Tested at 700°C, 207 MPa.

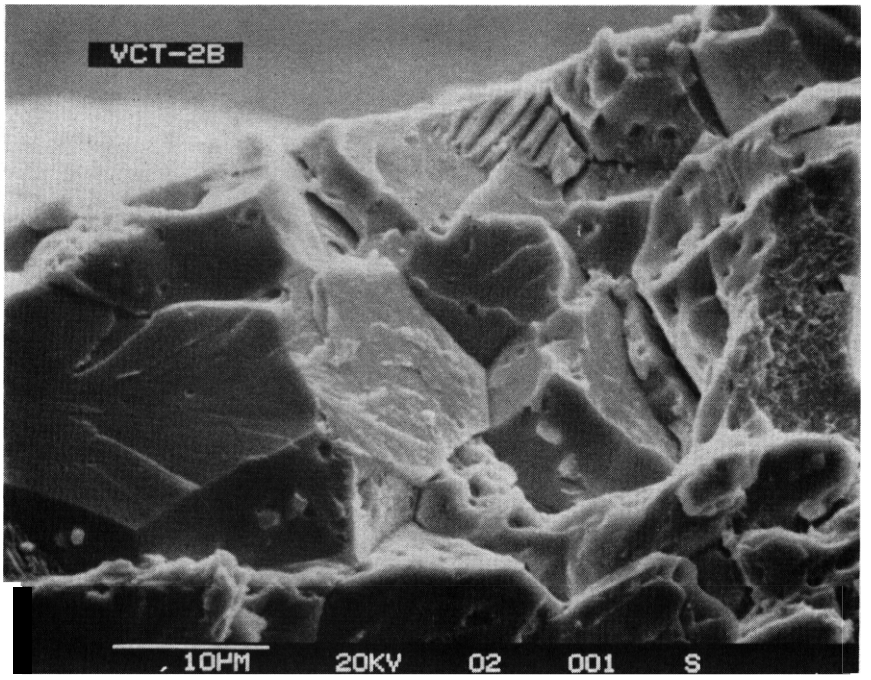

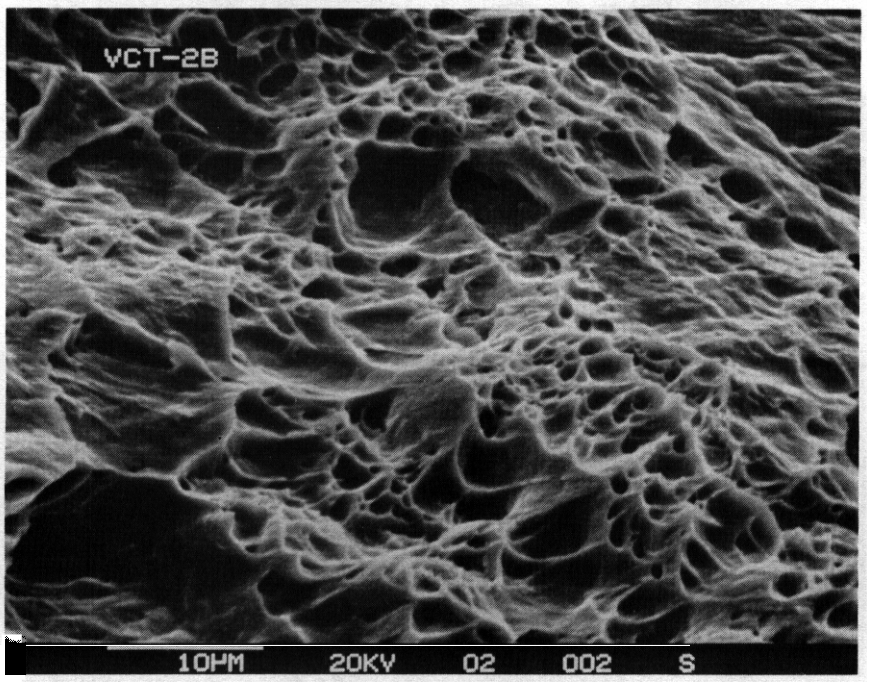

Figure 5.1.6 Scanning Electron Micrographs of V-15Cr-5Ti Creep Tested at 750°C, 345 MPa.

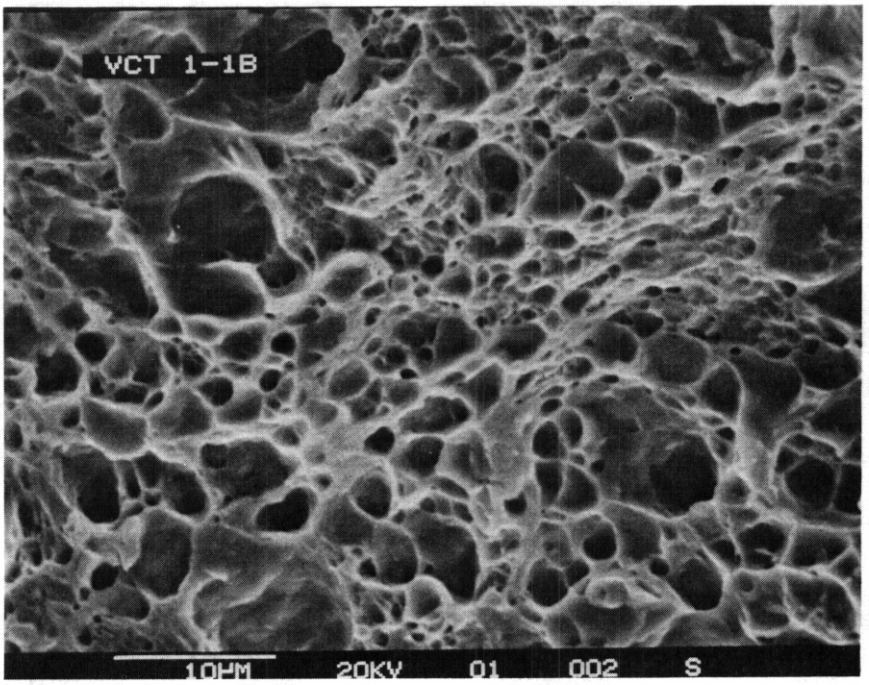

Figure 5.1.7. **Scanning Electron Micrograph of V-15Cr-5Ti Creep Tested at 750°C, 345 MPa.**

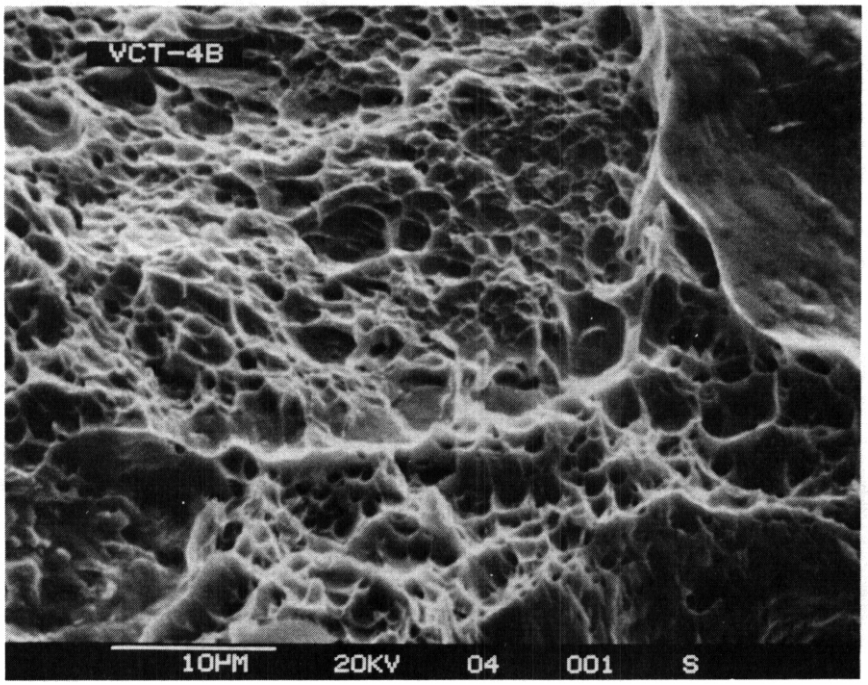

Figure 5.1.8 **Scanning Electron Micrograph of V-15Cr-5Ti Creep Tested at 800°C, 276 MPa.**

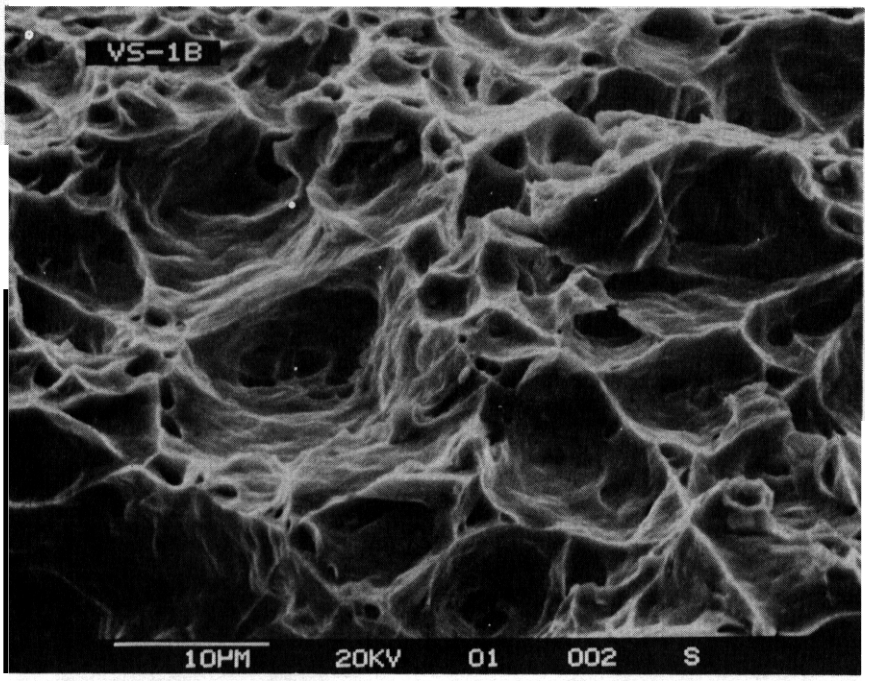

Figure 5.1.9 Scanning Electron Micrograph of VANSTAR-7 Creep Tested at 750°C, 276 MPa.

Differences in the fracture mode observed here for the contaminated creep specimens compared to previously reported, identically contaminated, tensile specimens suggest that the longer times at elevated temperature required for the creep tests may be facilitating more uniform distribution of the added oxygen. The tensile specimens, particularly those tested at room temperature and 500°C, displayed cleavage fracture in the near-surface regions although final bulk fracture was by ductile rupture. For the creep specimens. with test temperatures in the range 650 to 800°C, virtually all fracture surface features were those of ductile shear.

An evaluation of the relative performance of various alloys can be made by comparison on the basis of a Larson-Miller parametric analysis. This method was chosen over the log (stress)-log (strain) correlation for two reasons. First, the data base is limited and data is available for only one stress level at each temperature. Second, a Larson-Miller analysis combines the effect of temperature and time and can therefore be used more readily for rough comparisons. It should be pointed out that it was not the purpose of this program to develop stress-rupture correlations for vanadium base alloys since the program is still at a scoping level.

Figure 5.1.10 shows a Larson-Miller plot versus stress for the three alloys. A curve for 316SS, developed from a correlation reported in Reference 3, is also included for the purpose of comparison. In the calculations of the Larson-Miller parameter the constant, C, was taken as 20 for all the alloys. This value of C gives a reasonable correlation for vanadium and its alloys. The 700°C tensile data for the three vanadium alloys are also plotted on Figure 5.1.10; these data were taken from Reference 4. The time-to-rupture was derived from the total elongation and strain rate data, and the computed Larson-Miller parameter was plotted against the flow stress ($\sigma_f = \sigma_{ys} + 1/2\ \sigma_{uts}$). In Figure 5.1.10 the curves are best

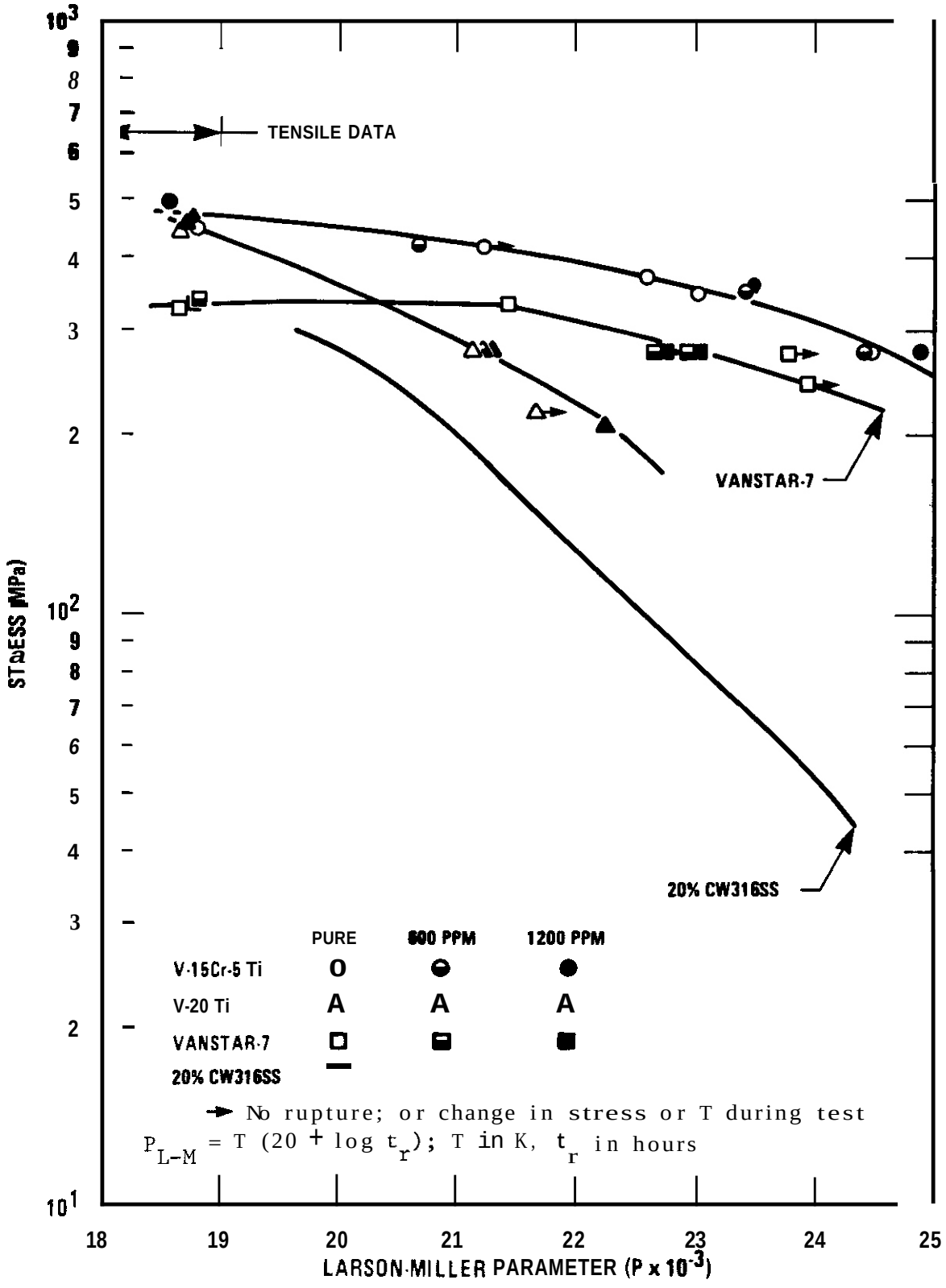

Figure 5.1.10 A Larson–Miller Plot of Tensile and Creep Data for the Vanadium Scoping Alloys and 20% CW 316SS.

Differences in the fracture mode observed here for the contaminated creep specimens compared to previously reported, identically contaminated, tensile specimens suggest that the longer times at elevated temperature required for the creep tests may be facilitating more uniform distribution of the added oxygen. The tensile specimens, particularly those tested at room temperature and 500°C, displayed cleavage fracture in the near-surface regions although final bulk fracture was by ductile rupture. For the creep specimens, with test temperatures in the range 650 to 800°C, virtually all fracture surface features were those of ductile shear.

An evaluation of the relative performance of various alloys can be made by comparison on the basis of a Larson-Miller parametric analysis. This method was chosen over the log (stress)-log (strain) correlation for two reasons. First, the data base is limited and data is available for only one stress level at each temperature. Second, a Larson-Miller analysis combines the effect of temperature and time and can therefore be used more readily for rough comparisons. It should be pointed out that it was not the purpose of this program to develop stress-rupture correlations for vanadium base alloys since the program is still at a scoping level.

Figure 5.1.10 shows a Larson-Miller plot versus stress for the three alloys. A curve for 31655, developed from a correlation reported in Reference 3, is also included for the purpose of comparison. In the calculations of the Larson-Miller parameter the constant, C, was taken as 20 for all the alloys. This value of C gives a reasonable correlation for vanadium and its alloys. The 700°C tensile data for the three vanadium alloys are also plotted on Figure 5.1.10; these data were taken from Reference 4. The time-to-rupture was derived from the total elongation and strain rate data, and the computed Larson-Miller parameter was plotted against the flow stress [$\sigma_f = 1/2\ (\sigma_{ys} + \sigma_{uts})$]. In Figure 5.1.10 the curves are best

'eyeball' estimates and disregard the oxygen content. The contribution of oxygen can be deduced by a careful examination of the figure.

It is clear from this comparison that: (1) the V-15Cr-5Ti alloy is superior to V-20Ti and VANSTAR-7 in stress rupture properties; (2) vanadium base alloys are far superior to Type 316 stainless steel [For example, at 300 MPa, the V-15Cr-5Ti is clearly superior to Type 316 SS]; (3) oxygen content of up to 1200 wppm may not be significant to stress rupture behavior of vanadium base alloys. In some cases, such as V-15Cr-5Ti, modest oxygen increases may lead to an increase in the stress-rupture properties. The last conclusion is tentative at present and subject to further study.

5.1.6 References

1. R. E. Gold, "Mechanical Property Evaluations of Path C Vanadium Scoping Alloys," Alloy Development for Irradiation Performance, Progress Report for Period Ending Sept. 30, 1981, DOE/ER-0045/7, p. 122 (March 1982).

2. R. E. Gold, "Mechanical Property Evaluations of Path C Vanadium Scoping Alloys," Alloy Development for Irradiation Performance, Progress Report for Period Ending March 31, 1982, DOE/ER-0045/8, p. 281 (September 1982).

3. G. D. Johnson, J. L. Straalsund, and G. L. Wire, "A New Approach to Stress-Rupture Data Correlations," Mat. Sci. Eng., 28 (1977) 69.

4. R. E. Gold and R. L. Ammon, "Mechanical Property Evaluations of Path C Vanadium Scoping Alloys," Alloy Development for Irradiation Performance, Progress Report for Period Ending March 31, 1981, DOE/ER-0045/6, p. 96 (July 1981).

Acknowledgments

The authors would like to acknowledge the support of J. E. Strain of the Oak Ridge National Laboratory for the neutron activation analyses of oxygen concentrations in the contaminated specimens. The cooperation and general support of E. E. Bloom, F. W. Wiffen, and P. F. Tortorelli of the Metals and Ceramics Division of the Oak Ridge National Laboratory are also gratefully acknowledged.

6. INNOVATIVE MATERIAL CONCEPTS

6.1 MICROSTRUCTURE OF WELDS IN AN IRON-BASE LONG-RANGE-ORDERED ALLOY — D. N. Braski and S. A. David (Oak Ridge National Laboratory)

6.1.1 ADIP Tasks

ADIP Task I.A.5, Perform Fabrication Analyses.

6.1.2 Objective

The objective of this research is to determine the weldability of iron-base long-range-ordered (LRO) alloys by common welding techniques. The overall goal is to determine the potential use of these alloys as structural materials for fusion energy systems.

6.1.3 Summary

The microstructure of gas tungsten arc (GTA) welds of a $(Ni,Fe)_3(V,Ti)$ LRO alloy has been investigated. Crack-free welds were produced in which the heat-affected zone (HAZ) and fusion zone were disordered and softened. A postweld heat treatment increased the hardness of both zones by reordering the structure and produced additional hardening in the fusion zone due to precipitation of small VC particles on grain boundaries and matrix dislocations.

6.1.4 Progress and Status

6.1.4.1 Introduction

Long-range-ordered alloys are a unique class of materials with an atomic arrangement distinctly different from conventional or "disordered" alloys. Different alloying atoms in LRO alloys arrange themselves periodically and form an ordered crystal structure. These alloys are candidates for use in future fusion reactors.[1]

A series of LRO alloys with the general composition $(Ni,Fe)_3(V,Ti)$ are being developed for elevated-temperature application. These alloys generally exhibit high strength, excellent ductility, low creep rates, and good fatigue properties at temperatures below their critical ordering temperature, T_c (~670°C). They also exhibit relatively low swelling under neutron or heavy-ion irradiation.[2]

An important area in the development of any alloy is the ease with which it may be joined or welded. This report describes some of the first attempts to weld $(Ni,Fe)_3(V,Ti)$ and gives details of the weld microstructure. The specific alloy used in the investigation was designated LRO-37-5 and is designed to be scaled up to commercial production processes.

6.1.4.2 Experimental

A 0.4-kg ingot of LRO-37-5 having a composition of *40* Ni, 37.6 Fe, 22 V, and *0.4* Ti (wt %) was arc cast under argon. The alloy was melted from ferrovanadium feedstock. The ingot was clad in molybdenum sheet, hot rolled at 1100°C to a thickness of 2.5 mm, and cold rolled to a final thickness of 0.76 mm. The sheet was annealed at 1100°C and quenched into water to produce a disordered structure. The sheet was subsequently aged at 630°C for 1 d, 600°C for 1 d, and 500°C for 2 d to produce the LRO structure.

Autogenous GTA welds were made on the sheet inside a dry box in a 75% He—25% Ar atmosphere. The welds were made by using a stationary arc over a traveling carriage with variable speed control. The welding parameters used were: arc voltage = 12–14 V; current = 40 A, and speed = 0.42 mm/s.

Sections of the welds were prepared for metallographic examination by standard techniques using an etchant consisting of 40% HNO_3, 40% H_2O, and 20% HF (by volume). Microhardness traverses were made across the welds with a Kentron microhardness tester with a 1-kg load. Disks were machined from the weld fusion zone, HAZ, and base metal by electrical discharge machining (EDM). The 3-mm-diam disks were ground on 400-grit emery paper to a thickness of 0.3 mm and electropolished in a solution of 87.5% methanol and 12.5% H_2SO_4 (by volume) at –10°C. The voltage was approximately 15 V dc and the current approximately 100 mA. The polished disks were examined in a transmission electron microscope (TEM) at 120 kV.

6.1.4.3 Results

6.1.4.3.1 Optical Metallography. The GTA welds in the LRO–37–5 sheet showed no signs of hot cracking. Figure 6.1.1 shows the macrostructure of the weldment, which consists of three distinct regions: (1) the fusion zone, (2) the HAZ, and (3) the base metal. The fusion zone is composed of columnar grains with a dendritic or cellular dendritic substructure within the grains. The HAZ and base metal consist of twinned grains with a dispersion of VC particles. The boundary between the HAZ and base metal had the appearance of a diffuse line, revealed by the etching process. Along this boundary region, second–phase carbides were etched more severely than in either the base metal or HAZ. Within the diffuse boundary zone an extremely sharp boundary separates the ordered base metal from the HAZ, which was disordered by the welding process. That is, the HAZ was heated above the critical ordering temperature of about 670°C for this alloy. The order–disorder boundary was examined by TEM and will be discussed later. A microhardness traverse across the weld is shown directly below the micrograph in Pig. 6.1.1. The microhardness of the base metal averaged 222 DPH, 198 DPH in the HAZ, and 204 DPH in the fusion zone. The weldment was given a reordering heat treatment identical to that used in ordering the original base metal. After reordering, a hardness traverse (Fig. 6.1.1) showed that the hardness increased to approximately 235 DPH in the HAZ and to 264 DPH in the fusion zone. These changes in the hardness of the HAZ and fusion zone will be discussed in a subsequent section.

6.1.4.3.2 Microstructure of As–Welded Base Metal. The microstructure of the LRO–37–5 base metal (before welding) is illustrated in Figs. 6.1.2, 6.1.3, and 6.1.4. The alloy consists of an ordered matrix and small quantities of three different precipitate phases, which were analyzed by analytical TEM. Titanium nitride was dispersed throughout the matrix as faceted particles that ranged in size from 0.1 to 0.3 μm (Fig. 6.1.2). The TiN particles usually punched out dislocations, which were invariably decorated with 100– to 200–nm–diam VC particles. Figure 6.1.2 shows that

ORNL-PHOTO 4442-82

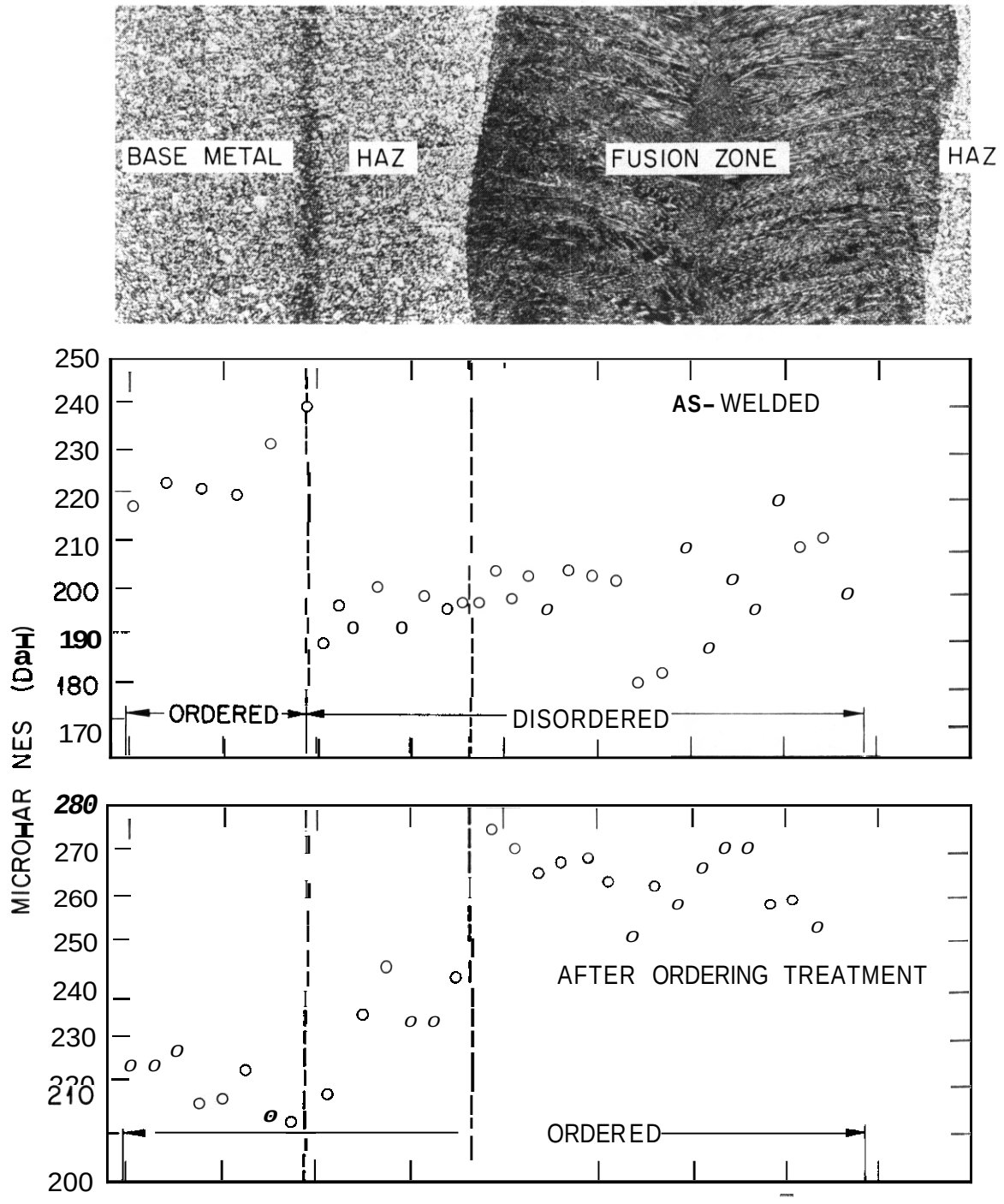

Fig. 6.1.1. **Gas Tungsten Arc Weld of LRO-37-5 Showing Base Metal, Heat-Affected Zone (HAZ), and Fusion Zone. Note boundary between base metal (ordered) and HAZ (disordered). Microhardness traces across the weld before and after a postweld heat treatment to reorder the HAZ and fusion zone.**

H-62164

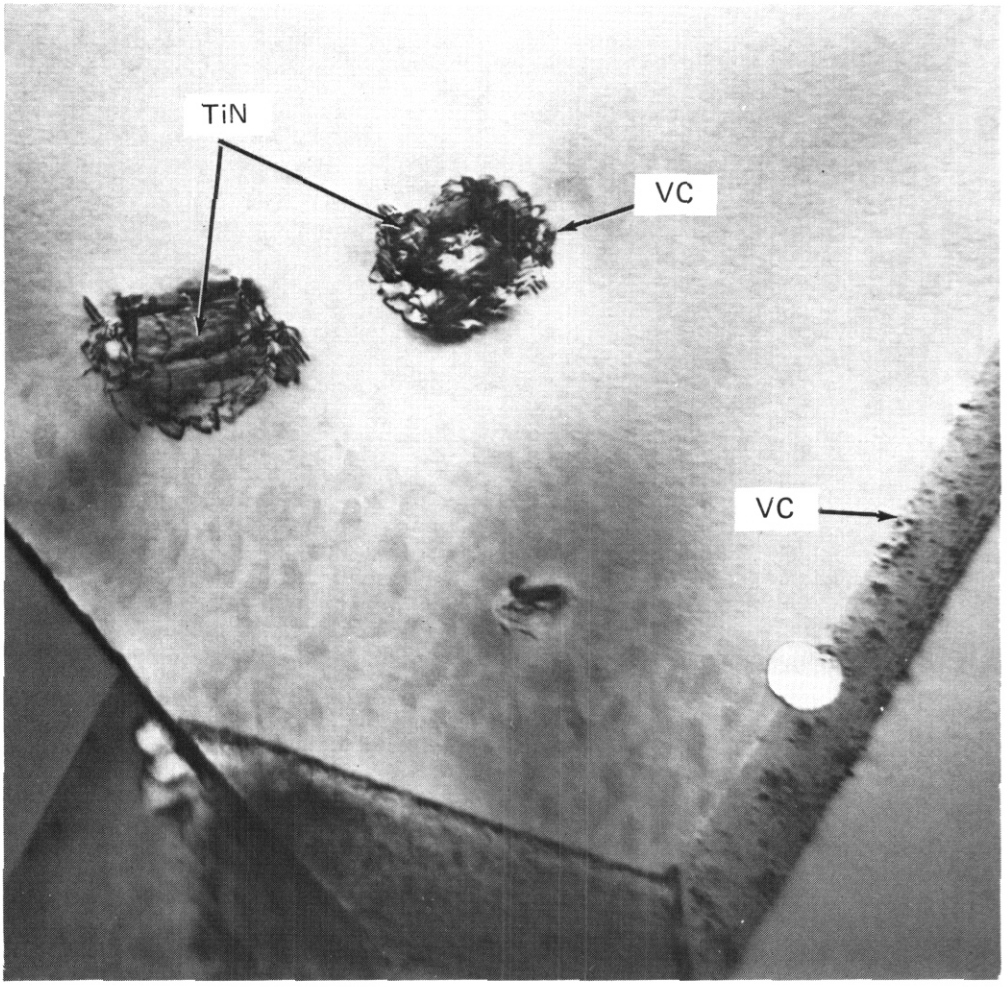

Fig. 6.1.2. Microstructure of LRO-37-5 Base Metal with TiN Particles, Which Have Punched out Dislocations. The dislocations and grain boundaries are decorated with VC particles.

VC particles were also found in the grain boundaries. The third phase was present as widely scattered inclusions with rounded shapes, shown in Fig. 6.1.3. This phase could not be identified, but EDS showed that the phase was rich in titanium and contained small amounts of vanadium, nickel, and iron. The phase may also contain one or more of the ligh elements, such as oxygen, nitrogen, or carbon, which are not detected by our EDS system. Like the TiN particles, these titanium-rich particles

Fig 6 1 3 Unidentified Titanium-Rich Phase in LRO-37-5 Base Metal with Punched-Out Dislocations Decorated with VC. (a) Bright field. (b) Dark field using a VC reflection; the light areas are VC.

E-35711

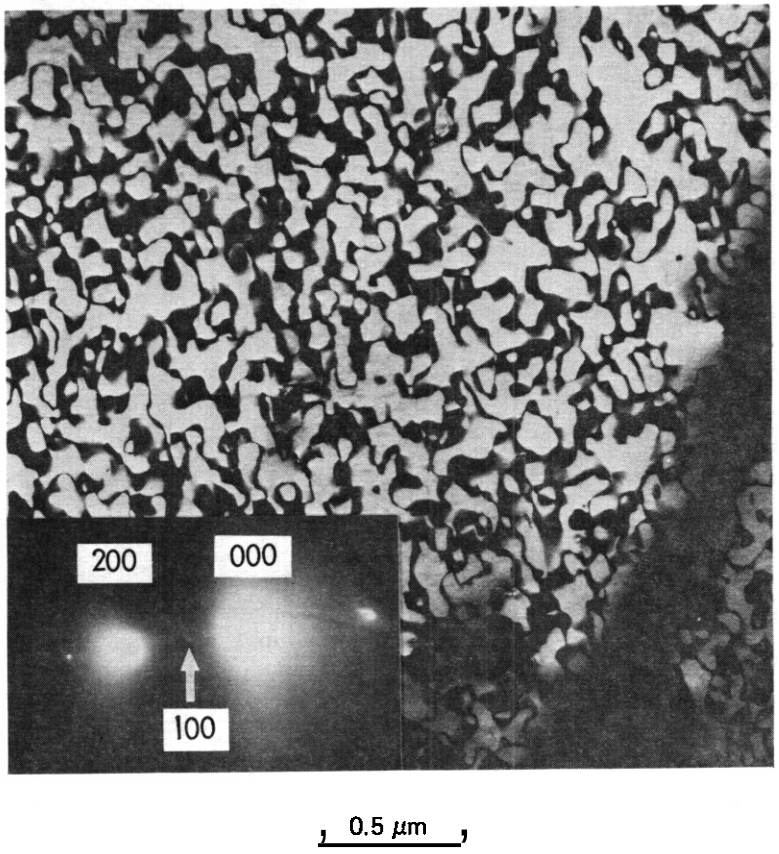

Fig. 6.1.4. Ordered Domains (Light Areas) and Antiphase Boundaries (Dark Areas) in LRO-37-5 Base Metal. The image is formed with the (100) superlattice reflection shown in the inset.

punched out dislocations [Fig. 6.1.3(a)], which were decorated with VC, as shown in the dark-field micrograph in Fig. 6.1.3(b). Another feature in the microstructure of the ordered LRO-37-5 alloy is the ordered domains and antiphase boundaries (APBs). This structure is revealed in dark field by using a superlattice reflection, as shown in Fig. 6.1.4, with the light areas being ordered domains and the dark areas, APBs. In this case, the image was formed by using a (100) superlattice spot, and only two-thirds of the existing APBs are in contrast. The wavy APBs have isotropic energies and $(a/2)\langle 110\rangle$ displacement vectors.[3] When the alloy became disordered, as was the case for the HAZ and fusion zone of the weld, the ordered domains and APBs were nonexistent.

6.1.4.3.3 Microstructure of As-Welded HAZ. A micrograph of the material in the HAZ is given in Fig. 6.1.5. The microstructure was essentially the same as that just described for the base metal except that it was disordered by the weld process and contained more dislocations. A dislocation density of about 9×10^9 cm/cm^3 was measured in the HAZ compared with about 2×10^9 cm/cm^3 in the base metal. Presumably, the additional dislocations were introduced by thermal stresses caused by the

E-35724

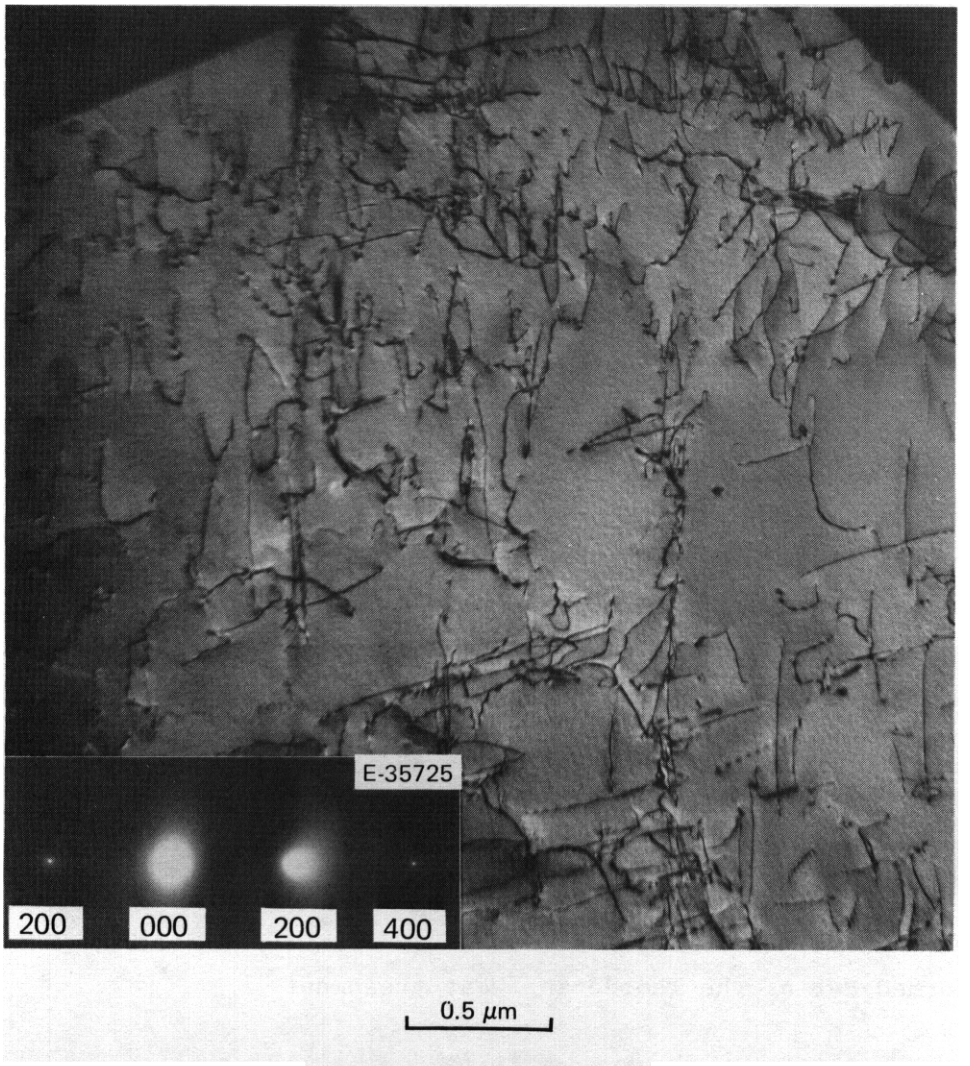

Fig. 6.1.5. Microstructure of Heat-Affected Zone in LRO–37–5 Gas Tungsten Arc Weld. Inset shows selected-area diffraction pattern. The absence of superlattice reflections indicates disorder.

welding process. The boundary between the HAZ and base metal (Fig. 6.1.1) was investigated by TEM, and it turned out to be a narrow interface between ordered and disordered regions. The ordered structure of the base metal changed abruptly, within several tens of nanometers, to completely disordered HAZ. There were no unusual features observed along this interface. The order-disorder interface was found to coincide with the drop in microhardness from the base metal to the HAZ (see the as-welded hardness trace in Fig. 6.1.1). This was determined by mounting the TEM specimens in a translucent metallographic mount (so that the shape of the center hole could be observed) and polishing the rim of the specimen. The order-disorder interface was then carefully oriented in a light microscope with respect to new hardness indentations on the polished rim.

6.1.4.3.4 Microstructure of As-Welded Fusion Zone. The fusion zone consists of columnar grains with a cellular dendritic substructure (Fig. 6.1.1). However, the grain boundaries no longer contain the fine VC particles found in the base metal. Only a few coarse VC particles were observed in the grain boundaries of the as-welded fusion zone [Fig. 6.1.6(a)]. The dislocation density in the fusion zone was about 6×10^9 cm/cm^3 — nearly the same as in the HAZ. The dislocations were probably introduced by the combination of solidification shrinkage and thermal stresses. Most of the dislocations in the fusion zone were decorated with fine VC particles, as shown in the bright-fielddark-field pair of micrographs in Fig. 6.1.6(b) and 6.1.6(c). These small VC particles formed on the dislocations during cooling of the fusion zone.

6.1.4.3.5 Microstructure of Reordered Base Metal and HAZ. Reordering of the LRO-37-5 weld caused very little change in the base metal and HAZ microstructures other than the creation of ordered domains and APBs in the HAZ. A few fine VC precipitate particles on matrix dislocations in the HAZ formed during the reordering heat treatment.

6.1.4.3.6 Microstructure of Reordered Fusion Zone. Reordering did not appear to change the fusion zone dislocation density markedly ($\sim 8 \times 10^9$ cm/cm^3), as shown in Fig. 6.1.7(a). However, the heat treatment

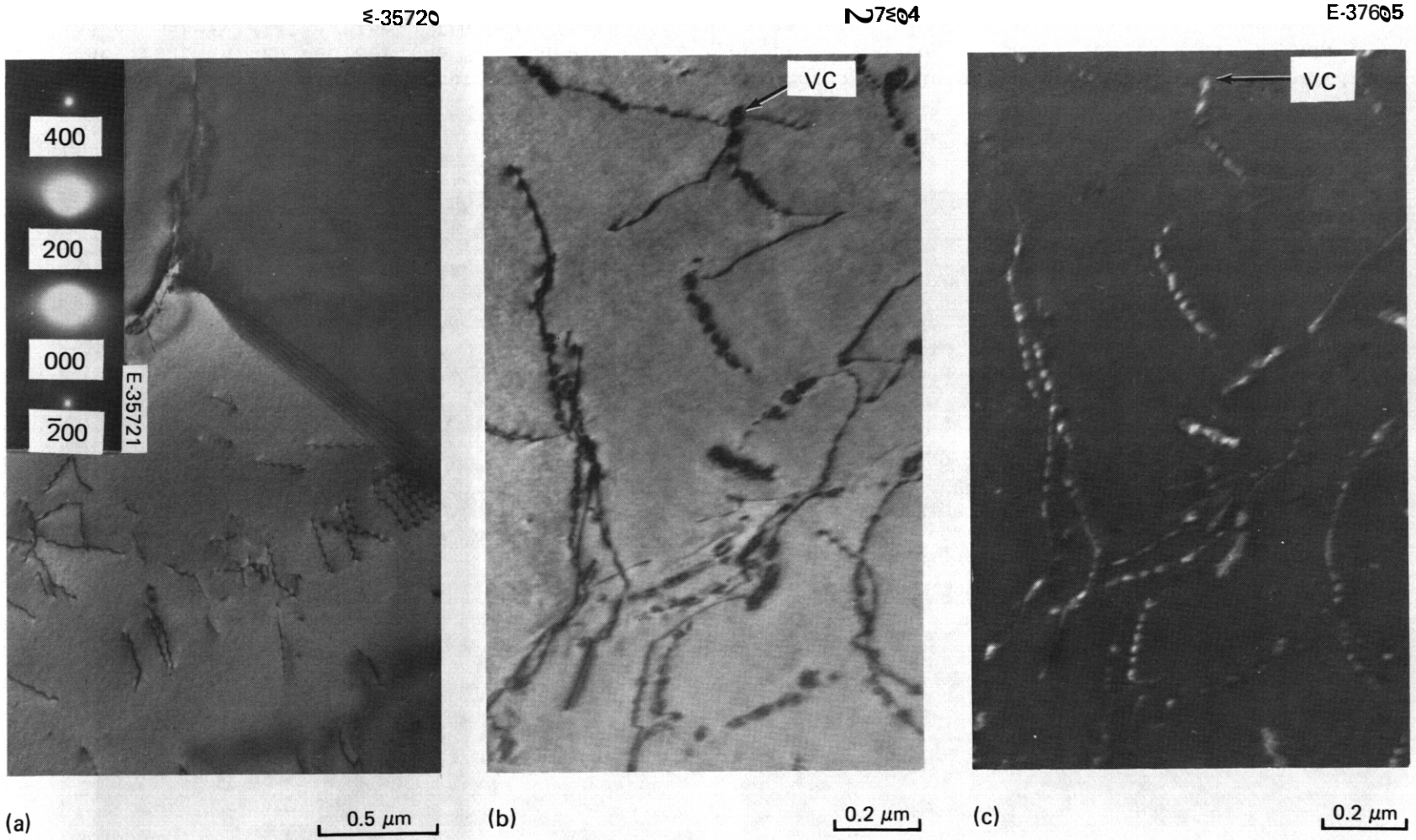

Fig. 6.1.6. Microstructure of Fusion Zone in LRO-37-5 Gas Tungsten Arc Weld. (a) General microstructure with coarse VC particles on grain boundary. Inset shows selected-area diffraction pattern without superlattice reflection, indicating disorder. (b) Higher magnification micrograph showing small VC particles on matrix dislocations, and (c) precipitate reflection dark-field micrograph of area in (b). The VC particles appear as white spots.

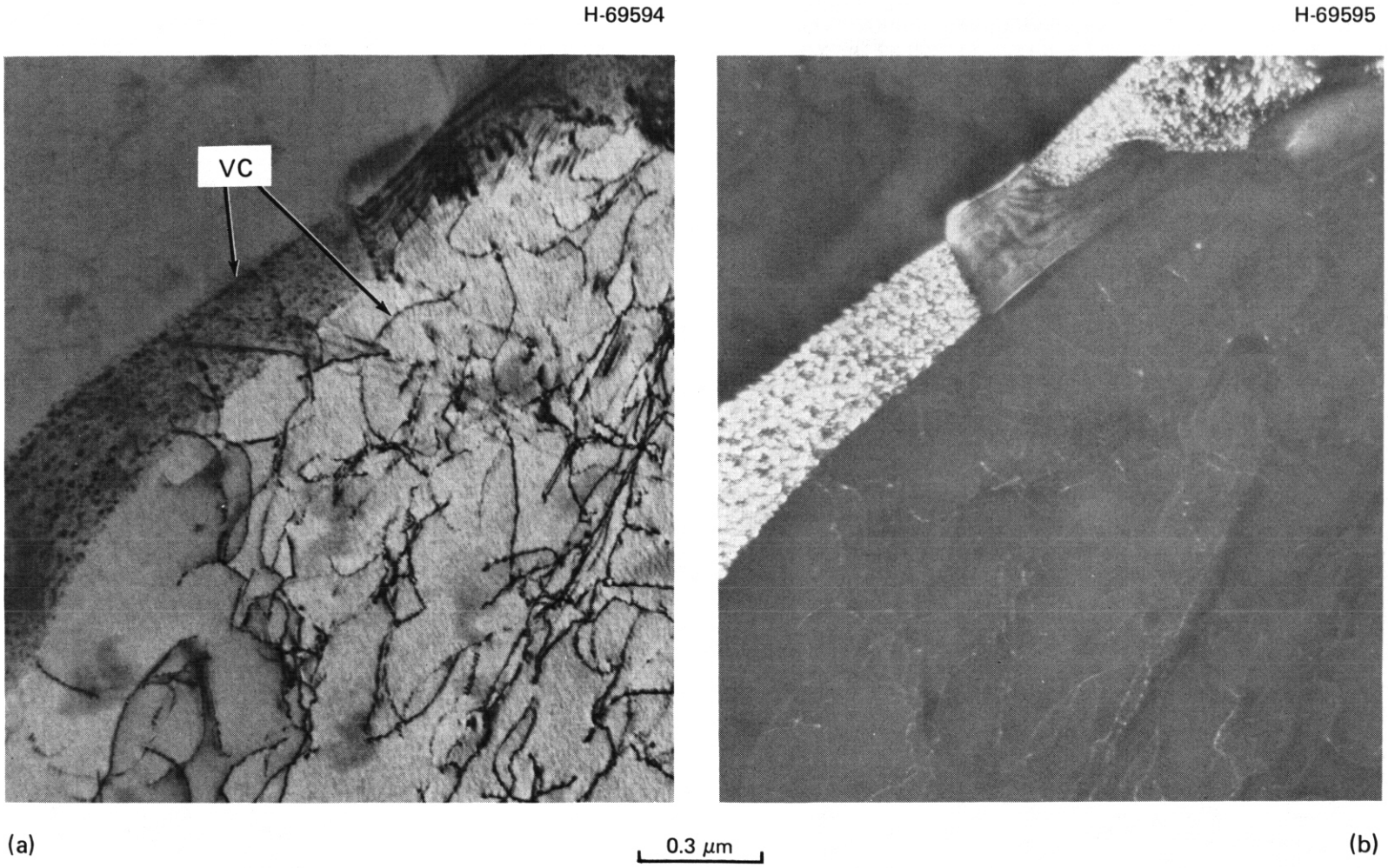

Fig. 6.1.7. Microstructure of Fusion Zone in LRO-37-5 Gas Tungsten Arc Weld After Postweld Heat Treatment to Reorder the Structure. (a) Bright field showing VC particles in grain boundary and on matrix dislocation. (b) Dark field of same area using (200) VC reflection; VC appears white.

caused rather extensive precipitation of fine VC on the grain boundaries as well as on the matrix dislocations, as shown in the precipitate dark-field micrograph of the same area, Fig. 6.1.7(b). It is probable that melting of the fusion zone dissolved most of the VC particles present in the original material. Upon cooling, some VC reprecipitated on matrix dislocations, as was observed in Fig. 6.1.6 for the as-welded fusion zone. Further aging by the reordering treatment allowed more precipitation to occur, as shown in Fig. 6.1.7. Little additional VC precipitation occurred in either the base metal or HAZ because most of the carbon was already tied up in existing VC particles. Therefore, welding of the LRO-37-5 alloy followed by a reordering heat treatment produced a more uniform distribution and refinement of the VC precipitate in the fusion zone of the weld.

6.1.4.4 Discussion

The relationship between the hardness traces across the as-welded and reordered welds (Fig. 6.1.1) can be related to their respective microstructures (Figs. 6.1.2-6.1.7). The microhardness in the as-welded HAZ was about 198 DPH, 24 DPH lower than the 222 DPH of the base metal. This decrease in hardness resulted from disordering of the structure during welding. Liu and Inouye[4] have shown that the ultimate tensile strength of an alloy similar to LRO-37-5 decreased about 30% from the ordered to disordered state. This is adequate to account for the hardness loss in the HAZ after welding. The hardness drop in the as-welded fusion zone was slightly less (204 DPH) than that in the HAZ. This zone was also disordered, and carbides in the fusion zone were dissolved during welding. However, TEM examination (Fig. 6.1.6) showed that some VC reprecipitated during cooling. This precipitation probably increased the strength, giving rise to slightly higher hardness values of the fusion zone than of the HAZ. Reordering of the fusion zone produced a 60 DPH increase in hardness. A portion of the increase was certainly due to the increased strength of the ordered structure, and further hardening was probably caused by the additional VC precipitation that occurred during the reordering. Some residual strain, introduced by the 0.4% reduction in

lattice parameter on ordering, may have also added to the increased hardness in the fusion zone. However, this contribution must be minimal because the dislocation density of the reordered fusion zone was nearly the same as that in the as-welded specimen. The reordered HAZ showed a hardness increase of 37, to 235 DPH, which can be attributed, for the most part, to reordering itself. Only a few VC particles precipitated on matrix dislocations because virtually all the carbon was already tied up in VC that existed in the base metal or starting material.

This preliminary investigation can serve as base for future welding studies for this class of ordered alloys. The results have shown that the HAZ and fusion zones of as-welded specimens were disordered and softer then ordered base metal. Nevertheless, the strength of the weld may still be sufficient for most applications. On the other hand, reordering increased the strength of the HAZ and fusion zone significantly, and these welds should be stronger than the base metal. For practical reasons, it may be advantageous to develop a much shorter postweld reordering heat treatment. The LRO-37-5 alloy can be reordered in much shorter times, and the chances of developing a shorter reordering treatment are quite good. It might be unnecessary to reorder the welds if the application is for use at elevated temperatures below T_c. In that case, the welds would reorder rather quickly during service.

6.1.5 Conclusions and Recommendations

An investigation of the microstructure of autogenous GTA welds of alloy LRO-37-5 showed

1. Sound, crack-free welds can be produced using the GTA process.
2. The order-disorder boundary separating the base metal from the HAZ was a thin interface rather than a diffuse zone.
3. The HAZ and fusion zones were disordered and softened by the weld process.
4. A postweld heat treatment increased the hardness of the HAZ and fusion zone by reordering the structure. The precipitation of small VC particles on grain boundaries and matrix dislocations in the fusion zone produced additional hardening of the material in that area.

Sheet tensile specimens with GTA welds across the gage sections should be fabricated and tested to determine the tensile properties of the welds. The effect of elevated-temperature aging as well as irradiation on the tensile properties of the welds should also be investigated.

6.1.6 References

1. C. T. Liu, "Development of Ductile Long-Range Ordered Alloys for Fusion Systems," *J. Nucl. Mater.* 85&86: 907–11 (1979).
2. D. N. Braski, "The Resistance of $(Fe,Ni)_3V$ Long-Range-Ordered Alloys to Neutron and Ion Irradiation," *J. Nucl. Mater.* 103&104: 1199–1203 (1981).
3. D. N. Braski, R. W. Carpenter, and J. Bentley, "Microstructure of Ordered $(Co_{.78}Fe_{0.22})_3V$ Alloy," *Acta Metall.* 30: 799–812 (1982).
4. C. T. Liu and H. Inouye, "Control of Ordered Structure and Ductility of $(Fe,Co,Ni)_3V$ Alloys," *Metall. Trans. A* 10A: 1515–25 (1979).

6.2 STATUS OF SCALE-UP OF AN IRON-BASE LONG-RANGE-ORDERED ALLOY — T. K. Roche, D. N. Braski, and C. T. Liu (Oak Ridge National Laboratory)

6.2.1 ADIP Tasks

ADIP Tasks I.A.5, Perform Fabrication Analyses, and I.D.l, Materials Stockpile for MFE Programs.

6.2.2 Objective

The objective of this work is to perform semiproduction scale-up of an iron-base long-range-ordered (LRO) alloy to gain some commercial experience with this class of developmental alloy. The activity will provide material for irradiation, mechanical property, compatibility, and other property tests to evaluate the potential of the alloy class for use in fusion energy systems.

6.2.3 Summary

Three ingots of the iron-base alloy LRO-37, produced by a commercial source, have been successfully hot forged to slab in preparation for the production of sheet stock. Microstructural analysis of the commercially pure alloy showed a second phase that is not sigma phase but is rich in vanadium and also contains nickel and iron. Work is in progress to determine if the phase is a complex carbide, nitride, or oxide of these elements.

6.2.4 Progress and Status

Long-range-ordered alloys of the system $(Fe,Ni)_3(V,Ti)$ have been developed on a laboratory scale at ORNL. These alloys have unique properties that make them attractive as structural materials for advanced energy systems. The alloy development program has reached the important phase of alloy scale-up.

Semiproduction scale-up of the alloy LRO-37 (Fe—39.4 Ni—22.4 V—0.43 Ti, wt %), is in progress at the facilities of High Technology Materials Division, Cabot Corporation. As previously reported,[1] stage I involving ingot preparation has been completed. Three ingots

were produced – one from high-purity materials (LRO-37-HP) and two from commercial-grade materials (LRO-37-CG). Chemical analysis showed the composition of the ingots to be reasonably close to the alloy specification.

Stage II of this scale-up program, ingot forging, was completed during the present reporting period. Three-fourths of the ingot stock of each of the two alloy grades, HP and CG, was easily press forged from 102-mm-diam (4.0-in.) round to approximately 35-mm-thick (1.4-in.) slab at 1150°C. The unforged ingot stock will be retained for future studies. A sample piece of the CG forging was subsequently hot rolled at 1150°C to approximately 6.4 mm (0.25 in.) thickness with no difficulty. Thus, we expect the next stage of the program, production of sheet stock by hot and cold rolling of the forged slab, to proceed smoothly.

Microstructural analysis has continued. Initial microstructural examination of the hot-forged LRO-37-CG showed the presence of a second phase, which could not be dissolved by subsequent heat treatment at 1200°C for 30 min. This result indicated that the second phase was probably not sigma phase. Further investigation of the microstructure by transmission electron microscopy (TEM) showed that the unknown phase was less dense than the alloy itself and did not have a cubic structure. The d spacings obtained by selected-area electron diffraction could not be indexed to the standard ASTM index. Analysis of the phase by energy-dispersive x-ray in the TEM showed that, unlike sigma phase, it was rich in vanadium. The second phase was extracted electrolytically from the alloy and analyzed by x-ray diffraction. Again, the numerous d spacings could not be indexed to the standard ASTM index. X-ray fluorescense of the extracted phase showed it to contain (in order of decreasing amounts) vanadium, nickel, and iron. An additional quantity of the second phase has been extracted and submitted for analysis for the elements carbon, nitrogen, and oxygen. It is hoped that the phase can be identified as a carbide, nitride, or oxide. Identification of the phase may help determine how it formed during melting and/or fabrication.

6.2.5 Reference

1. T. K. Roche and C. T. Liu, "Status of Scale-up of an Iron-Base Long-Range-Ordered Alloy," *ADIP Semiannu. Prog. Rep. March 31, 1982*, DOE/ER-0045/8, pp. **321—26.**

7. PATH E ALLOY DEVELOPMENT — FERRITIC STEELS

7.1 MICROSTRUCTURAL EXAMINATION OF HT-9 IRRADIATED IN THE HFIR-CTR-32 EXPERIMENT - D. S. Gelles and L. E. Thomas (Westinghouse Hanford Company)

7.1.1 ADIP Task

The Department of Energy (DOE)/Office of Fusion Energy (OFE) has cited the need to investigate ferritic alloys under the ADIP program task, Ferritic Steels Development (Path E). The tasks involved are akin to task number 1.C.2, Microstructures and Swelling in Austenitic Alloys and task number l.C.l, Microstructural Stability.

7.1.2 Objective

The objective of this work is to provide guidance on the applicability of martensitic stainless steels for fusion reactor structural components.

7.1.3 Summary

Specimens of HT-9 (heat 91354) have been examined by analytical electron microscopy following irradiation in HFIR at 300 and *400°C* to doses on the order of 10 dpa. Dislocation loops and G-phase particles but no voids formed during irradiation. Higher densities occurred at the lower irradiation temperature. Comparisons with microstructures of HT-9 specimens irradiated in EBR-II allow the conclusion that a twenty fold increase in helium production has no significant effect on microstructural development in HT-9 for irradiation at *400°C* to doses on the order of 10 dpa.

7.1.4 Progress and Status

7.1.4.1 Introduction

The present study is one in a series intended to characterize the irradiation induced changes in microstructure of Path E alloys in order to predict response in fusion reactor first wall applications. The first study of this series examined HT-9 and Modified 9Cr-1Mo following irradiation in a fast reactor (EBR-II) to 11 dpa at 400, 450 and 550°C.[1] The present study examines the same heat of HT-9 following irradiation in a mixed spectrum reactor (HFIR) to 6 and 10 dpa at 300 and 400°C. From

not same Heat Treat though

these two studies, it should be possible to assess the irradiation response of HT-9 at 400°C in a fusion environment which is in several ways intermediate between those in EBR-II and HFIR. In addition, the effect of irradiation at temperatures below those of standard fast reactor operation (i.e., 300°C) can be determined.

The examination results of HT-9 following irradiation at 400°C in EBR-II[1] may be summarized as follows. No voids were observed but the initial dislocation structure was altered by the formation of irradiation induced loops and tangles. The number density of $M_{23}C_6$ particles on boundaries appeared to increase and a high density of 8 nm diameter equiaxed precipitates was found in the matrix. The fine precipitate phase was identified as G-phase, a nickel silicide with face centered cubic crystal structure and lattice parameter 1.12 nm.

7.1.4.2 Experimental Procedure

The specimens examined in this work were 3 mm diameter transmission electron microscopy (TEM) disks of normalized and tempered HT-9 (heat 91354) which had been irradiated in the HFIR-CTR-32 experiment.[2] Heat treatment was performed at ORNL. Table 7.1.1 gives the irradiation conditions. Since only one TEM disk of each specimen condition was available, the same disk was used to prepare a "carbide" extraction replica and a thin foil specimen for TEM. The procedure involved lightly electropolishing each as-received disk to remove surface contamination, then making the extraction replica and finally jet electropolishing the disk specimen to produce thin areas for TEM examination. The electropolishing and extraction techniques were described previously.[1]

Table 7.1.1. Irradiation Conditions of HT-9 Specimens Examined From the HFIR-CTR-32 Experiment"

Specimen I.D.	Irradiation Temperature	Position	Approximate Dose
SA14	300°C	12	6 dpa
SA24	300°C	8	10 dpa
SA11	400°C	1	6 dpa
SA21	400°C	8	10 dpa

"from letter of March 24, 1982, JM Vitek, ORNL to DT Peterson. WHC.

Most of the TEM examinations, energy-dispersive x-ray (EDX) microanalyses and electron diffraction analyses of extracted particles were performed on a JEOL 100CX TEM/STEM at 100 KV. However, electron energy loss spectrometry (EELS) was also performed on the extracted particles using a Gatan double-focusing spectrometer on a Vacuum Generators HB-501 STEM. EELS provides analyses for light elements such as carbon, nitrogen and oxygen. Although the extraction replicas had carbon film substrates, in some cases particles protruding from torn edges of the substrate could be analyzed without interference from the substrate carbon. The EELS analyses were performed at 100 KV using a 2 nm diameter electron probe and a 20 mrad spectrometer acceptance half-angle.

7.1.4.3 Results

7.1.4.3.1 Extraction Replica Analysis. Extraction replicas were produced from three of the four irradiated specimens. All three extractions contained similar types and distributions of particles, as shown in the micrographs of Fig. 7.1.1. In all, four types of particles were identified by single crystal electron diffraction, EDX and EELS microanalysis.

The most prominant second phase is $M_{23}C_6$, which appears as equiaxed 0.15 to 0.8 μm diameter particles. The $M_{23}C_6$ has a lattice parameter of 1.07 nm, and contains mainly chromium, iron, molybdenum and a small amount of vanadium. Compositions obtained by EDX microanalysis are given in Table 7.1.2. $M_{23}C_6$ normally forms at martensite lath and prior austenite boundaries in HT-9 during tempering. However, in these HFIR irradiated specimens the $M_{23}C_6$ particles appear to be distributed at random.

Another second phase observed in these specimens is (V,Cr)N. This phase appears as thin plates and laths having edge dimensions from 0.05 to 0.5 μm. This is an MC-type phase with a FCC crystal structure and lattice parameter of about .417 nm, and contains mainly vanadium and chromium with a trace of iron. Due to the presence of a carbon film substrate and the close proximity of low energy x-ray peaks from V, Cr, C, N and O in EDX spectra, it normally is not possible to analyze for light elements in cases such as this. By using EELS, and analyzing

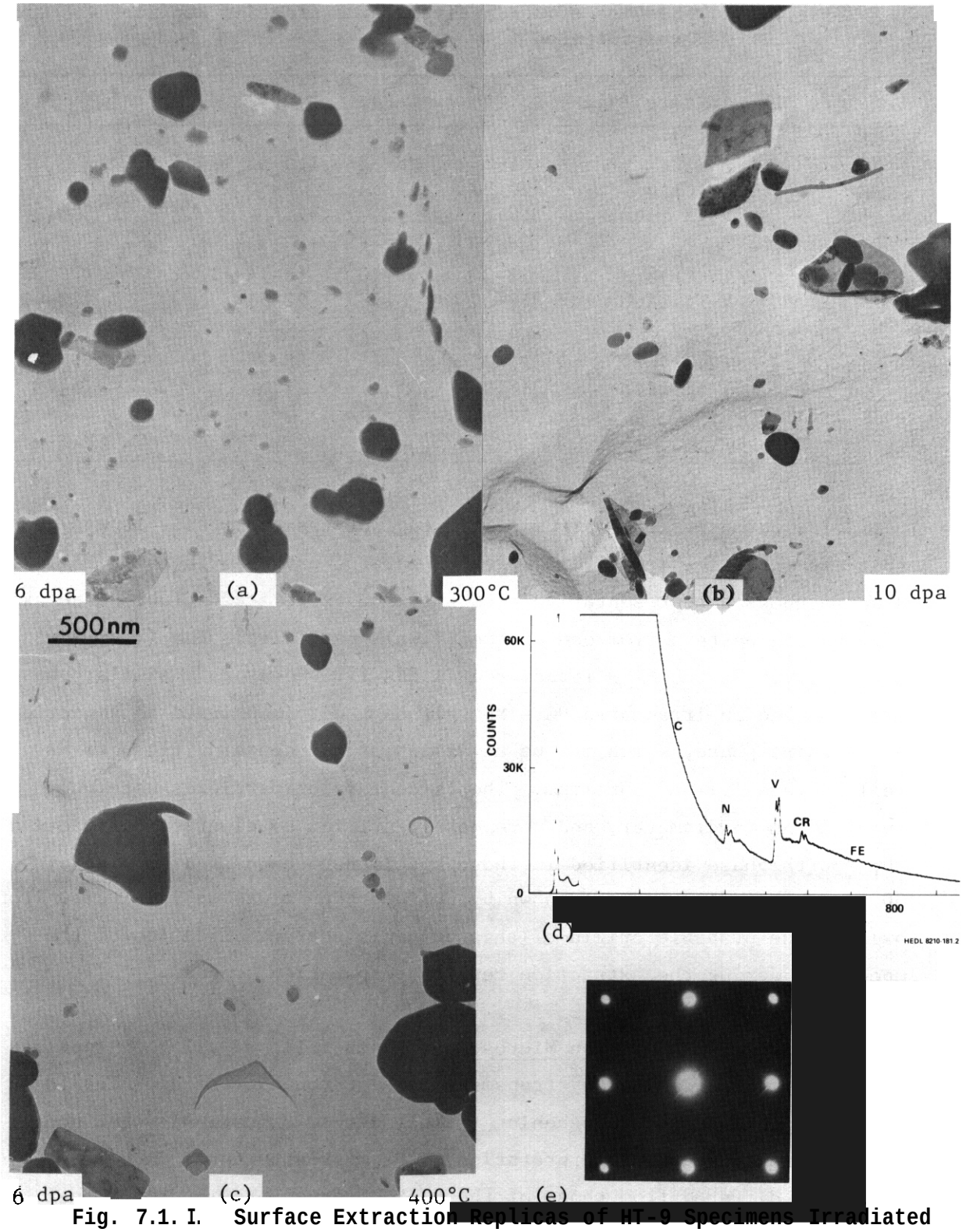

Fig. 7.1. I. Surface Extraction Replicas of HT-9 Specimens Irradiated in HFIR-CTR-32 a) SA14, b) SA24 and c) SA11. Fig. 7.1.1d Shows an EELS Spectrum of a Vanadium Rich Platelet in SA14 and Fig. 7.1.1e Provides an Electron Diffraction Pattern of the Platelet Demonstrating that the Platelet is (V,Cr)N.

Table 7.1.2. Results of EDX Analysis of Extraction Replica Precipitates

Specimen	Precipitate Type	Cr	Fe	V	Mo	Ti
SA14	$M_{23}C_6$	61–65	28–32	1.5–4	4.5–5.5	
	(V,Cr)N	20–28	3–6	72–80		
	V-Ti rich	19–6		47.1		33.3
SA24	$M_{23}C_6$	58–61	33–35	1.3–1.7	5.4–5.6	
	(V,Cr)N	23–34	3.5–10.5	56–74		
	V-Ti rich	10–30	5–7	22–51		22–60
SA11	$M_{23}C_6$	58–66	28–36	0–9	4–6	
	(V,Cr)N	21–35	3–8	58–78		
	V-Ti rich	18.2	5.5	21.5		54.8
	Fe O_x	5–7	85–90	0–5	0–9	

particles which protruded from a torn edge of the substrate, it was found that the particles are (V,Cr)N with no carbon, oxygen or boron. Fig. 7.1.1 d and e shows a representative EELS spectrum as well as a (OO1) zone axis diffraction pattern from one of the (V,Cr)N particles. The (V,Cr)N was not observed in the HT-9 irradiated in EBR-II. However, a similar phase was observed in irradiated 9Cr-1Mo[1] although not identified as a nitride.

A third phase, which may be a variant of MC, contains titanium as well as vanadium and chromium. The Ti-containing particles were only about 30 nm in diameter, and were not identified by electron diffraction. The fourth phase identified in these specimens occurs as 8 nm wide by 50 nm long needles and was shown by EDX and EELS microanalysis to be iron oxide. The probable origin of this phase is surface oxidation of the specimens during the extraction replica preparation process.

7.1.4.3.2 Transmission Microscopy. Thin foils of all four specimen conditions were examined by transmission electron microscopy. The foils exhibited some surface roughening (likely due to oxidation) which complicated microstructural interpretation. The microstructures in these specimens differed from those of the "I-9 observed previously in that neither martensite lath or $M_{23}C_6$ decorating lath boundaries were found. However, many examples of recovered subgrain boundary structure typical

don't see $M_{23}C_6$ @ g.b. + lath boundaries. Do we have any unirrad. controls to check unirrad. cond.?

of tempered martensite were identified indicating that a martensite transformation had probably occurred. These features are shown in the low magnification series of micrographs given in Fig. **7.1.2** and large blocky $M_{23}C_6$ precipitate particles can be identified. However, there is no evidence of plate and rod shaped vanadium nitride particles which were observed in the replicas. Therefore, it is anticipated that vanadium nitride and other atypical phases which were found in extraction replicas only existed near or at specimen surfaces.

do we have any evidence to show ppt in foil too?

Effects of irradiation were identified in each specimen condition examined. All specimens contained unfaulted dislocation loops. The maximum loop diameters were **7** nm for SA14, 10 nm for SA24, **17** nm for SA11 and 25 nm for SA21. No attempt was made to determine loop number densities or Burgers vectors. Loop densities were non-uniform but in general, the densities increased with decreasing irradiation temperature. No irradiation induced voids were found in these specimens. Cavitation associated with large carbide particles were identified but are believed to have formed prior to irradiation. Such cavities are typically produced during cold working when carbide particles fracture and the resulting cavities do not annealed out during normalization. Examples of dislocation structures are given in Figs. **7.1.3** and **7.1.4** for **300** and 400°C irradiation temperature.

All specimen conditions were examined for the presence of G-phase by dark field imaging techniques. It was possible to demonstrate the presence of G-phase following irradiation both at 300 and 400°C using (333) imaging. Following irradiation at **300°C** to **6** dpa, G-phase was found to consist of discrete 2.0 nm diameter particles which decorated dislocation loops. After irradiation at 400°C to 10 dpa, the particles were as large as 8.0 nm. 'The largest particles were found in linear arrays which coincided with dislocation images. Examples are shown in Figs. **7.1.5** and **7.1.6.** Fig. **7.1.6** shows the same area in precipitate dark field contrast and $\bar{g}$ = (110) bright field dislocation contrast. The correspondence between dislocations and G-phase particles is apparent from this figure. Therefore, precipitation occurs after low irradiation dose in HFIR. The precipitate is identified as G-phase based on the diffraction characteristics and morphology of G-phase observed previously in irradiated HT-9.[1]

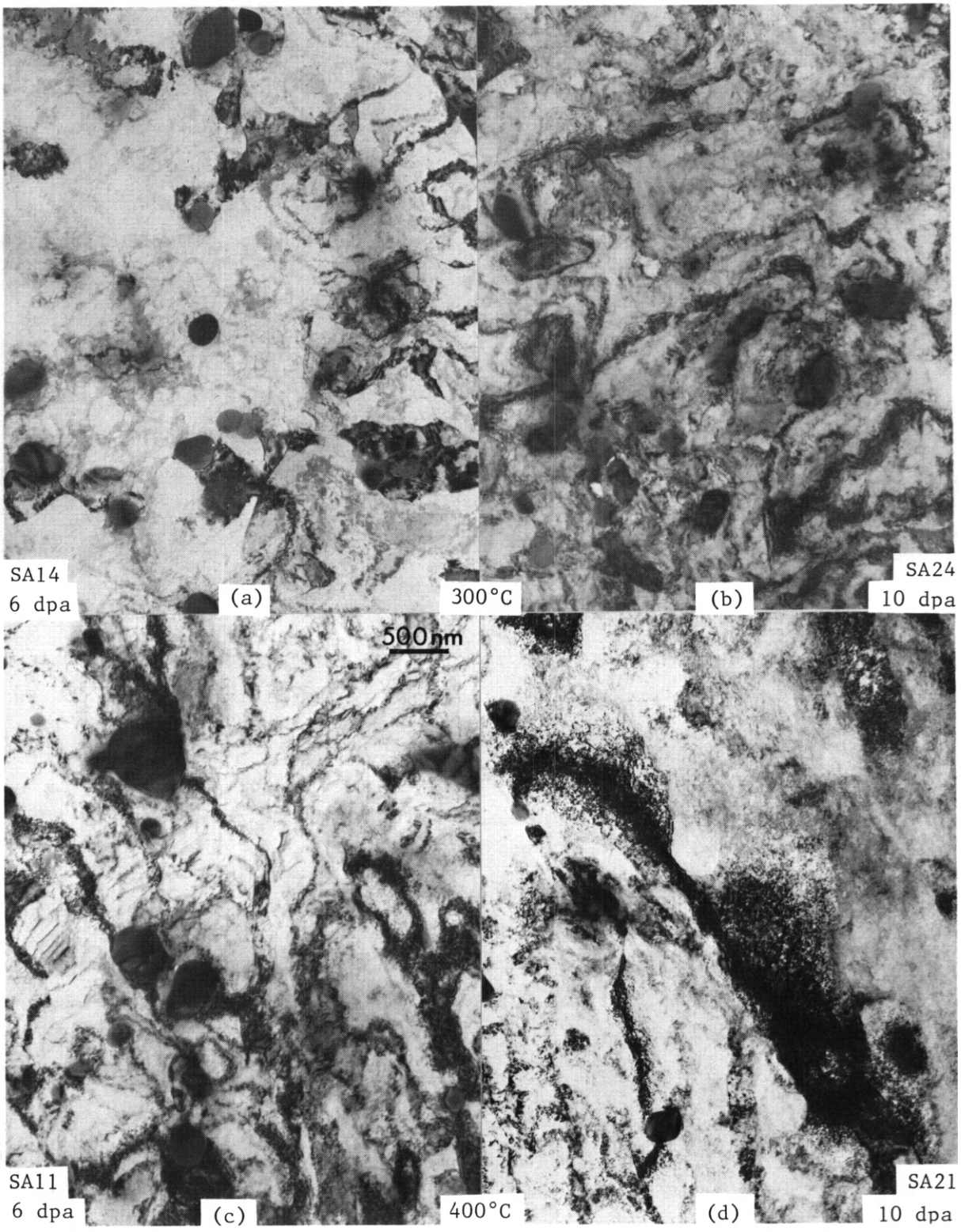

Fig. 7.1.2. Low Magnification Micrographs of Irradiated HT-9 Specimens.

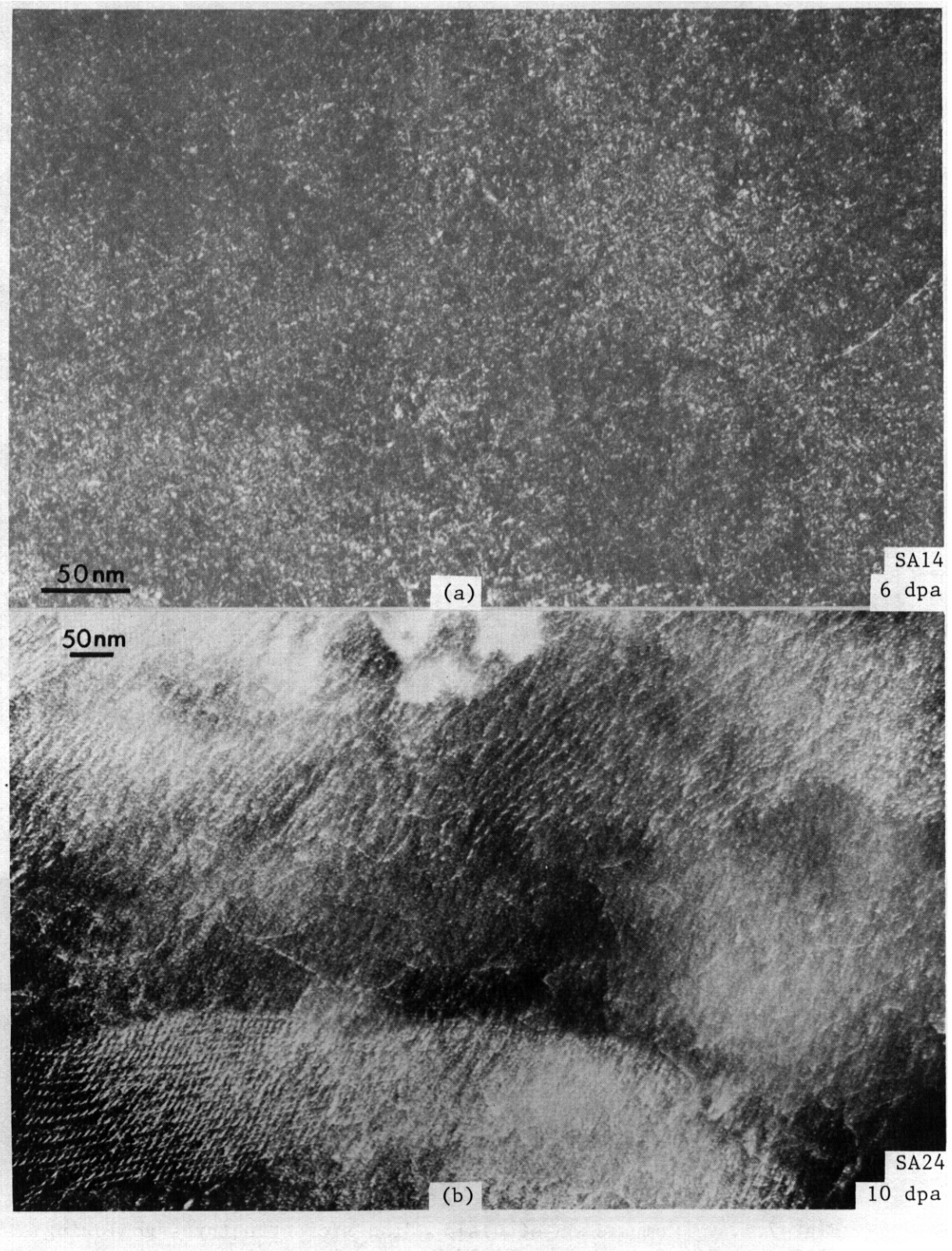

Fig. 7.1.3. Comparison of Dislocation Microstructures Following Irradiation at 300°C in Weak Beam Dislocation Dark Field Contrast.

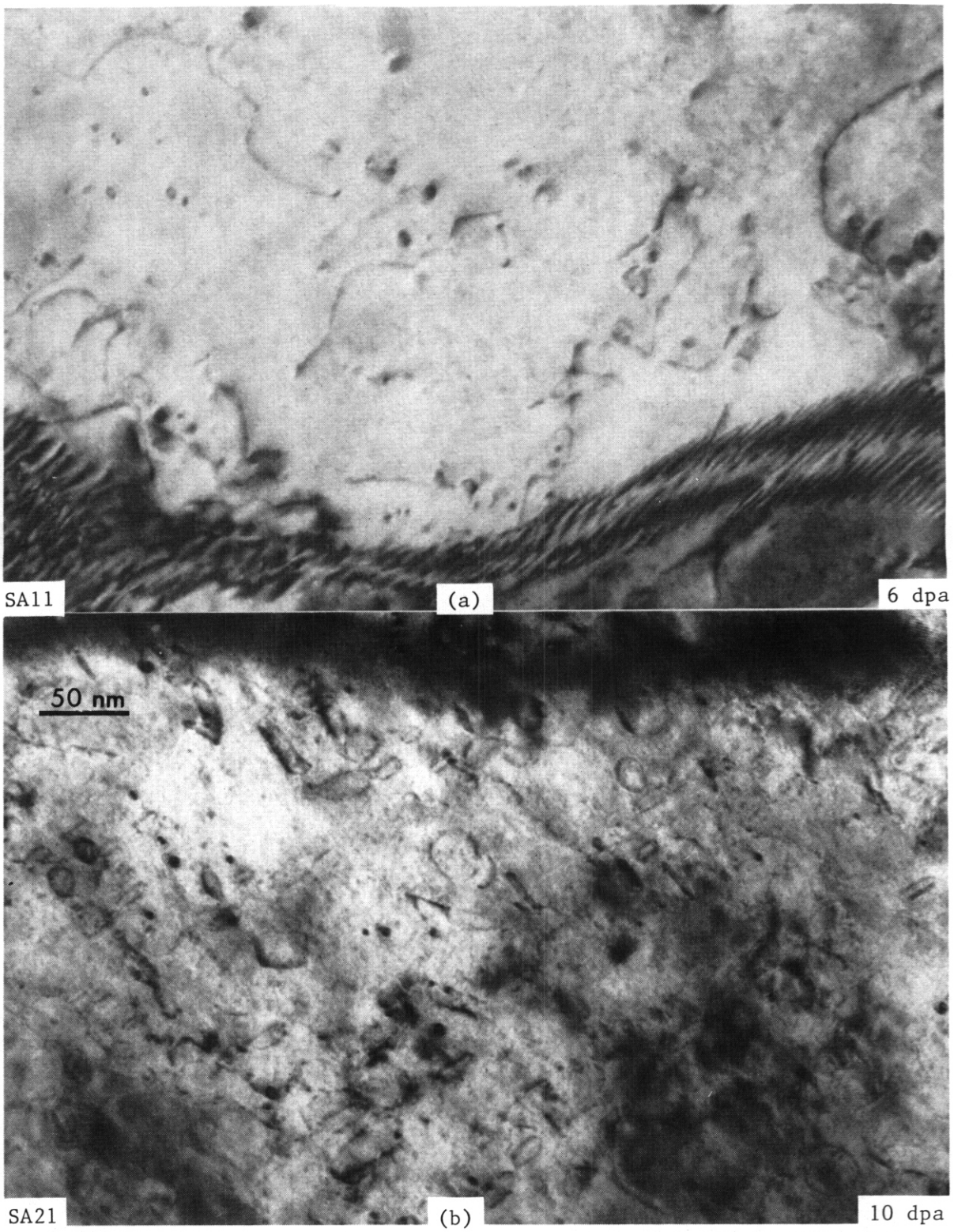

Fig. 7.1.4. Comparison of Dislocation Microstructures Following Irradiation at 400°C in Bright Field Dislocation Contrast.

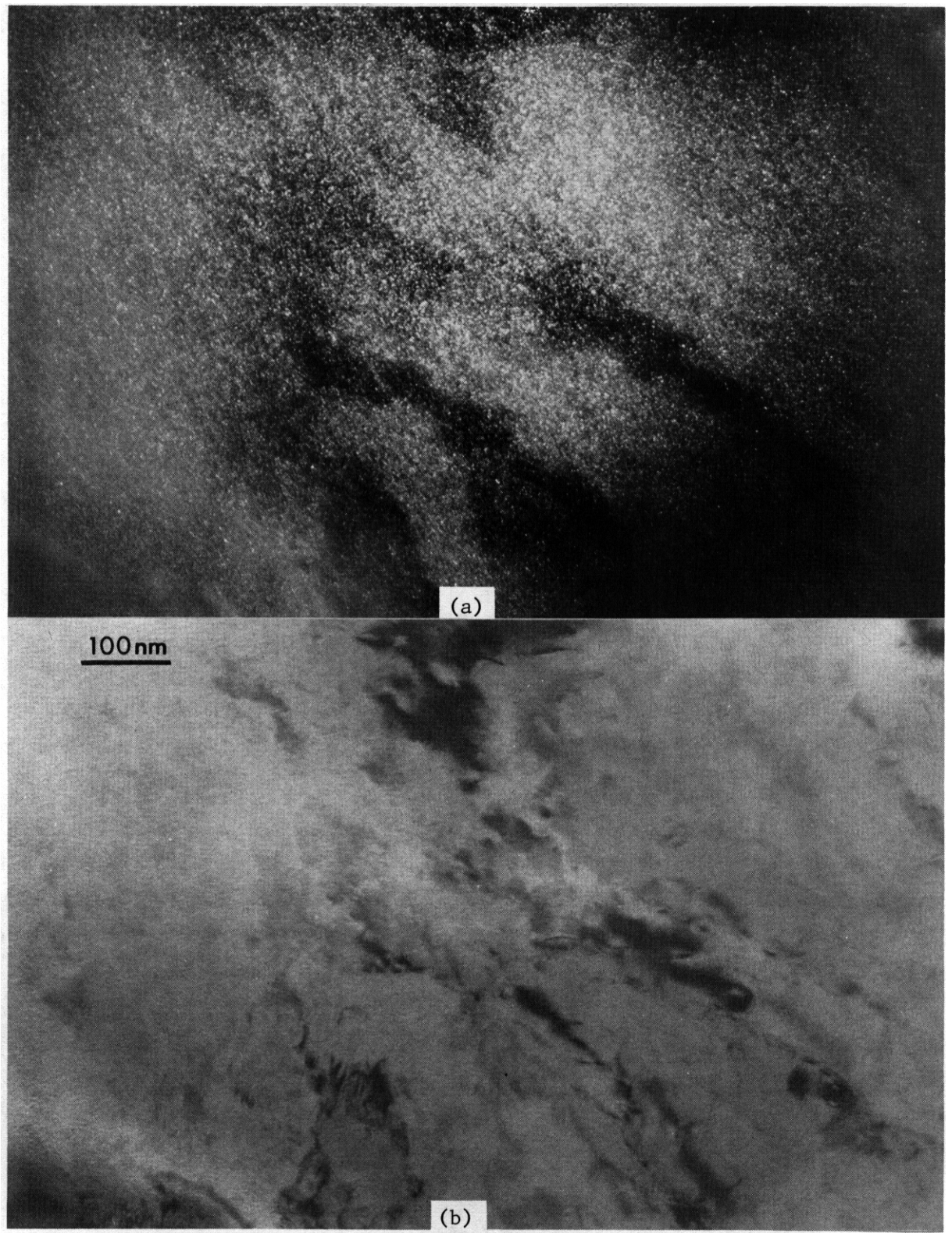

Fig. 7.1.5. G–Phase Precipitate Dark Field and Bright Field Imaging of Specimen *SA24* Irradiated at 300°C to 10 dpa.

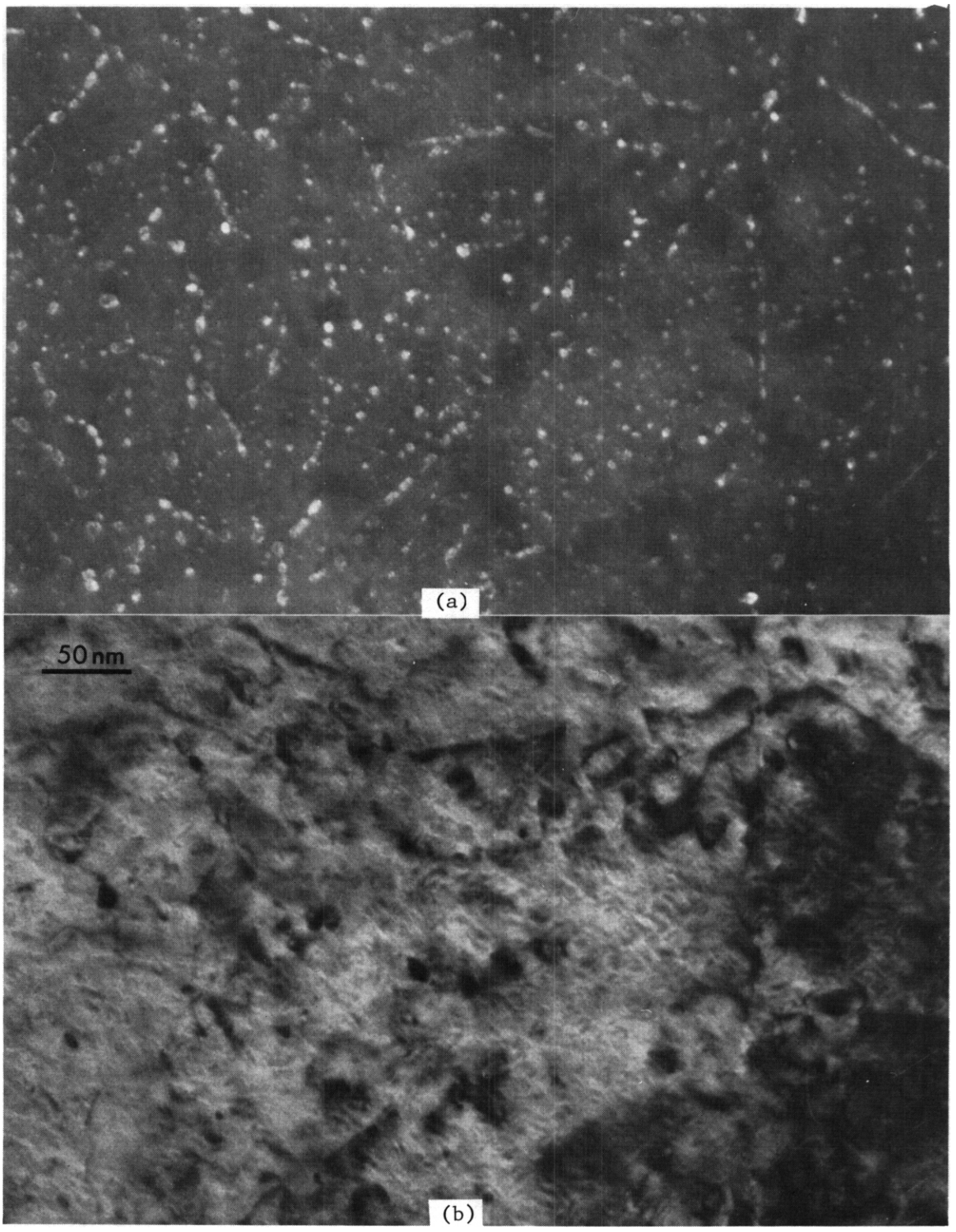

Fig. 7.1.6. G-Phase Precipitate Dark Field and Dislocation Bright Contrast Images of the Same Area of Specimen SA21 Irradiated at *400°C* to 10 dpa.

7.1.4.4 Discussion

The present effort, which was intended to provide microstructural results on HT-9 irradiated in HFIR, indicates that a mixed spectrum environment produces microstructures similar to those obtained in a fast spectrum environment. Also, dislocation and precipitate structures are found to develop on a finer scale as the irradiation temperature is decreased, even for temperatures below those previously examined. However, it is now apparent that comparisons between HFIR and EBR-II irradiation results on HT-9 must be made with caution due to apparent differences in starting microstructures. It is the intent of this discussion to expand on these points and to consider the causes and the consequences of these observations.

7.1.4.4.1 Reactor Spectrum Effects. Comparison of the present microstructural results for specimen SA21, irradiated at 400°C to 10 dpa in HFIR, and those obtained previously for specimen 2HCK, irradiated in EBR-II at 400°C to 11 dpa shows a similar irradiation response in both cases. The major effects of irradiation are dislocation loop development and G-phase formation. Maximum loop sizes following irradiation are very similar and G-phase precipitation both as a function of size and distribution is almost identical. Therefore, it is likely that: 1) dose and temperature estimates for the two experiments are in good agreement, and 2) effects of different helium production levels (on the order of 20 ppm for HFIR and 1 ppm for EBR-II[3]) do not alter microstructural development significantly. In a fusion reactor the helium content would be on the order of 150 ppm at 11 dpa[3] and therefore in HFIR, helium levels are almost an order of magnitude lower than those expected at a similar dose in a fusion reactor.

7.1.4.4.2 Irradiation Temperature Effects. The present results confirm that lower irradiation temperatures favor finer distributions of precipitates and dislocation loops. Identification of G-phase in HFIR-irradiated specimens is somewhat tentative (moreso than was the identification for specimens irradiated in EBR-II[1]) as diffraction pattern evidence is based on patterns which showed $(333)_G$, $(114)_G$ and $(044)_G$

diffuse spots with insufficient contrast to allow successful reproduction in publication.

Consequences of such a temperature dependence on precipitate and loop densities can be expected to be manifested in post-irradiation mechanical properties. Strength should increase with decreasing irradiation temperature. Data is now available to demonstrate such an effect. Post-irradiation tensile tests on HT-9 (heat 91354) irradiated in HFIR at 50°C to 9 dpa[4] can he compared with HT-9 (heat 91354 hut in a somewhat different heat treatment condition) irradiated in EBR-II at 420°C to 5 dpa.[5] The results are reproduced in Table 7.1.3 and demonstrate that for testing at 25°C, the 50°C irradiation caused more hardening than did the 420°C irradiation. Recent hardness measurements on Charpy specimens of HT-9 (heat 91354) irradiated in the AD-2 experiment in EBR-II[6] confirm this trend. Following irradiation at 390°C to 11 dpa, a hardness of 31.7 R_C was measured and following irradiation at 500°C to 11 dpa, 21.7 R_C was measured. This compares with the value of 22.9 R_C for the unirradiated condition. Unfortunately, no post-irradiation tensile data or hardness measurements are available for irradiation at 300°C. Nor is there sufficient data to estimate the irradiation temperature which will produce the greatest hardening. The peak hardening irradiation temperature is of major concern because it can he expected to correspond to the temperature at which greatest emhrittlement will occur.

Table 7.1.3. Post-Irradiation Tensile Data for HT-9 Heat 91354[4,5]

Irradiation Temp. (°C)	Irradiation Fluence (10^{22} n/cm²)	Irradiation Fluence (dpa)	Test Temp. (°C)	Strength Yield (MPa)	Strength Ultimate (MPa)	Elongation Uniform (%)	Elongation Total (%)	Ratio $\sigma_y/\sigma_{y(0)}$
–	0	0	25	549	716	6.64	9.91	
50	1.3	9.3	25	983	987	0.31	2.12	1.8
–	0	0	300	490	649	5.53	8.63	
50	1.2	9.1	300	784	800	1.36	4.49	1.6
–	0	0	25	653	823	7.5	16.4	
420	1.1	5	25	971	1037	6.3	13.9	1.5

7.1.4.4.3 Heat Treatment Variations. Two significant differences can be identified between the preirradiation microstructures for HT-9 contained in the HFIR-CTR-32 and EBR-II AD-2 experiments. Vanadium and titanium rich particles were not found in EBR-II specimens and $M_{23}C_6$ precipitate decoration of martensite lath boundaries was not found in HFIR specimens. As differences in preirradiation microstructure can be expected to complicate interpretations which require comparisons of results from the two experiments, the causes for the differences are of considerable interest.

It is likely that the differences are not of the same origin. Vanadium rich particles in HFIR specimens are found to be nitrides. Based on the size of the particles and their distribution through the thickness of the specimen, it can be concluded that these particles have not formed in-reactor from transmutation products. Rather, the particles probably formed due to nitriding during heat treatment (private communication from ORNL staff). Since the nitrides were not present in foils from the centers of specimens, it is unlikely that the nitriding had a significant effect on TEM microstructural analysis. Therefore, the reason for the unusual carbide distributions must be traced to another cause. As shown by Lichtenberg, $M_{23}C_6$ forms on martensite lath boundaries as a result of precipitation during tempering from carbon-rich retained austenite.[7] Therefore, if the lath boundary decoration by carbides is not present, it is probably because the quench rate following normalization was too rapid.

The consequences of these heat treatment variations cannot be assessed definitively. Effects of specimen nitriding on microstructural analysis can probably be ignored because the nitrogen was absorbed as vanadium (and possibly V-Ti) nitride particles in the vicinity of the specimen surface whereas microstructural analysis was only based on examination in the center of the specimen. Effects of quench rate can be expected to redistribute $M_{23}C_6$ precipitation. The effect of this redistribution on subsequent G-phase precipitation and dislocation evolution cannot be easily assessed. However, based on the fact that HFIR and EBR-II experiments gave identical dislocation and 6-phase development for similar irradiation conditions, it is probable that redistribution of

carbides due to heat treatment differences do not affect in-reactor behavior significantly. Therefore, it appears reasonable to conclude that no significant differences in microstructural development arise in HT-9 as a consequence of differences between HFIR and EBR-II neutron energy spectra.

7.1.5 Conclusions

Microstructural examination of HT-9 (heat 91354) following irradiation in the HFIR-CTR-32 experiment at 300 and 400°C has shown that irradiation produces dislocation loop and G-phase precipitate development but no void swelling. Loop and precipitate densities increase with decreasing irradiation temperature. It can be expected that increased hardening and embrittlement will therefore result with decreasing irradiation temperature. Comparison of the present results with previous results for an HT-9 specimen irradiated at 400°C in EBR-II demonstrates no significant differences in irradiation induced microstructure. Therefore, a twenty fold increase in helium production has negligible effect on microstructural development for doses on the order of 10 dpa.

Interpretation of this work has been complicated by the presence of vanadium and vanadium-titanium rich particles found in surface extraction replicas. The vanadium rich particles were identified as (V,Cr)N. Although the nitriding was restricted to specimen surfaces and therefore probably did not invalidate experimental conclusions, it is apparent that more care must be taken to ensure that irradiation experiment fabrication errors do not jeopardize future program objectives.

7.1.6 Future Work

Examination of HFIR irradiated HT-9 specimens will be expanded to include 50°C irradiation conditions and higher dose levels.

7.1.7 References

1. D. S. Gelles and L. E. Thomas, "Microstructural Examination of HT-9 and 9Cr-1Mo in the AD-2 Experiment," *ADIP* Semi-Annual *Prog. Rep. March 31, 1982,* DOE/ER-0045/8, p. 343.

2. M. L. Grossbeck, J. W. Woods and G. A. Potter, "Experiments HFIR-CTR -30, -31 and -32 for Irradiation of Transmission Electron Microscopy Disk Specimens," ADIP *Quart. Prog. Rep. September 30, 1980,* DOE/ER-0045/4, p. 36.

3. F. M. Mann, "Transmutation of Alloys in MFE Facilities as Calculated by REAC," HEDL-TME 81-37, August 1982.

4. R. L. Kleuh, J. M. Vitek and M. L. Grossheck, "Effect of Low-Temperature Irradiation with (n,α) Helium Production on Tensile Properties of 12Cr-1MoVW Type Steels," *J NucZ Matl* 103 & 104: 887 (1981).

5. F. A. Smidt, Jr., J. R. Hawthorne and V. Provenzano, "Fracture Resistance of HT-9 After Irradiation at Elevated Temperature," p. 269 in *Effects of Radiation on Materials*, D. Kramer, H. R. Brager and J. S. Perrin, eds., ASTM-STP-725, 1981.

6. D. S. Gelles and W. L. Hu, "Fractographic Examination of HT-9 Charpy Specimens Irradiated in the AD-2 Test," this document.

7. T. Lechtenherg, "The Effect of Microstructure on the Mechanical Properties of a Commercial 12Cr-1Mo Steel (HT-9)," *J Nucl Matl* 103 & 104: 1133 (1981).

7.2 FRACTOGRAPHIC EXAMINATION OF HT-9 AND 9Cr-1Mo CHARPY SPECIMENS IRRADIATED IN THE AD-2 TEST - D. S. Gelles and W. L. Hu (Westinghouse Hanford Company)

7.2.1 ADIP Task

The Department of Energy/Office of Fusion Energy (DOE/OFE) has cited the need to investigate ferritic alloys under the ADIP program task Ferritic Steels Development (Path E). The tasks involved are akin to Task Number 1.B.13, Tensile Properties of Austenitic Alloys, and Task Number 1.C.2, Microstructure and Swelling in Austenitic Alloys.

7.2.2 Objective

The objective of this effort is to provide fractographic data for Charpy specimens of the irradiated ferritic alloys HT-9 and Modified 9Cr-1Mo in order to provide improved understanding of toughness degradation as a result of irradiation for the ferritic alloy class.

7.2.3 Summary

Fracture surface topologies have been examined using scanning electron microscopy for 20 selected half sized Charpy impact specimens of HT-9 and Modified 9Cr-1Mo in order to provide improved understanding of fracture toughness degradation as a result of irradiation for Path E alloys. The specimen matrix included unirradiated specimens and specimens irradiated in EBR-II in the AD-2 experiment. Also, hardness measurements have been riade on selected irradiated Charpy specimens. The results of examinations indicate that irradiation hardening due to 6-phase formation at 390°C is responsible for the large shift in ductile-to-brittle transition temperature (DBTT) found in HT-9. Toughness degradation in HT-9 observed following higher temperature irradiations is attributed to precipitation at delta ferrite stringers. Reductions in toughness as a consequence of irradiation in Modified 9Cr-1Mo are attributed to in-reactor precipitation of (V,Nb)C and $M_{23}C_6$. It is shown that crack propagation rates for ductile and brittle failure modes can be measured, that they differ by over an order of magnitude and that unexpected multiple shifts in fracture mode from ductile to brittle failure can be attributed to the effect of delta ferrite stringers on crack propagation rates.

7.2.4 Progress and Status

7.2.4.1 Introduction

It has been shown that fracture toughness degradation as measured by Charpy tests occurs in ferritic stainless steels as a consequence of fast neutron irradiation.'" Sandvik alloy HT-9 showed a significant increase in DBTT and a reduction in the upper shelf energy (USE) following irradiation at temperatures from 390 to 550°C to fluences of 13 dpa. This result applied both for fully heat treated base metal and for weld metal. Heat-affected-zone (HAZ) metal was only altered following irradiation at *390°C.* However, the worst case occurred for irradiation at 390°C where a 124°C DBTT shift was measured with a corresponding 15 J/cm^2 drop in the USE. Modified 9Cr-1Mo was less sensitive to irradiation. No shift in DBTT was measured following irradiation from 450 to 550°C and a shift of 55°C occurred following irradiation at 390°C. In all cases, however, the USE was reduced significantly.

The causes of fracture toughness degradation in ferritic stainless steel as a consequence of irradiation are thought to be temper embrittlement,[2] irradiation hardening" [3] and irradiation enhanced or induced precipitation.[3] Temper emhrittlement is generally associated with intergranular failure which is *a* consequence of weakening at prior austenite grain boundaries due to microchemical segregation. Fractographic examination would he expected to reveal failure at prior austenite grain boundaries. Irradiation hardening increases the stress required for plastic deformation without a change in mechanism and therefore the only change to be observed would be a shift in test temperature corresponding to an identical fracture appearance. Irradiation enhanced precipitation could cause fractographic changes similar to those from irradiation hardening or could change the size and distribution of dimples.

The present effort was undertaken in order to provide insight into the mechanisms which control this fracture toughness degradation found in AD-2 specimens. A large number of specimens had been tested and it was therefore necessary to limit the number of fractographic examinations. In order to do *so,* a series of experimental objectives was determined and samples were selected in order to allow investigation of those

objectives. The objectives as outlined in Table 7.2.1 covered three areas of investigation: 1) effects of irradiation on crack propagation with regard to DBTT and USE changes, 2) quantitative correlations of COD versus K_{ID} and 3) Rockwell hardness measurements on irradiated specimens. The second objective was to be based on COD measurements using stereometric fractography.[4] The third objective was intended to provide insight into irradiation hardening and was needed because relevant tensile data are not yet available. Fig. 7.2.1 is provided to aid in understanding the selection of specimens intended to satisfy the first set of objectives. The results of Charpy tests as a function of test temperature are shown and each of the specimens selected for examination is identified by I.D. number.

7.2.4.2 Experimental Procedure

Specimens selected for fractographic examination are listed in Table 7.2.2 along with Charpy test conditions and fracture energy. In general, specimens were selected which were tested at approximately the DBTT so that both ductile and brittle fracture surface features could be studied. However, the unirradiated conditions and a series of HT-9 base metal specimens irradiated at 550°C were selected to also show the complete fractographic response as a function of test temperature. As previously noted, Table 7.2.1 defines the objectives of fractographic examinations on this series of specimens.

Prior to examination, specimens TT10, TT30, TT69, TT05, TT12, TV09, TV14 and AF48 were used to determine the effect of irradiation on hardness. Measurements were made on a Wilson Rockwell hardness tester model 3JR with a diamond Brale indenter at 150 kg load. The tester had been installed in a hot cell and was operated remotely by manipulators. All specimens were then sectioned using a slow speed saw to provide the fracture surface with a minimum amount of adjacent material. This operation was intended to reduce radioactivity and minimize magnetic interactions with the electron beam. The sectioning operation reduced specimen sizes sufficiently so that the specimens could be examined in a standard scanning electron microscope equipped with a two inch lead brick shield to protect the operator. Examinations were performed on

Table 2.1 Objectives for Fractography/Microstructure Study of Precracked Charpy Specimens

Objective	Specimens to be Investigated: Specimen I.D.*	Test Temperature (°C)	Irradiation Temperature (°C)
I Effects of irradiation on DBTT shift and USE reduction.			
a. Identify microstructural characteristics associated with lower DBTT in 9Cr-1Mo base metal as compared with HT-9 base metal.	TV09	25	390
	TV21	-25	500
	TT16	116	390
	TT30	28	500
b. Investigate the effect of irradiation temperature on the microstructure of 9Cr-1Mo base metal. T_i = 390°C versus 450, 500 or 550°C.	(TV09)	25	390
	(TV21)	-25	500
c. Investigate the effect of irradiation temperature on the microstructure of HT-9 base metal at T_i = 390°C and T_i = 550°C versus 450 or 500°C.	(TT16)	116	390
	TT05	40	550
	TT30	28	500
d. Characterize fracture behavior in HT-9 weldment	(TT05)	40	550
	TI34	50	550
	TI27	132	390
e. Characterize fracture behavior in HT-9 heat-affected-zone.	TX11	85	390
	TX04	0	500
f. Study the stress state variation in specimens as a function of test temperature.	TT66	160	550
	TT12	300	550
	(TT05)	40	550
	TT69	-20	550
g. Investigate the effect of irradiation temperature on USE in 9Cr-1Mo base metal.	TV14	50	390
	TV13	0	500

*Specimen identity: TT - HT-9 Base Metal, TI - HT-9 Weldment, TX - HT-9 HAZ, TV - 9Cr-1Mo Base Metal Irradiated, AF - 9Cr-1Mo Base Metal Unirradiated; ( ) denotes redundancy.

Table 2.1 Continued

	Objective	Specimens to be Investigated: Specimen I.D.*	Test Temperature (°C)	Irradiation Temperature (°C)
II	Quantitative correlation between COD and K_{ID} in 9Cr-1Mo base metal and HT-9 base metal (unirradiated specimens only).	AF38	-80	-
		AF41	-10	-
		AF46	40	-
		TT03	73	-
		TT31	0	-
		TT10	-58	-
III	Rockwell hardness measurements for the evaluation of irradiation hardening on DBTT			

Total: 14 Irradiated Specimens, 6 Unirradiated Specimens

*Specimen identity: TT - HT-9 Base Metal, TI - HT-9 Weldment, TX - HT-9 HAZ, TV - 9Cr-1Mo Base Metal Irradiated, AF - 9Cr-1Mo Base Metal Unirradiated; ( ) denotes redundancy.

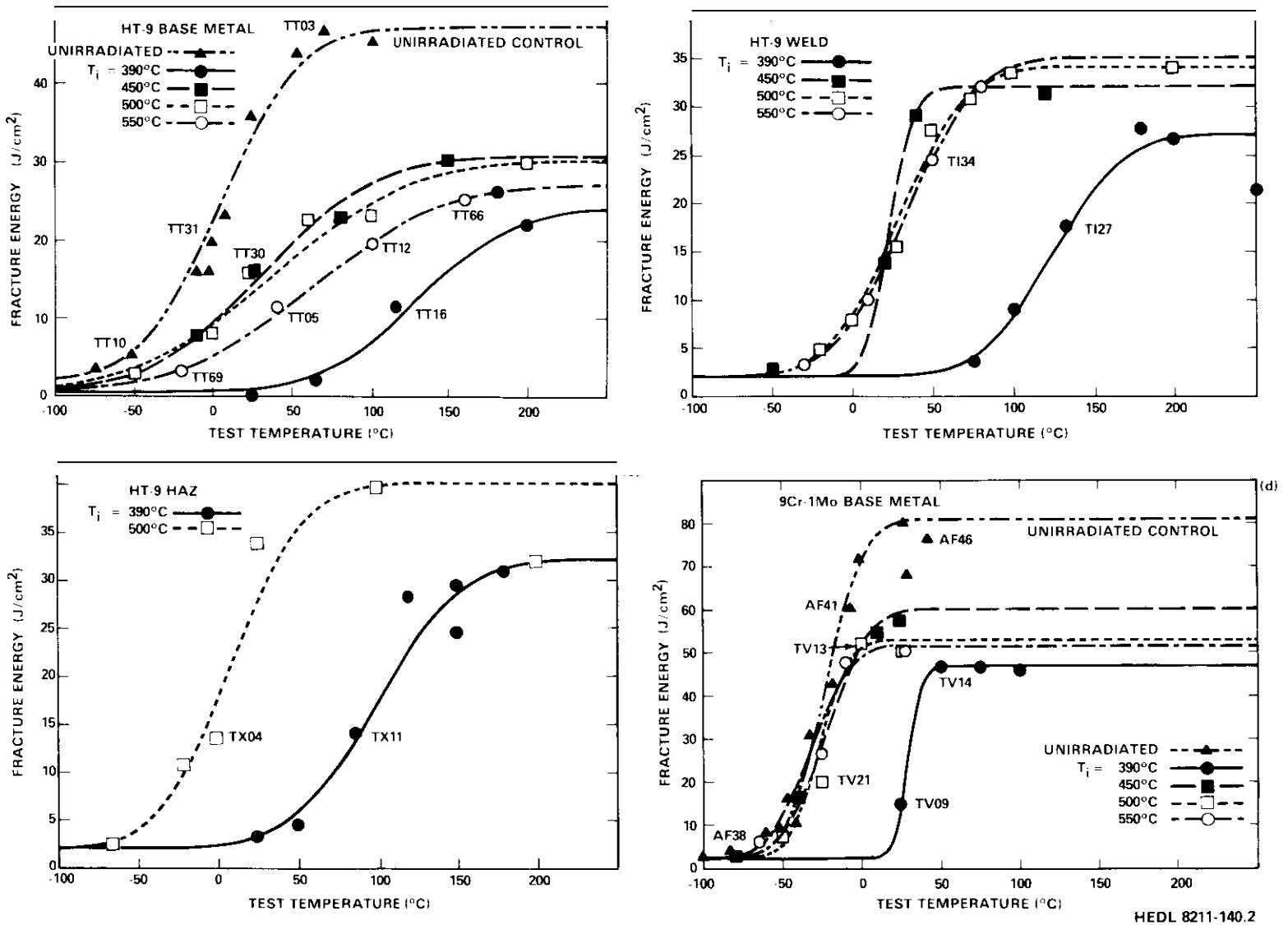

Fig. 7.2.1. Fracture Energy Results for Miniature Charpy Specimens of Three Conditions of HT-9 and Condition of Modified 9Cr-1Mo. Specimens Selected for Fractographic Examination are Identified by Num

Table 7.2.2 Charpy Specimens Selected for Fractographic Examination

Alloy	Condition	I.D.	Irradiation Temperature* (°C)	Test Temperature (°C)	Fracture Energy** (J/cm^2)	Estimates of K_{ID} ($MPa\sqrt{m}$)
HT-9	Base Metal	TT10	-	-58	5.0	27
		TT31	-	0	20.0	53
		TT03	-	73	47.0	58
		TT16	390	116	11.5	
		TT30	500	28	16.6	
		TT69	550	-20	3.2	
		TT05	550	40	11.4	
		TT12	550	100	19.5	
		TT66	550	160	25.2	
HT-9	Weld Metal	TI27	390	13	17.5	
		TI34	550	50	24.5	
HT-9	HAZ	TX11	390	85	14.0	
		TX04	550	0	13.6	
9Cr-1Mo	Base Metal	AF38	-	-80	3.1	
		AF41	-	-10	61.1	
		AF46	-	40	78.3	
		TV09	390	23	14.8	
		TV14	390	50	46.9	
		TV21	500	-21	20.2	
		TV13	500	0	52.1	

*Irradiated to 13 dpa.
**Normalized by Fracture Area.

a JSM-35C scanning electron microscope operating at 25KV and procedures were as previously described.[4]

7.2.4.3 Results

7.2.4.3.1 Hardness Measurements. Results of Rockwell C hardness measurements on irradiated specimens were as follows: Specimen TT16, 31.7 ± 0.8; TT30, 21.7 ± 0.3; TT69, 21.8 ± 0.4; TT12, 18.7 ± 1.4; TV09, 24.3 ± 0.1 and TV14, 25.3 ± 0.6. Unirradiated control measurements were: Specimen TT10, 22.9 ± 0.3 and AF48, 15.2 ± 1.0. These results are plotted as a function of irradiation temperature in Fig. 7.2.2. From Fig. 7.2.2, the following observations can be made. For HT-9 irradiated to 2.3 x 10^{22} n/cm^2, irradiation temperatures below 475°C produce an increase in hardness so that following irradiation at 400°C, the hardness increases from 22.9 to 31.7 R_C. Above 475°C, irradiation results in decreased hardness. For 9Cr-1Mo, irradiation to 2.3 x 10^{22} n/cm^2 results in an increase in hardness from 15.2 R_C to approximately 25 R_C but the hardness level is insensitive to irradiation temperature.

7.2.4.3.2 Fractography. General behavior - Charpy specimen fracture surfaces contained three distinct surface topologies. A relatively flat region adjacent to the notch which contained fine river pattern steps running in the direction of crack propagation was formed during fatigue precracking (and prior to irradiation). The edge of this region defined a sharp thumb nail crack about half way through the Charpy specimen. The remaining area consisted of surface which was created during the instrumented Charpy impact test. The center of this region was generally flat and rectangular in shape whereas the edges which were adjacent to the specimen surface were more steeply inclined. Therefore, the central region was in a stress state approaching plane strain whereas the edges which were steeply inclined failed under conditions approaching plane stress. The region of greatest interest in the Charpy specimen fracture surface is therefore the flat rectangular central region.

The topology of the flat central region was found to change as a function of test temperature and alloy. Fracture surfaces created at

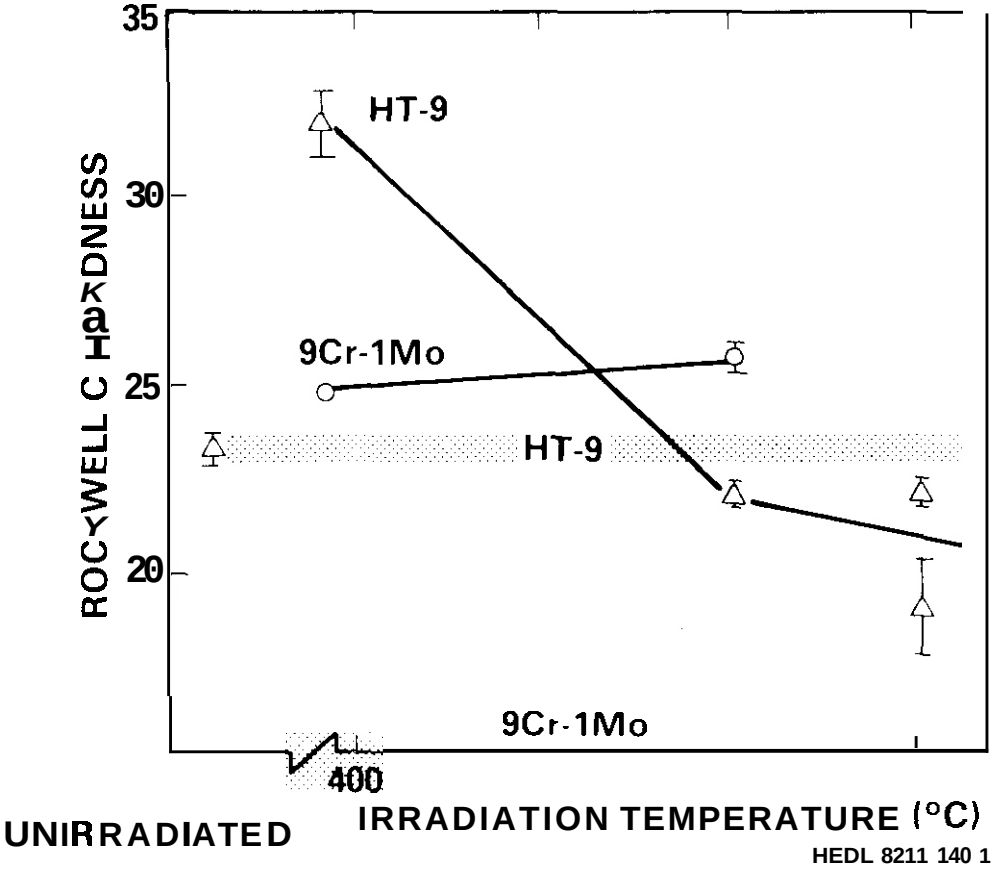

Fig. 7.2.2. Rockwell C Hardness Measurements as a Function of Irradiation Temperature for HT-9 and Modified 9Cr-1Mo Base Metal Charpy Specimens Contained in the ***AD-2*** Test.

lower temperatures which corresponded to lower shelf behavior contained features typical of brittle failure with relatively small steeply inclined shear lips at specimen surfaces. Fracture surfaces created at higher temperatures were less flat and more typical of ductile behavior with larger shear lips at specimen surfaces. Ductile HT-9 specimens displayed prominent linear structure due to delta ferrite stringers running across the specimen which were parallel to the initial crack front and to the rolling direction. 9Cr-1Mo specimens did not display such features. Intermediate temperature test conditions corresponding to the DBTT contained both brittle and ductile features. The brittle region was generally near the fatigue surface and the ductile region away from the fatigue surface. However, many specimens showed a narrow

ductile ridge immediately adjacent to the fatigue surface and often examples were found where ductile failure was observed adjacent to delta ferrite stringer features whereas adjacent regions were brittle.

7.2.4.4 Examples

7.2.4.4.1 HT-9 Unirradiated. The fracture surface topology as a function of test temperature can best be shown by comparison of unirradiated HT-9 specimens TTIO, TT31 and TT03. Specimen TTlO was tested at -58°C, gave a low fracture energy of 5 J/cm^2 and was found to be brittle in fracture appearance. No evidence of a stretch zone and ductile fracture were found adjacent to the fatigue crack but linear structure due to plasticity near delta ferrite stringers was found in about the final 25% of the fractured ligament. This fracture surface is shown in Fig. 7.2.3. A stereo pair at low magnification showing the thumb nail fatigue crack and the fracture surface created during the Charpy test is given in Part a and a higher magnification stereo pair showing both halves of a region adjacent to the fatigue surface is given in Part b. Part b has been arranged so that the viewer can envision in a stereogram the two halves of the specimen folded open along a central vertical line with the right hand side matching the left hand side. Of particular note is the plateau-like structure of the brittle fracture. Planar regions parallel to the fatigue surface, which have failed in a brittle manner, are separated by steeply inclined shear surfaces. Examination of such shear surfaces showed plastic deformation and abrasion as the two surfaces rubbed past one another. The plateau regions are 0.015 mm in diameter which corresponds very closely with the average prior austenite grain size for this material.' (ASTM grain size 8 to 9 corresponds to an average grain diameter of 0.022 to 0.016 mm.)

Specimen TT31 was tested at 0°C, gave a moderate fracture energy of 20 J/cm^2 and was found to have a fracture surface with both brittle and ductile regions typical of a test near the DBTT. This condition had both

(a) X20

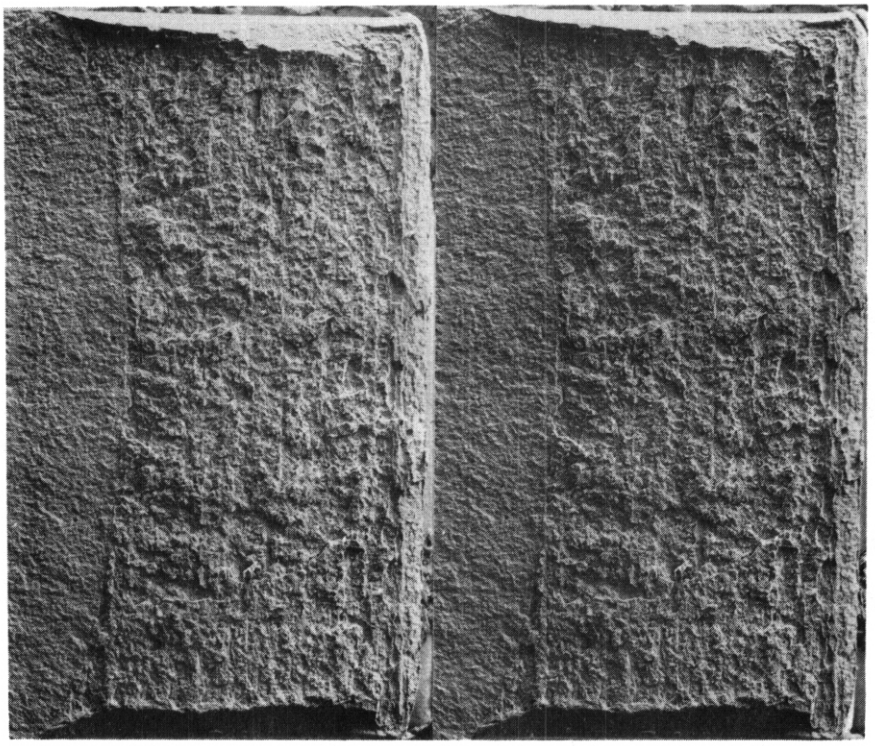

(b) X200

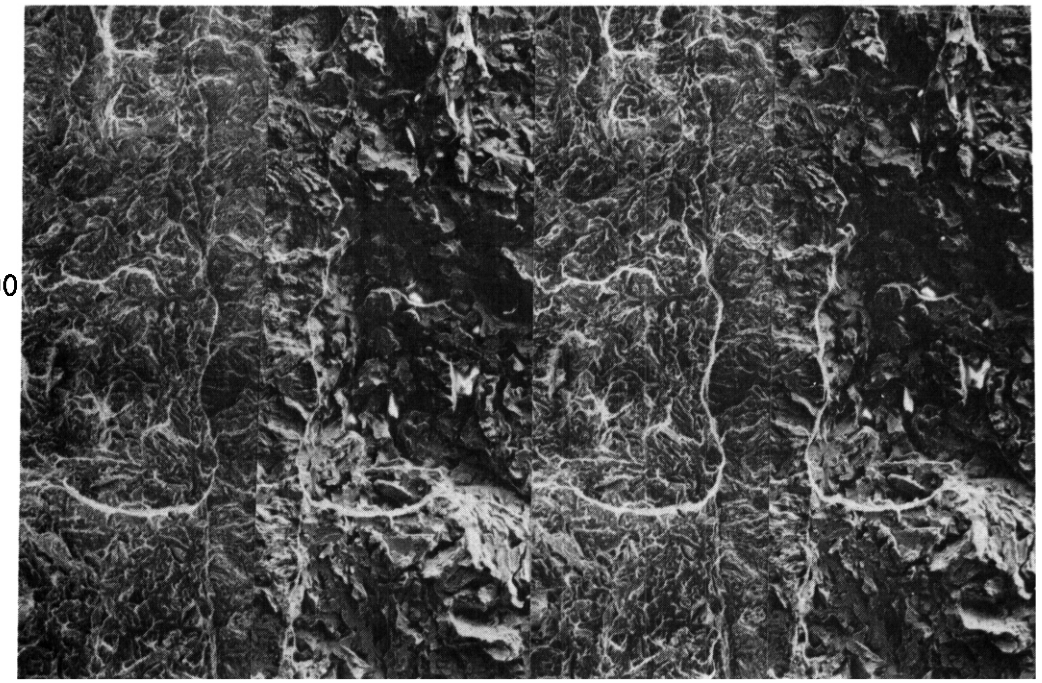

Fig. 7.2.3. Stereo Pair Fractograms of Unirradiated HT-9 Base Metal Specimen TT10 Which was Tested at -58°C.

a stretch zone and a narrow band of ductile fracture adjacent to the fatigue surface. However, beyond 0.0075 mm, crack propagation became brittle and remained brittle for about the first 25% of the fractured ligament. The next 20% of the fractured ligament failed by ductile fracture and showed linear features typical of failure in association with delta ferrite stringers. The next 15% of the fractured ligament failed by brittle fracture and the remaining ligament failed by ductile fracture. This fracture surface is shown in Fig. 7.2.4 with a low magnification stereo pair given in Part a and a higher magnification stereo pair of both halves of the fracture surface given in Part b. Comparisons between Fig. 7.2.3 and Fig. 7.2.4 reveal that the shear lips at specimen surfaces were larger in the more ductile case.

Specimen TT03 was tested at 73°C, gave a high fracture energy of 47 J/cm^2 and was found to have a ductile fracture surface. No evidence of brittle fracture was found whereas ductile failure in association with delta ferrite stringers was very prominent. This fracture topology is shown in Fig.7.2.5, as a low magnification stereo pair in Part a and as a higher magnification stereo pair with both halves of the fracture surface adjacent to the fatigue crack in Part b. Well defined ridges can be seen running parallel to the fatigue crack but the two halves of the fracture surface match up so that the trough in one surface corresponds to a ridge on the other surface. Therefore, the ridges are not so much due to growth of a large highly elongated cavities which separated by dimple rupture as they are to smaller highly elongated cavities which were linked by tearing. Compared to the less ductile condition of specimen TT31, specimen TT03 is much more corregated and rougher. Therefore, as ductility increases, crack nucleation occurs at delta ferrite stringers further removed from the plane of the fatigue crack and failure occurs when these crack nuclei link up.

7.2.4.4.2 HT-9 Base Metal. Fracture surfaces of HT-9 base metal specimens irradiated at 550°C to 13 dpa were found to be very similar to those of the unirradiated specimens. Examples of these fracture surfaces

(a) X20

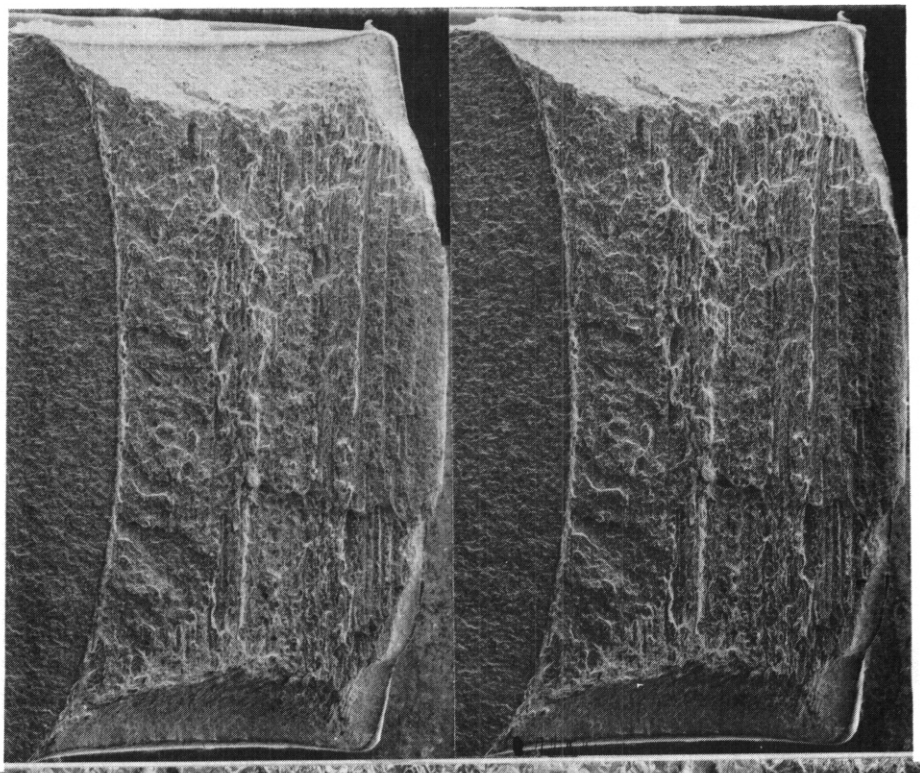

(b) x200

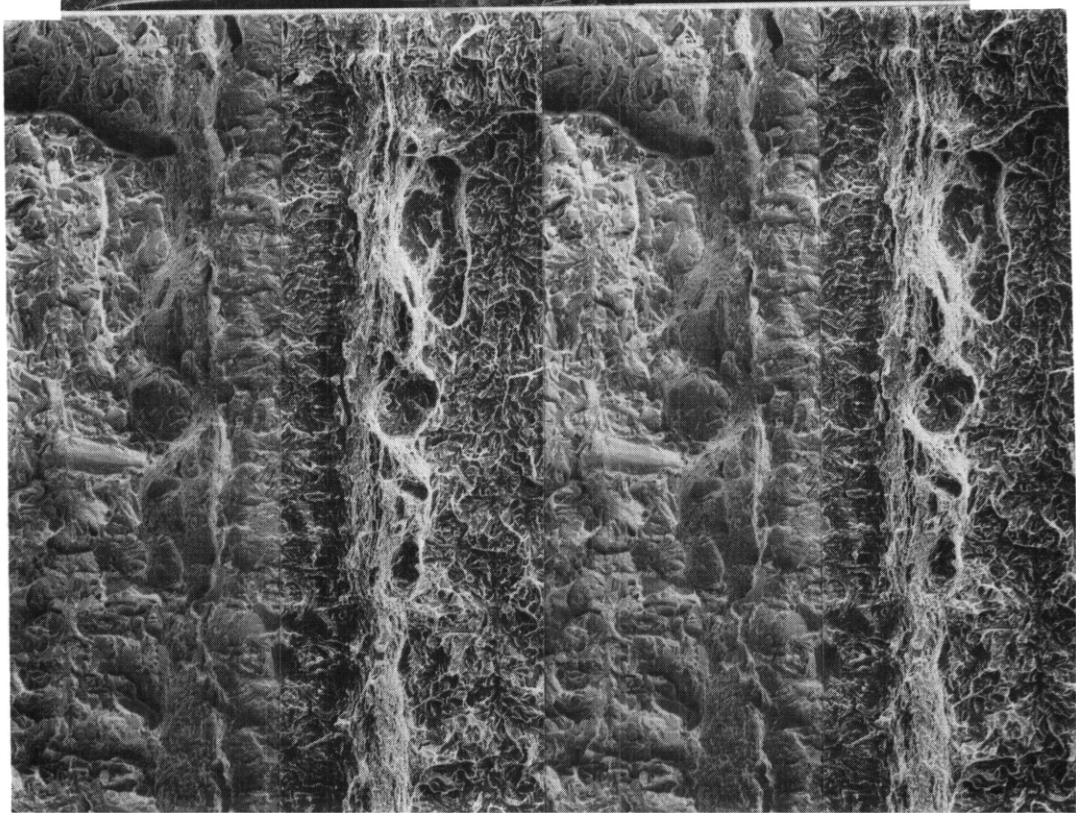

Fig. 7.2.4. Stereo Pair Fractograms of Unirradiated HT-9 Base Metal Specimen TT31 Which was Tested at 0°C.

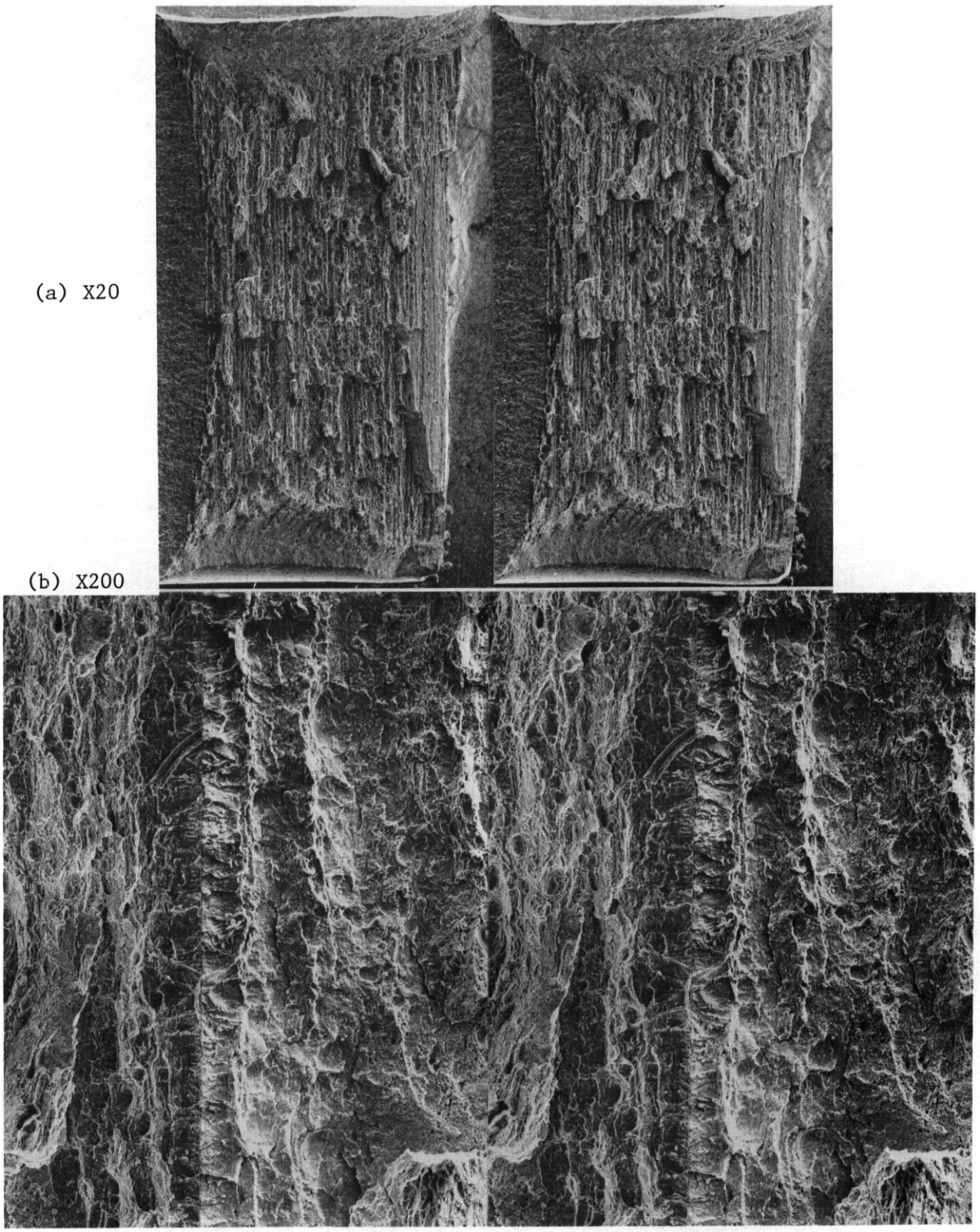

Fig. 7.2.5. Stereo Pair Fractograms of Unirradiated HT-9 Base Metal Specimen TT03 Which was Tested at 73°C.

are provided in Fig. 7.2.6 through Fig. 7.2.9. Fig. 7.2.6 shows low and high magnification fractographs arranged as stereo pairs for specimen TT69 which was tested at −20°C and had a fracture energy of 3.2 J/cm^2. Fig. 7.2.7 shows a similar sequence for specimen TT05 which was tested at 40°C and had a fracture energy of 11.4 J/cm^2. Fig. 7.2.8 provides a similar sequence for specimen TT12 which was tested at 100°C with a fracture energy of 19.5 J/cm^2 and Fig. 7.2.9 shows the sequence for specimen TT66 which was tested at 160°C and had a fracture energy of 25.2 J/cm^2 The major differences between the unirradiated conditions and these irradiated conditions that have been identified are the distributions of delta ferrite stringer features. The lower shelf behavior, as can be shown in Fig. 7.2.6, displays delta ferrite stringer effects very close to the fatigue crack. Fracture behavior in the vicinity of the DBTT as found in Figs. 7.2.7 and 7.2.8 is more uniform compared to Fig. 7.2.4; regions showing brittle fracture appearance also display delta ferrite stringer markings. It is therefore anticipated that the lower value obtained for USE due to irradiation at 550°C in HT-9 may be a consequence of reduced toughness in the vicinity of delta ferrite stringers.

The fracture surface of HT-9 base metal specimen TT30 irradiated at 500°C to 13 dpa and tested at 28°C was most similar to that for unirradiated HT-9 tested at the DBTT. A ridge of ductile fracture 0.05 mm wide developed immediately adjacent to the fatigue surface and then brittle failure occurred over the next 15% of the remaining ligament. The fracture mode transferred to ductile failure for the next 30% of the fracture surface, then back to brittle failure for another 15% and then the remaining ligament failed by ductile fracture. Delta ferrite stringers were generally not observed in brittle fracture areas. Fractographs for this condition are shown in Fig. 7.2.10.

In comparison with other HT-9 base metal specimens, the fracture surface of specimen TT16 irradiated at 390°C to 13 dpa and tested at 116°C was very different. The fracture surface again contained both ductile and brittle fracture in alternating bands and brittle failure produced plateau-like features. However, ductile fracture displayed few examples of linear structure associated with delta ferrite stringers and shear lips at specimen surfaces were wider but not as steep. Therefore, the

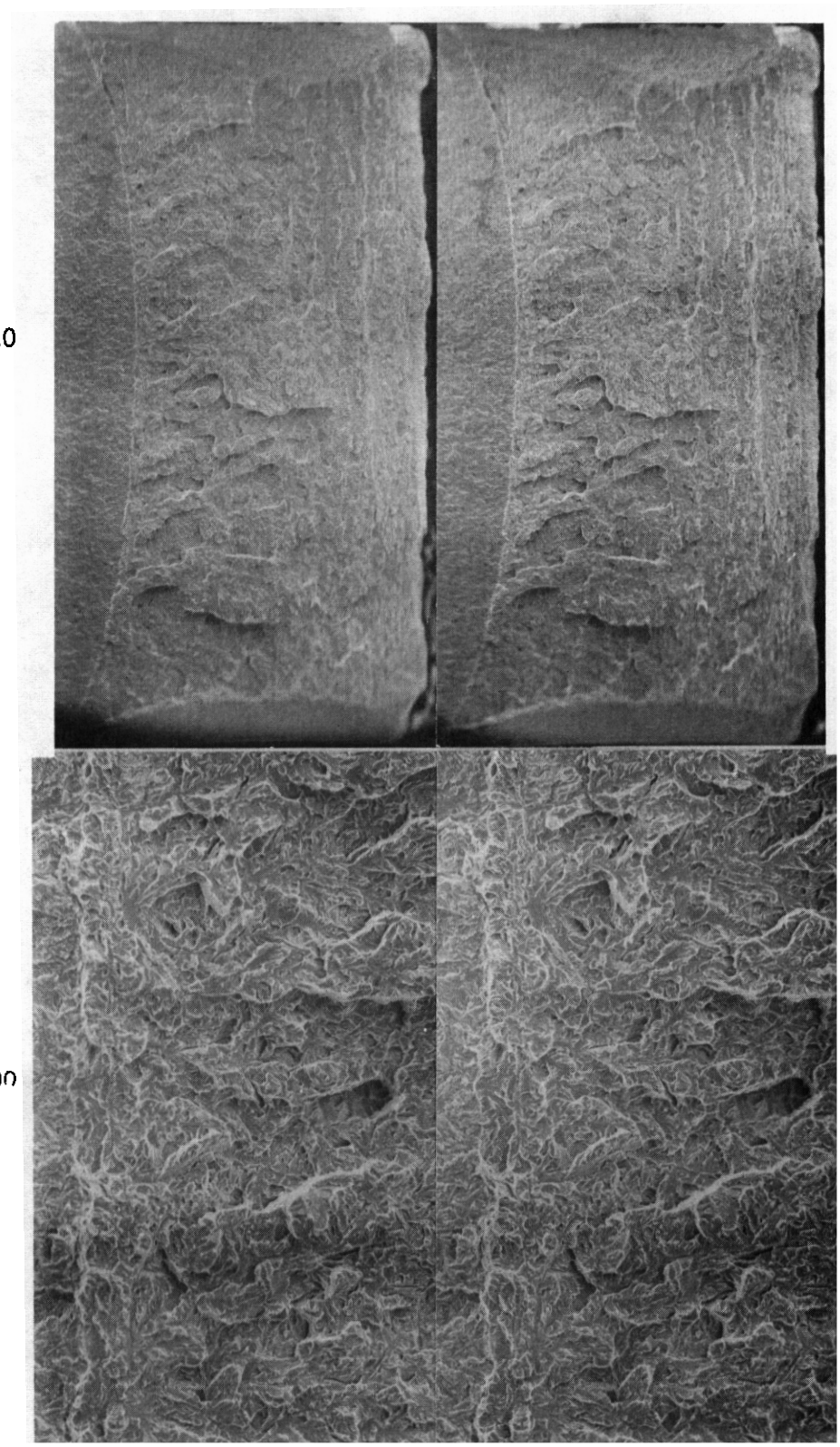

(a) X20

(b) X200

Fig. 7.2.6. Stereo Pair Fractograms of HT-9 Base Metal Specimen **TT69** Irradiated at 550°C and Tested at -20°C.

(a) X20

(b) X200

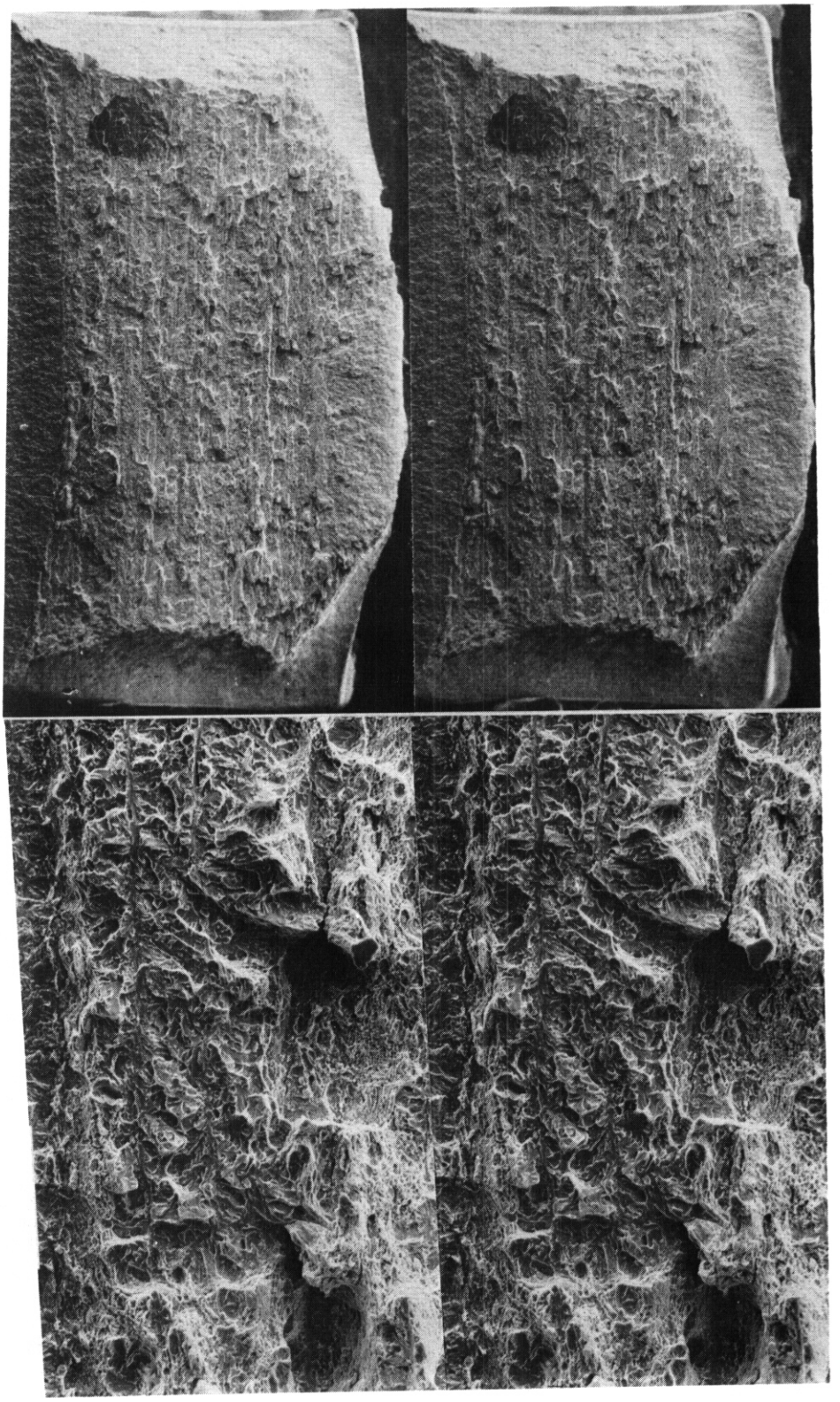

Fig. 7.2.7. Stereo Pair Fractograms of HT-9 Base Metal Specimen TT05 Irradiated at 550°C and Tested at *40°C*.

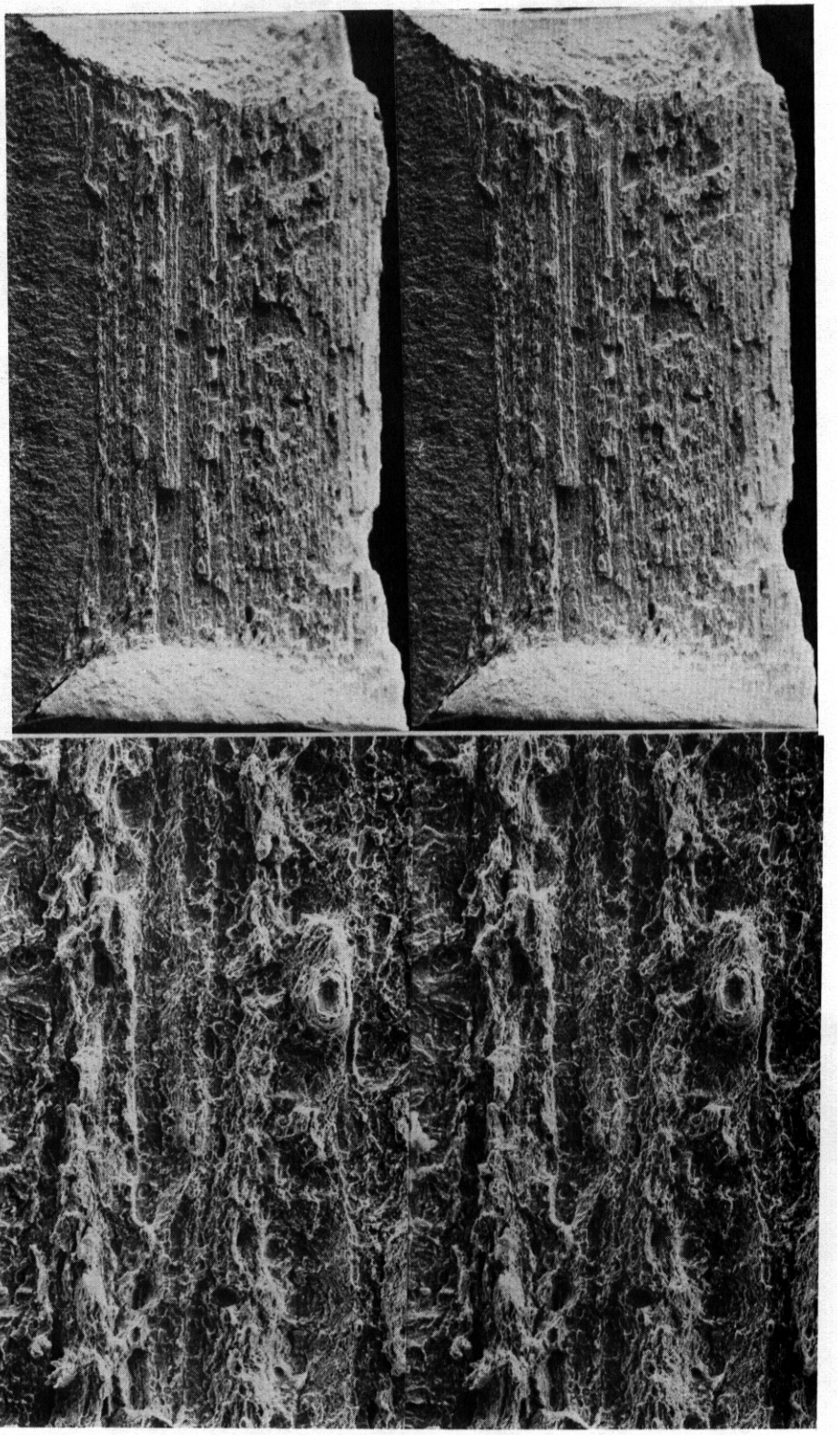

(a) X20

(b) X200

Fig. 7.2.8. Stereo Pair Fractograms of HT-9 Base Metal Specimen TT12 Irradiated at 550°C and Tested at 100°C.

(a) X20

(b) X200

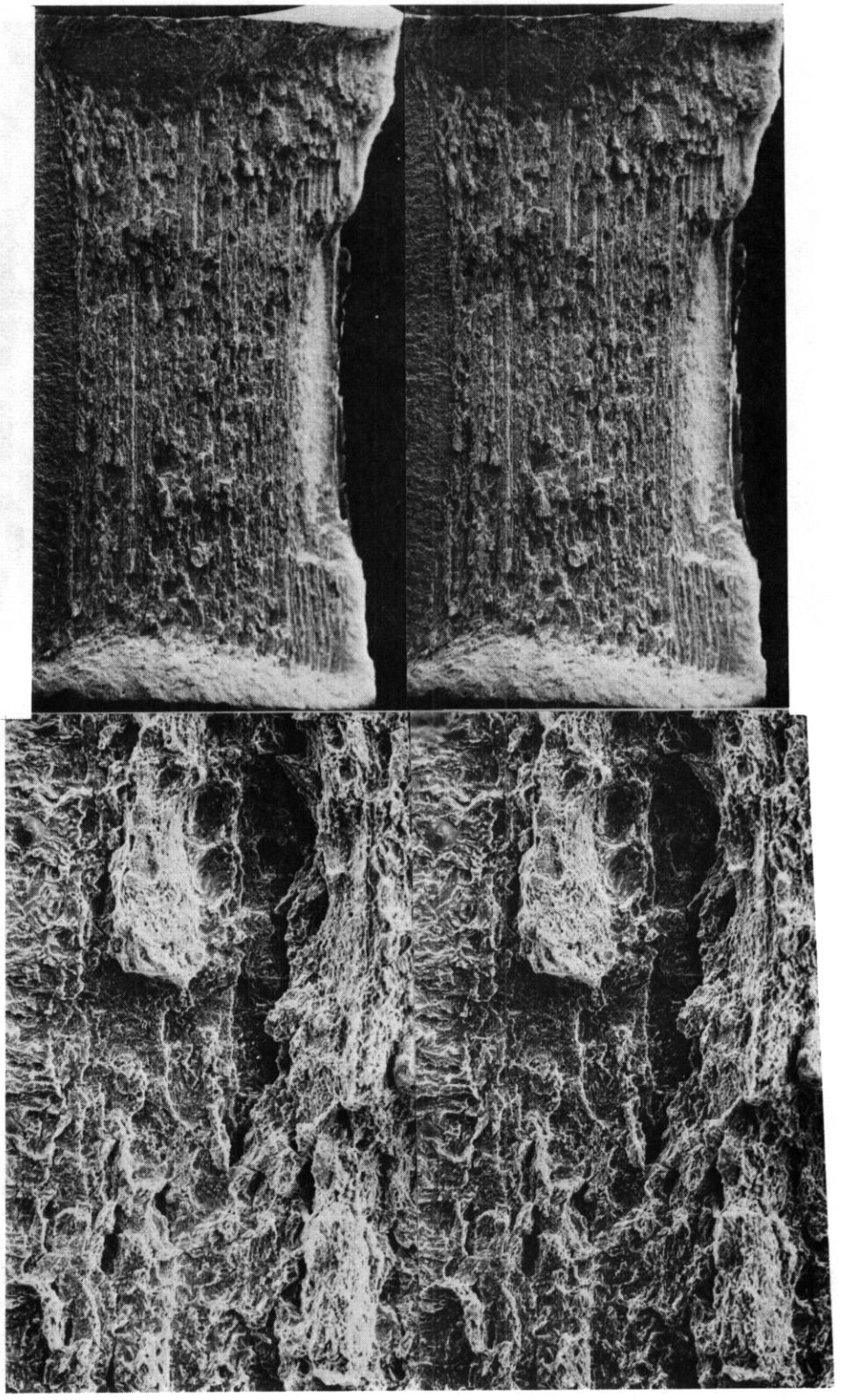

Fig. *7.2.9.* **Stereo Pair Fractograms of** HT-9 **Base Metal Specimen TT66 Irradiated at 550°C and Tested at 160°C.**

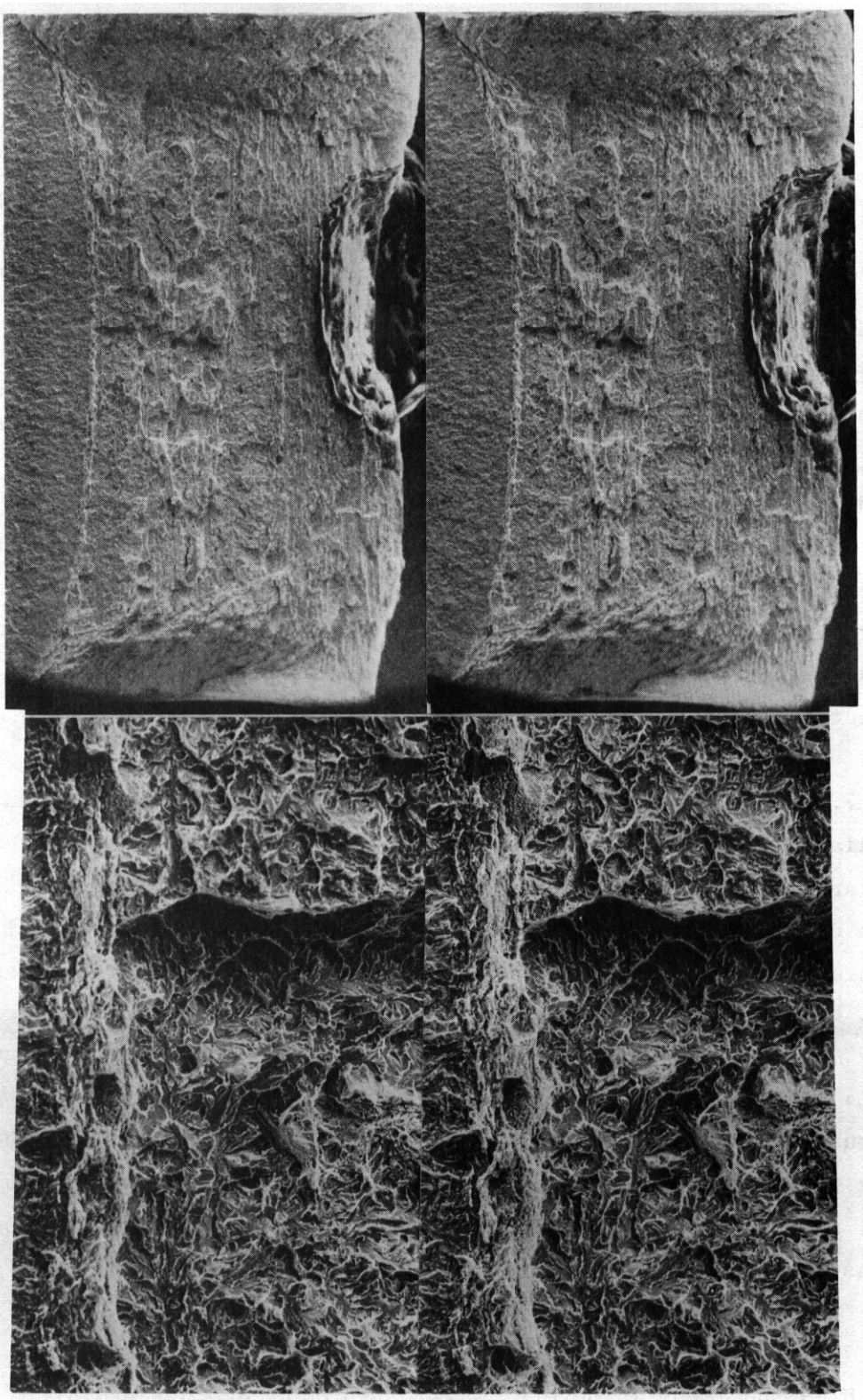

Fig. 7.2.10. Stereo Pair Fractograms of HT-9 Base Metal Specimen TT30 Irradiated at 500°C and Tested at 28°C.

fracture surface appeared to be flatter. This fracture surface is shown in Fig. 7.2.11. Apparently, increased hardness due to irradiation has resulted in reduced likelihood of cavitation at delta ferrite stringers.

7.2.4.4.3 HT-9 Weld Metal. Weld metal specimens which had been irradiated and tested at the DBTT developed fracture surfaces which were very similar to fracture surfaces found in base metal specimens irradiated at the same temperature and tested at the DBTT. For example, the fracture surface of specimen TI34 which was irradiated at 550°C and tested at 50°C is shown in Fig. 7.2.12. This may be compared with specimen TT05 in Fig. 7.2.7. Also, the fracture surface of specimen TI27 which was irradiated at 390°C and tested at 132°C is shown in Fig. 7.2.13. It is very similar to that of specimen TT16 shown in Fig. 7.2.11. The major differences are found in regions which failed by brittle fracture. The distribution of steeply inclined shear surfaces separating planar regions are distributed on a coarser scale indicative of the fact that the "effective prior austentie grain size" was coarser.

7.2.4.4.4 HT-9 Heat-Affected-Zone. HAZ specimens which had been irradiated and then tested at the DBTT developed fracture surfaces similar to those observed in base metal unirradiated specimens. Regions which had failed by brittle fracture did not show evidence of delta ferrite stringers. Also, the fracture surface of specimen TXll irradiated at 390°C did not show the reduced relief found in other specimens irradiated at 390°C. Examples of these specimen conditions are shown in Figs. 7.2.14 and 7.2.15. Specimen TX04 irradiated at 550°C and tested at 0°C is found to have developed a narrower ductile band adjacent to the fatigue crack than has specimen TXll irradiated at 390°C and tested at 85°C. However, in neither case is the delta ferrite stringer banding as corregated as was observed in unirradiated HT-9 as seen in specimen TT31 (Fig. 7.2.4).

7.2.4.4.5 9Cr-1Mo Unirradiated. Modified 9Cr-1Mo specimens differed from HT-9 specimens in several ways. Specimens did not exhibit a corregated fracture appearance. This is because delta ferrite is not present in this alloy and therefore delta ferrite stringers do not influence fracture

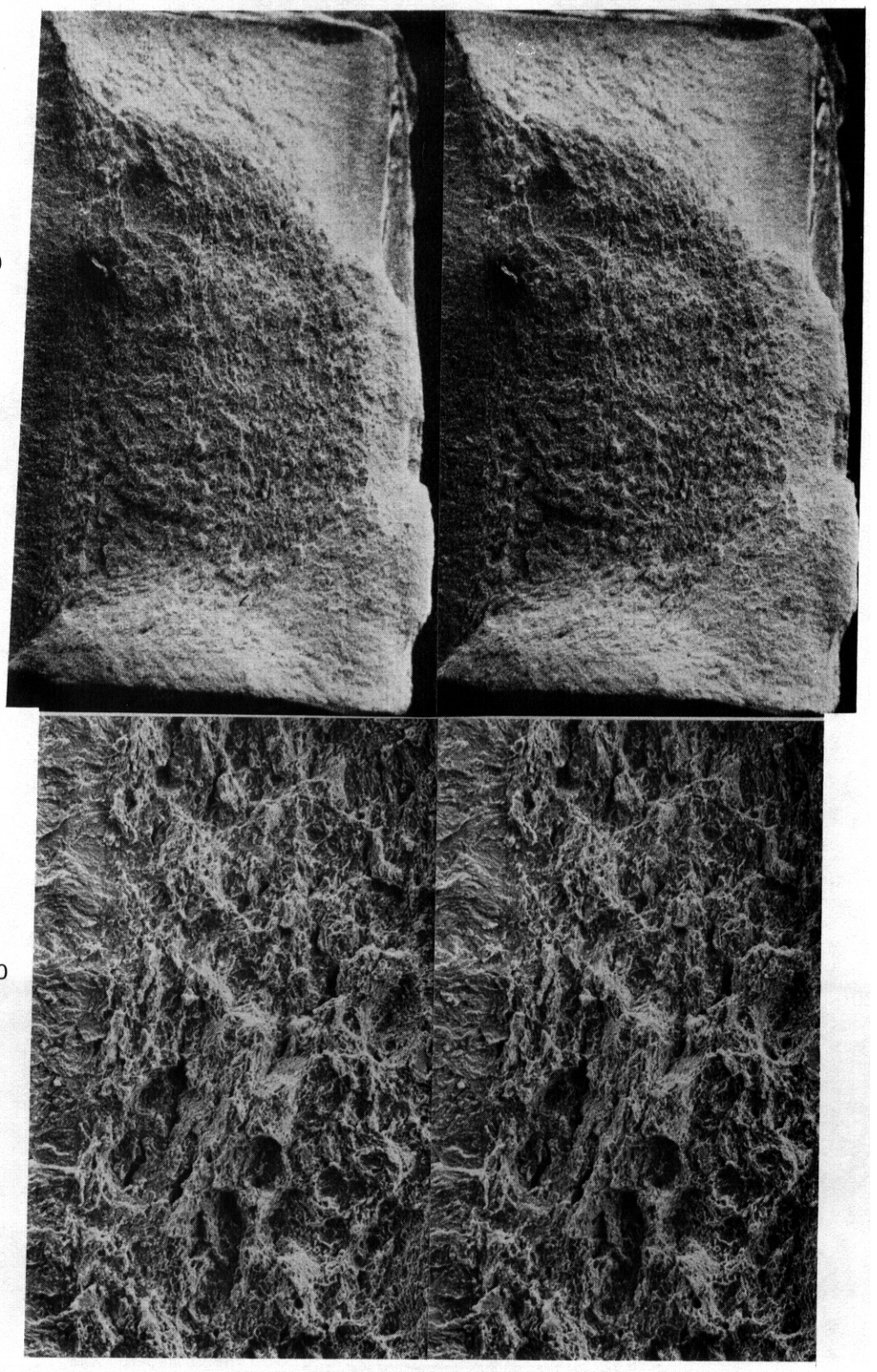

Fig. 7.2.11. Stereo Pair Fractograms of HT-9 Base Metal Specimen TT16 Irradiated at 390°C and Tested at 116°C.

(a) X20

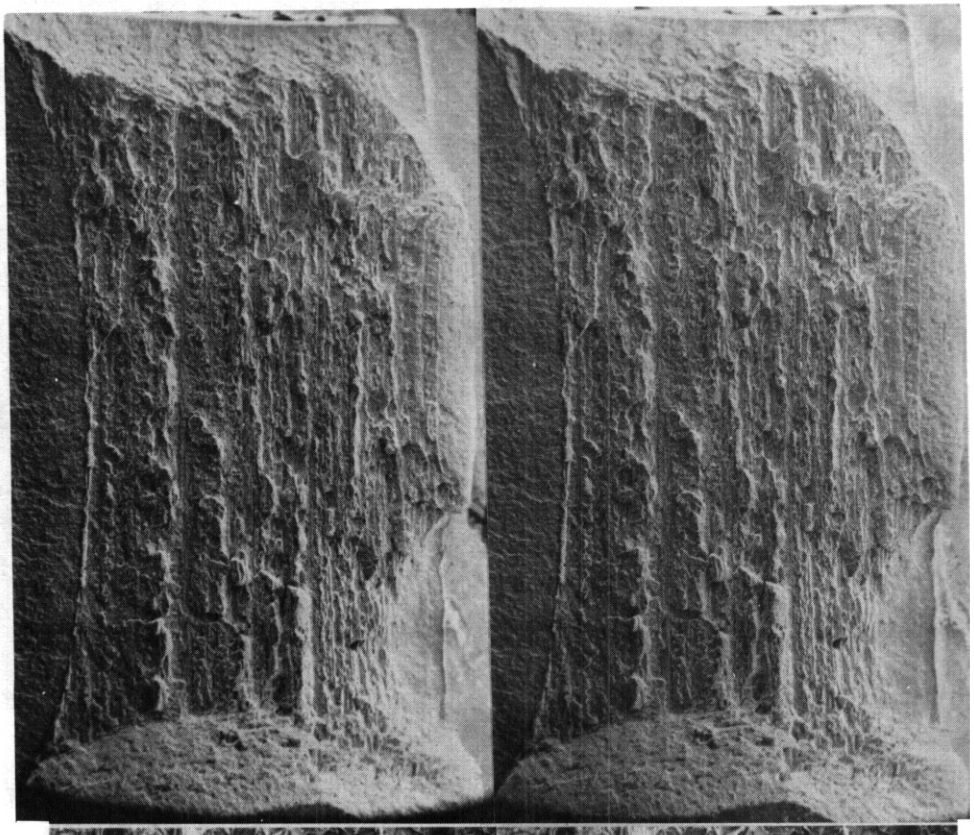

(b) X200

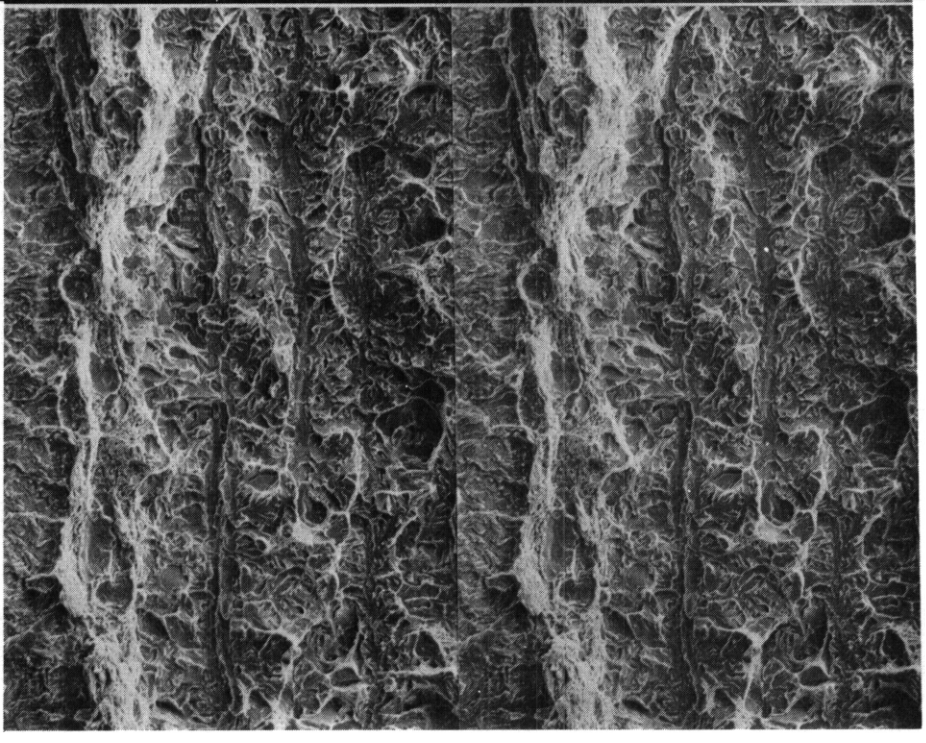

Fig. 7.2.12. **Stereo Pair Fractograms of HT-9 Weld Metal Specimen TI34 Irradiated at 550°C and Tested at** 50°C.

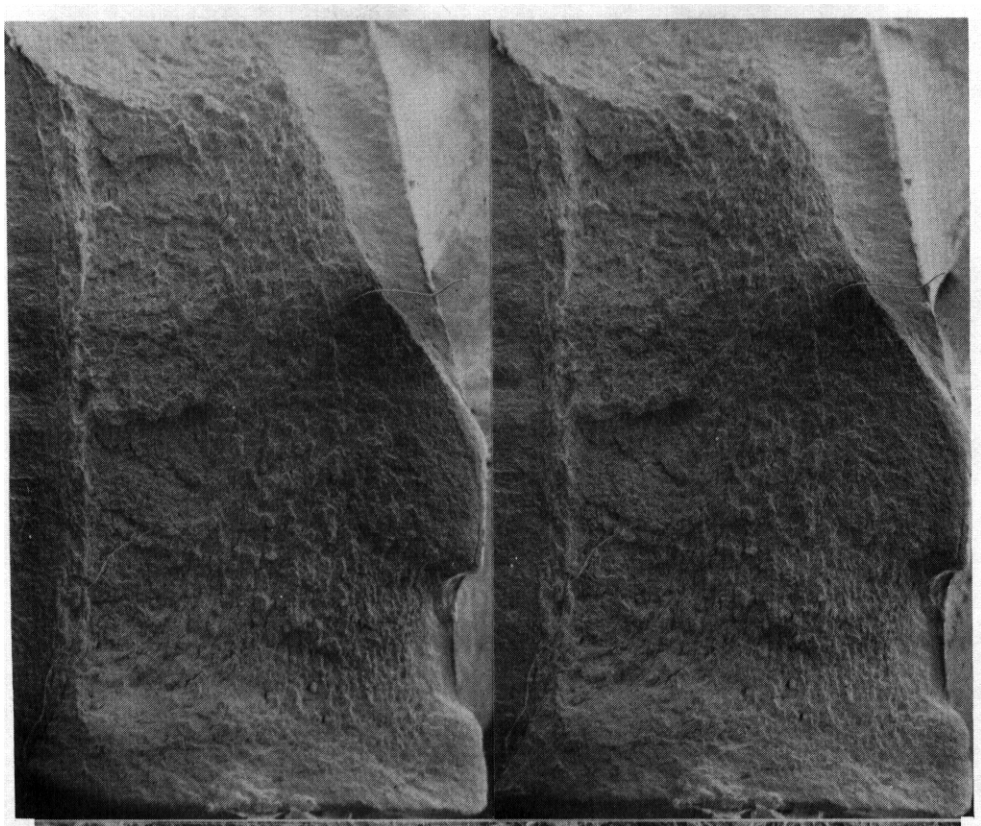

(a) X20

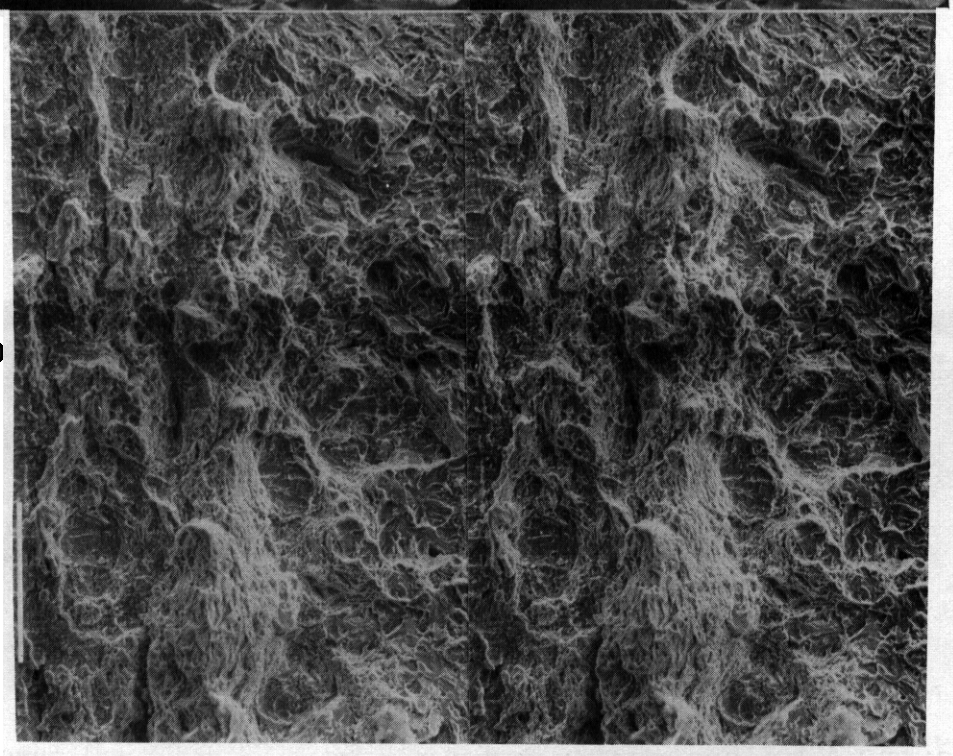

(b) X200

Fig. 7.2.13. Stereo Pair Fractograms of HT-9 Weld Metal Specimen TI27 Irradiated at 390°C and Tested at 132°C.

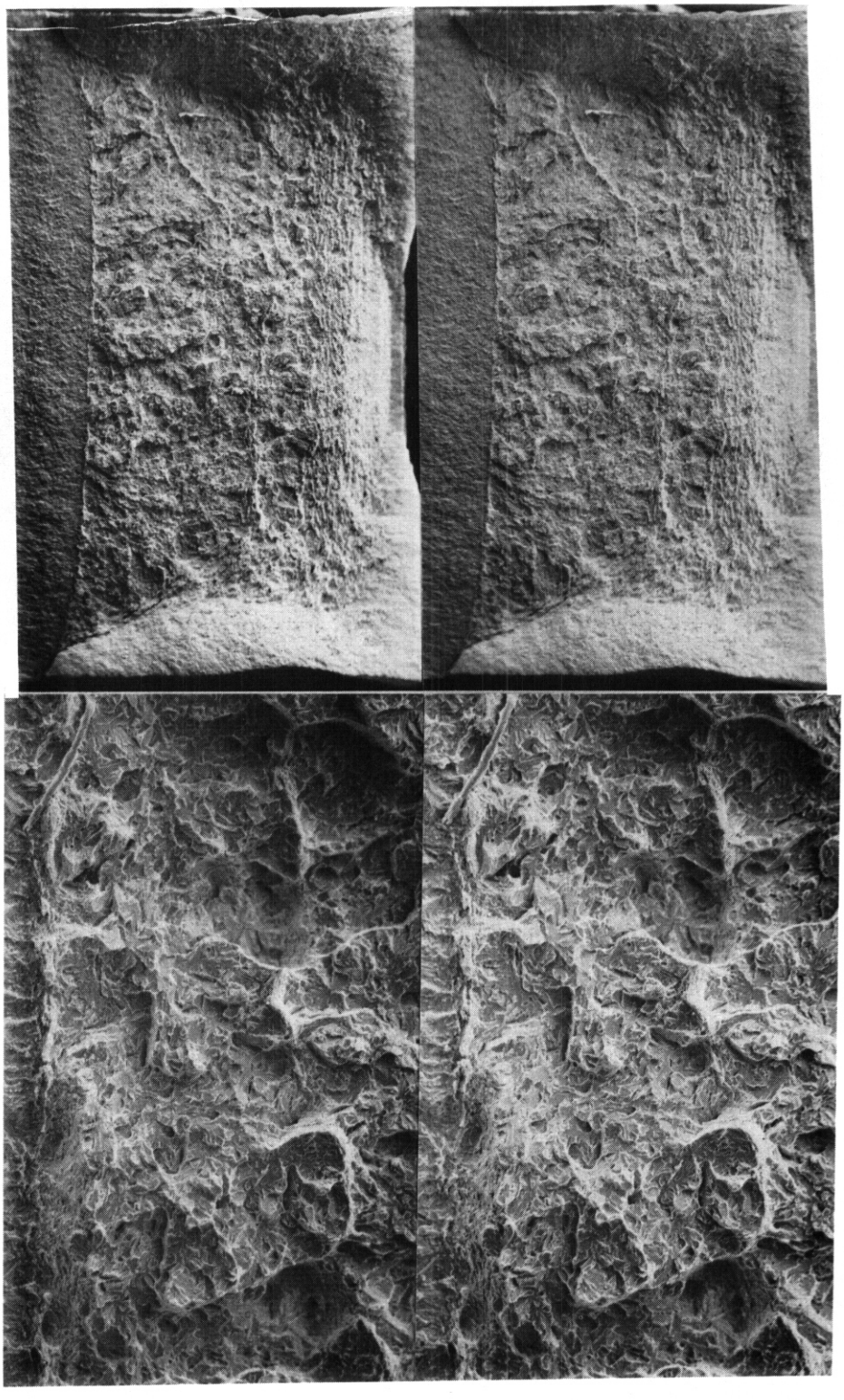

(a) x20

(b) X200

Fig. 7.2.14. **Stereo Pair Fractograms** of HT-9 HAZ Metal **Specimen** TX04 Irradiated at 550°C and Tested at 0°C.

(a) X20

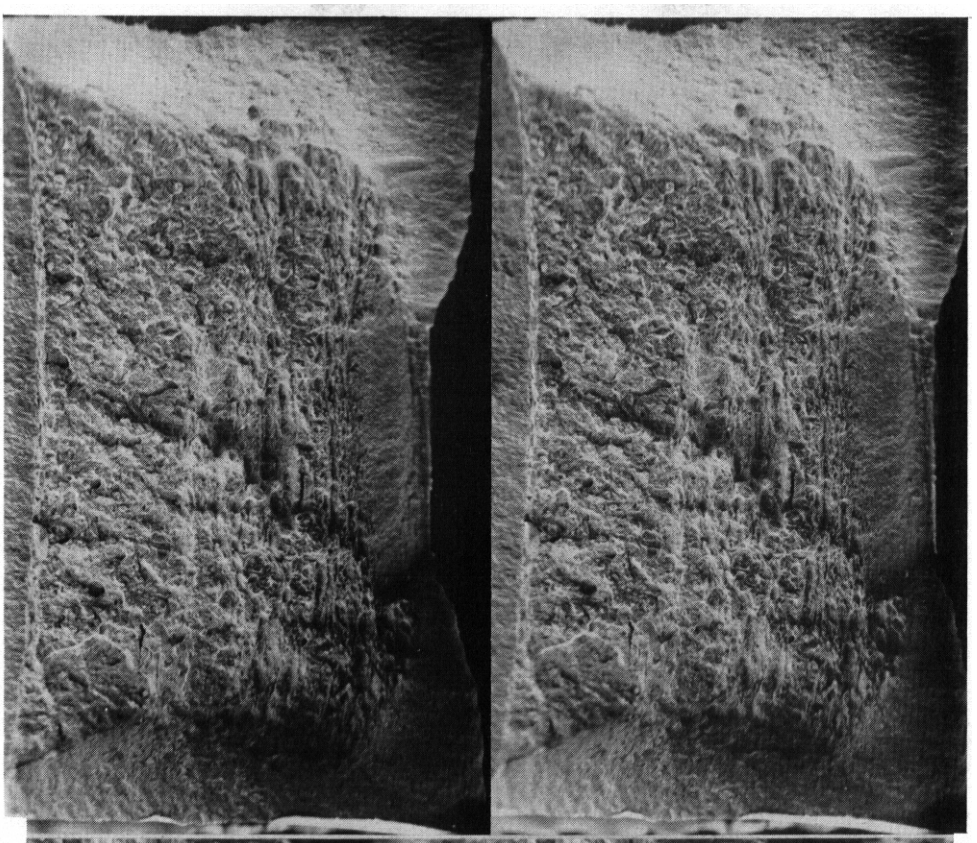

(b) x200

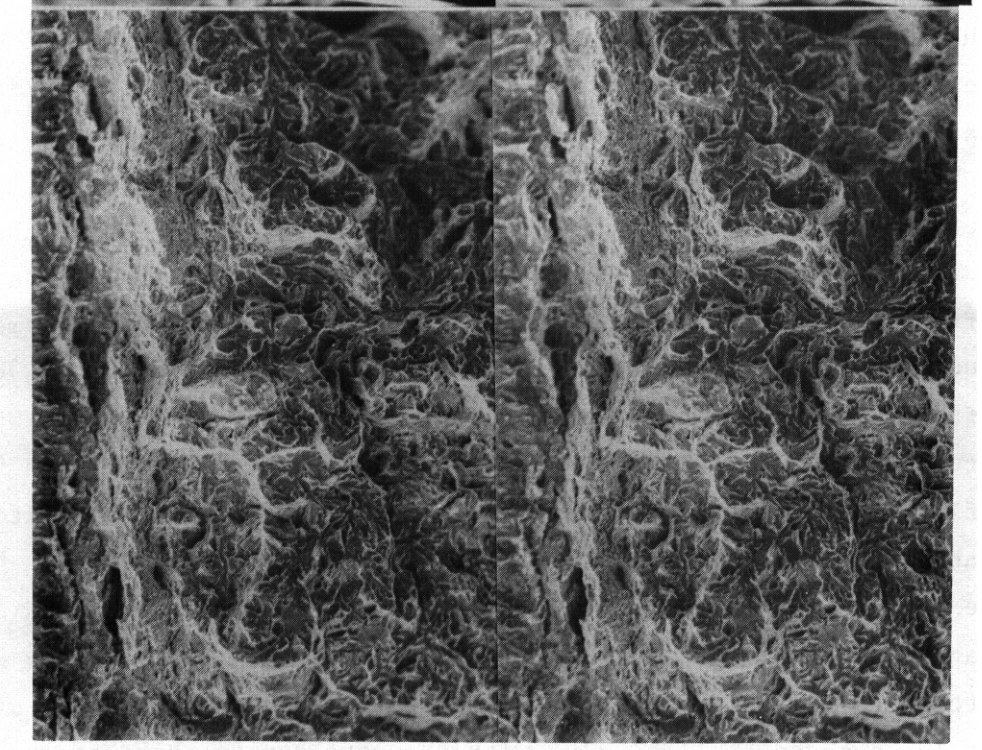

Fig. 7.2.15. **Stereo Pair Fractograms of** HT-9 HAZ **Metal Specimen** TX11 **Irradiated at** 390°C **and Tested at** 85°C.

surface topology. Also, dimples were often larger and more equiaxed indicating that cavitation occurs on a coarser scale. However, regions which failed by brittle cleavage were very similar to those in HT-9. Examples of the fracture appearance in unirradiated 9Cr-1Mo are shown in Figs. 7.2.16, 7.2.17 and 7.2.18. Fig. 7.2.16 shows specimen AF38 which was tested at -80°C and gave a low fracture energy of 3.1 J/cm^2. Specimen AF41 which was tested at -10°C and gave a fracture energy of 61.1 J/cm^2 is shown in Fig. 7.2.17. Fig. 7.2.18 provides micrographs of specimen AF46 which was tested at 40°C and gave the highest fracture energy of all specimens examined, 78.3 J/cm^2.

Brittle failure in unirradiated 9Cr-1Mo can be seen in Fig. 7.2.16. As with the unirradiated HT-9 specimen conditions, both a low magnification and a higher magnification stereo pair are given, the higher magnification series providing comparison of both halves of the fracture surface. The fracture surface is plateau-like with nearly parallel cleavage facets defining a series of surfaces which are connected by steeply inclined boundaries. Again, the size of the plateaus corresponds to that of the prior austenite grain size, 0.02 mm. No evidence of a ductile stretch zone was found immediately adjacent to the fatigue surface. Shear lips at specimen surfaces are very small.

Fig. 7.2.17 is particularly unusual because the region of the fracture surface which shows brittle fracture is not immediately adjacent to the fatigue crack. Instead, the first 40% of the fractured ligament failed by ductile fracture. Brittle fracture then occurred over about 30% of the fracture ligament and finally the remaining ligament failed by ductile fracture. Fig. 7.2.18 provides an example of ductile failure in 9Cr-1Mo, typified by large cavities separated by a series of smaller cavities. In many cases, the cavities are not circular but instead appear "C" shaped. This is a consequence of the fact that cavitation ahead of the propagating crack is sufficiently infrequent that a given cavity will be stretched to the point where it becomes part of the propagating crack front (as opposed to linking up with the next cavity ahead of the propagating crack).

(a) X20

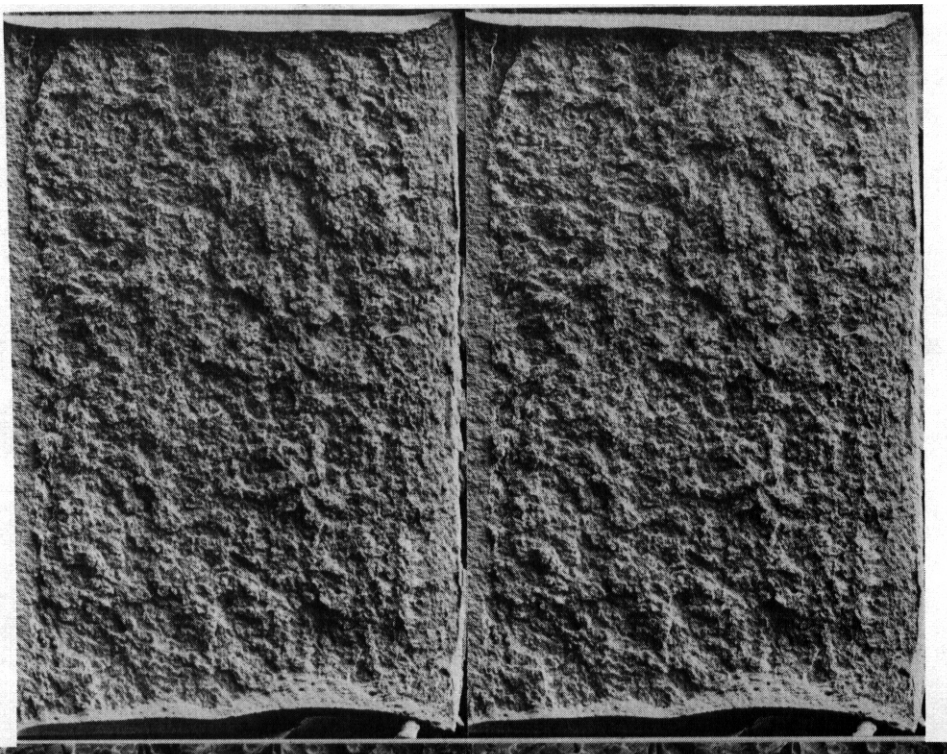

(b) X200

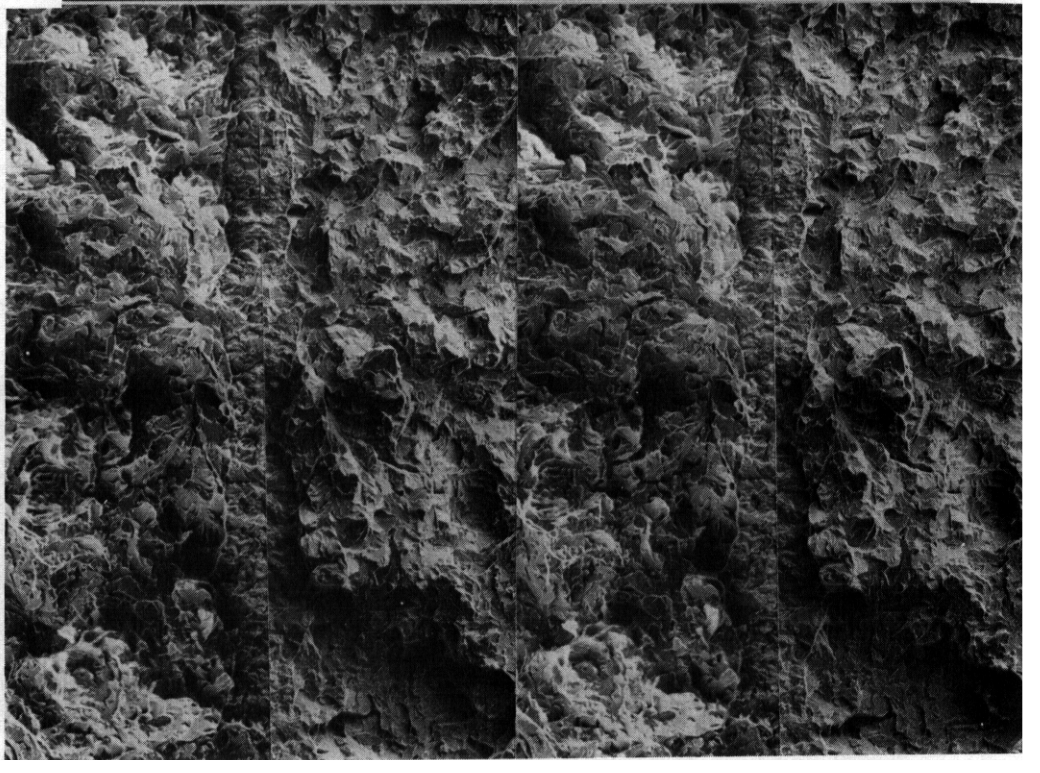

Fig. 7.2.16. Stereo Pair Fractograms of Unirradiated Modified 9Cr-1Mo Base Metal Specimen AF38 Tested at -80°C.

(a) X20

(b) X200

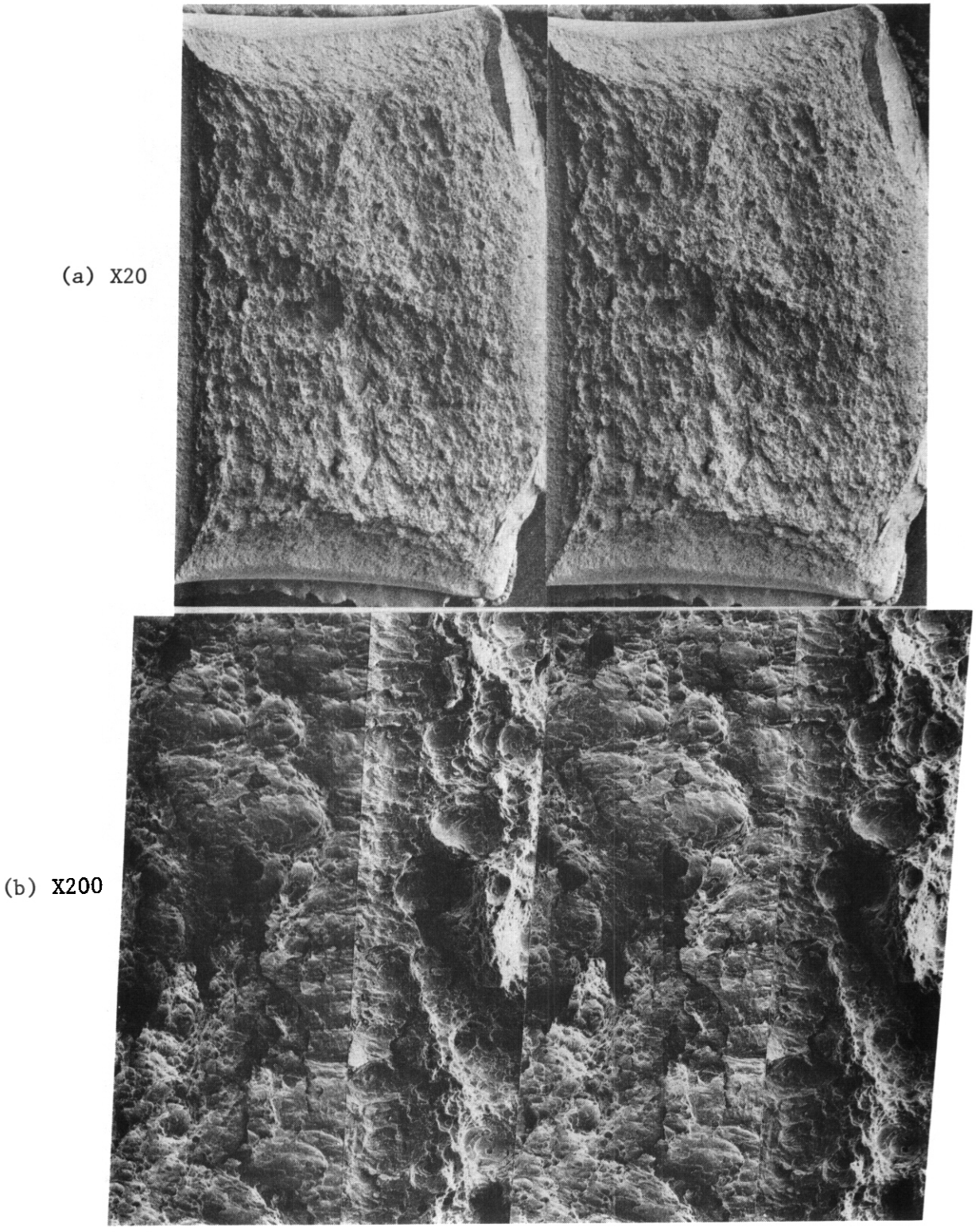

Fig. 7.2.17. Stereo Pair Fractograms of Unirradiated Modified 9Cr-1Mo Base Metal Specimen AF41 Tested at -10°C.

(a) X20

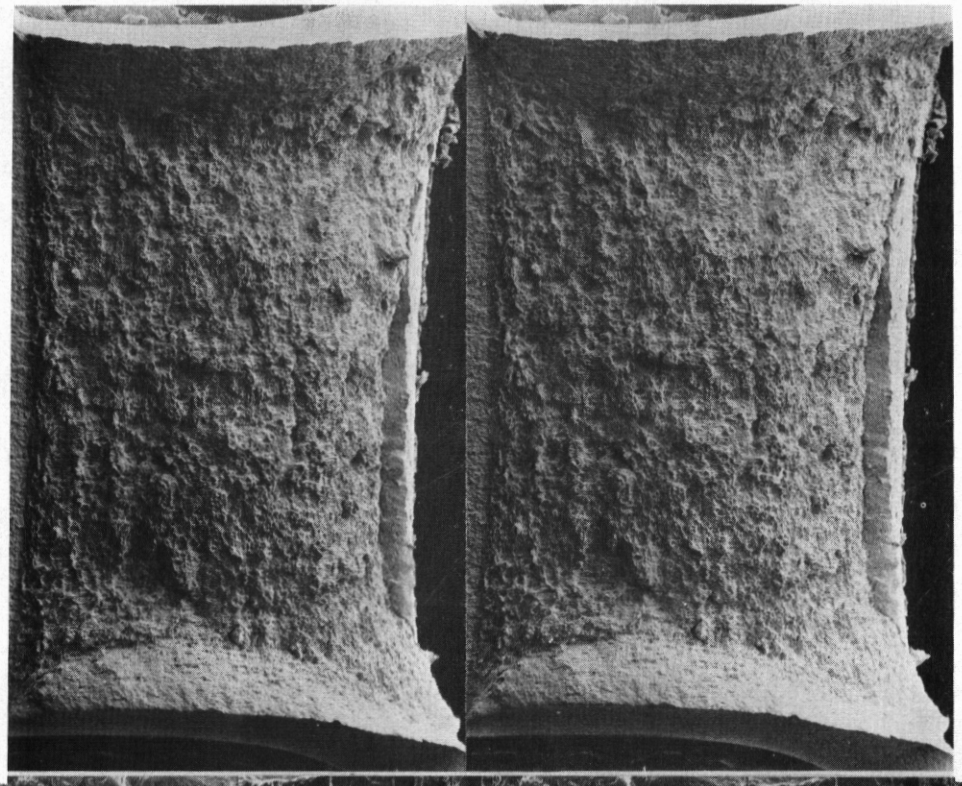

(b) X200

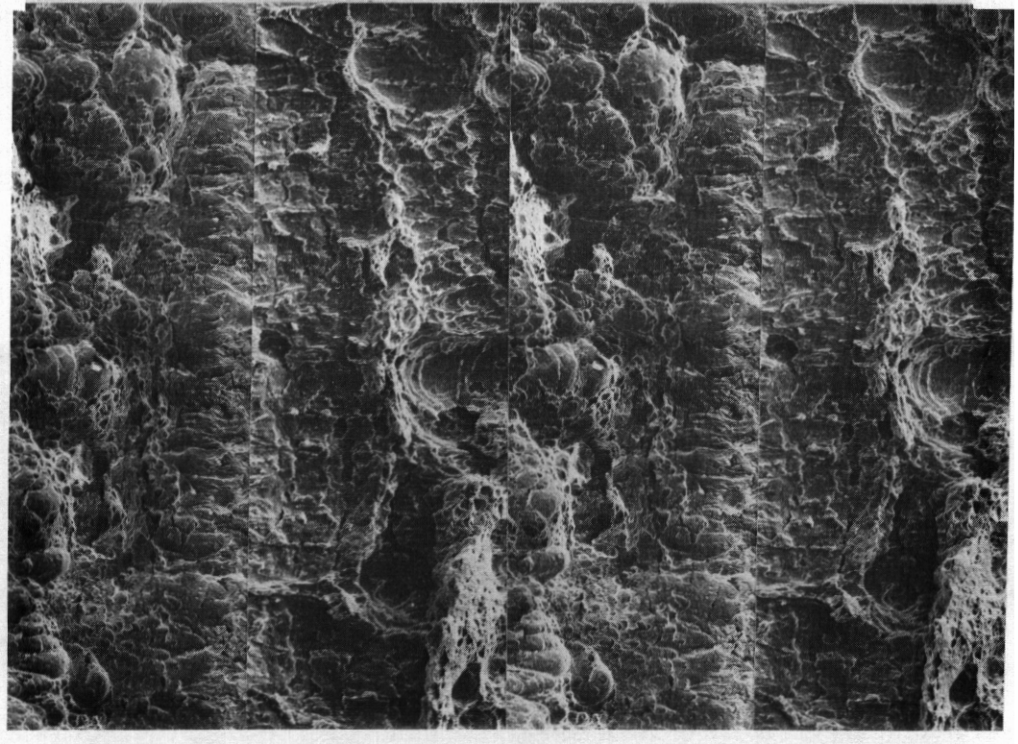

Fig. 7.2.18. Stereo pair fractograms of unirradiated Modified 9Cr-1Mo Base Metal Specimen AF46 Tested at *40°C.*

7.2.4.4.6 9Cr-1Mo Base Metal. Fracture surfaces of 9Cr-1Mo base metal specimens irradiated both at 390°C and at 550°C were found to be very similar in fracture appearance to those of unirradiated specimens. Brittle cleavage produced cleavage facets which were indistinguishable from those produced in unirradiated specimens. However, ductile failure of irradiated specimens resulted in several larger dimples and greater surface undulations in comparison with unirradiated specimens. Examples of these fracture surfaces are given in Fig. 7.2.19 through Fig. 7.2.22. Fig. 7.2.19 shows specimen TV21 irradiated at 500°C, and tested at -21°C (near the DBTT). This specimen had a fracture energy of 20.2 J/cm^2. Approximately 50% of the fractured ligament failed by brittle fracture and evidence of a narrow plastic stretch zone can be seen immediately adjacent to the fatigue crack. Of particular note is the observation that the cleavage plane of the grain which cleaved near the fatigue surface is considerably below the plane of the fatigue surface. Parallax measurements demonstrate a difference of 0.11 mm and therefore failure has occurred a remarkable distance from the region of maximum stress.

Fig. 7.2.20 gives fractographs for specimen TV13 irradiated at 500°C and tested at 0°C with a fracture energy of 52.1 J/cm^2. Large dimples, on the order of 0.10 mm in diameter can be observed but most of the fracture surface is covered with dimples on the order of 0.01 mm. In comparison, unirradiated specimen AF46 as shown in Fig. 7.2.18 had a fine dimple size on the order of 0.01 mm but a coarse dimple size of about 0.05 mm and a flatter fracture surface. Therefore, irradiation at 500°C has created features which produce cavitation at lower strain but these features do not significantly reduce toughness.

Fig. 7.2.21 provides fractographs for specimen TV09 which was irradiated at 390°C, was tested at 25°C and had a fracture energy of 14.8 J/cm^2. Stretch zone formation can be seen immediately adjacent to the fatigue crack but after approximately 0.05 mm crack propagation becomes brittle and remains brittle over 60% of the fractured ligament. Thereafter, ductile fracture is similar to that of the unirradiated conditions.

Fig. 7.2.22 shows fractographs for specimen TV14 which was irradiated at 390°C, tested at 50°C and required a fracture energy of 46.9 J/cm^2. The fracture surface contains large dimples similar in size to the

(a) X20

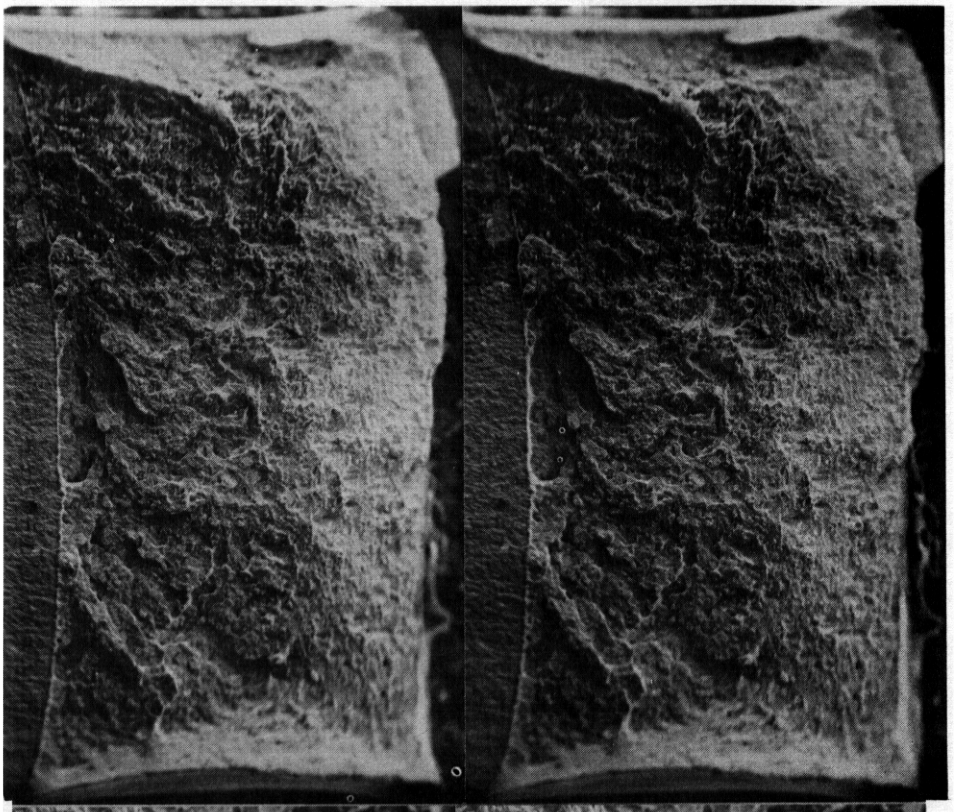

(b) X200

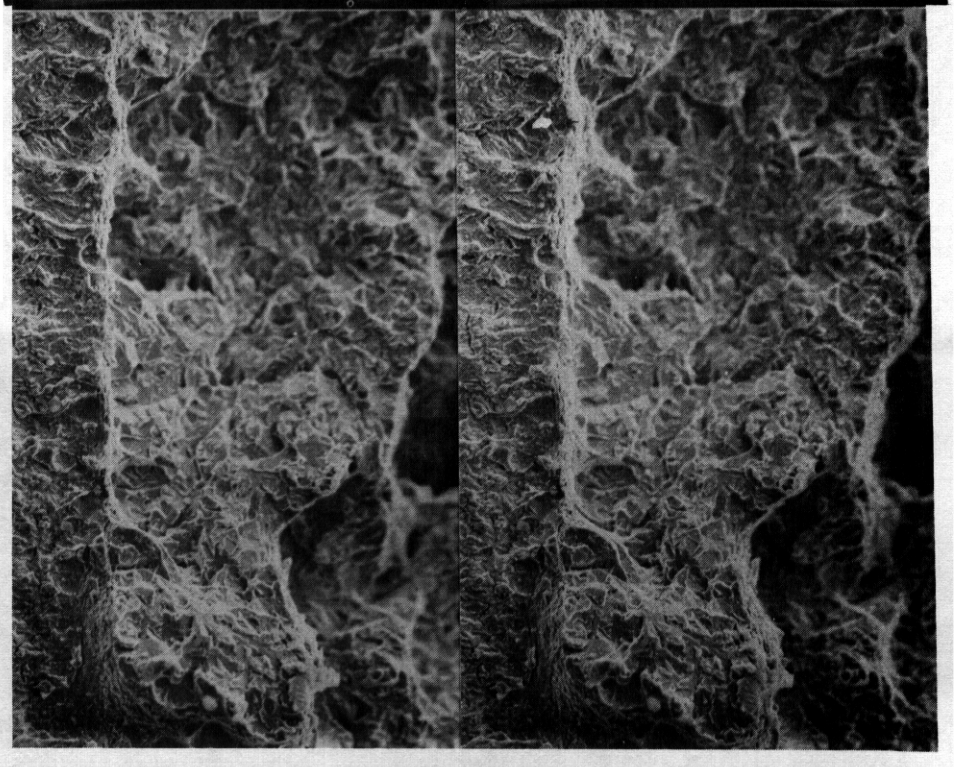

Fig. 7.2.19. Stereo Pair Fractograms of Modified 9Cr-1Mo Base Metal Specimen TV21 Irradiated at 500°C and Tested at −21°C.

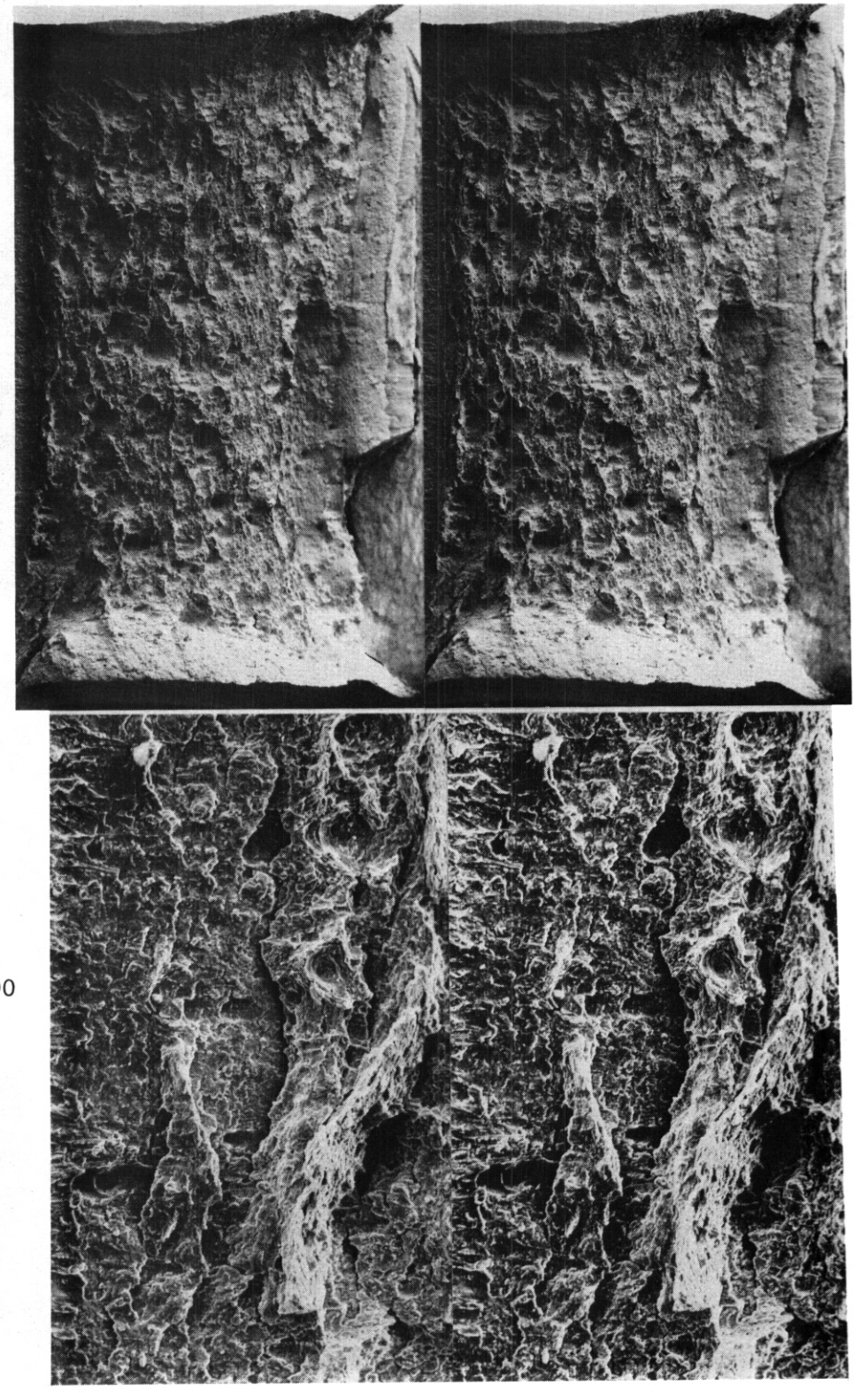

(a) X20

(b) X200

Fig. 7.2.20. Stereo Pair Fractograms of Modified 9Cr-1Mo Base Metal Specimen TV13 Irradiated at 500°C and Tested at 0°C.

(a) X20

(b) X200

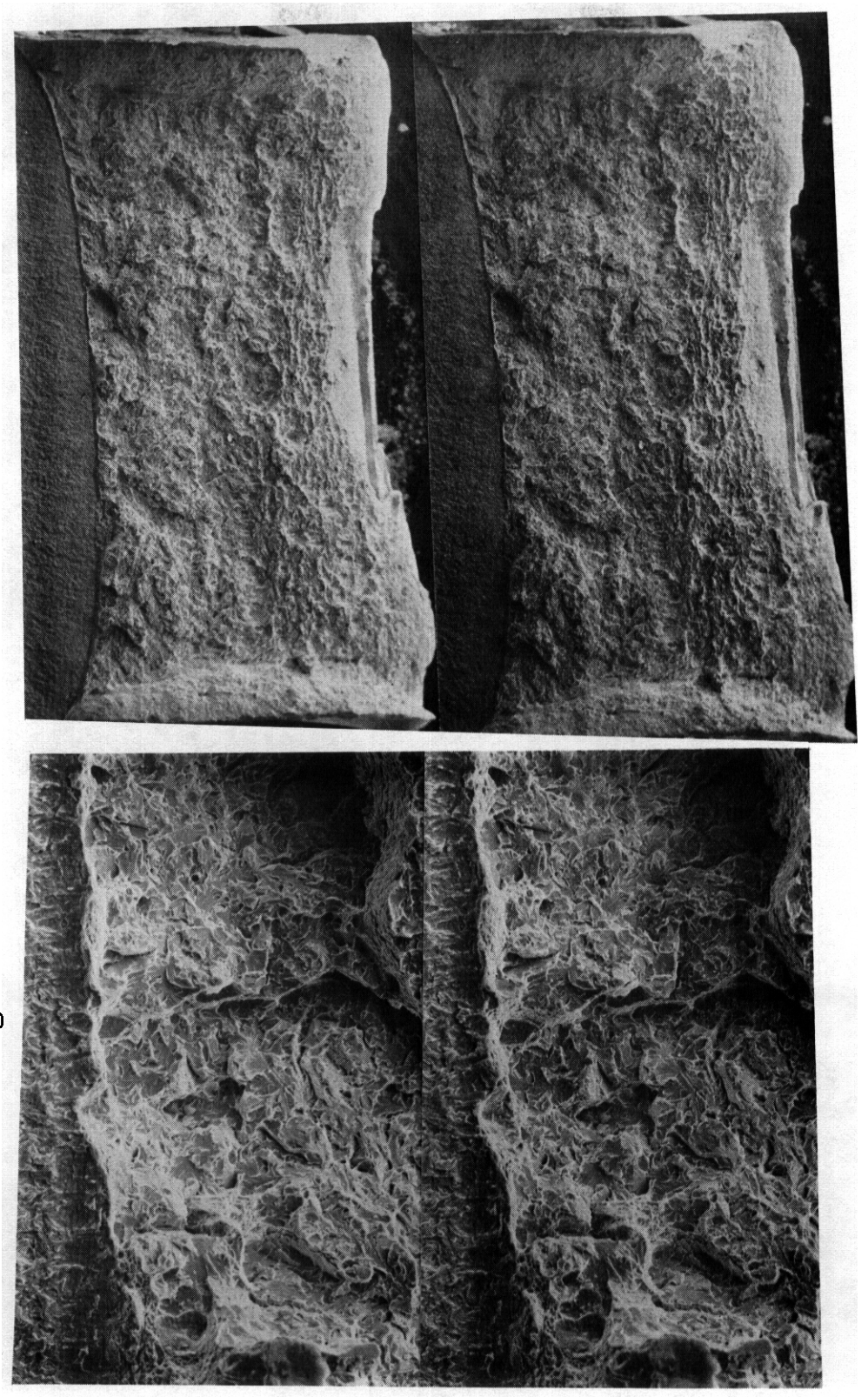

Fig. 7.2.21. Stereo Pair Fractograms of Modified 9Cr-1Mo Base Metal Specimen TV09 Irradiated at 390°C and Tested at 25°C.

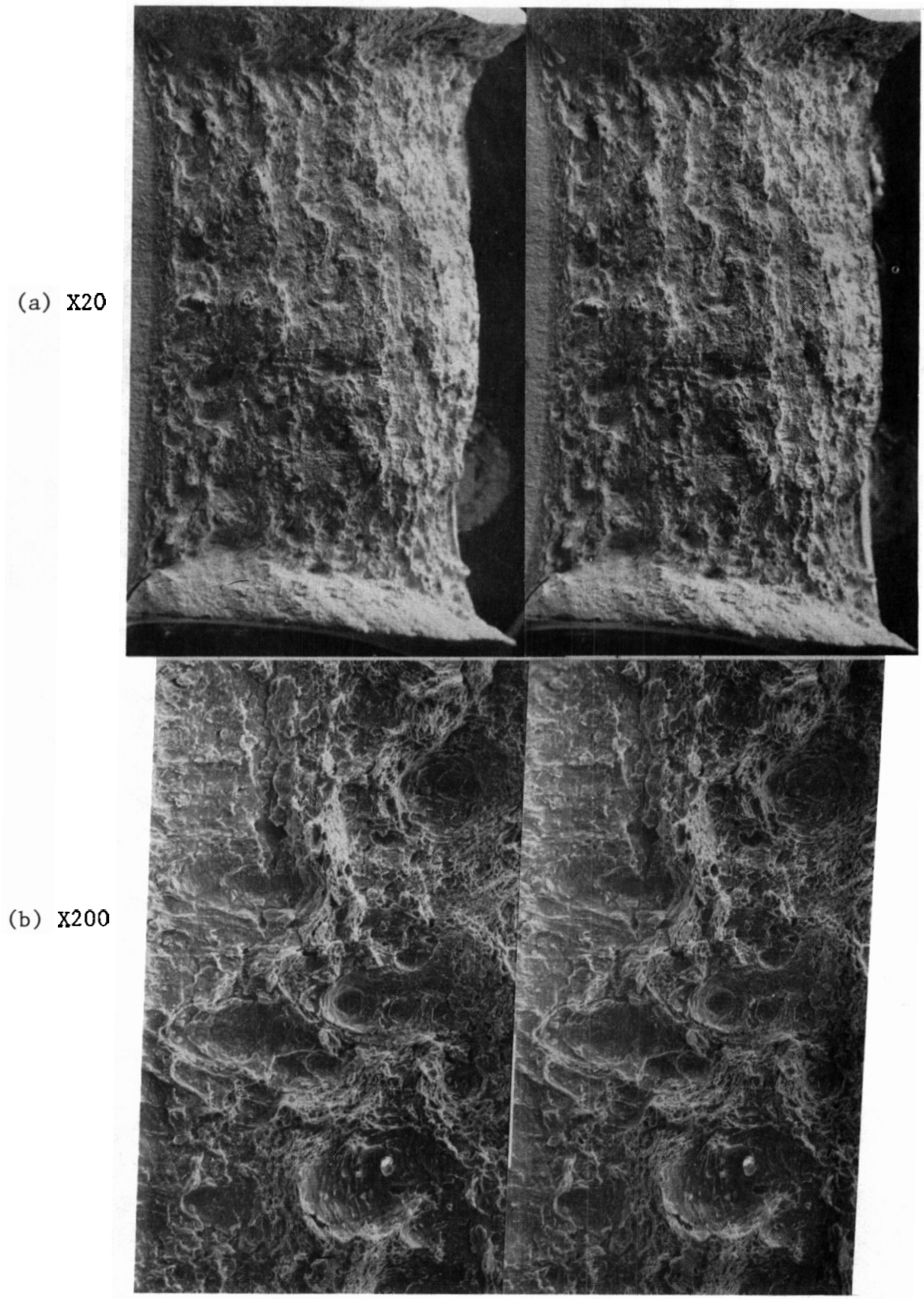

Fig. 7.2.22. Stereo Pair Fractograms of Modified 9Cr-1Mo Base Metal Specimen TV14 Irradiated at 390°C and Tested at 50°C.

unirradiated condition *AF46* (shown in Fig. *7.2.18)* but the scale of surface undulations is more like the 500°C irradiation condition TV13 (shown in Fig. *7.2.20).*

7.2.4.5 Discussion

The present effort has provided several experimental findings which provide insight into the fracture behavior of Path E alloys. The purpose of this discussion will therefore be to interpret these findings.

7.2.4.5.1 Mechanisms Controlling Fracture Toughness - HT-9. The present results for HT-9 have clearly demonstrated: 1) that hardening as measured by hardness occurs as a consequence of irradiation at 390°C but for irradiation temperatures of *500°C* and above, softening results and *2)* delta ferrite stringers have a significant effect on the fracture appearance of ductile failure. Therefore any attempts to explain degradation in fracture toughness, DBTT shift or USE reduction as a consequence of irradiation must take into account these phenomena. Irradiation hardening in HT-9 is a result both of dislocation loop evolution and 6-phase formation.[3] The fractographic observation that no change in brittle fracture appearance apart from delta ferrite stringer effects is found as a function of irradiation condition indicates that irradiation hardening (as opposed to formation of a brittle phase during irradiation) is the main cause of DBTT shifts. Furthermore, as will be shown by comparison with 9Cr-1Mo behavior, the shift in DBTT following irradiation at 390°C is directly attributable to G-phase formation. However, this explanation can only apply for specimens irradiated at 390°C.

Concurrent with a shift in DBTT, reduction of the USE is observed following irradiation. The most prominent fractographic change which occurs as a result of irradiation is with regard to delta ferrite stringer effects. Irradiation appears to increase the tendency for cavitation at delta ferrite stringers ahead of the propagating crack. This is evidenced both by the observation that delta ferrite stringer effects appear on brittle fracture surfaces following irradiation at 550°C and by the more uniform distribution of delta ferrite stringer features at temperatures near the DBTT following irradiation at 550°C. The hypothesis

is therefore suggested that observed USE reductions are a result of effects of irradiation on or near delta ferrite stringers; the most likely cause is enhanced carbide precipitation[3] on delta ferrite stringer surfaces which can be expected to cause carbide cracking at lower levels of stress. It may be noted that such a mechanism would provide an explanation for the observed DBTT shift following irradiation at 450°C and above: the lower shelf has not been altered but the upper shelf reduction has caused an apparent shift in DBTT when DBTT is defined at any fracture energy above the lower shelf.

Approaches for fracture toughness improvements in HT-9 can be suggested based on the above discussion. In order to reduce DBTT shifts due to irradiation at 390°C, G-phase forming elements such as nickel and/or silicon should be reduced or eliminated. In order to reduce USE degradation due to irradiation, improvements in tempering procedure could be developed, intended to increase carbide precipitation prior to irradiation and reduce carbide precipitation in-reactor.

7.2.4.5.2 Mechanisms Controlling Fracture Toughness - 9Cr-1Mo. Results on 9Cr-1Mo indicate that somewhat different mechanisms control behavior than in the case of HT-9. Experiments demonstrate that hardening occurs at all temperatures in-reactor (as indicated by hardness measurements) but hardening is not a strong function of irradiation temperature. No evidence of a phenomenon comparable to failure at delta ferrite stringers was found and only a small shift in DBTT was measured following irradiation at temperatures of *450°C* and above whereas a somewhat larger shift was found following irradiation at 390°C.

Comparison of microstructural[3] and fractographic differences between HT-9 and 9Cr-1Mo indicate that the strong temperature dependence of hardness as a function of irradiation temperature in HT-9 is due to G-phase precipitation. The microstructures were found to be similar following irradiation at 400°C except that HT-9 contained G-phase and 9Cr-1Mo contained voids. Therefore, the large difference in DBTT shift between the two alloys must be attributed to G-phase. However, a shift was found in 9Cr-1Mo as a function of irradiation temperature, but no significant difference in hardness was found. The most likely explanation

for such response is that the irradiation induced dislocation structure is responsible. At the high strain rates of a Charpy test, irradiation induced dislocations could have caused sufficient hardening to cause a shift in the DBTT whereas at the lower strain rates of a hardness test, the hardening could be overcome, resulting in negligible hardness increase.

Irradiation does apparently cause hardening in 9Cr-1Mo at all irradiation temperatures. The most likely explanation is that precipitation of (V,Nb)C and $M_{23}C_6$ occurs in-reactor[3] and is because incomplete precipitation was achieved during tempering. The consequences of this precipitation apparently have negligible effect on DBTT but do lower the USE for all irradiation conditions.

No straightforward approaches for fracture toughness improvement appear promising for Modified 9Cr-1Mo. This is in large part because Modified 9Cr-1Mo has been optimized for fracture toughness. Significant degradation is only observed as a result of irradiation at 390°C and the cause, irradiation induced dislocations and voids, would only be eliminated if a means for preventing point defect clustering can be found. Options such as thermomechanical heat treatment exist, but because significant improvement is not required at this time, no optimization program is recommended.

7.2.4.5.3 Effects of Crack Propagation Rate on Fracture Topology. Several examples have been found where fracture mode changed several times as the crack propagated through the specimen ligament. Fur example, in specimen TT31, unirradiated HT-9 tested at 0°C, crack propagation was first by ductile fracture, then by brittle failure, then ductile, then brittle and finally ductile. Such variations in crack propagation were not expected. It is well known that unprecracked Charpy specimens when tested near the lower shelf generally exhibit ductile fracture prior to the onset of brittle failure. However, this is thought to be a consequence of the fact that a sharp crack does not exist prior tu testing whereas in precracked specimens a very sharp crack is already present. Therefore, the onset of ductile failure prior to brittle fracture must be a consequence of something other than the state of stress at the crack tip and the test temperature.

The most likely explanation for multiple shifts in fracture mode is a strain rate effect. Materials such as ferritic alloys, which show strong thermally activated deformation behavior, are very strain rate sensitive: the higher the strain rate, the higher the yield stress. Therefore the behavior observed in specimen TT31 can be explained as follows. When the tup strikes the specimen, a load is applied to the specimen crack tip. Because the crack tip is at rest, the loading rate is relatively slow and plastic deformation can occur. However, as the crack tip begins to move, the effective loading rate at the crack tip increases. When the crack tip is moving sufficiently fast, brittle failure occurs and the failure mode therefore changes. However, fracture in HT-9 is affected by delta ferrite stringers. The stringers allow cavities to form ahead of the propagating crack tip and cavitation at delta ferrite stringers involves plastic deformation. As the crack propagates, the stress state at the crack tip changes eventually becoming fully plane stress and this change in stress state reduces the tendency for brittle failure. When plastic deformation at a delta ferrite stringer ahead of the propagating crack becomes sufficiently large, it is anticipated that the crack propagation rate will be sufficiently reduced to change the fracture mode to ductile failure. However, if the propagation rate can eventually increase again to the point where brittle failure will occur, another two shifts in fracture mode will take place. Thus, several shifts in fracture mode can be envisioned as a result of variation in crack propagation rate.

Shifts in crack propagation rate can be observable in dynamic Charpy test records. Earlier dynamic test records did not have sufficient resolution to record such events but recent acquisition of a high speed digital oscilloscope has improved resolution so that changes in propagation rate may be observed. This is demonstrated in Fig. 7.2.23 which shows the recording traces for specimens of unirradiated 9Cr-1Mo. A large drop in the measured load can be identified at 2.8 msec in the trace for specimen AF41. An inflection in the absorbed energy can also be seen. However, similar effects cannot be identified in recording traces of specimens AF38 and AF46. Specimen AF41 provided the unusual example (shown in Fig. 7.2.17) where brittle failure was delayed until after the

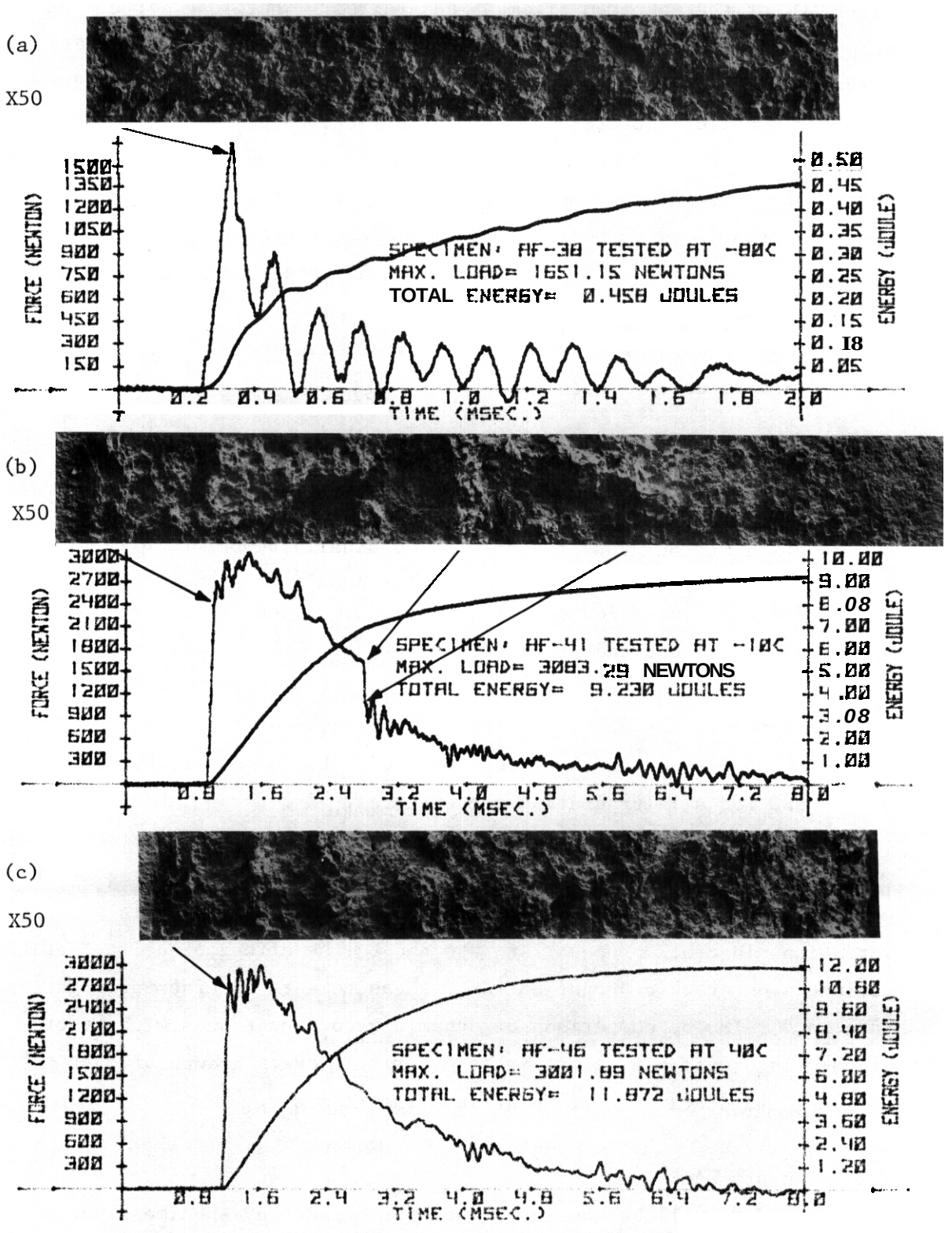

Fig. 7.2.23. Dynamic Recording Traces of Load and Absorbed Energy as a Function of Time for Unirradiated Modified 9Cr–1Mo Base Metal Specimens AF38, AF41 and AF46. Corresponding Fractographic Features are Shown.

first 40% of the specimen ligament had failed. Therefore, it can be shown that it took approximately 1.8 msec for the crack to propagate through 40% of the specimen ligament or 1.3 mm. The crack propagation rate for ductile fracture in that test was therefore 0.72 m/sec. Brittle failure then occurred over 30% of the specimen ligament or 1.0 mm. The recording trace for specimen AF41 indicates that the corresponding load drop occurred over the period of 0.04 msec. Therefore, the crack propagation rate for brittle fracture in that test can be estimated at 25.0 m/sec and brittle fracture in specimen AF41 occurs at crack propagation rates over an order of magnitude faster than ductile crack propagation rates.

7.2.5 Conclusions

Toughness degradation due to irradiation as measured in HT-9 miniature Charpy specimens is attributed to irradiation hardening due to G-phase formation at 390°C in-reactor which results in a large shift in DBTT and to precipitation at delta ferrite stringers which results in a reduction of the USE and a concurrent shift in DBTT. Toughness degradation due to irradiation as measured in Modified 9Cr-1Mo Charpy specimens is attributed to the effect of irradiation induced dislocations and voids at 390°C on DBTT and to the effect of precipitation of (V,Nb)C and $M_{23}C_6$ on the USE for all irradiation temperatures.

The surprising result is found in HT-9 that fracture surface topology can shift several times between ductile and brittle fracture as the crack propagates across the specimen. The behavior is attributed in part to variations in crack propagation rate and to the effect of delta ferrite stringers on crack propagation rate. Measurements of crack propagation rate in 9Cr-1Mo by comparison of dynamic recording traces with fractographic information give estimates of brittle crack growth at over 10 m/sec and ductile fracture at less than 1 m/sec.

7.2.6 Future Work

This work will be continued when further Charpy specimens become available for examination.

7.2.7 References

1. W. L. Hu, "Miniature Charpy Impact Test Results for Irradiated Ferritic Alloys," (This Document: 7.9).

2 F. A. Smidt, Jr., J. R. Hawthorne and V. Provenzano, "Fracture Resistance of HT-9 After Irradiation at Elevated Temperature,'' p. 269 in Effects of *Radiation on Materials,* ASTM STP 725, D. Kramer, H. R. Brager and J. S. Perrin, eds., 1981.

3 D. S. Gelles and L. E. Thomas, "Microstructural Examination of HT-9 and 9Cr-1Mo Contained in the AD-2 Experiment,''*ADIP Semi-Annual* Prog. *Rep. March 31, 1982,* DOE/ER-0045/8, p. 343.

4 D. S. Gelles, F. H. Huang and N. F. Panayotou, "Fractographic Examination of Compact Tension Specimens of Unirradiated HT-9 and Modified 9Cr-1Mo Welds," IBID, p. 442.

5 R. J. Puigh and N. F. Panayotou, "Specimen Preparation and Loading for the AD-2 Ferritics Experiment," *ADIP Quart. Prog. Rep. June 30, 1980,* DOE/ER-0045/3, p. 261.

7.3 THE WELDABILITY OF HT-9: PREHEAT AND POSITION EFFECTS — T. A. Lechtenberg (General Atomic Company)

To be reported in the next semiannual report.

7.4 FRACTURE TOUGHNESS OF UNIRRADIATED HT-9 AND MODIFIED 9Cr-1Mo WELDS - F. H. Huang (Westinghouse Hanford Company)

7.4.1 ADIP Task - ADIP Fusion

7.4.2 Objective

The objective of this work is to evaluate the fracture toughness of HT-9 and modified 9Cr-1Mo welds. The preirradiation data were obtained for future comparison with properties of irradiated weld specimens.

7.4.3 Summary

The fracture toughness of HT-9 weld metal, HT-9 HAZ and modified 9Cr-1Mo weld metal was measured using electropotential techniques. Circular (2.54 mm thick) compact tension specimens were fabricated from welded materials with the notch orientation parallel to the fusion line. Tests were performed at 93, 205, 427 and 538°C. The test results were analyzed using the J-integral approach. It was found that the fracture toughness of HT-9 and modified 9Cr-1Mo was not significantly reduced due to welding.

7.4.4 Progress and Status

7.4.4.1 Introduction

The fracture behavior of unirradiated HT-9 and 9Cr-1Mo base metals was studied and the results reported.'" In developing the ferritic alloys such as HT-9 and 9Cr-1Mo as fusion first wall materials, the fracture and weld properties of these materials are of particular concern. The main difference between the base metals and the welds or heat-affected-zone (HAZ) regarding fracture properties is that the welds usually contain defects such as small cracks or shrinkage porosity. These stress raisers of small radii are not easily detected by the NDT test methods. They may constitute a potential problem to the strength of these materials, therefore, such a possibility must be investigated.

The fracture toughness of HT-9 welds and HAZ, and modified 9Cr-1Mo welds were evaluated using a single specimen J-integral method.' The electropotential technique was used to monitor continuous crack extension during the test. The purpose of the present work was to establish electro-potential calibration curves and to provide preirradiation data for unirradiated ferritic alloy welds and HAZ materials.

7.4.4.2 Experimental Procedure

The specimens tested in this work were part of the AI-2 experiment which was designed to provide data concerning the radiation effects on the mechanical properties of ferritic alloys. Details of specimen fabri-cation were reported in Reference 3. The orientation of the specimen with respect to the welded plate stock is shown in Fig. 7.4.1. The notch orientation of the weld specimen is parallel to the fusion line of the HT-9 welded material. HAZ specimens were machined *so* that the crack would propagate in the center of HAZ material along the fusion line. Fig. 7.4.2(a) shows the configuration of the 2.54 mm thick circular compact tension specimen. Four copper electrodes (2 mm diameter) were resistance welded at the lead positions for power supply and potential output shown in Fig. 7.4.2(b), by an in-cell lead attachment apparatus.

All specimens were fatigue precracked with a hydraulic testing system to a crack length of 1.3 mm at a stress intensity factor of 28 MPa$\sqrt{m}$ for HT-9 weld and HAZ specimens and 30 MPa$\sqrt{m}$ for 9Cr-1Mo weld specimens. During the test a constant DC current of 12 amp was applied to the specimen, and the potential output and the load-time were monitored. A calibration curve relates potential output to crack extension *as* revealed by heat tinting (indicated by the arrow in the inset of Fig. 7.4.3). Fracture toughness tests were conducted at 93, 205, 427 and 538°C.

7.4.4.3 Results and Discussions

The load and electropotential output versus load-line displacement curves of HT-9 weld material are plotted in Fig. 7.4.3. The values of J were calculated from load versus displacement curves. The crack extensions were obtained from electropotential via the electropotential calibration curves shown in Fig. 7.4.4. J versus Aa curves for HT-9 welds tested at

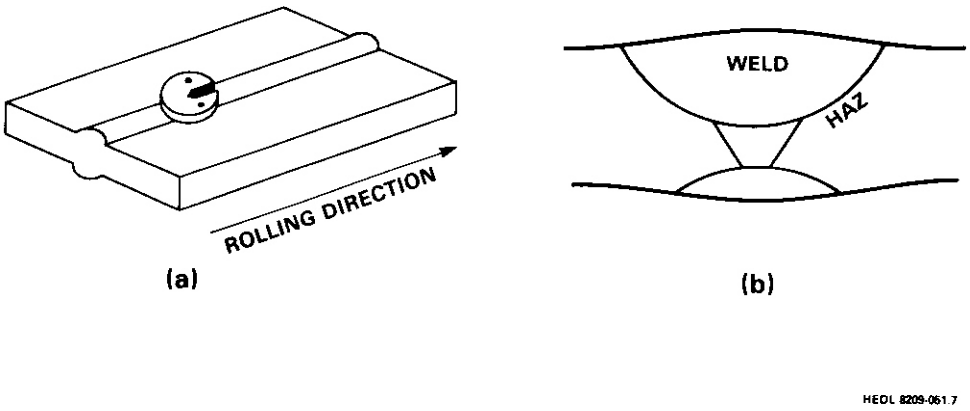

Fig. *7.4.1.* (a) Orientation of Fracture Toughness Specimen with Respect to Weld Material.
(b) Transverse Section of HT–9 Weld Metal.

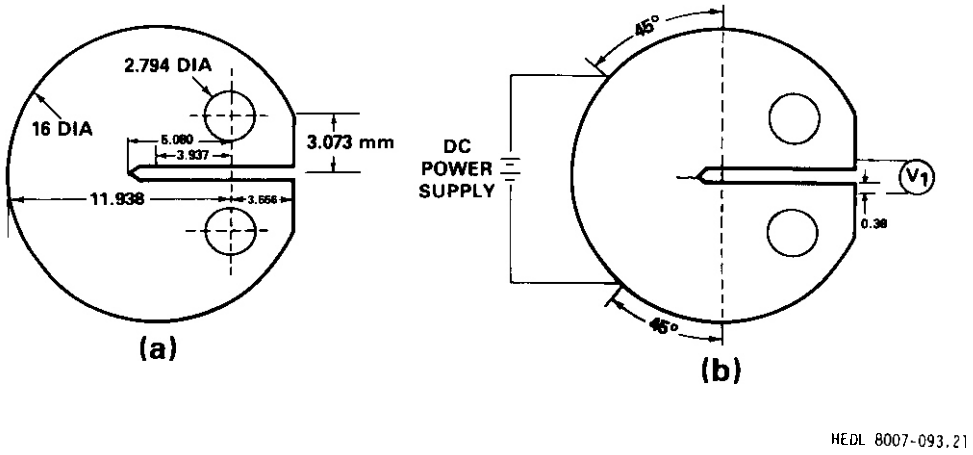

Fig. *7.4.2.* (a) Circular Compact Tension Specimen Dimensions.
(b) Schematic Drawing of Electropotential Technique.

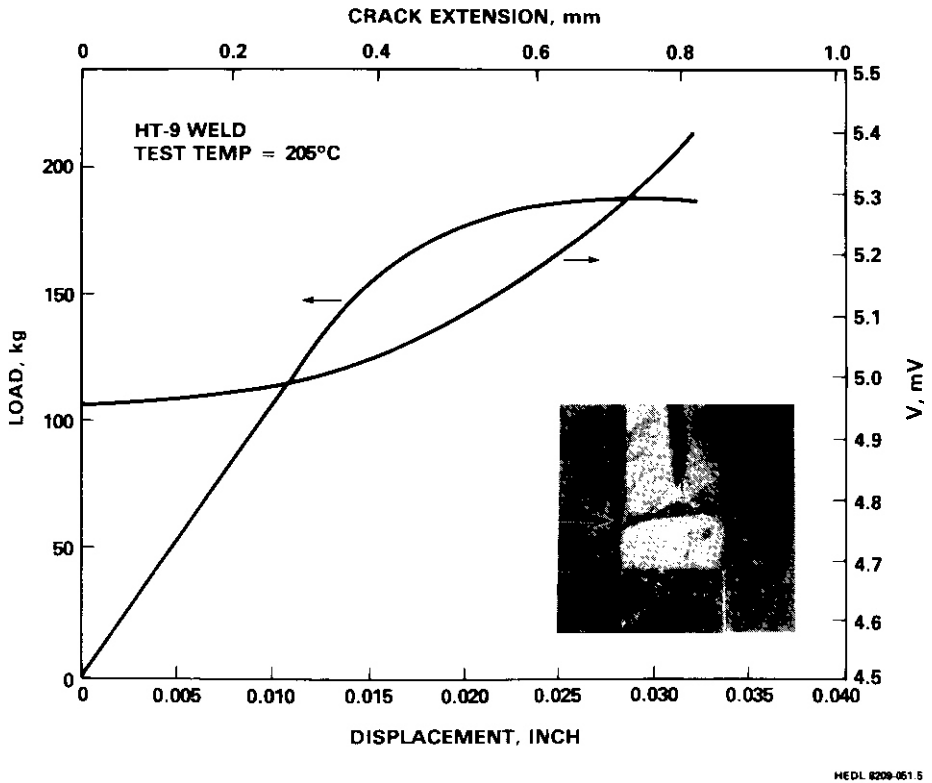

Fig. 7.4.3. Potential Output and Load Versus Load-Line Displacement Curves for Unirradiated HT-9 Weld. The Micrograph Inset Shows the Crack Extension Revealed by Heat Tinting.

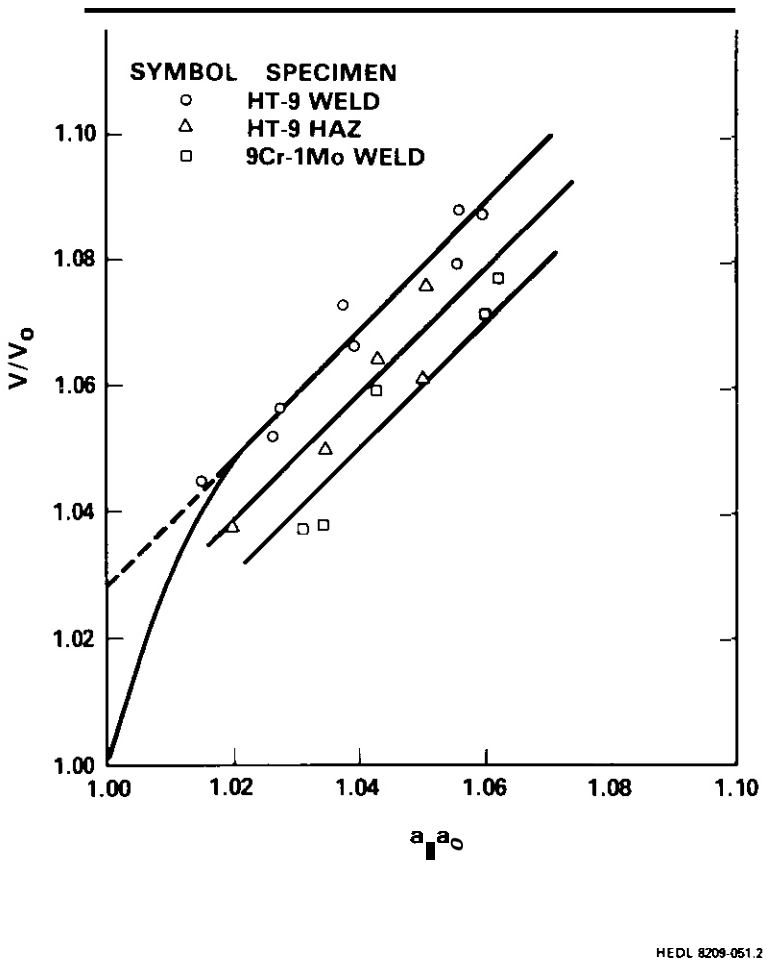

Fig. 7.4.4. Electropotential Calibration for HT-9 Welds, HT-9 HAZ Material and 9Cr-1Mo Welds.

205°C are shown in Fig. 7.4.5. The values of J were determined from both multi-specimen and single specimen methods. The results of 205°C tests obtained from both methods were in good agreement. It demonstrated that the single specimen method using the electropotential technique can be used to measure the fracture toughness of ferritic welds.

The test results of unirradiated HT-9 weld, HAZ and 9Cr-1Mo weld samples at elevated temperatures are listed in Table 7.4.1. The temperature dependence of J_{1c} for the welds of HT-9 and 9Cr-1Mo are shown in Figs. 7.4.6 and 7.4.7, respectively. The values of J_{1c} obtained from HT-9 and 9Cr-1Mo base metals are also plotted in these figures for comparison. Also listed in Table 7.4.1 are the values of tearing modulus (T). In Fig. 7.4.8 the temperature dependence of the tearing moduli for the various materials shown. Surprisingly, it was found that HT-9 weld metal and HAZ material exhibited a higher toughness than the base metal at 205°C. Overall, the toughness of HT-9 and 9Cr-1Mo was not significantly reduced due to welding, although the tearing modulus was reduced at temperatures below *400°C.*

The fracture surfaces of specimens tested in this work were examined by scanning electron microscopy and the results were reported in Reference 4. The fracture surfaces of both weld metals appear to contain two structure morphologies whereas the HAZ is more uniform. Higher magnification fractographs reveal that crack propagation occurs by nucleation and coalescence of cavities ahead of the crack tip. It appears that carbide precipitates provide cavity nucleation sites.

7.4.5 Conclusions

The fracture toughness of weld specimens of HT-9 and modified 9Cr-1Mo decreases with increasing temperature. The values of J_{1c} for welds are close to those of the base metal, except for alloy HT-9 at 205°C. The results demonstrate that the toughness of HT-9 and 9Cr-1Mo is not significantly reduced due to welding. However, the tearing modulus of welds is lower than that of base metals indicating that the alloys become less resistant to crack propagation as a result of welding.

Table 7.4.1. Fracture Toughness Test Results of Unirradiated HT-9 and 9Cr-1Mo Welds

Material	Test Temp. (°C)	J_{1c} (in-lb/in^2)	J_{1c} (KJ/m^2)	Tearing Modulus
HT-9 Weld	93	565.0	98.9	86.2
	205	520.6	91.1	93.9
	427	378.0	66.2	92.1
	538	353.0	61.8	192.9
HT-9 HAZ	93	506.1	88.6	104.7
	205	510.0	89.3	98.2
	427	370.8	64.9	105.6
	538	329.3	57.6	202.0
9Cr-1Mo Weld	93	495.0	86.6	133.0
	205	445.0	77.9	106.7
	427	466.1	81.6	145.4
	538	378.0	66.2	188.7

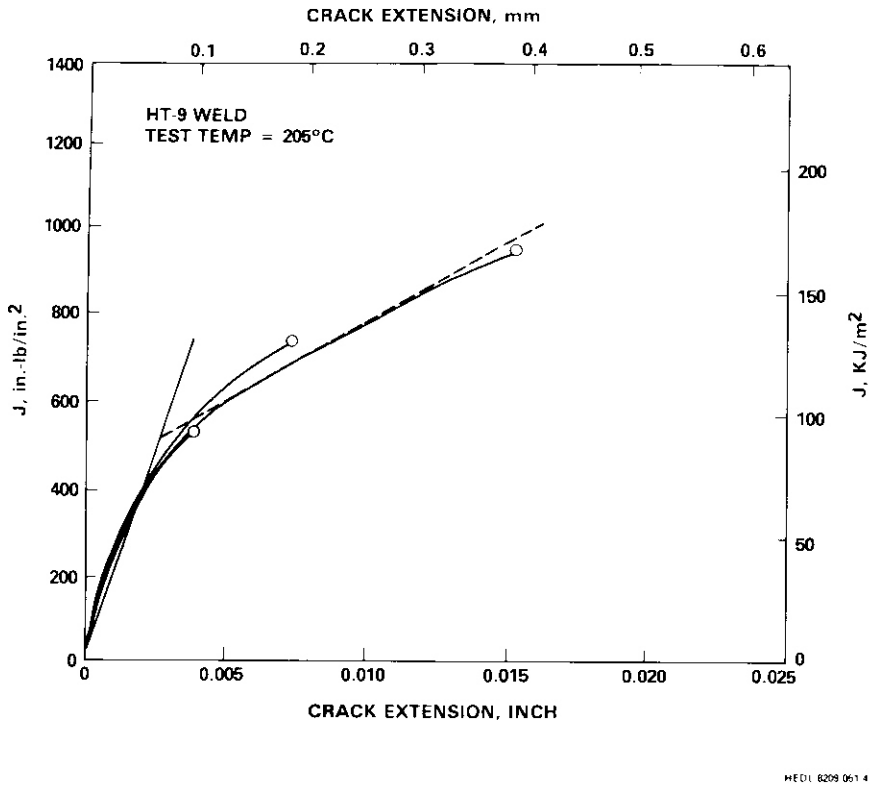

Fig. 7.4.5. J Versus Δa Curves Obtained via an Electropotential Calibration Curve for HT-9 Weld Material.

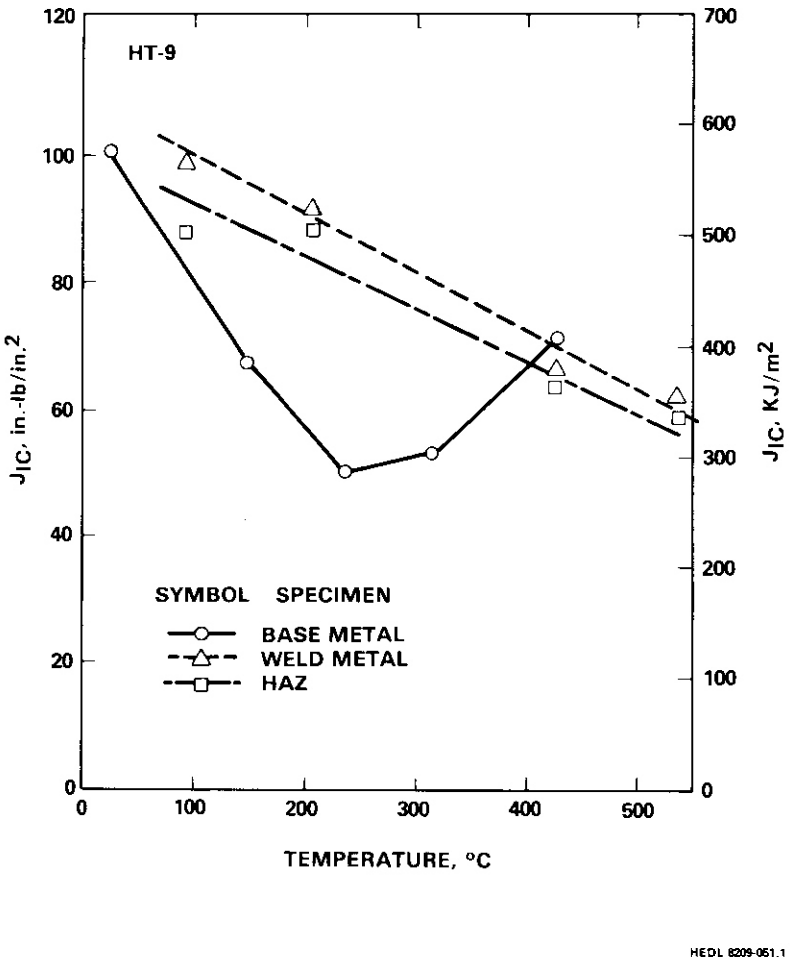

7.4.6. Temperature Dependence of Fracture for HT-9 Welds and HAZ Samples

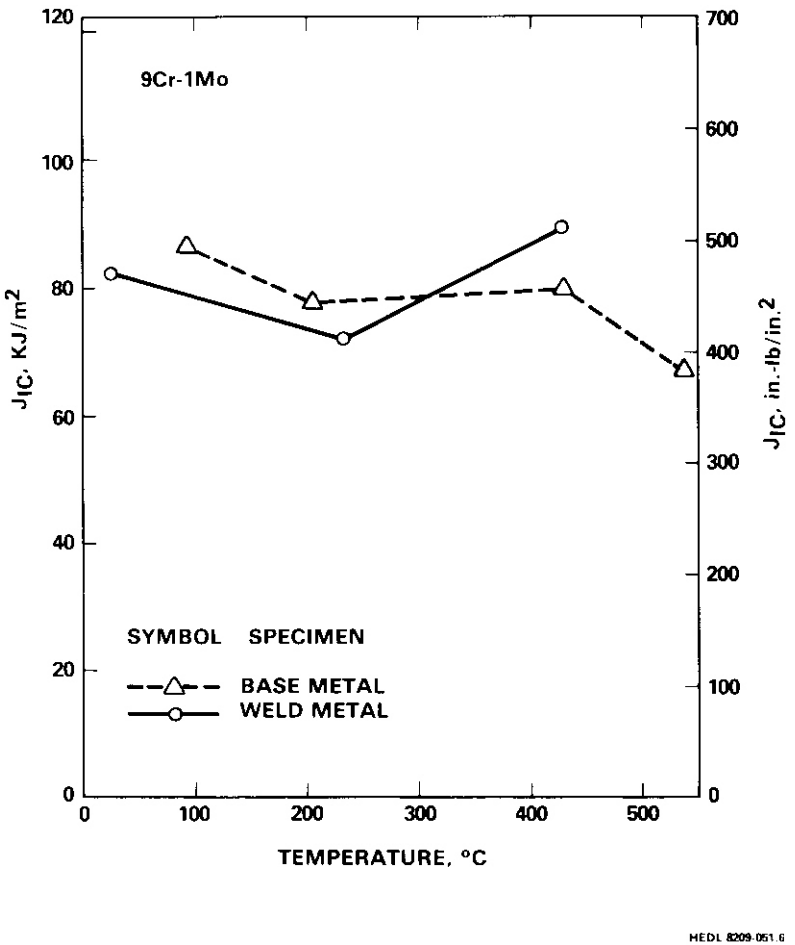

7.4.7. Temperature Dependence of Fracture for 9Cr-1Mo Welds.

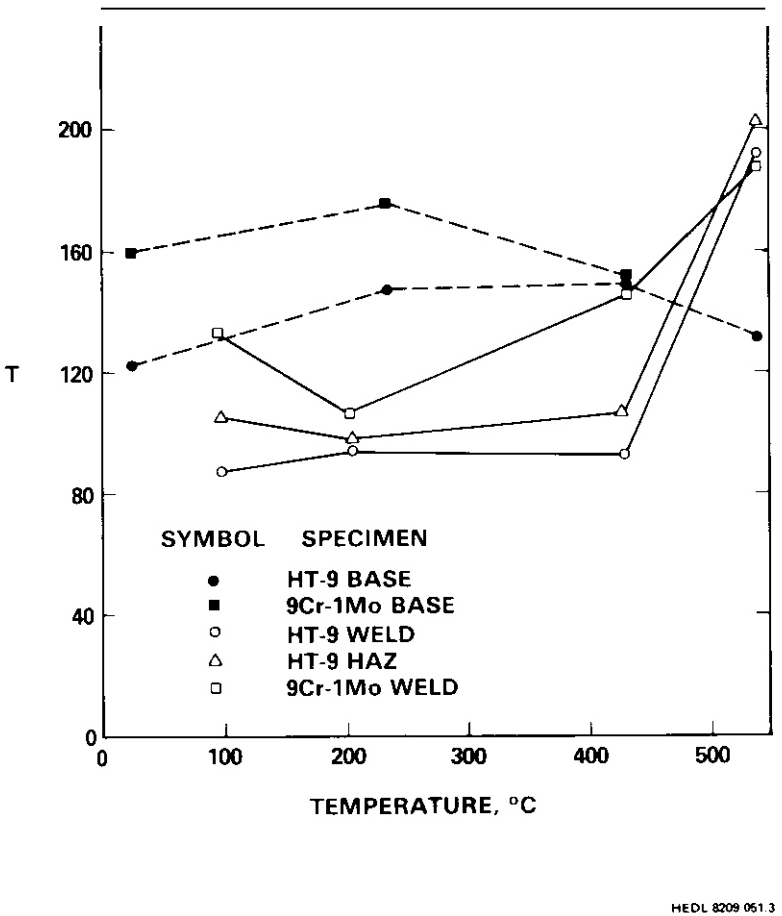

Fig. 7.4.8. Temperature Dependence of Tearing Modulus for HT-9 Welds, HT-9 HAZ Material and 9Cr-1Mo Welds.

7.4.6 References

1. F. H. Huang and G. L. Wire, "Analysis of Single Specimen Tests on HT-9 for J_{1c} Determination," *ADIP Quart. Prog. Rep. Sept. 1980, DOE/ER-0045/3*, pp. 236-254.

2. F. H. Huang and G. L. Wire, "Fracture Toughness Measurements for Unirradiated 9Cr-1Mo Using Electropotential Techniques," ADIP *Quart. Prog. Rep. Sept. 1981, DOE/ER-0045/7*, pp. 220-229.

3. R. J. Puigh and N. F. Panayotou, "Specimen Preparation and Loading for the AD-2 Ferritics Experiment," *ADIP Quart. Prog. Rep. Sept. 1980, DOE/ER-0045/3*, pp. 260-293.

4. D. S. Gelles, F. H. Huang and N. F. Panayotou, "Fractographic Examination of Compact Tension Specimens of Unirradiated HT-9 and Modified 9Cr-1Mo Welds," *ADIP Semi-Annual Prog. Rep. March 1982, DOE/ER-0045/8*, pp. 442-459.

7.5 THE TOUGHNESS OF SIMULATED HEAT AFFECTED ZONE MICROSTRUCTURE IN HT-9 (ESR MELT PRACTICE) — J. C. Lippold (Sandia National Lahoratories, Livermore, CA)

To be reported in the next semiannual report.

7.6 THE EFFECT OF MELT PRACTICE (ESR VS. AOD) ON THE TOUGHNESS OF HT-9 LASER WELDS - J. C. Lippold (Sandia National Laboratories, Livermore, CA)

7.6.1 ADIP Task

The Department of Energy (DOE)/Office of Fusion Energy has cited the need for these data under the ADIP program task Ferritic Steels Development (Path E).

7.6.2 Objective

The melting process used when producing steel can have a significant effect on the chemistry and subsequent properties of the wrought product. In order to assess the effect of melt practice on the properties of HT9 a portion of the original AOD (argon-oxygen decarburization) National Fusion Heat has been electroslag remelted (ESR). The ESR process results in both microstructural refinement and reduction in overall inclusion content relative to the AOD-melted material. The combination of these two factors generally results in improved mechanical properties in the wrought base material. Unfortunately, this improvement in properties *does* not necessarily carry over when the material is welded. Based upon this observation, a study was conducted to contrast the toughness of welded AOD- and ESR-processed material and to compare the toughness of the weld region to that of the wrought base material.

7.6.3 Summary

The toughness behavior of Laser welded AOD- and ESR-processed material from the National Fusion Heat was evaluated. In general, the fusion zone toughness was equivalent, if not superior, to that of the base metal. The microstructural refinement which results from weld solidification is probably responsible for the improvement in properties. The chemical inhomogeneity due to partitioning during solidification appears to exert only a small effect on the properties. The fracture mode is analogous to that of the base material; lower shelf failure exhibits a cleavage mode while upper shelf failure occurs by ductile rupture.

7.6.4 Progress and Status

During welding of HT9 the fusion zone and portions of the heat-affected zone (HAZ) transform to untempered martensite upon cooling to room temperature from the welding temperature range. Segregation of alloying elements during solidification of the fusion zone results in a non-equilibrium distribution of ferrite along the solidification subgrain boundaries. Previous reports have shown that the majority of this ferrite remains in the structure after the postweld heat treatment.[1,2] The effect of the interdendritic ferrite on the mechanical properties, toughness, and irradiation performance is unclear. In addition, the segregation of impurity elements during weld solidification may significantly affect the properties of the fusion zone.

The impurity level of a heat of material is directly related to the purity of the starting material but can be significantly altered by the melting practice which is used. The AOD process tends to reduce sulfur contents and control the carbon level but has little effect on reducing other impurity elements. The ESR process is effective in uniformly reducing most of the common impurity elements (S, P, O, Sn, Sb) and, results in overall refinement of the microstructure. The variation in composition between the AOD- and ESR-melted heats of HT9 may have an important influence on both the weldability and subsequent properties of the fusion zone. This investigation addresses the influence of melt practice on the toughness of HT9 laser welds.

7.6.4.1 Experimental Approach

The chemical composition of both the AOD- and ESR-melted National Fusion Heat, as reported in a previous semiannual report[3], is listed in Table 1. The same report also details the melting and breakdown history of the ESR material. Plates 15 mm thick (0.625 in) from each heat were austenittzed for 0.5 hr at 1040°C, air cooled and then tempered at 760°C for 1 hr. The decarburized layer was machined off resulting in a final plate thickness of 11.5 mm *(0.450* in).

TABLE 1

CHEMICAL COMPOSITION

FOR HEATS OF HT-9

CHEMICAL COMPOSITON LIMITS

HEAT	C	Si	Mn	P	[illegible]	Cr	Mo	Ni	V	W	N	Al	Ti	Other (Max.)
DIN. SPEC (1.4935)	.17/ .23	.1/ .50	.3/ .80	0.035 (max)	0 5 ( )	11.0/ 12.5	0.8/ 1.20	.3/ .80	.25/ .35	.4/ .6				
AOD (9607)	.20	.24	.57	0.018	0.007	11.64	0.01	.52	.30	.57	.044	0.09	<.01	O_2 .013, Cb 0.01 Cu .04, Co 0.09, As 0.004 Zr .002, B 0.001, Pb .001, Sn 0.001, Sb trace
ESR (9607R2)	.20	.17	.57	0.016	0.003	12.1	1.04	.51	.28	.45	.027	.006 .007	.001	Cu .07, Co <0.05, As 0.003 O_2 .002, B <.001, Bi <.001 Pb <.0001, Sb 0.0005 Sn 0.004, Cb <.001

Autogenous laser welding was performed using a Sylvania continuous-wave CO_2 laser. Partial penetration welds were made on one side of the plate, then the plates were turned over and rewelded to effect a full penetration weld. All welds were made at a power level of 5.8 kW and a travel speed of 6.35 mm/sec (15 ipm) with the laser beam focussed on the plate surface. Following welding, the plates were subjected to a postweld heat treatment (PWHT) at 760°C for 1 hour. Charpy V-notch samples 10x10x50 mm were machined from the plates with the notch located in the fusion zone and oriented such that crack propagation would occur longitudinal to the welding direction.

Charpy tests were performed in the temperature range from -60 to 100°C. Multiple samples were tested at room temperature as a measure of reproducibility, otherwise single samples were tested at a given temperature. Microstructural analysis of the fusion zone was performed following etching with Vilella's reagent. Finally, the scanning electron microscope (SEM) equipped with an energy dispersive spectrometer (EDS) was used to determine the fracture mode and to identify particles associated with the fracture.

7.6.4.2 Weld Microstructure

Full penetration laser welds in the 11.5 mm plates were made by overlapping welds from opposite sides of the plate. Porosity was observed in the root area of the weld and resulted in a linear string of porosity along the centerline at the mid-thickness of the finished weld. A schematic illustration of the location of this porosity relative to the Charpy V-notch orientation is shown in Figure 1.

The microstructure of the laser weld prior to the PWHT is shown in Figure 2. The ferrite present in the microstructure along the solidification subgrain boundaries results from the partitioning of ferrite stabilizing elements (Cr, Mo, V) during solidification of the fusion zone. The remainder of the fusion zone transforms to martensite upon cooling below the M_S temperature *(~240°C).* In a previous report[2], it was shown that most of this ferrite remains in the microstructure after the PWHT. The microstructure of the AOD- and ESR-melted laser welds following PWHT is shown in Figure 3.

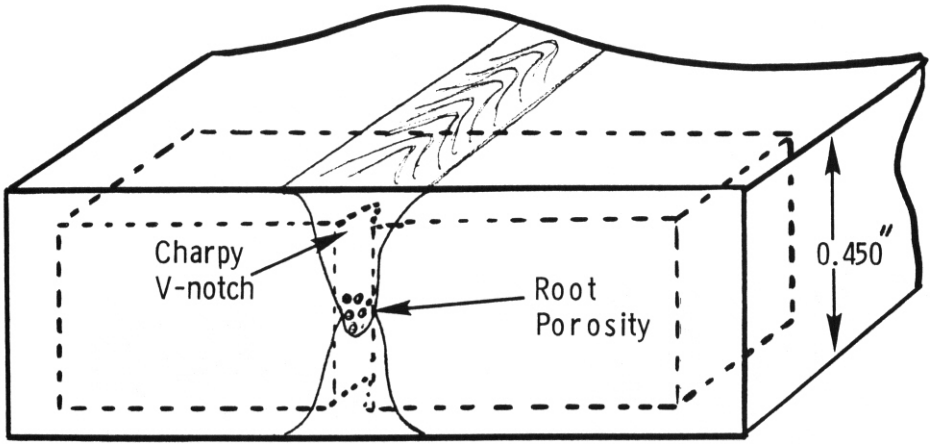

Figure 1. Schematic Illustration of the Location of the Charpy V–notch Samples Relative to the Two–Pass Laser Weld. Note the Root Porosity Associated with the Final Pass.

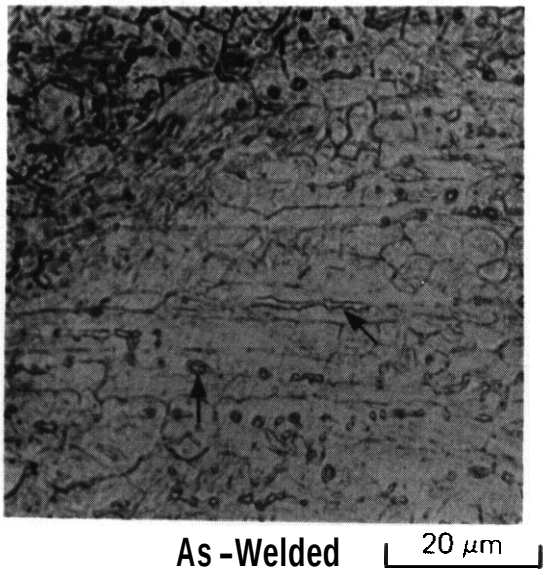

Figure 2. Laser Weld Microstructure, As–Welded. Arrows Indicate Ferrite Along Solidification Subboundaries.

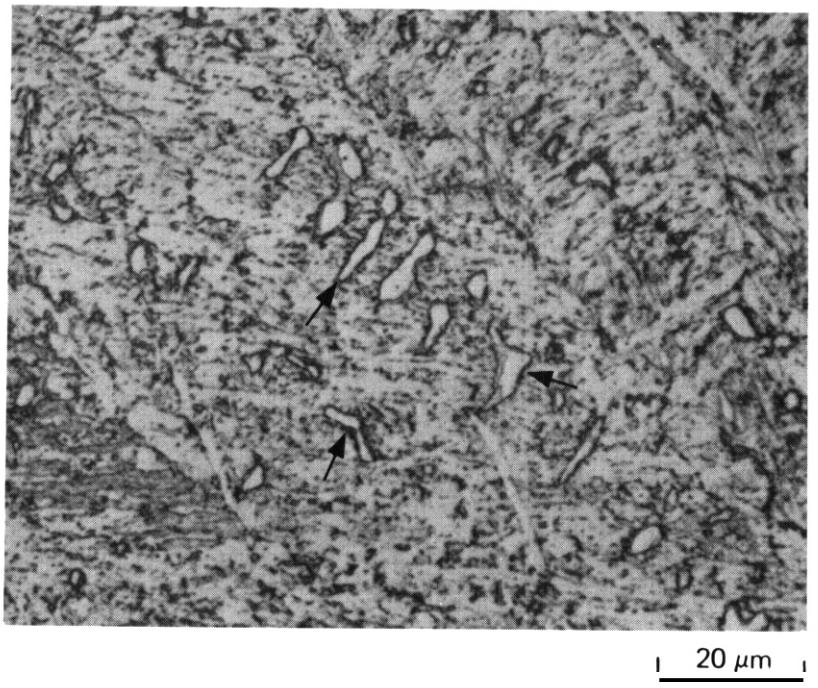

Figure 3. Laser Weld Microstructure, After PWHT (760°C/1 hr.). Arrows Indicate Ferrite.

7.6.4.3 Charpy V-notch Results

The Charpy V-notch toughness results for both the AOD- and ESR-processed laser welds are summarized in Figure 4. Note that the upper and lower shelf energies for both materials are nearly equivalent; however, the ductile-to-brittle transition temperature (DBTT) of the ESR material is nearly 20°C higher than the AOD specimens. The upper and lower shelf energies and DBTT of the laser welded material and the reference base material are listed in Table 2.

Table 2

Charpy V-notch Results

	Upper Shelf (ft-lb)	Lower Shelf (ft-lb)	DBTT (°C)
ESR Laser Weld	75	15	0
AOD Laser Weld	72	12	-17
ESR Base Plate*	a5	20	20
AOD Base Plate**	45	10	-18

*tempered 2.5 hr at 760°C (Ref. 3)
**tempered 1 hr. at 760°C, transverse orientation (Ref. 4)

Although both the ESR base and weld metal exhibit a higher upper shelf energy than the AOD heat the DBTT is shifted to higher temperatures. The increase in upper shelf energy of the AOD weld metal relative to the base metal probably results from the microstructural refinement which occurs during the melting and resolidification of the fusion zone.

7.6.4.4 Fractography

Fracture surface analysis was performed on Charpy samples from both the AOD and ESR laser welded plates. Representative samples were analyzed which represented upper shelf, lower shelf, and transition region behavior. The fracture morphology of samples exhibiting lower shelf behavior is shown in Figure 5. Note that at low magnification (Fig. 5a) the fracture surface exhibits an orientation representative

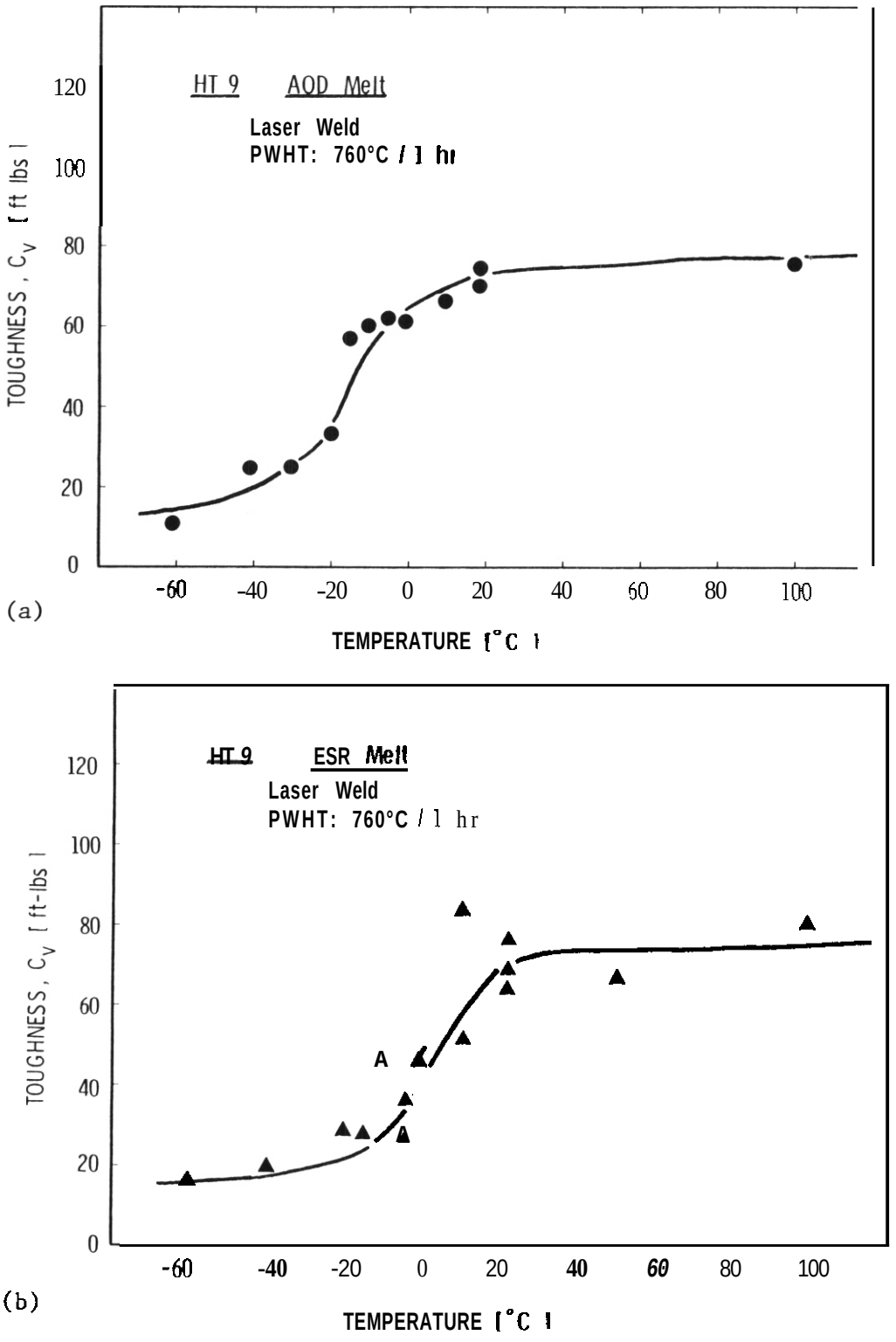

Figure 4. Charpy V-notch Results of Laser Welded HT9, a) AOD, b) ESR.

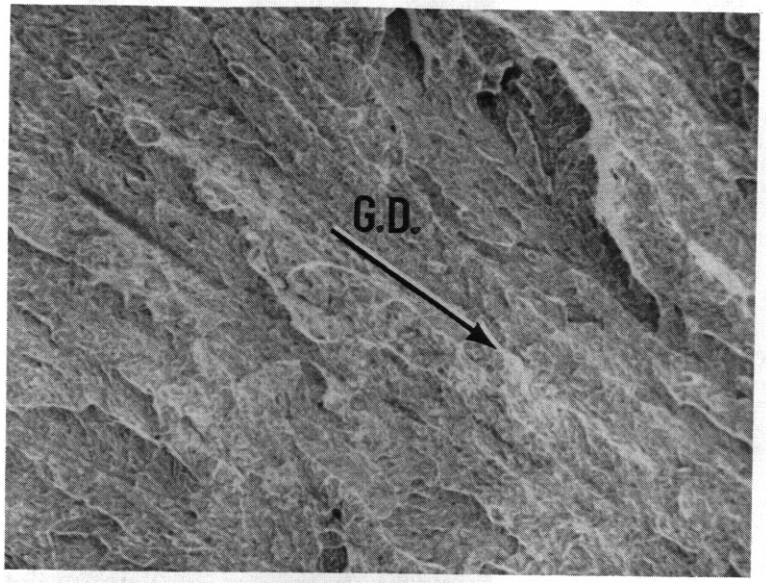

(a)

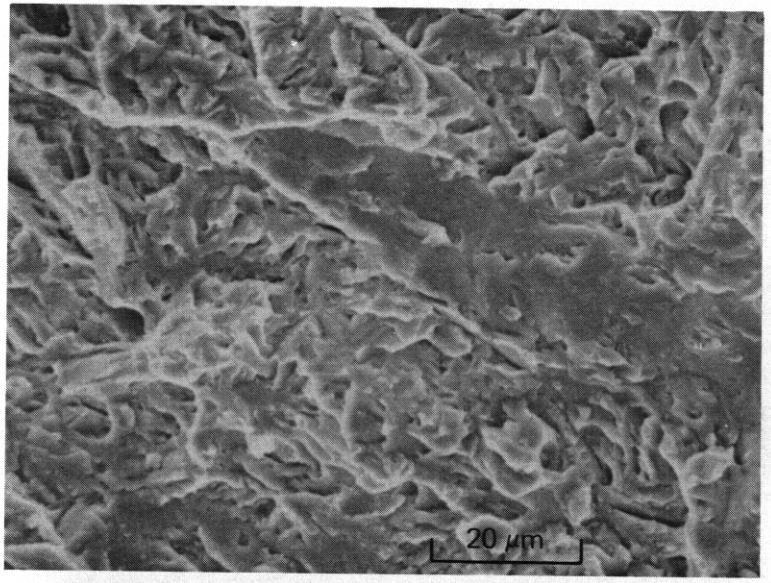

(b)

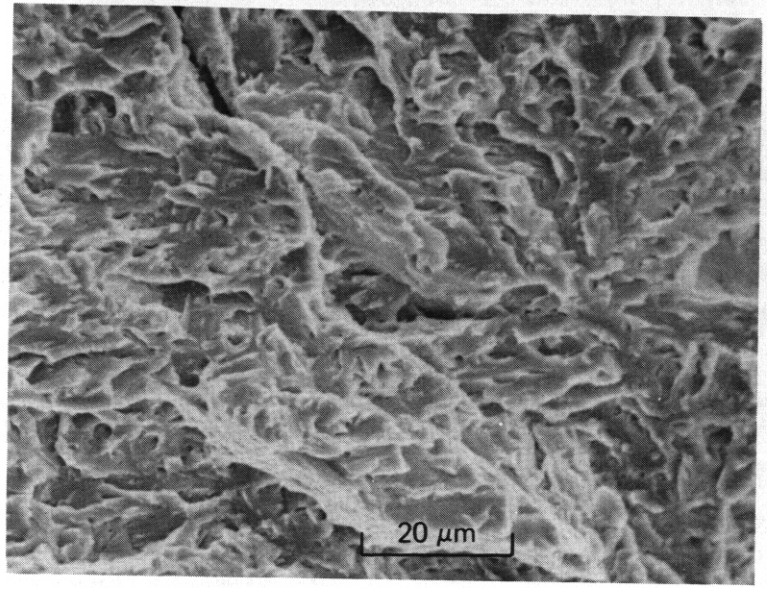

(c)

Figure 5. Fracture Morphology of Charpy Samples Exhibiting Lower Shelf Behavior, a) Low Magnification of ESR sample, arrow indicates solidification growth direction (G.D.), b) High Magnification of ESR sample, c) High Magnification of AOD Sample.

of the primary dendritic growth direction in the weld. At higher magnification (Fig. 5b, 5c) the fracture reflects the classic cleavage morphology typical of low energy fracture in martensitic materials.

The upper shelf fracture morphology (dimpled rupture) is shown in Figure 6 for both an AOD and ESR sample tested at room temperature. Again, note the directional nature of the fracture (Fig. 6a) resulting from the interaction of the crack path with the dendritic structure.

Regions of the fracture surface near the mid-thickness of the Charpy sample often exhibited porosity. A low magnification fractograph of an AOD processed sample tested at room temperature is shown in Figure 7. The location of the porosity corresponds to the root of the final laser weld which was made to achieve full penetration (Fig. 1). It is unclear how seriously the presence of this porosity affects the toughness behavior presented in Figure 4 and Table 2.

7.6.4.5 Discussion

Melting and solidification in the fusion zone during welding results in rapid reapportionment of alloying and impurity elements which may alter the properties of the weld relative to the base metal. The Charpy results of laser welded HT9 in both the ESR- and AOD-processed form indicate that, in general, the toughness of the weld fusion zone is at least equivalent to that of the base material. Reference to Table 2 reveals that although the upper and lower shelf values of the ESR weld and base material are nearly equivalent the DBTT of the weld is lower. In the case of the AOD material, the toughness characteristics of the weld were superior to the base material.

The improvement in properties can be related, at least in part, to the microstructural refinement which occurs during weld solidification. It does not appear that the chemical inhomogeneity resulting from elemental partitioning has any effect on the toughness characteristics; although the fracture morphology appears to reflect the weld growth direction (Figs. 5a and 6a).

The fracture mode of the laser-welded samples was similar to the failure observed in the base metal; fracture on the lower shelf

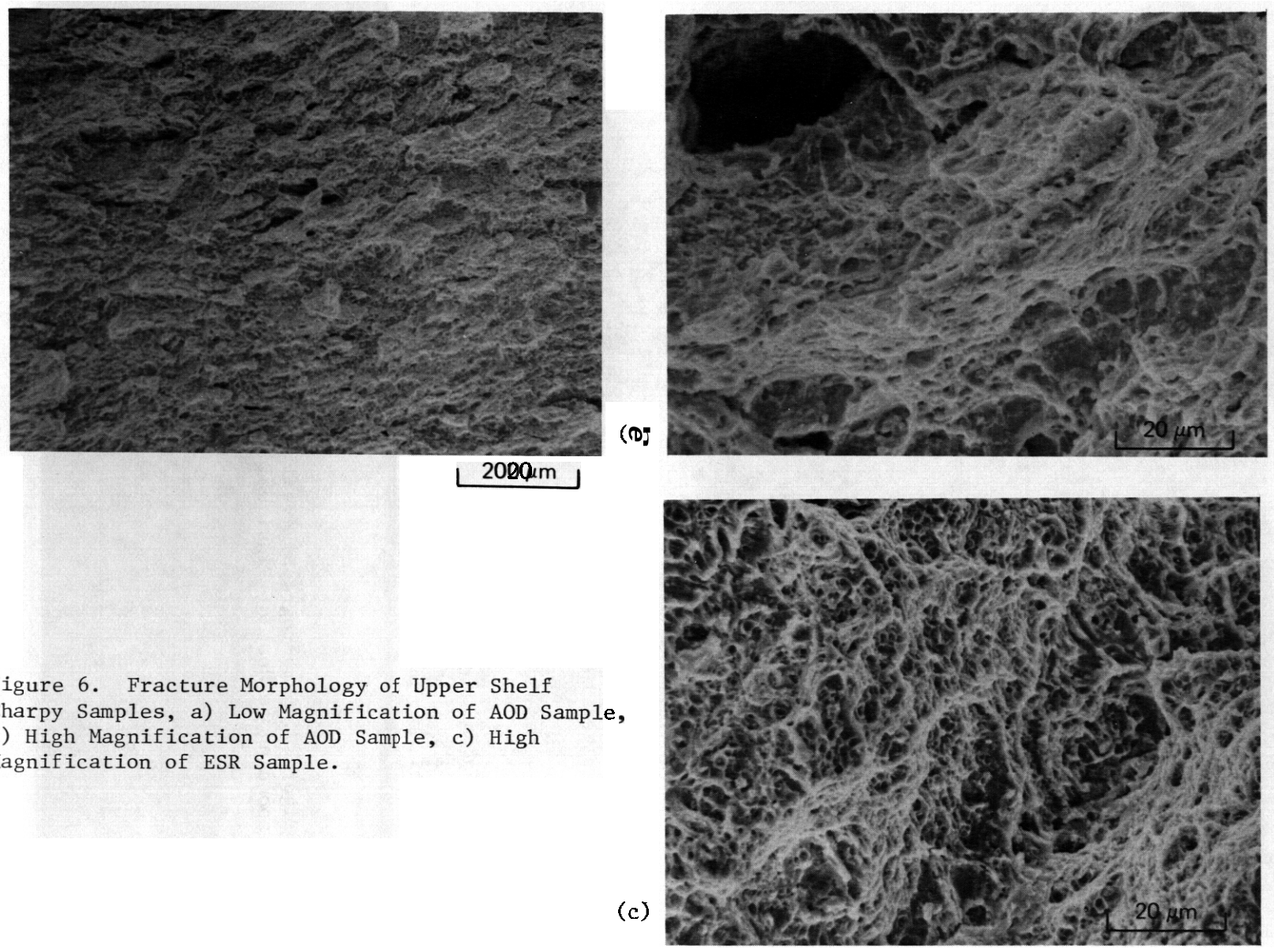

Figure 6. Fracture Morphology of Upper Shelf Charpy Samples, a) Low Magnification of AOD Sample, b) High Magnification of AOD Sample, c) High Magnification of ESR Sample.

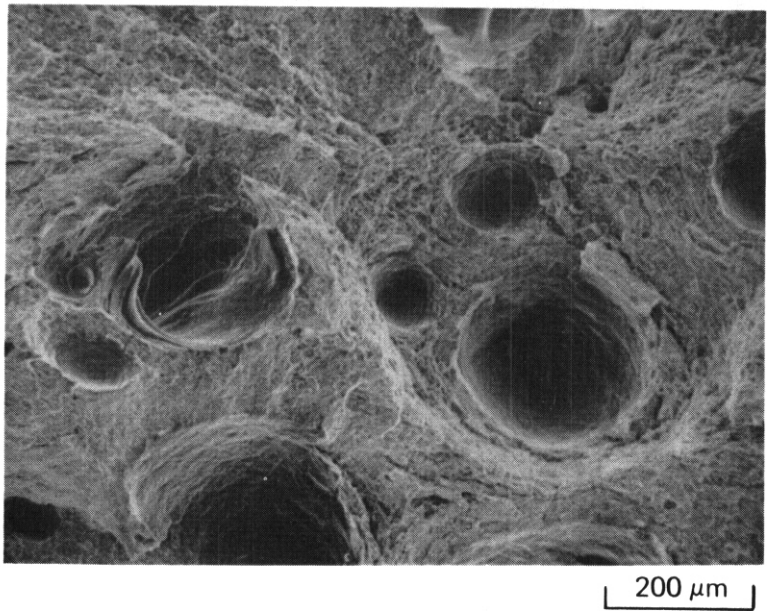

Figure 7. Fractograph Revealing Porosity on the Fracture Surface Corresponding to **Root** of Final Weld Pass (see Fig. 1).

exhibited a cleavage mode while upper shelf behavior was typically ductile rupture. Failure in the transition region was a mixture of these modes.

7.6.5 Conclusions

1. The toughness of the fusion zone following PWHT was at least equivalent to that of both the AOD- and ESR-processed National Fusion Heat base material.
2. The laser-welded AOD heat exhibited a lower ductile-to-brittle transition temperature (DBTT) than the ESR heat. The upper and lower shelf toughness values were equivalent.
3. The lower shelf fracture mode was cleavage while upper shelf behavior was primarily ductile rupture.
4. Both the AOD and ESR laser welds exhibited root porosity. It is unclear how significantly these defects affected the toughness behavior.

7.6.6 References

1. J. C. Lippold, "Analysis of Laser Welds in HT9, ADIP Progress Report for Period Ending 9/30/80. pp. 126-139.
2. J. C. Lippold, "Tempering Behavior of Laser Welds in HT9", ADIP Progress Report for Period ending 3/31/81, pp. 191-207.
3. T. A. Lechtenberg, "The Procurement and Characterization of the Electroslag Remelted National Fusion Program Heat of 12Cr-1Mo Steel", ADIP Progress Report for Period Ending 3/31/82, pp. 363-369.
4. Unpublished research performed at Sandia National Laboratories, Livermore, CA, 1982.

7.7 THE EFFECT OF QUENCH RATE AND REFRIGERATION ON THE MECHANICAL PROPERTIES OF ESR PROCESSED HT-9 – W. M. Garrison, Jr. and J. M. Hyzak (Sandia National Laboratories, Livermore, CA)

7.7.1 ADIP Task

The Department of Energy (DOE) Office of Fusion Energy (OFE) has cited the need for these data under the ADIP Program Task, Ferritic Alloy Development (Path E).

7.7.2 Objective

The goal of this work was to determine the effect of cooling rate from the austenitizing temperature and subsequent refrigeration in liquid nitrogen on the retained austenite content and Charpy impact toughness of ESR processed HT-9.

7.7.3 Summary

HT-9 contains about 9 volume percent retained austenite when air cooled after austenitizing. To reduce the retained austenite content of HT-9 from that of the air cooled (AC) condition, two other treatments after austenitizing were employed: oil quenching (OQ) and oil quenching followed by refrigeration in liquid nitrogen (OQLN). The OQ structure contained 6% retained austenite and the OQLN structure had only 4% retained austenite. Preliminary Charpy impact data indicate some beneficial effect of these treatments. The Charpy impact values of specimens tempered at 750°C were 78, 80 and 97 ft-lbs for the AC, OQ and OQLN structures respectively.

7.7.4 Progress and Status

7.7.4.1 Introduction

The 12% chromium martensitic/ferritic steel, HT-9, is being evaluated as a first wall blanket material in fusion devices. Tests at Sandia National Laboratories, Livermore, have shown that, when tempered at 750°C, this steel can be subsequently embrittled by internal

hydrogen introduced by cathodic charging.[1] This embrittlement is manifested by both reduced ductility and a fracture mode change in room temperature tensile tests. In the unembrittled condition HT-9 fails by micro-void coalescence, but when hydrogen charged the fracture is intergranular along prior austenite grain boundaries. These grain boundaries are highly enriched in phosphorous and over fifty percent of the prior austenite grain boundary area is covered with plate-like $M_{23}C_6$ carbides (Figure 1). The role of these carbides in the fracture of HT-9 is not totally clear. However, the large surface area covered by these carbides and their plate like shape provide a microstructure which offers less than optimum toughness and ductility, especially when exposed to hydrogen. The purpose of this work was to reduce the volume fraction of carbides at prior austenite grain boundaries by minimizing the retained austenite content after quenching. This should result in improved toughness.

When air cooled after austenitizing, HT-9 contains about 9% retained austenite which exists as films at prior austenite grain boundaries and between martensite laths. Because it has a much higher carbon content than the matrix,[1] the retained austenite provides a source of carbon for the precipitation of carbides at prior austenite grain boundaries. Therefore, by minimizing the amount of retained austenite one would hope to minimize the volume fraction of grain boundary carbides after tempering. To reduce the retained austenite content of HT-9 from that of the air cooled condition two other treatments after austenitizing were employed: oil quenching and oil quenching followed by refrigeration in liquid nitrogen.

7.7.4.2 Experimental Procedure

The material used was from the portion of the National Fusion Heat of HT-9 which had been electroslag remelted (ESR). The material was obtained from General Atomic Co. in the form of 5/8" plate.

Blanks for both Charpy impact specimens and retained austenite measurements were austenitized at 1040°C for 30 minutes. After

austenitizing three cooling procedures were used: air cooling; oil quenching; and oil quenching followed by refrigeration in liquid nitrogen for four hours. Specimen blanks were then tempered in the range of 200°C to 750°C. The AC and OQ specimens were tempered for one hour, while the CQLN specimens received three one hour tempers at a given temperature. The OQLN specimens were refrigerated in liquid nitrogen for four hours after the first and second temper. All specimens were water quenched after tempering.

Charpy impact specimens were taken from the HT-9 plate stock in the longitudinal orientation with the notch directed from the edge of the plate perpendicular to the rolling direction.

The retained austenite content for each heat treatment was determined from flat tensile specimens using a magnetic saturation device.[3] The mechanical stability of retained austenite was assessed by mounting the magnetic saturation device on the crosshead of an Instron machine and measuring the amount of retained austenite in the same flat tensile specimens as a function of strain. The tensile specimens used for these measurements were of the longitudinal orientation and had a gage length of 1.125 in, a gage width of 0.125 in and a thickness of 0.050 in. The tensile tests were conducted at room temperature at an initial strain rate of .018/minute.

7.7.4.3 Experimental Results

The Charpy impact toughnesses of the AC, OQ, and OQLN structures are given as a function of tempering temperature in Table 1. At low tempering temperatures, the AC structure exhibited significantly greater toughness than either the OQ or OQLN structures. The AC structure tempered at 200°C had an impact energy of 44.5 ft-lbs, while the OQ and OQLN structures had impact energies of 9.7 and 8.1 ft-lbs respectively. This difference in toughness correlated with a difference in fracture modes. The AC structure failed by void coalescence, while both the OQ and OQLN structures failed by quasi-cleavage(Fig. 2).

The toughness of the AC structure decreased as the tempering temperature was increased from 200°C and reached a minimum of

TABLE 1

EFFECT OF TEMPERING TEMPERATURE
ON CHARPY IMPACT TOUGHNESS*

Tempering Temperature	Air Cool (AC)	Oil Quench (OQ)	Oil Quench & LN (OQLN)
200	44.5	9.7	8.1
300	39.6	8	13.7
400	24.2	4.3	5.8
500	8.1	3.1	4.3
550	10	6.3	12.8
600	17.9	18	21
650	22.6	28	30
700	31.7	37.9	56
750	78.6	80	97

*ft-lbs

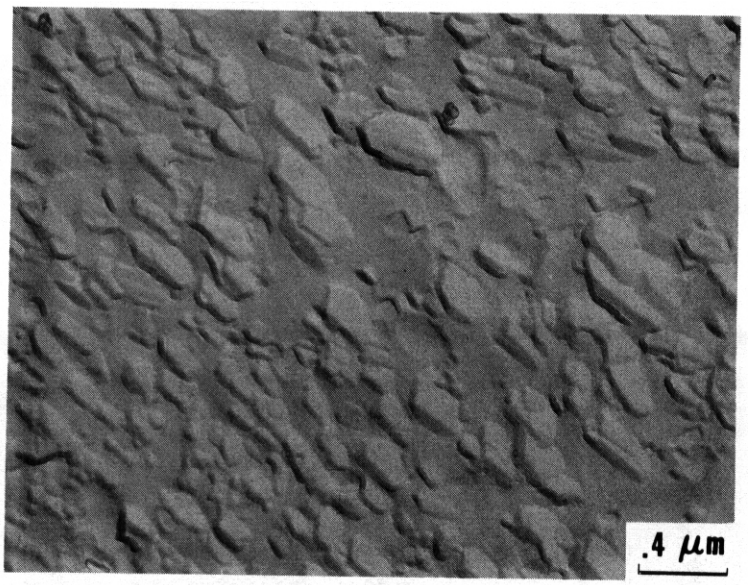

Figure 1. A carbon replica of a prior austenite grain boundary fracture of HT-9 tempered at 750°C and charged with hydrogen. The carbides cover a substantial fraction of the grain boundary area.

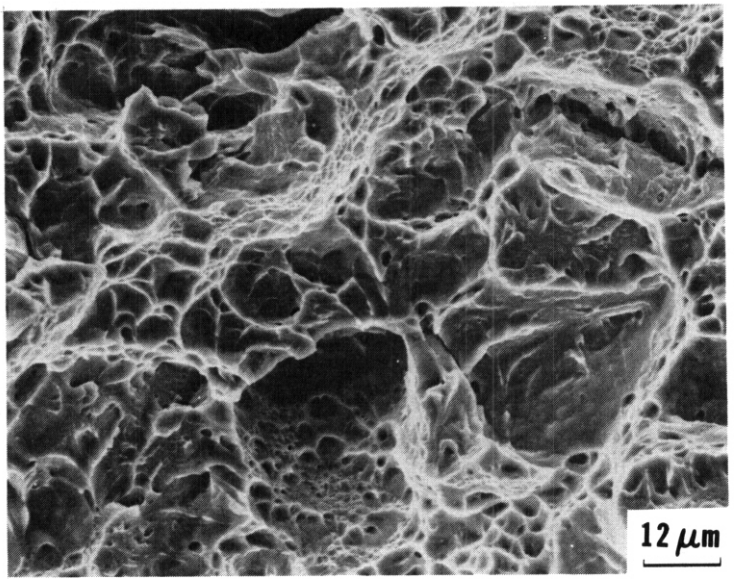

Figure 2a. A fractograph of the AC HT-9 tempered at 200°C.

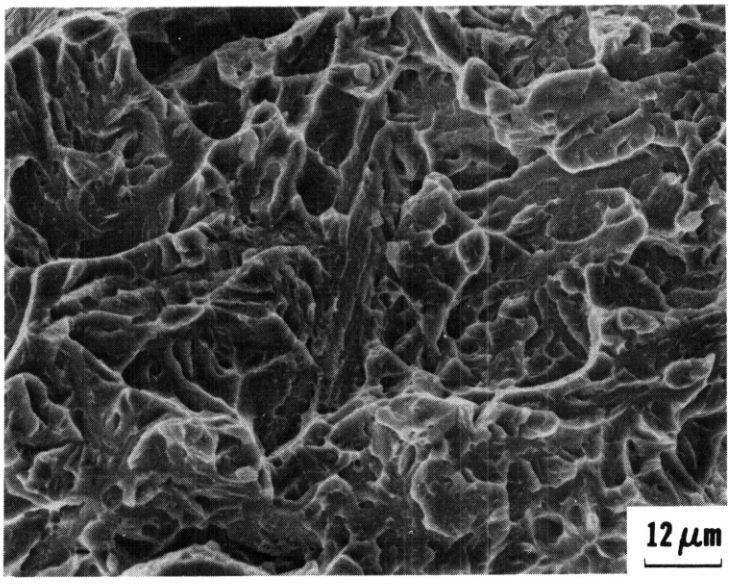

Figure 2b. A fractograph of the OQ HT-9 tempered at 200°C.

8.1 ft-lbs when tempered at 500°C (Table 1). Above 500°C the toughness of the AC structure increased with tempering temperature and reached a maximum of 78.6 ft-lbs when tempered at 750°C.

The toughness of the OQ and OQLN structures remained low until tempered above 500°C. When tempered above 500°C, the toughnesses of these structures also increased with tempering temperature. The AC and OQ materials had comparable impact toughness after tempering at 750°C, which is the standard temper for this alloy. However, the toughness of the OQLN structure was about 20 ft-lbs higher. The increased toughness of the OQLN material can be attributed partly to its lower hardness. The Rockwell (C scale) hardnesses of the AC, OQ, and OQLN structures tempered at 750°C were 25.8, 25.6 and 23.2 respectively. This corresponds to a difference in ultimate tensile strength of about 8 ksi between the AC and OQLN structures. The increased toughness of the CQLN material may also be due to a lower volume fraction of grain boundary carbides.

The effect of heat treatment on the retained austenite content of HT-9 is described in Table 2. After tempering at 200°C the AC structure contained about 9.5% retained austenite, while the OQ and OQLN structures contained about 6% and 4% retained austenite respectively. The effect of tempering temperature on the decomposition of the retained austenite was similar for the three structures. Some decomposition took place on tempering at 400°C and 500°C, but substantial decomposition was not observed until the structures were tempered at 550°C or higher.

Retained austenite can be transformed to untempered martensite by deformation. The more mechanically stable the retained austenite, the greater the strains required to induce its transformation to untempered martenstte. The effect of tempering on the mechanical stability as well as the volume fraction of retained austenite was assessed for the AC structure. These results are given in Table 3. After tempering at 200°C the mechanical stability of the retatned austenite was somewhat lower than normally observed for low alloy steels tempered at 200°C.[4] However, the retained austenite in this structure was very stable after

TABLE 2

VOLUME PERCENT RETAINED AUSTENITE

Tempering Temperature (°C)	Air Cool (AC)	Oil Quench (OQ)	Oil Quench & LN (OQLN)
200	9.5	6	4
400	8.8	5.1	3.7
500	7.9	4.6	3
550	4.7	2.8	1.2
600	0.7	0	0
650	0	0	0
700	0	0	0
750	0	0	0

TABLE 3

THE VOLUME PERCENT RETAINED AUSTENITE IN THE AC MICROSTRUCTURE AS A FUNCTION OF TENSILE STRAIN

Tempering Temperature (°C)	0% Strain	0.2% Strain	2% Strain
200	9.5	6.5	3.7
400	8.8	7.1	6.8
500	7.9	6.3	4.4
550	4.7	1.4	.3
600	0.7	0	0
650	0	0	0
700	0	0	0
750	0	0	0

tempering at 400°C; only 25% of the retained austenite transformed after 2% tensile strain. The mechanical stability of the retained austenite decreased as the tempering temperature was increased to 500°C and it was extremely low after tempering at 550°C.

7.7.5 Conclusions

Alternative heat treatments have been studied with the goal of minimizing the retained austenite content of as-quenched HT-9 and improving its impact toughness when tempered at 750°C. Oil quenching from the austenitization temperature followed by refrigeration in liquid nitrogen and multiple tempering at 750°C have resulted in a 20 ft-lb increase in Charpy impact toughness over the air cooled and tempered at 750°C microstructure. Research is continuing to determine the effect of this heat treatment on carbide precipitation at prior austenite grain boundaries. Work is also planned to assess the hydrogen compatibility of the **OQLN** microstructure.

7.7.6 References

1. J. M. Hyzak and W. M. Garrison, Jr., "Hydrogen Embrittlement of ESR Processed 12Cr-1Mo Steel", ADIP Semiannual Progress Report 3/31/81, DOE/ER-0045-8, pp. 401-413.
2. M. Sarikaya, G. Thomas, J. W. Steeds, S. J. Barnard, and G. D. W. Smith, Proceedings of the International Conference on Phase Transformations, TMS-AIME, Pennsylvania, H. I. Aaronson and C. M. Wayman (eds), in press.
3. B. de Miramon, "Quantitative Investigation of Strain Induced Strengthening in Steels", M. S. Thesis, University of California, Berkeley, CA, (Lawrence Berkeley Laboratory Report UCRL-17849) 1967.
4. R. M. Horn and R. O. Ritchie, "Mechanisms of Tempered Martensite Embrittlement", Metall. Trans., Vol. 9A, pp. 1039-1053, 1978.

7.8 PREPARATION OF ESR ALLOY HT-9 AND MODIFIED 9Cr-1Mo ALLOY FOR UBR IRRADIATION MPERIMENTS - J. R. Hawthorne (Naval Research Laboratory)

7.8.1 ADIP Task

The Department of Energy (DOE)/Office for Fusion Energy (OFE) has stated the need to investigate ferritic alloys under the ADIP program task. Ferritic Steels Development (Path E).

7.8.2 Objectives

Objectives of the present research task were to plan and obtain requisite specimens for advanced irradiation tests of Alloy HT-9 and Alloy 9Cr-1Mo (Mod.).

7.0.3 Summary

Alloy HT-9 and Alloy 9Cr-1Mo (Mod.) are being evaluated for potential application as first wall materials in magnetic fusion reactors. Objectives of the current studies are the assessment of material notch ductility and fracture toughness in the pre- and postirradiation conditions and the correlation of miniature test specimens required for high flux reactor experiments with standard size specimens.

Planning and preparations for two irradiation experiments involving Alloy HT-9 and Alloy 9Cr-1Mo (Mod.) have been completed. The experiments are designed to attain specific research objectives recommended by the OFE Working Group on Irradiation Effects in Martensitic Stainless Steels.

7.8.4 Progress and Status

7.8.4.1 Introduction

The ferritic stainless steel compositions, HT-9 and 9Cr-1Mo (Mod.), are being assessed for possible first wall applications in magnetic fusion reactors by the Magnetic Fusion Materials Program and €or duct applications in liquid metal fast breeder reactors by the

Cladding/Duct Alloy Development Program of the Department of Energy. For these proposed uses, fracture resistance properties before and after elevated temperature are being investigated. Specimen types include Charpy-V (C_v) specimens for notch ductility determinations, fatigue precracked Charpy-V (PCC_v) specimens for dynamic fracture toughness (K_J) determinations and compact tension (CT) specimens for static fracture toughness determinations.

Recent NRL studies[1] explored the radiation resistance of AOD-melted Alloy HT-9 (plate) as a function of service temperature (93°C and 288°C). The studies employed C_v and PCC_v specimens irradiated in controlled temperature assemblies in the water cooled reactor at the State University of New York at Buffalo (UBR). Miniature PCC_v specimens (half standard size) and *2.54* mm thick CT specimens (0.5T size except for thickness) were included in the irradiation assemblies also. The 93°C irradiation data showed the alloy to be unacceptable for 93°C high fluence service. The C_v and K_{Jd} transition temperatures were elevated to 93°C with only 7.3 x 10^{19} n/cm^2, E >0.1 MeV. On the other hand, the C_v transition temperature elevation produced by 288°C irradiation was only one third that produced by the 93°C irradiation. The resultant transition temperature remained below ambient. Accordingly, the OFE Working Group on Irradiation Effects in Martensitic Stainless Steels (WGIEMSS) has recommended the 288°C radiation resistance of ESR-melted HT-9 be evaluated at the same fluence as a follow-on effort. It recommended, in addition, that an ESR-melted 9Cr-1Mo (Mod.) plate be evaluated with 150°C irradiation as a first step in determining the low temperature service limit of this alloy.

7.8.4.2 Progress

Plans have been completed for the follow-on experiments in the UBR. The one experiment to be irradiated at 150°C will contain C_v, tensile and miniature C_v specimens (standard notch) of the *25.4* mm thick 9Cr-1Mo (Mod.) plate from the OFE/ESR reference melt (heat 30176). A very limited number of C_v specimens of an HT-9 plate will also be included for correlating back to the earlier (HT-9) experiment

discussed above. The specimen inventory for the 150°C experiment has been completed; experiment construction has commenced.

The second experiment will contain C_v, PCC_v, tensile and miniature C_v specimens of a 15.9 mm thick HT-9 plate from the OFE/ESR reference melt (heat 9607R2). This experiment will be irradiated at 300°C rather than 288°C as first planned in the interest of matching the exposure temperature of a planned ORNL-HIFR experiment. The results jointly should provide insight into the fluence dependency and potential for radiation embrittlement saturation in this alloy. The specimen inventory for the UBR experiment is not yet complete; experiment construction should commence in December.

7.8.4.3 Future Plans

It is planned that the irradiation phase of the experiments be completed in time to have the C_v and PCC_v test results available by mid-1983.

7.8.4.4 References

(1) J. R. Hawthorne, "Postirradiation Notch Ductility and Fracture Toughness Behavior of AOD Heat of Alloy HT-9," Alloy Development for Irradiation Performance, Semiannual Progress Report for the Period Ending 31 Mar 1982, DOE/ER-0045/6, pp. 336-341.

7.9 MINIATURE CHARPY IMPACT TEST RESULTS FOR IRRADIATED FERRITIC ALLOYS - W. L. Hu (Westinghouse Hanford Company)

7.9.1 ADIP Task

The Office of Fusion Energy/Department of Energy, has established the need to determine the fracture toughness of candidate fusion program ferritic alloys (Path E).

7.9.2 Objective

The objective of this work is to perform Charpy impact tests on the candidate ferritic alloys that have been irradiated in EBR-II as a part of the AD-2 experiment, and to evaluate the shift of ductile-to-brittle transition temperature (DBTT) and the reduction of upper shelf fracture energy due to neutron irradiation.

7.9.3 Summary

Impact tests of irradiated Charpy specimens made of ferritic alloys were conducted at temperatures from -68°C to 250°C. The specimens involve four different material stocks, namely, HT-9 base metal, HT-9 weld metal, HT-9 heat-affected-zone (HAZ) and modified 9Cr-1Mo base metal. The specimens were irradiated in EBR-II to a peak exposure of approximately 13 dpa at temperatures of 390, 480, 500 and 550°C. Specimens made of unirradiated HT-9 base metal and modified 9Cr-1Mo base metal were also tested.

For HT-9, unirradiated base metal specimens had a DBTT at 5°C and an upper shelf energy of 47 J/cm^2. Following irradiation, all conditions showed a significant increase in DBTT and a decrease in the upper shelf energy to approximately 30 J/cm^2. Irradiation at 390, 450, 500 and 550°C resulted in DBTT shifts of 124, 26, 32 and 56°C, respectively. For modified 9Cr-1Mo, unirradiated base metal specimens had DBTT at -25°C and an upper shelf energy of 80 J/cm^2. Following irradiation at 480, 500 and 550°C no shift in DBTT was observed but the upper shelf energy was reduced to approximately 88 J/cm^2. However, following irradiation at 390°C the DBTT was shifted 58°C with the upper shelf energy reduced to 47 J/cm^2. Therefore, irradiation results in a lowering of

the upper shelf energy and in many cases a shift in DBTT. The shift in DBTT is greatest at lower irradiation temperatures.

The weldment and HT-9 HAZ samples exhibited the same or slightly lower DBTT and similar upper shelf energies as the base metal HT-9. Therefore, ferritic alloys when used in fusion first wall applications are not expected to suffer any degradation in performance due to the presence of welds.

7.9.4 Progress and Status

7.9.4.1 Introduction

Ferritic alloys are susceptible to brittle failure under certain service conditions. It is well known that the temperature at which ferritic alloys undergo a transition in fracture mode from ductile to brittle shifts toward higher temperatures with increasing neutron exposure. Accordingly, the change in the DBTT with fluence as well as irradiation temperature is an important factor in the selection of alloys for fusion reactor applications.

Miniature Charpy specimens were prepared for the study of the effect of irradiation on the transition of fracture mode. The specimens were irradiated in EBR-II to a peak exposure of approximately 13 dpa at temperatures of 390, 450, 500 and 550°C. Base metal, weldments and HAZ samples of HT-9 and base metal samples of modified 9Cr-1Mo were investigated in this experiment. Specimens were precracked prior to irradiation. Details of material processing and specimen preparation were described in Reference 1.

The Westinghouse Hanford Company miniature Charpy specimen has the same cross sectional dimensions as a half-size standard Charpy specimen but differs in length and notch dimensions. The overall specimen length is sufficient to permit the use of the standard span dimension 4W (W = 5.00 mm) for both precracking and Charpy type testing. The orientation in which the Charpy specimens were machined from the HT-9 and 9Cr-1Mo alloy stock and HT-9 weld plate is shown in Fig. 7.9.1. The HT-9 weld and HT-9 HAZ Charpy specimens were machined so that properties of the fusion metal and the heat-affected-zone would be sampled. The location

of the notch within the weld region was verified for each specimen by visual examination following an oxalic acid electrolytic etch. Although the notch in both weld and weld/HAZ Charpy specimens was located within the weld, fatigue cracks were produced in each specimen, which, in the case of the HAZ specimen, extended into the heat-affected-zone.

The specimens were loaded into two *B-7c* weeper capsules, which were designed to maintain the specimen temperature at 390°C, and into four B-7c subcapsules designed to maintain the specimen temperatures at *450, 500* (two subcapsules) and 550°C during irradiation. The specimens were irradiated in EBR-II to approximately *13* dpa as part of the AD-2 experiment.

7.9.4.2 Experimental Procedure

A drop tower was employed as the impact test device. The test system was described in Reference 2. Details of the specimen, the anvil and the dynamic tup are outlined in Fig. *7.9.2.* A temperature conditioning chamber and specimen transfer mechanism, which permits remote control for the testing of irradiated specimens, was designed and integrated with the drop tower, Fig. *7.9.3.* The specimen is heated by direct electric resistance heating. Fig. *7.9.4* shows the arrangement of the electrodes and the Charpy specimen. The electrodes are made of stainless steel and are gold plated. A notch was machined in each electrode near the contact surface to streamline the current flow and thus achieve an uniform temperature profile in the specimen. The specimen was brought to the electrodes, and was seated in the conditioning chamber by a pneumatically actuated air piston. The contact force was approximately *40* Newtons. A spring loaded thermocouple with special surface probe monitored the temperature in the specimen. Table *7.9.1* shows the temperature profile in the specimen which was determined by spot welded thermocouples positioned along the specimen. The middle portion of the specimen shows a temperature uniformity within ±2°C. Toward the ends of the specimen where the electrode is attached, the temperature is generally higher. This effect is expected to be compensated by the fact that when the specimen is brought to the testing station, both ends of the specimen are rested on a massive anvil which works as a thermal sink. The temperature variation across

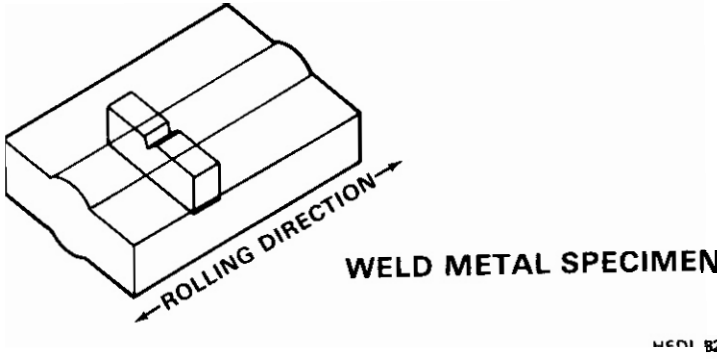

Fig. 7.9.1. Orientation of Charpy Specimens with Respect to the Stock Material.

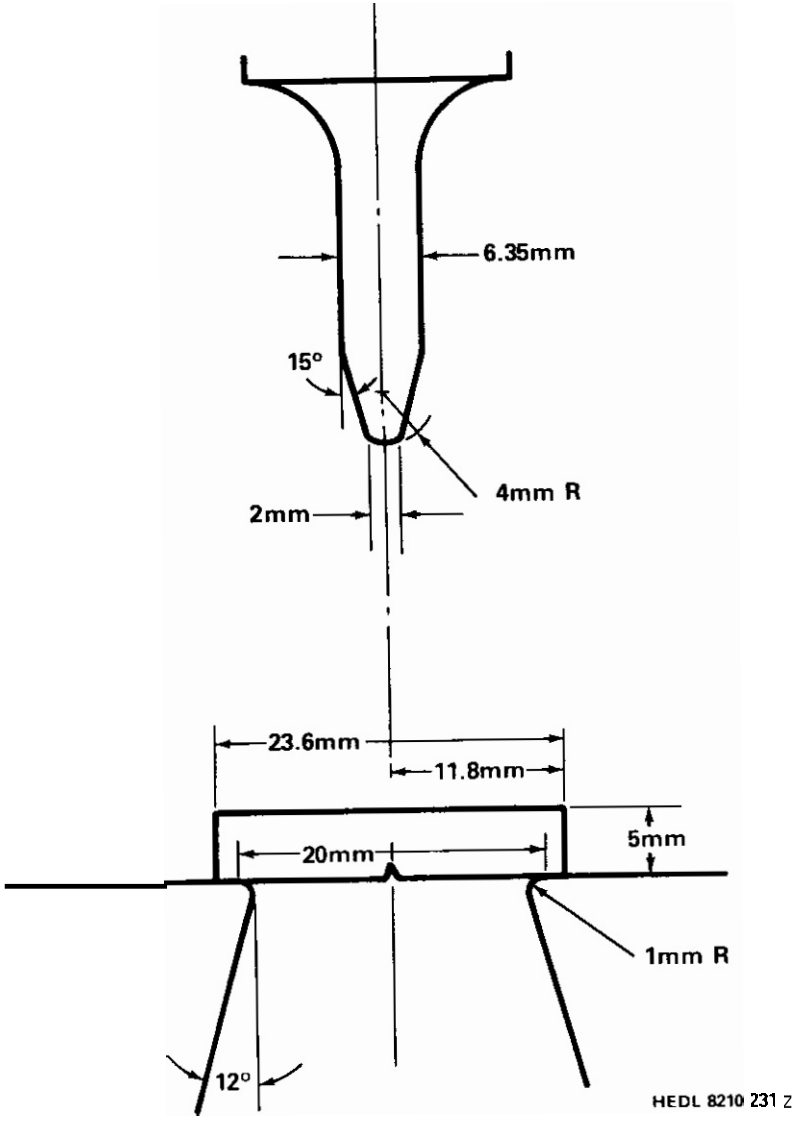

Fig. 7.9.2. Details of Dynamic Tup, Charpy Specimen and Anvil.

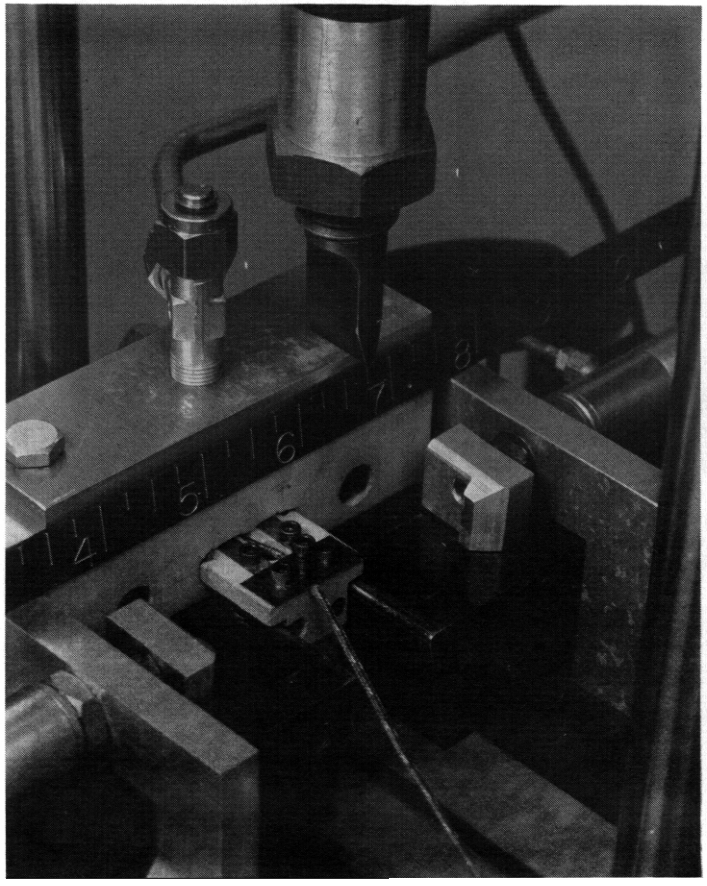

(a)

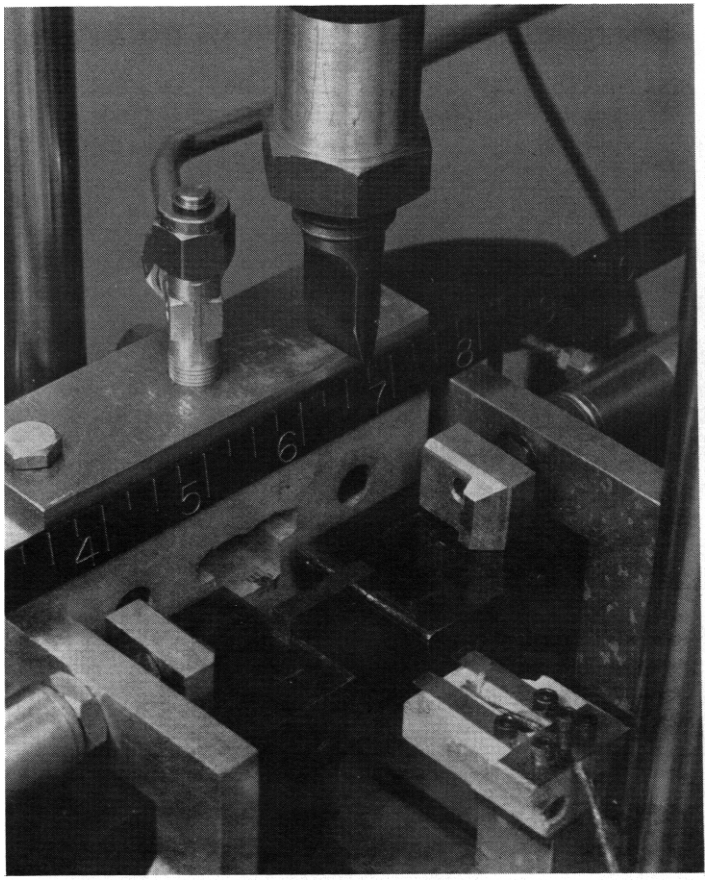

(b)

Fig. 7.9.3. Automated Testing Equipment for Charpy Impact Tests. (a) Specimen in Furnace, (b) Specimen in Testing Position.

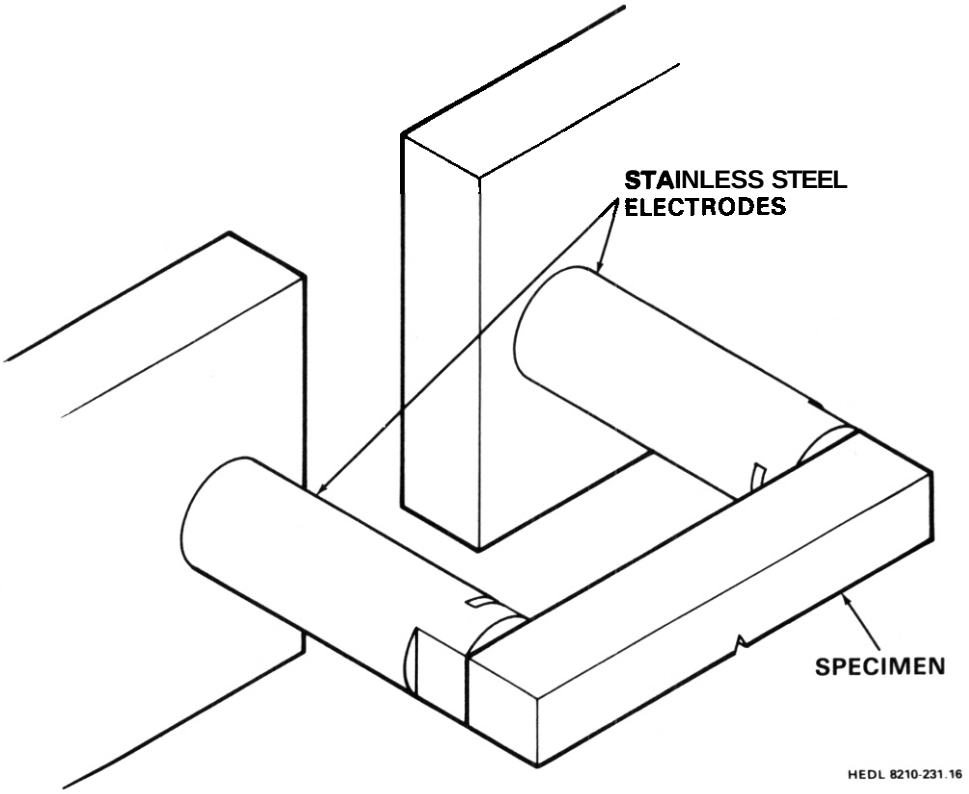

Fig. *7.9.4.* Detail of Specimen Heating Arrangement.

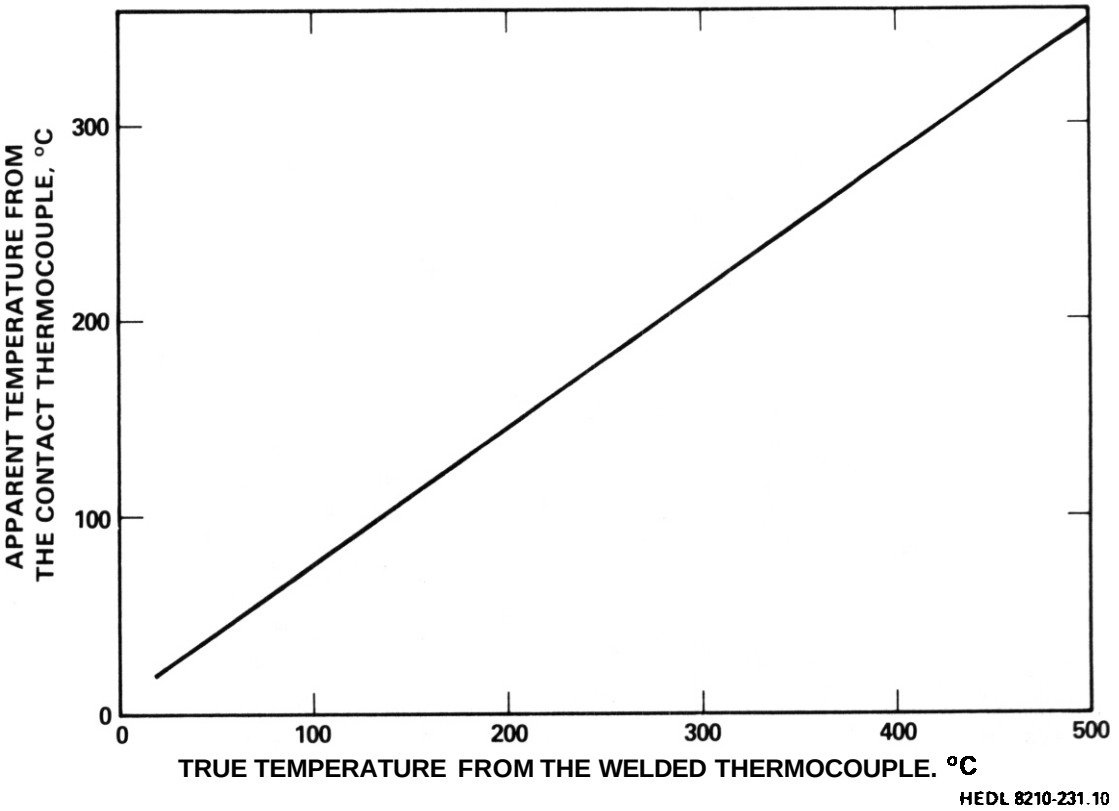

Fig. 7.9.5. Temperature Calibration Curve.

Table 7.9.1. Temperature Profile Along the Charpy Specimen

T.C.	# 1	# 2	# 3	# 4	# 5	# 6
Position from the Center of the Specimen	-9.1mm	-5.5mm	-1.8mm	+1.8mm	+5.5mm	+9.1mm
Experiment I	108°C 218°C 316°C 422°C 525°C 622°C		101°C 201°C 300°C 401°C 503°C 601°C	100°C 198°C 300°C 401°C 503°C 601°C		106°C 206°C 320°C 429°C 538°C 642°C
Experiment II		152°C 202°C 305°C 405°C 506°C 604°C	149°C 200°C 301°C 400°C 501°C 599°C	149°C 200°C 302°C 400°C 502°C 602°C	152°C 206°C 312°C 411°C 516°C 620°C	

the fracture path was measured and tabulated in Table 7.9.2. A temperature calibration was conducted for the contact thermocouple versus a thermocouple welded at the notch root of the specimen. The result is shown in Fig. 7.9.5. The calibration was made with specimens of all four different material stocks. The agreement was better than 2°C in all cases. The specimen was maintained at the testing temperature for a minimum of two minutes before the impact. The transient temperature change during the specimen transfer from the conditioning chamber to the testing station was also measured. For a specimen heated to 600°C and then removed from the conditioning chamber, the temperature in the specimen dropped to 596°C in four seconds. Since the impact normally took place in less than 0.2 seconds, the transient temperature loss is insignificant.

Table 7.9.2. Temperature Variation Across the Fracture Path

	Temperature in °C					
T.C. # 1 Positioned at Notch Root	~ i 0	Z00	298	402	501	600
T.C. # 2 Positioned at Back of the Specimen	111	201	299	404	503	602

The automation mechanism is illustrated in Fig. 7.9.6. During the impact test, the specimen was transferred from the conditioning chamber to the testing position in less than 0.1 second. Two precisely timed air pistons activate the specimen stripper to release the specimen from the specimen carriage and center the specimen in the testing position while the specimen carriage continues to move out of the impact path. The strippers retract automatically and leave only the specimen on the anvil. As the specimen carriage moves to the end of its travel, the instrumented tup is trigged from a predetermined height by an air switch. The positioning mechanism has an accuracy better than 0.05 mm. The impact test was completed within 0.2 seconds after the specimen left the conditioning chamber. For the tests conducted below the room temperature, vaporized liquid nitrogen was driven into the chamber by means of compressed air to cool the specimen. The temperature of the specimen was controlled by adjusting the flow rate.

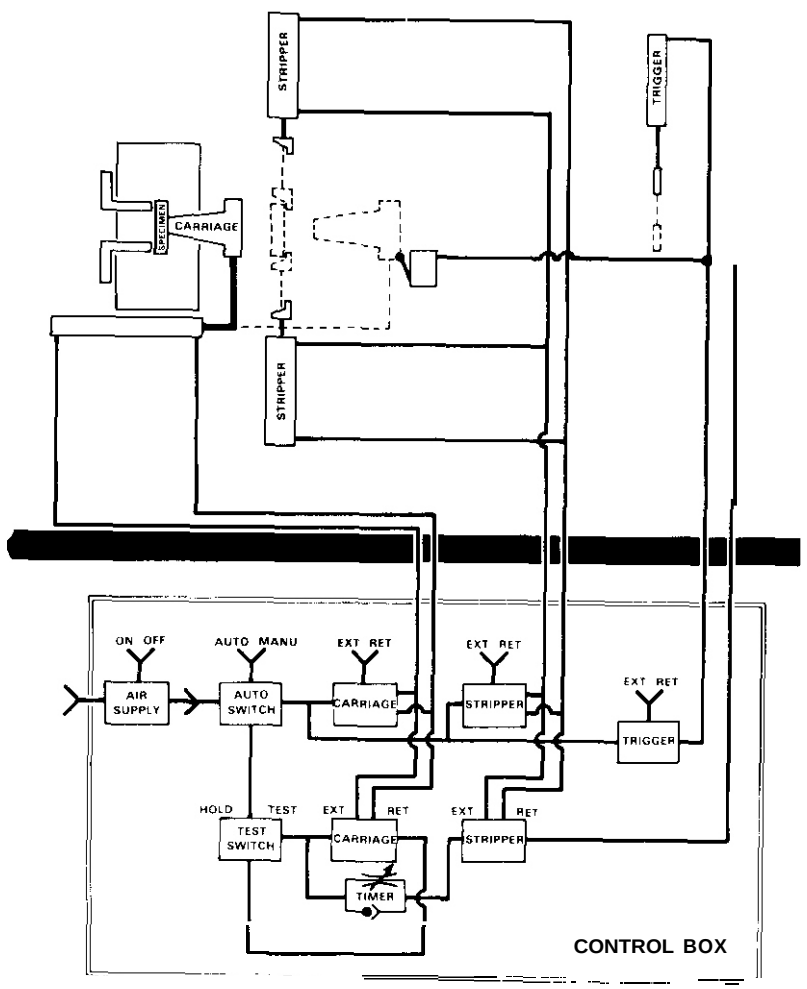

Fig. 7.9.6. Schematic Illustration of Automated Testing Mechanism.

The calibration of the instrumented tup required the adjustment of the load signal gain control so that the maximum load obtained during dynamic testing was identical to the maximum load determined during the slow bend testing of a strain rate insensitive alloy. The specimen used for calibration was a one-half size Type A CVN specimen of 6061 aluminum in the T651 heat treated condition. The impact velocity was determined by measuring the time interval required for a flag passing through the infrared sensor in a free fall. The velocity of the crosshead just prior to specimen contact was 3.3 m/sec. During the two week testing period, the instrumented tup and the impact velocity were checked daily. The maximum fluctuation was less than five percent.

The fracture energy of the specimen was electronically integrated from the load-time trace. Both load-time and energy-time traces were recorded by photographs. Typical load and energy traces are shown in Fig. 7.9.7. The apparent energy absorbed by the specimen during the impact, E_a, was then measured from the photographs. The true fracture energy was calculated by the following equation

$$E = Ea\left(1 - \frac{E_a}{4E_o}\right) \qquad (1)$$

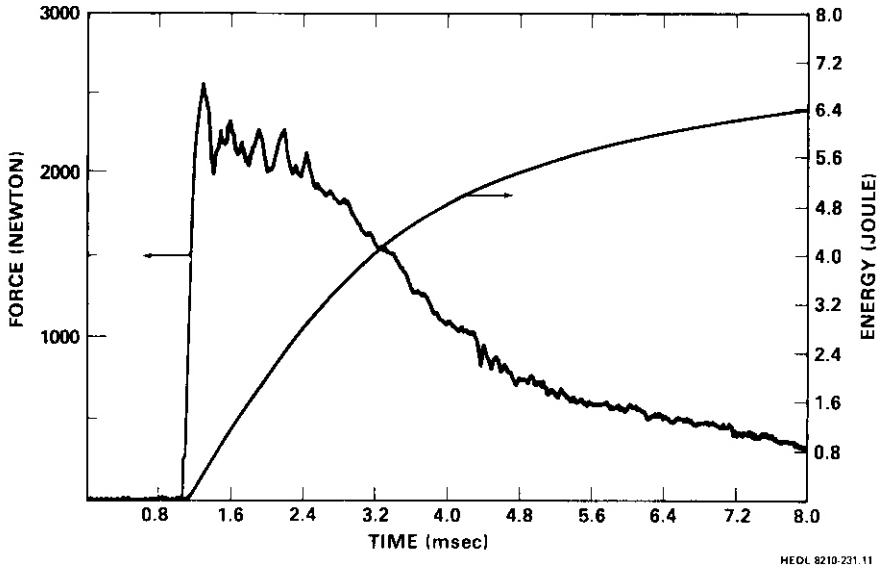

Fig. 7.9.7. A Typical Load Trace for the Impact Test.

when E_o is the total available energy at impact. The fracture energy was scaled by the cross section area of the remaining ligament (after the fatigue precrack) of each specimen. For unirradiated 9Cr-1Mo specimens a digital oscilloscope was employed to collect the test results. Each load-time trace was divided into 4000 digitized points and stored permanently on magnetic tape. The data are later processed through a computer to generate the fracture energy, maximum load and other relevant information.

7.9.4.3 Results and Discussion

The results for the HT-9, HT-9 weld, HT-9 HAZ and 9Cr-1Mo specimens irradiated to 13 dpa (3×10^{22} n/cm^2) at temperatures of 390, 450, 500 and 550°C are tabulated in Tables 7.9.3 through 7.9.6 and are shown in Figs. 7.9.8 through 7.9.11. The transition curves for the unirradiated HT-9 and modified 9Cr-1Mo base metal are included in Fig. 7.9.8 and Fig. 7.9.11, respectively for comparison.

Table 7.9.3. HT-9 Base Metal (13 dpa)

Irradiation Temperature (°C)	Specimen I.D. (TT)	Test Temperature (°C)	Fracture Energy (ft-lb)	(J)	Fracture Energy Normalized by Area (J/cm^2)
390	55	200	2.12	2.87	21.9
	04	182	2.54	3.44	20.1
	16	116	1.14	1.55	11.5
	51	60	0.2	.27	2.1
	01	25	0	0	0
450	43	150	2.94	3.99	30.1
	22	80	2.18	2.96	22.7
	08	26	1.53	2.07	16
	45	-10	0.72	.98	7.6
500	21	200	2.86	3.88	29.7
	13	100	2.24	3.04	23
	46	60	2.12	2.87	22.4
	30	28	1.6	2.17	16.6
	47	0	0.78	1.06	8.0
	64	-50	0.27	.37	2.8
550	66	160	2.45	3.32	25.2
	12	100	1.8	2.44	19.5
	05	40	1.09	1.48	11.4
	09	-20	0.29	.39	3.2

Table 7.9.4. HT–9 **Weld Metal** (13 **dpa)**

Irradiation Temperature (°C)	Specimen I.D. (TI)	Test Temperature (°C)	Fracture Energy (ft-lb)	Fracture Energy Normalized by Area (J/cm^2)
390	59	450	2.06	22.1
	58	250	2.11	21.3
	32	200	2.57	26.5
	30	180	2.66	27.6
	27	132	1.68	17.5
	48	100	0.9	9.0
	28	75	0.35	3.62
450	33	120	3.13	31.3
	42	40	2.81	29.1
	52	20	1.29	13.8
	57	–50	0.28	2.8
500	46	200	3.15	33.9
	29	100	3.28	33.5
	56	75	2.85	30.8
	50	50	2.73	27.7
	35	28	1.46	15.5
	37	0	0.8	7.9
	47	–20	0.49	5.0
550	41	80	2.98	32
	34	50	2.4	24.5
	43	10	0.91	10.0
	55	–30	0.32	3.3

Table 7.9.5. HT–9 **Heat-Affected-Zone** (13 **dpa)**

Irradiation Temperature (°C)	Specimen I.D. (TX)	Test Temperature (°C)	Fracture Energy (ft-lb)	Fracture Energy Normalized by Area (J/cm^2)
390	10	180	3.1	30.8
	15	150	2.84	29.3
	03	150	2.39	24.5
	07	120	2.74	28.2
	11	85	1.36	14.0
	06	50	0.43	4.5
	22	25	0.3	3.3
500	09	200	3.07	31.9
	01	100	3.95	39.6
	16	26	5.59	57.2
	21	26	3.26	33.8
	04	0	1.35	13.6
	23	–20	1.07	10.9
	05	–65	0.24	2.6

Table 7.9.6. Modified 9Cr-1Mo Heat 30182 (13 dpa)

Irradiation Temperature (°C)	Specimen T.D. (TV)	Test Temperature (°C)	Fracture Energy (ft-lb)	(J)	Fracture Energy Normalized by Area (J/cm^2)
390	01	100	4.39	5.95	46.0
	12	75	4.55	6.17	46.7
	14	50	4.51	6.12	46.9
	09	25	1.39	1.88	14.8
450	15	10	5.24	7.11	54.5
	04	-40	1.56	2.12	16.4
	17	-60	0.21	.28	2.2
	26	24	5.54	7.51	57.5
500	02	25	4.9	6.64	51.1
	13	0	5.08	6.89	52.1
	21	-25	1.93	2.62	20.2
	05	-50	0.69	.94	7.2
550	03	27	5.11	6.93	50.8
	07	-10	4.61	6.25	47.7
	08	-25	2.58	3.50	26.6
	18	-65	0.56	176	5.8
	(AF)				
Unirradiated	46	40	11.87	16.10	78.3
	31	25	10.46	14.18	70.3
	32	25	12.16	16.49	81.5
	34	0	10.93	14.82	72.6
	41	-10	9.24	12.53	61.1
	33	-20	6.41	8.69	42.6
	42	-30	4.67	6.33	31.3
	40	-40	1.64	2.50	12.3
	43	-40	2.63	3.57	17.6
	44	-50	1.42	1.93	9.51
	39	-60	1.32	1.79	8.81
	38	-80	0.46	.62	3.08
	45	-100	0.25	.34	1.71

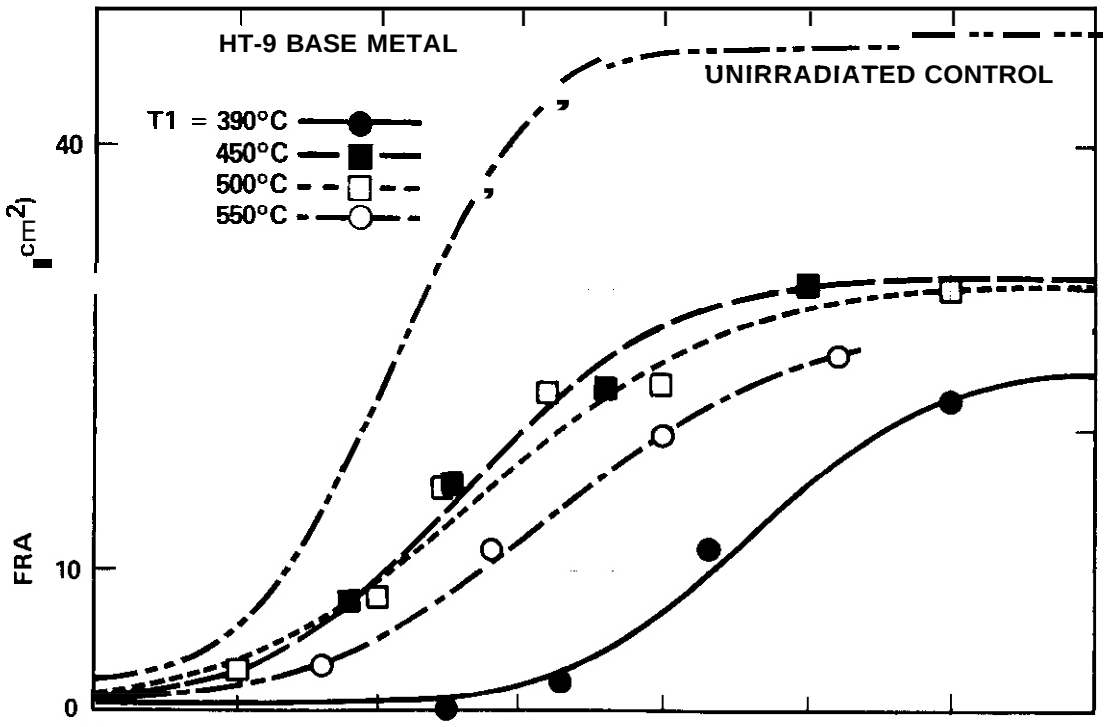
HT-9 BASE METAL
UNIRRADIATED CONTROL
T1 = 390°C
450°C
500°C
550°C
40
10
0
FRA
cm2)

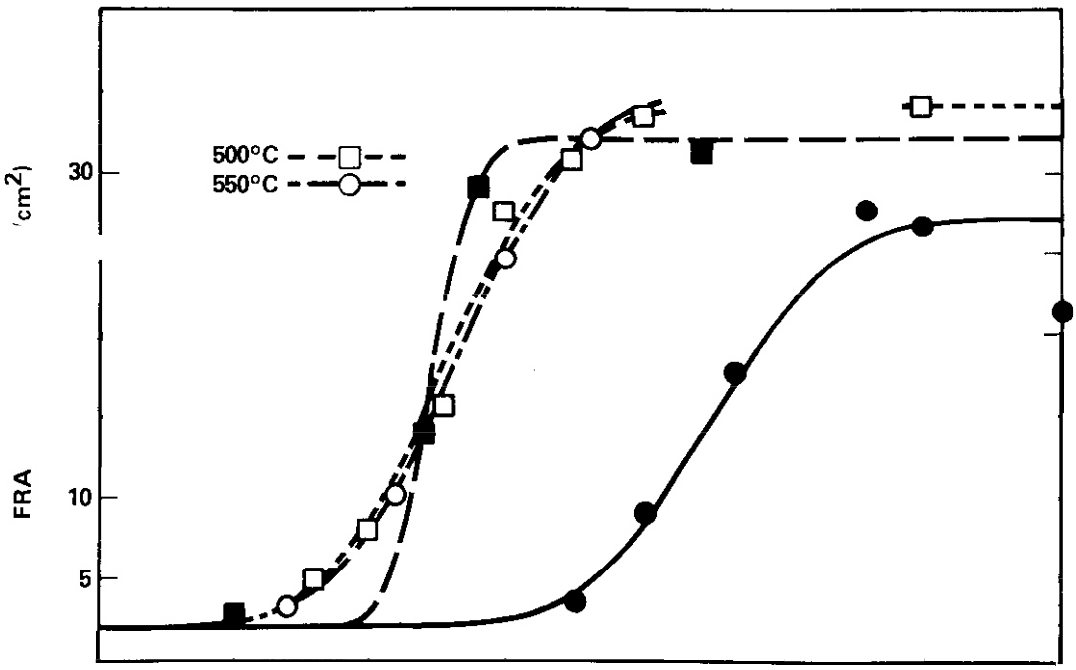
500°C
550°C
30
10
5
FRA
cm2)

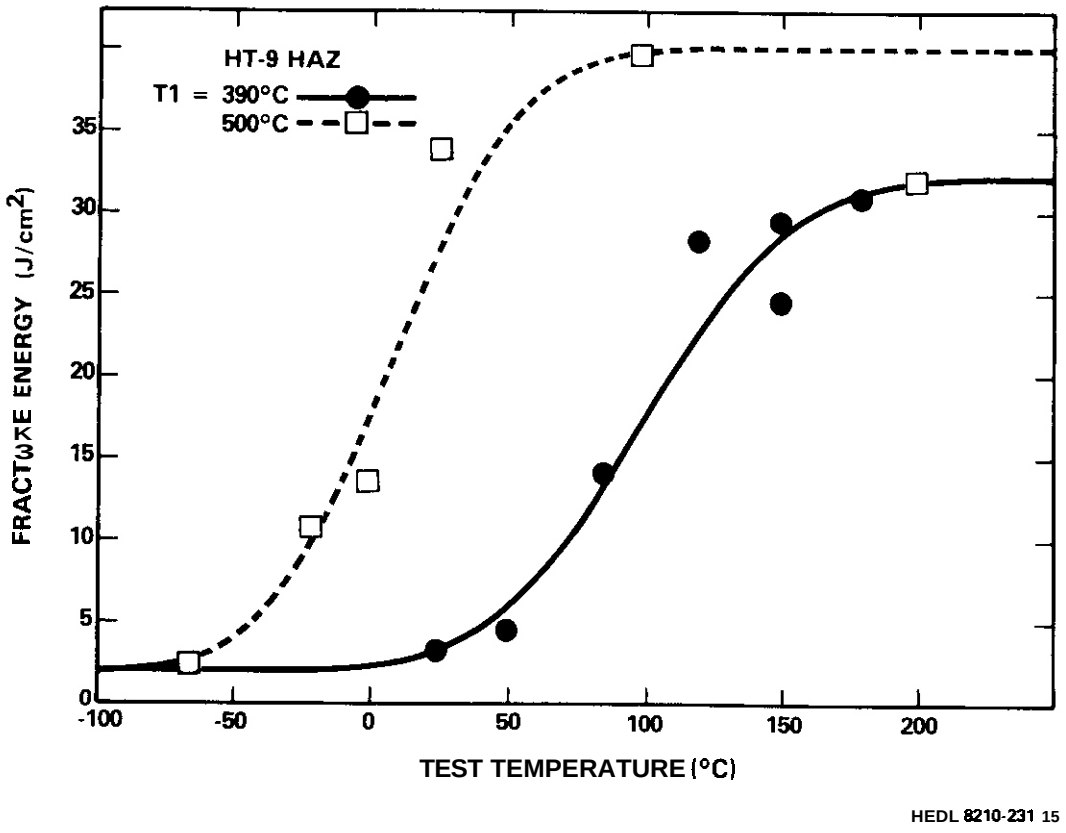

Fig. 7.9.10. The Total Fracture Energy E(T) as a Function of Temperature for HT-9 Heat-Affected-Zone.

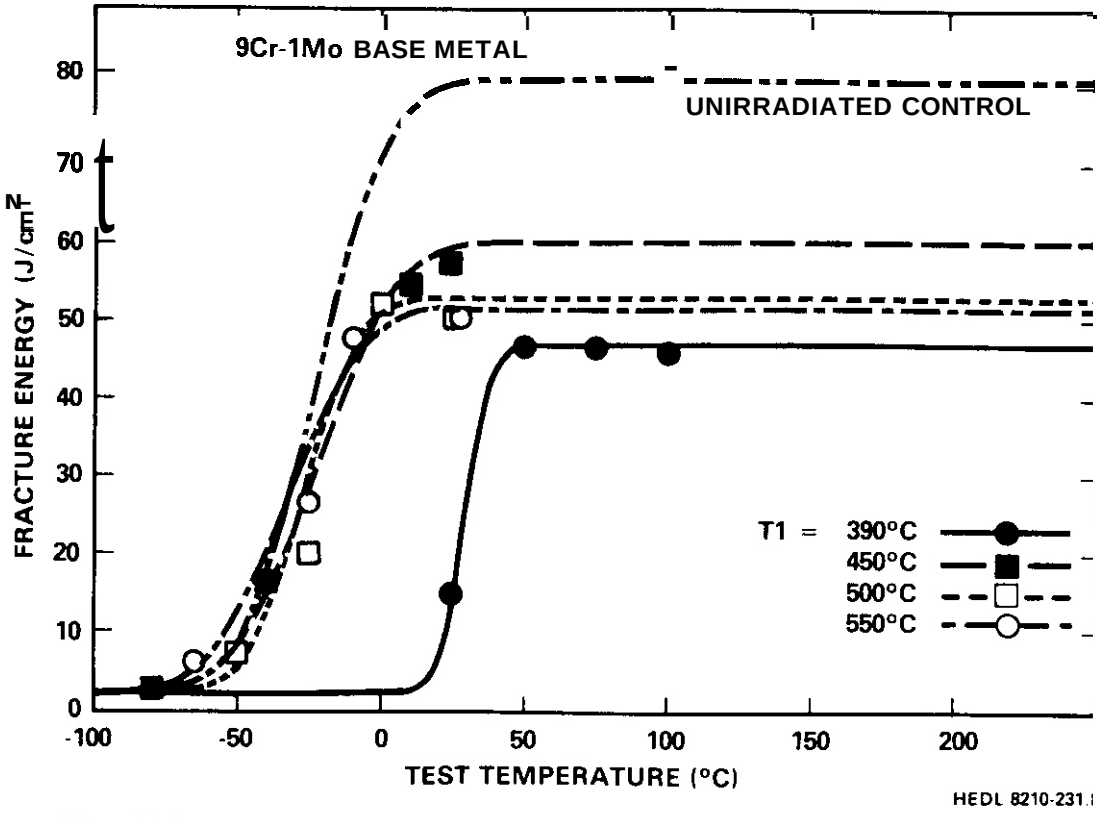

Fig. 7.9.11. The Total Fracture Energy E(T) as a Function of Temperature for 9Cr-1Mo Base Metal.

The results for the HT-9 base metal show a 40 percent reduction in upper shelf fracture energy as well as a shift in DBTT due to irradiation. Specimens irradiated at 390, 450, 500 and 550°C have a shift in DBTT of 124, 26, 32 and 56°C, respectively. The comparison of unirradiated and irradiated 9Cr-1Mo base metal result shows a reduction of 25 percent in upper shelf fracture energy, hut only specimens irradiated at 390°C exhibit a shift of DBTT of 55°C. Test results for the specimens irradiated at 450, 500 and 550°C do not show any change in DBTT due to neutron exposure. The results from HT-9 weld and HT-9 HAZ are also very interesting in that they demonstrated that the HT-9 weldment has the same, or slightly lower, DBTT as HT-9 base metal. This result is significant because it indicates that the ferritic alloys used in fusion first wall applications may not suffer any degradation in performance due to the presence of welds.

The fracture surfaces of selected specimens have been examined and reported in Reference 3. The results indicate that irradiation hardening due to G-phase formation at 390°C is responsible for the large shift in DBTT found in HT-9. Reduction in upper shelf fracture energy of HT-9 following higher temperature irradiation is attributed to precipitation at delta ferrite stringers. Reduction in toughness as a consequence of irradiation in modified 9Cr-1Mo is attributed to carbide precipitation.

7.9.4.4 Correlations

A correlation method was developed to describe the transition behavior of the fracture mode. The temperature dependence of the fracture energy is divided into three regions, namely, the upper shelf region, the transition region and the lower shelf region. In general, two parameters were employed to characterize each region. Outside the transition region a linear dependence was assumed, i.e.,

$$E_B(T) = \alpha_B + \beta_B T \qquad \text{for the lower shelf region,} \qquad (2)$$

and

$$E_D(T) = \alpha_D + \beta_D T \qquad \text{for the upper shelf region.} \qquad (3)$$

$E_B(T)$ denotes the fracture energy of purely brittle fracture and $E_D(T)$ denotes the fracture energy of purely ductile fracture. In the transition

region, the contribution of a particular fracture mode to the total fracture energy is weighted by a Gauss integral $P_D(T)$

$$E(T) = E_D(T)\ P_D(T) + E_B(T)(1 - P_D(T)) \quad . \qquad (4)$$

The Gauss integral $P_D(T)$ is defined by

$$P_D(T) = \frac{1}{b\sqrt{2\pi}} \int_{-} \left| \frac{(X - T)^2}{} \right|$$

where the parameter b is the band width of the transition region, and T_o is the mid-transition temperature.

This correlation treatment, unlike other S-shaped functions, allows more flexibility outside the transition region. Nevertheless, from the limited data currently obtained, both the upper shelf region and the lower shelf region are assumed to be temperature independent. Accordingly, β_B and β_D are identically zero and α_B and α_D are denoted by the lower shelf fracture energy and upper shelf fracture energy. As a consequence each transition curve is defined by four parameters, namely, E_B, b, T_o and E_D. The transition curve E(T) can be generated from Equations (4) and *(5).* The parameters E_D, b, T_o are tabulated in Table *7.9.7.* E_B is *0.5* J/cm^2 for HT-9 base metal and *2* J/cm^2 for all the other three alloys.

7.9.5 Conclusions

An impact testing device has been automated to handle the irradiated Charpy specimens. Specimens made of four ferritic alloys irradiated at temperatures 390, *450, 500* and 550°C were tested. The DBTT and the upper shelf fracture energies for each of the four alloys at each irradiation conditions were determined. The results indicate a lowering of the upper shelf energy and in many cases an upward shift of DBTT due to irradiation. It was found that the shift was greatest at the lowest irradiation temperature. The HT-9 weldment and HAZ exhibited the same or slightly lower DBTT and similar upper shelf energies as the base metal HT-9.

Table 7.9.7. Correlation Parameters

	Irradiation Temperature (°C)	E_D (J/cm^2)	b (°C)	T_o (°C)
HT-9 Base Metal	Unirradiated	47	45	5
	390	24	50.1	129
	450	30.5	56.3	30.8
	500	30	68.4	37.0
	550	27	65.9	60.8
HT-9 Weld	390	27	35.6	124
	450	32	12.7	23.4
	500	34	33.9	28.2
	550	35	35.4	33.2
HT-9 HAZ	390	32	43.5	98.9
	500	40	36.4	8.9
9Cr-1Mo Base Metal	Unirradiated	80	20	-25
	390	47	7.3	29.2
	450	60	21.3	-23.2
	500	53	14.8	-27.3
	550	52	20.9	-32.6

E_D = Upper Shelf Energy
b = Transition Band Width
T_o = Mid-Point Transition Temperature

7.9.6. Future Work

This work will continue when the specimens irradiated in HFIR at a low temperature (50°C) become available.

7.5.7 References

1. R. J. Puigh and N. F. Panayotou, "Specimen Preparation and Loading for the AD-2 Ferritics Experiment," ADIP Quart. Prog. Rep. June 30, 1981, DOE/ER-0045/3, pp. 261-293.
2. W. L. Hu and N. F. Panayotou, "Miniature Charpy Specimen Test Device for the Ferritic Alloy HT-9," ADIP Quart. Prog. Rep. Sept. 30, 1981, DOE/ER-0045/7, pp. 235-251.
3. D. s. Gelles and W. L. Hu, "Fractographic Examination of HT-9 and 9Cr-1Mo Charpy Specimens Irradiated in the AD-2 Test," (This Document: 7.2).

8. STATUS OF IRRADIATION EXPERIMENTS AND MATERIALS INVENTORY

8.1 IRRADIATION EXPERIMENT STATUS AND SCHEDULE — M. L. Grossbeck (Oak Ridge National Laboratory)

There are a large number of planned, in-progress, or completed reactor irradiation experiments that support the ADIP program. Table 8.1.1 presents a summary of the parameters that describe experiments that have been completed. Experiments that have been removed from the reactor only recently, are currently undergoing irradiation, or are planned for future irradiation are included in the schedule bar charts of Table 8.1.2.

Experiments are now under way in the Oak Ridge Research Reactor (ORR) and the High Flux Isotope Reactor (HFIR), which are mixed-spectrum reactors, and in the Experimental Breeder Reactor (EBR-II), which is a fast reactor.

During the reporting period experiments HFIR-CTR-34 and -35 were removed from the HFIR. These are the first elevated-temperature HFIR experiments with Charpy specimens of ferritic alloys. Experiment HFIR-MFE-T1, containing ferritic alloys, also completed irradiation at 55°C. In addition, HFIR-MFE-RB1, containing a wide variety of specimens of ferritic alloys, completed irradiation. Some of these specimens will be reencapsulated and irradiated in HFIR-MFE-RB3. Three elevated-temperature experiments containing tensile specimens of ferritic alloys — HFIR-CTR-39, -40, and -41 — were loaded into the reactor.

The ORR-MFE-4A spectral tailoring experiment developed a containment leak on April 26, 1982. The capsule was removed from the reactor, disassembled in hot cells, and examined in detail to determine the cause of failure. Following diameter measurements on the pressurized tube specimens and removal of some transmission electron microscopy disk specimens, the specimens were reencapsulated and the assembly returned to the reactor. Although unplanned, the operation verified the techniques of interim examination and reencapsulation of the ORR-MFE-4 experiment.

The initial scheduling of a new series of experiments for the HFIK, the HFIR-JP series, is shown on the final page of Table 8.1.2. The experiments are part of a joint program between the United States and Japan. They will contain specimens from both national programs, with the first eight experiments devoted to path A alloys. Irradiation will be in the outer target rod positions in the flux trap region of HFIK.

Table 8.1.1. Descriptive Parameters for Completed ADIP Program Fission Reactor Irradiation Experiments

Experiment	Major Objective	Alloy	Reactor	Temperature (°C)	Displacement Damage (dpa)	Helium (at. ppm)	Duration (months)	Date Completed
ORR-MFE-1	Scope the effects of composition and microstructure on tensile, fatigue, and irradiation creep	P ths A, B C	ORR	250–600	z	≤10	4	6 78
ORR-MFE-2	Scope the effects of composition and microstructure on tensile, fatigue, and irradiation creep	Paths A, B, C	ORR	300–600	6	≤60	15	4 80
ORR-MFE-5	In-reactor fatigue crack growth	Path A	ORR	325–460	1	<10	2	2/81
Subassembly X-264	Effect of preinjected helium on microstructure, tensile properties, and irradiation creep	316, PE-16, V–20% Ti, V–15% Cr–5% Ti, Nb–1% Zr	EBR-II	500–825	8	2–200	4	1/77
AA-X Subassembly X-287	Effect of preinjected helium on microstructure, tensile properties, and irradiation creep	316, PE-16, V–20% Ti, V–15% Cr–5% Ti, Nb–1% Zr	EBR-II	400–700	z0	2–200	23	12 78
Subassembly X-217D	Stress relaxation	Titanium alloys	EBR-II		2		1	1/78
Pins B285, B286, and B284	Swelling, fatigue, crack growth, and tensile properties	Titanium alloys	EBR-II	37 50	25		14	9/79

Table 8.1.1. (Continued)

Experiment	Major Objective	Alloy		Temperature (°C)	Displacement Damage (dpa)	Helium (at. ppm)		Date mpleted
mFI⌀-<TR-0	Swelling and tensile properties	PE-16, Inconel 600	HFIR	300–700	4.3–9	350–1800		2/75
HFIR-CTR-4	Swelling and tensile properties	PE-16	HFIR	300–700	2.2–4.5	100–350	2	3/77
HFIR-CTR-5	Swelling and tensile properties	PE-16, Inconel 600	HFIR	300–700	4.3–9	350–1800	3	4/75
HFIR-CTR-6	Swelling and tensile properties	PE-16, Inconel 600	HFIR	300–700	4.3–9	350–1800	3	4/75
HFI⌀-.TR-7	Swelling and tensile properties	PE-16	HFIR	300–700	9–18	1250–3000	7	8/77
HFIR-CTR-8	Swelling and tensile properties	PE-16	HFIR	300–700	9–18	1250–3000	7	8/77
HFIR-CTR-9	Swelling and tensile properties	316, 316 + Ti	HFIR	280–680	10–16	400–1000	6	5/77
HFIR-CTR-10	Swelling and tensile properties	316, 316 + Ti	HFIR	280–680	10–16	400–1000	6	5/77
mFIR-CTR-11	Swelling and tensile properties	316, 316 + Ti	HFIR	280–680	10–16	400–1000	6	5/77
HFIR-CTR-12	Swelling and tensile properties	316, 316 + Ti	HFIR	280–680	7–10	200–500	4	2/77
HFIR-CTR-ω3	Swelling and tensile properties	316, 316 + Ti	HFIR	280–680	7–10	200–500	4	2/77
HFIR-CTR-14	Fatigue	316	HFIR	430	9–15	400–1000	7	12/77
HFIR-CTR-15	Fatigue	316	HFIR	550	6–9	200–400	4	10/78
HFIR-CTR-16	Weld characterization, swelling, and tensile properties	316, PE-16, Inconel 600	HFIR	55	6–9	150–2700	4	8/77
HFI⌀-CTR-ω7	Weld characterization	316		280–620	7–13	180–460		
HFIR-CTR-18	Swelling and tensile properties	316, PE-16		280–700	17–27	1600–5600		

Table 8.1.1. (Continued)

Experiment	Major Objective	Alloy	Reactor	Temperature (°C)	Displacement Damage (dpa)	Helium (at. ppm)	Duration (months)	Date Completed
HFIR-CTR-19	Weld characterization	316	HFIR	280–620	7–10	200–500	4	12/77
HFIR-CTR-20	Fatigue	316	HFIR	430	6–9	200–400	4	1/78
HFIR-CTR-21	Fatigue	316	HFIR	550	9–15	400–1000	7	7/78
HFIR-CTR-22	Fatigue	316	HFIR	430	6–9	200–400	4	3/78
HFIR-CTR-23	Fatigue	PE-16	HFIR	430	6–9	370–1000	3.5	2/79
HFIR-CTR-24	Temperature calibration and tensile properties	316	HFIR	300–620	2.2	30	1	12/78
HFIR-CTR-26	Swelling and tensile properties	316	HFIR	284–620	30	1900	10	4/80
HFIR-CTR-27	Swelling and tensile properties	316	HFIR	284–620	56	3500	18	1/81
HFIR-CTR-28	Swelling and tensile properties	316	HFIR	370–560	30	1900	10	12/80
HFIR-CTR-29	Swelling and tensile properties	316	HFIR	370–560	56	3500	18	8/81
HFIR-CTR-32	Swelling, microstructure, and ductility	Paths A, B, C, D, E	HFIR	300–600	10	$\leq$3000	4	12/81
HFIR-CTR-33	Swelling, tensile properties, weld characterization	Paths A and E	HFIR	55	10	0–510	4	10/80

Table 8.1.2 Objectives and Schedule for Current and Planned ADIP Program Reactor Irradiation Experiments

Experiment Designation	Major Objective
A. Oak Ridge Research Reactor	
ORR-MFE-4	Effect of irradiation on tensile, fatigue, and irradiation creep of path A PCA (Prime Candidate Alloy) and path B base research alloys. Spectral tailoring to maintain correct He/dpa ratio. Irradiation on continuing basis. 330–600°C (1)

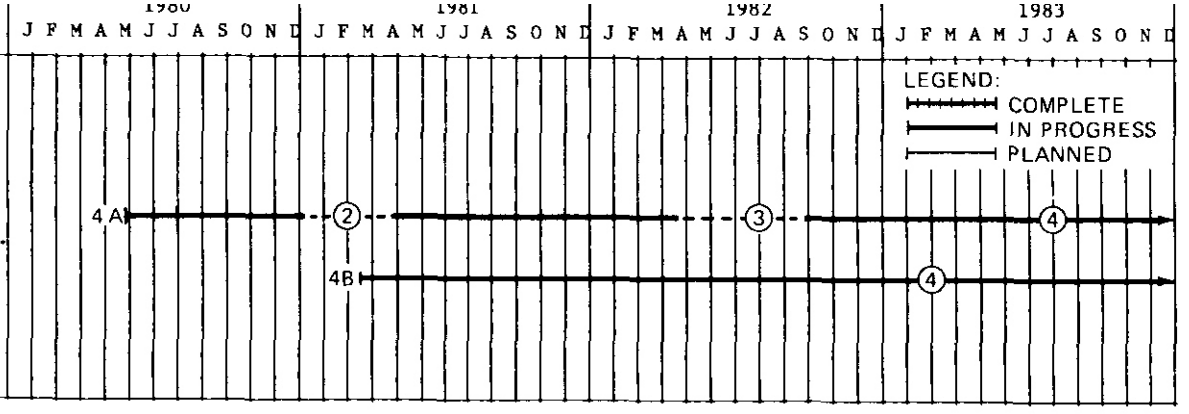

(1) MFE-4A operates at 330 and 400°C. MFE-4B operates at 500 and 600°C.

(2) Removed from reactor for thermocouple repairs.

(3) Removed from reactor for containment repairs.

(4) Approximate schedule for specimen charge out.

Table 8.1.2 (Continued)

Designation	Major Objective	1980 J F M A M J J A S O N D	1981 J F M A M J J A S O N D	1982 J F M A M J J A S O N D	1983 J F M A M J J A S O N D
B. Experimental Breeder Reactor (EBR-II)					
Experiment plan depends on alloy availability. EBR-II space not yet identified.	Effect of irradiation on swelling, tensile, fatigue, and crack growth properties of V and Nb scoping alloys. 370, 450, 550, and 650°C. Position in reactor not finalized, therefore no fluence estimate.(1)				
AD-2 (6 pins in separate subassemblies of row 4)	To supplement present EBR-II data on ferritic alloys with data on crack growth, fatigue, and fatigue toughness. Temperature 390, 450, 500, and 550°C. 19 and 38 dpa.			(2)	

(1) Delayed for undetermined period.

(2) Interim examination. Experiment out of reactor.

Table 8 1 2 (Continued)

Experiment Designation	Major Objective
C. High Flux Isotope Reactor (HFIR)	
HFIR-CTR-25	Temperature calibration, tensile properties of MFE ref. 316, 2.25 dpa, 30 at. ppm He.(1)
HFIR-CTR-30	Swelling and tensile properties, paths A, B, and D microstructural variations, 40 dpa, 2500 at. ppm He (*path* A).
HFIR-CTR-31	Swelling and tensile properties, paths A, B, and D microstructural variations, 20 dpa, 1200 at. ppm He (path A).

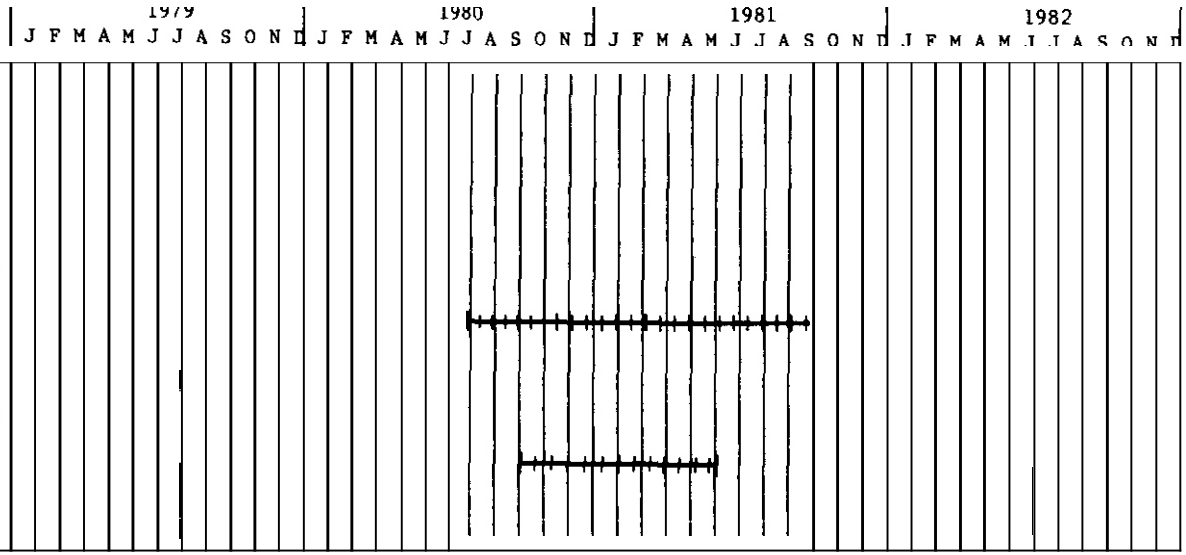

(1) Delayed for undetermined period.

Table 12 (Continued)

Experiment Designation	Major Objective
HFIR-CTR-34	Impact properties of path E alloys. 10 dpa, 0 to 75 ppm He, 300, 400°C.
HFIR-CTR-35	Impact properties of path E alloys. 10 dpa, 0 to 75 ppm He, 300, 400°C.
HFIR-CTR-36	Fatigue properties of path A alloys. 30 dpa, 2000 ppm He.
HFIR-CTR-39	Swelling, tensile properties of path E alloys. 12 dpa, up to 90 ppm He, 300 to 500°C.
HFIR-CTR-40	Swelling, tensile properties of path E alloys. 12 dpa, up to 90 ppm He, 300 to 500°C.
HFIR-CTR-41	Swelling, tensile properties of path E alloys. 12 dpa, up to 90 ppm He, 300 to 500°C.
HFIR-CTR-42	Swelling, tensile properties of path A alloys. 20 dpa, 1100 ppm He, 300 to 600°C.

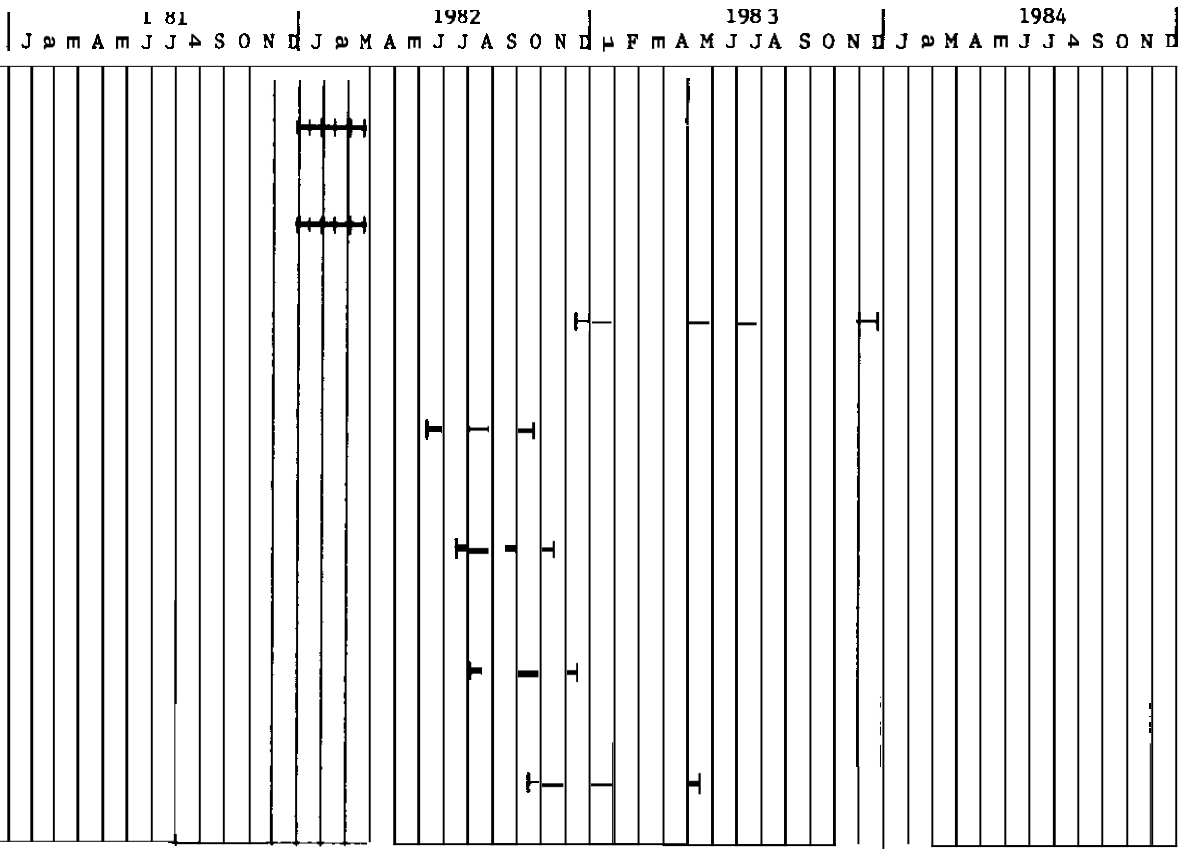

Table 2.1.2 (Continued)

Experiment Designation	Major Objective	1981 J F M A M J J A S O N D	1982 J F M A M J J A S O N D	1983 J F M A M J J A S O N D	1984 J F M A M J J A S O N D
HFIR-CTR-43	Swelling, tensile properties of path A alloys. 20 dpa, 1100 ppm He, 300 to 600°C.				
HFIR-CTR-44	Swelling, tensile properties of path A alloys. 10 dpa, 500 ppm He, 250–400°C. Joint experiment of U.S., European Community, and Japan.				
HFIR-CTR-45	Similar to HFIR-CTR-44.				
HFIR-CTR-46	Impact properties of path E alloys. 10 dpa, 75 ppm He, 300 and 400°C.				
HFIR-CTR-47	Impact properties of both E alloys. 40 dpa, 400 appm He, 300 and 400°C.				
HFIR-CTR-48	Similar to HFIR CTR 47				
HFIR-CTR-49	Tensile properties of both E alloys. 40 dpa, 400 appm He, 300 to 500°C.				
HFIR-CTR-50	Similar to HFIR-CTR-49.				

Table 3.2 (Continued)

Experiment Designation	Major Objective
HFIR-MFE-T1	Swelling, tensile properties and fatigue of path E alloys. 70 dpa, up to 650 ppm He depending upon alloy, 55°C.
HFIR-MFE-T2	Swelling, tensile properties and fatigue of path E alloys. 10 dpa, up to 75 ppm He depending upon alloy, 55°C.
HFIR-MFE-T3	Impact properties of path E alloys. 10 dpa, up to 75 ppm He depending upon alloy, 55°C.
HFIR-MFE-RB1	Swelling, microstructure, crack growth, fracture toughness, impact, tensile, and fatigue properties of path E alloys. 10 dpa, 90 ppm He, 55°C.
HFIR-MFE-RB2	Similar to HFIR-MFE-RB1, to 20 dpa, 200 ppm He.
HFIR-MFE-RB3	Similar to HFIR-MFE-RB1, to 10 dpa, 90 ppm He.

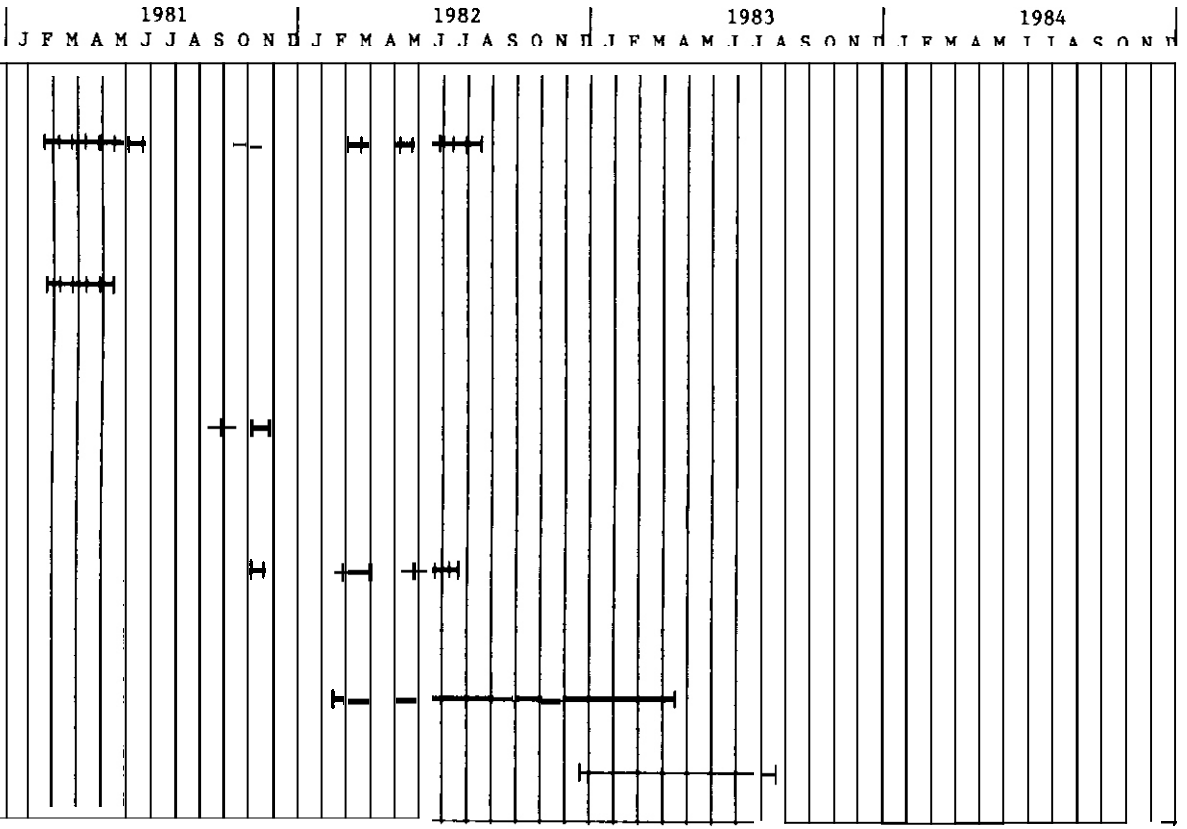

Table 8.1.2 (Continued)

Experiment Designation	Major Objective	1983 J F M A M J J A S O N D	1984 J F M A M J J A S O N D	1985 J F M A M J J A S O N D	1986 J F M A M J J A S O N D
HFIR-JP-1[U]	Swelling, tensile, and fatigue properties, and microstructure of path A alloys. 300–600°C, 30 dpa, 2000 ppm He.	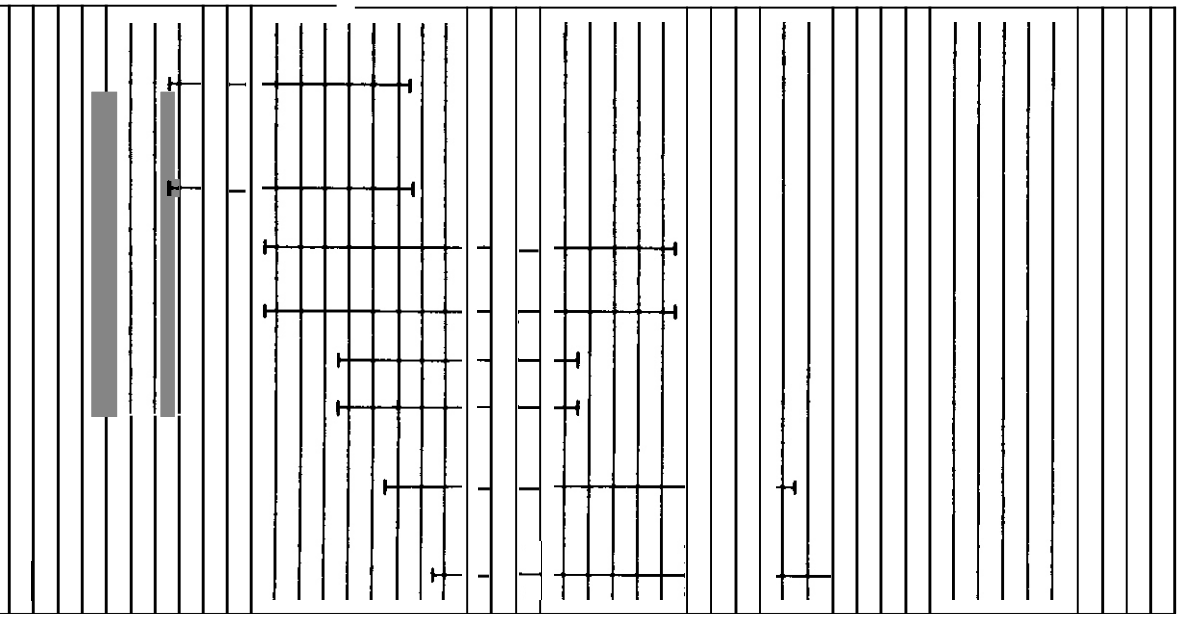			
HFIR-JP-2	Similar to HFIR-JP-1.				
HFIR-JP-3	Similar to HFIR-JP-1, but to 50 dpa, 3500 ppm He.				
HFIR-JP-4	Similar to HFIR-JP-3.				
HFIR-JP-5	Similar to HFIR-JP-1.				
HFIR-JP-6	Similar to HFIR-JP-1.				
HFIR-JP-7	Swelling, tensile properties and microstructure of path A alloys. 55°C, 50 dpa, 3500 ppm He.				
HFIR-JP-8	Similar to HFIR-JP-3.				

[U] The HFIR-JP experiment series is a joint program shared by the U.S. and Japan Fusion Reactor Materials activities.

8.2 FUSION PROGRAM RESEARCH MATERIALS INVENTORY — F. W. Wiffen, T. K. Roche (Oak Ridge National Laboratory), J. W. Davis (McDonnell Douglas Company), and T. A. Lechtenberg (General Atomic Company)

8.2.1 ADIP Tasks

ADIP Task I.D.1, Materials Stockpile for MFE Programs.

8.2.2 Objective

Oak Ridge National Laboratory maintains a central inventory of research materials to provide a common supply of materials for the Fusion Reactor Materials Program. This will minimize unintended material variations and provide for economy in procurement and for centralized record keeping. Initially this inventory is to focus on materials related to first-wall and structural applications and related research, but various special purpose materials may be added in the future.

The use of materials from this inventory for research that is coordinated with or otherwise related technically to the Fusion Reactor Materials Program of DOE is encouraged.

8.2.3 Materials Requests and Release

Materials requests shall be directed to the Fusion Program Research Materials Inventory at ORNL (Attention: F. W. Wiffen). Materials will be released directly if:

(a) The material is to be used for programs funded by the Office of Fusion Energy, with goals consistent with the approved Materials Program Plans of the Materials and Radiation Effects Branch.

(b) The requested amount of material is available, without compromising other intended uses.

Materials requests that do not satisfy both (a) and (b) will be discussed with the staff of the Materials and Radiation Effects Branch, Office of Fusion Energy, for agreement on action.

8.2.4 Records

Chemistry and materials preparation records are maintained for all inventory material. All materials supplied to program users will be accompanied by summary characterization information.

8.2.5 Summary of Current Inventory and Material Movement During Period April 1, 1982 to September 30, 1982

A condensed, qualitative description of the content of materials in the Fusion Program Research Materials Inventory is given in Table 8.2.1. This table indicates the nominal diameter of rod or thickness of sheet for product forms of each alloy and also indicates by weight the amount of each alloy in larger sizes available for fabrication to produce other product forms as needed by the program. There was no material received into the inventory during this reporting period. Table 8.2.2 gives the materials distributed from the inventory.

Alloy compositions and more detail on the alloys and their procurement and/or fabrication are given in earlier ADIP quarterly progress reports.

Table 8.2.1 Summary Status of Materials Available in the Fusion Program Research Materials Inventory

Alloy	Product Form			
	Ingot or Bar,[a] Weight (kg)	Rod Diameter (mm)	Sheet Thickness (mm)	Thin-Wall Tubing, Wall Thickness (mm)
Path A Alloys				
Type 316 SS	900	16 and 7.2	13 and 7.9	0.25
Path A PCA[b]	490	12	13	0.25
USSR-Cr-Mn Steel[c]	-	10.5	2.6	
NONMAGNE 30[d]	-	18.5	10	
Path B Alloys				
PE-16	140	16 and 7.1	13 and 1.6	0.25
8-1	180	-	-	
8-2	180	-	-	
B-3	180	-	-	-
B-4	180	-	-	-
8-6	180	-	-	
Path C Alloys				
Ti-64	-	-	2.5 and 0.76	-
Ti-62425	-	63	6.3, 3.2, and 0.76	-
Ti-5621s	-	-	2.5 and 0.76	
Ti-38644	-	-	0.76 and 0.25	
Nb-1% Zr	-	6.3	2.5. 1.5, and 0.76	-
Nb-5% Mo-1% Zr	-	6.3	2.5, 1.5, and 0.76	
V-20% Ti	-	6.3	2.5. 1.5, end 0.76	
V-15% Cr-5% Ti	-	6.3	2.5, 1.5, and 0.76	
VANSTAR-7	-	6.3	2.5, 1.5, and 0.76	-
Path D Alloys — No Material in Inventory				
Path E Alloys				
HT9[e] (AOD fusion hear)	3400	-	28.5. 15.8, 9.5, and 3.1	-
HT9 (AOD/ESR fusion heat)	7000	25, 50, and 75	28.5, 15.8, 9.5, and 3.1	-
HT9	-	-	4.5 and 18	-
HT9 + 1% Ni	-	-	4.5 and 18	-
HT9 + 2% Ni	-	-	4.5 end 18	-
HT9 + 2% Ni + Cr adjusted	-	-	4.5 and 18	-
T-9[f] modified	-	-	4.5 and 18	-
T-9 modified + 2% Ni	-	-	4.5 and 18	-
T-9 modified + 2% Ni + Cr adjusted	-	-	4.5 and 18	-
2 1/4 Cr-1 Mo	-	-	[g]	

[a] Greater than 25 mm, minimum dimension.

[b] Prime candidate alloy.

[c] Rod and sheet of a USSR stainless steel supplied under the U.S.-USSR Fusion Reactor Materials Exchange Program.

[d] NONMAGNE 30 is an austenitic steel with base Composition of Fe-14% Mn-2% Ni-2% Cc. It was supplied to the inventory by the Japanese Atomic Energy Research Institute.

[e] Alloy 12 Cr-1 MoVW, with composition equivalent to Sandvik alloy HT9.

[f] T-9 is the alloy 9 Cr-1 MoVNb.

[g] Material is thick-wall pipe, rerolled as necessary to produce sheet or rod.

Table 8.2 Fusion Program Research Materials Disbursements 4-1-82 to 9-30-82

Alloy	Heat	Product Form	Dimensions[a] (mm)	Quantity (kg)	Quantity (m^2)	Sent to
Path A Alloys — Austenitic Stainless Steels						
USSR—Cr-Mn steel	EP838	Rod	10.2	0.66		Radiation Effects Group, ORNL
Path A-PCA	9230	Plate	6.2	2.74		Radiation Effects Group, ORNL
		Bar	102	0.1		EG&G Idaho, Inc.
Path C Alloys — Reactive and Refractory Alloys						
V—20 Ti	CAM 833-10	Sheet	0.76		0.008	Materials Compatibility Group, ORNL
	CAM 833-C	Sheet	1.5		0.008	Materials Compatibility Group, ORNL
V—15 Cr—5 Ti	CAM 834-6	Sheet	0.76		0.003	Materials Compatibility Group, ORNL
	CAM 835A-3	Sheet	1.5		0.003	Materials Compatibility Group, ORNL
VANSTAR-7	CAM 836-4	Sheet	0.76		0.003	Materials Compatibility Group, ORNL
	CAM 837-3	Sheet	1.5		0.003	Materials Compatibility Group, ORNL
Path F Alloys — Ferritic Steels						
12 Cr-1 MoVW	AOD/ESR-9607R	Sheet	28.5		1.0	Sandia Liner Test Laboratory
		Sheet	28.5		0.6	HEDL
		Sheet	9.5		0.6	HEDL

[a]Characteristic dimension — thickness for plate and sheet, diameter for rod and tubing.

9. MATERIALS COMPATIBILITY AND HYDROGEN PERMEATION STUDIES

9.1 CORROSION OF PATH A PCA, TYPE 316 STAINLESS STEEL AND Fe—12 Cr-1 MoVW STEEL IN FLOWING LITHIUM — P. F. Tortorelli and J. H. DeVan (Oak Ridge National Laboratory)

9.1.1 ADIP Task

ADIP Task I.A.3, Perform Chemical and Metallurgical Compatibility Analyses.

9.1.2 Objective

The purpose of this task is to evaluate the corrosion resistance of candidate first-wall materials to flowing lithium in the presence of a temperature gradient. Corrosion and deposition rates are measured as functions of time, temperature, additions to the lithium, and flow conditions. These measurements are combined with chemical and metallographic examinations of specimen surfaces to establish the mechanisms and rate-controlling processes for dissolution and deposition reactions.

9.1.3 Summary

Results from lithium thermal-convection loop (TCL) experiments with the path A prime candidate alloy (PCA), type 316 stainless steel, and Fe—12 Cr-1 MoVW are presented. The short-term (<3050 h) weight losses of PCA in flowing lithium were just slightly higher than those of type 316 stainless steel and may he attributable to the higher nickel concentration of PCA. The corrosion response of PCA specimens was not affected by cold work. A surface analysis of type 316 stainless steel specimens exposed in the hot leg of a TCL for over 7000 h confirmed earlier observations regarding preferential leaching of nickel and chromium and deposition of pure chromium. These analyses also showed that exposure temperature strongly affects surface porosity and that molybdenum enrichment occurs on surfaces undergoing dissolution. Weight loss data as a function of ttme for Fe—12 Cr-1 MoVW steel exposed to lithium at 500°C yielded the same dissolution rate as the "steady-state" value for nickel-depleted type 316 stainless steel. Significant weight losses were measured in the cold leg of this loop, and they appeared to he related to chromium depletion (possibly as a result of impurity reactions).

9.1.4 Progress and Status

We have continued our mass transfer studies in flowing lithium with previously described' TCLs with accessible specimens. These loops are designed so that lithium samples can be taken and corrosion coupons can be withdrawn and inserted without interrupting the lithium flow. During the period covered by the preceding progress report,' we began operation of a lithium—type 316 stainless steel TCL to observe the dissolution behavior of path A PCA specimens with different thermomechanical treatments. In this way, we can study the effects of microstructure on corrosion of austenitic stainless steel by lithium as well as determine the dissolution rate of PCA relative to that of standard type 316 stainless steel. In our initial loop experiment, coupons of path A PCA alloys A1 and A3 were placed at the 600 and 570°C positions in a TCL that had previously circulated lithium for greater than 10,000 h. Composition for path A PCA (alloys A1 and A3) is as follows:

Element	Composition (wt %)
Ni	15.9
Cr	13.0
Mo	1.9
Mn	1.7
Si	0.5
Ti	0.3
Al	0.05
C	0.05
N	<0.01

Both alloys were annealed for 15 min at 1175°C in argon and cold rolled 23 to 25%. Alloy A1 was annealed for an additional 15 min at 1175°C in argon. The inside surface of the loop's hot leg was already depleted of nickel. (This condition was similar to that of earlier experiments in which as—received type 316 stainless steel specimens had been placed in the nickel-depleted hot legs of type 316 stainless steel TCLs.) The cold leg of the loop had been replaced prior to operatton with the PCA specimens.

More than 3000 h of coupon exposure time has now been accumulated for the path A PCA specimens in the above-described lithium TCL. The weight loss results for the A1 and A3 specimens at the 600°C position in the loop are shown in Fig. 9.1.1, which also includes an indication of the approximate range of similar weight loss measurements gotten from several previous experiments with type 316 stainless steel. The latter range is indicated by the shaded area of the figure. Consideration of these data indicates that both A1 and A3 had consistently higher weight losses than standard type 316 stainless steel. However, the difference is not great compared with the upper bound of the type 316 stainless steel data. The weight losses measured for the A1 and A3 specimens in the 570°C loop position fall within the range of type 316 stainless steel data, as shown in Fig. 9.1.2. Both Figs. 9.1.1 and 9.1.2 also indicate that within the 3000-h test time there is a negligible difference between the respective weight losses of A1 and A3 in thermally convective lithium.

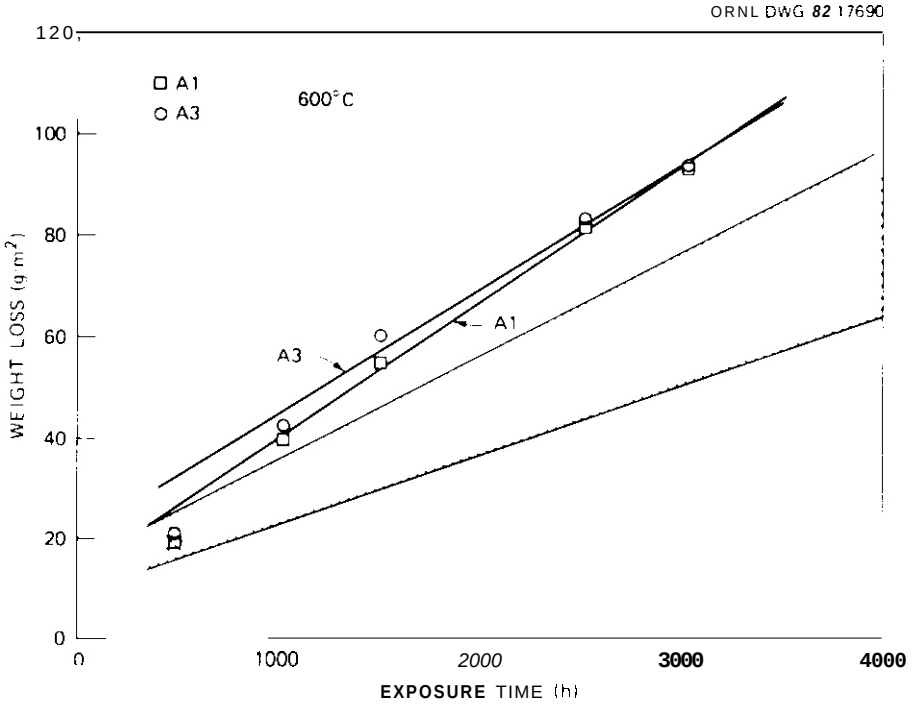

Fig. 9.1.1. Weight Loss Versus Exposure Time for Path A PCA A1 and A3 at 600°C in Thermally Convective Lithium. Shaded area represents envelope of similar data for type 316 stainless steel.

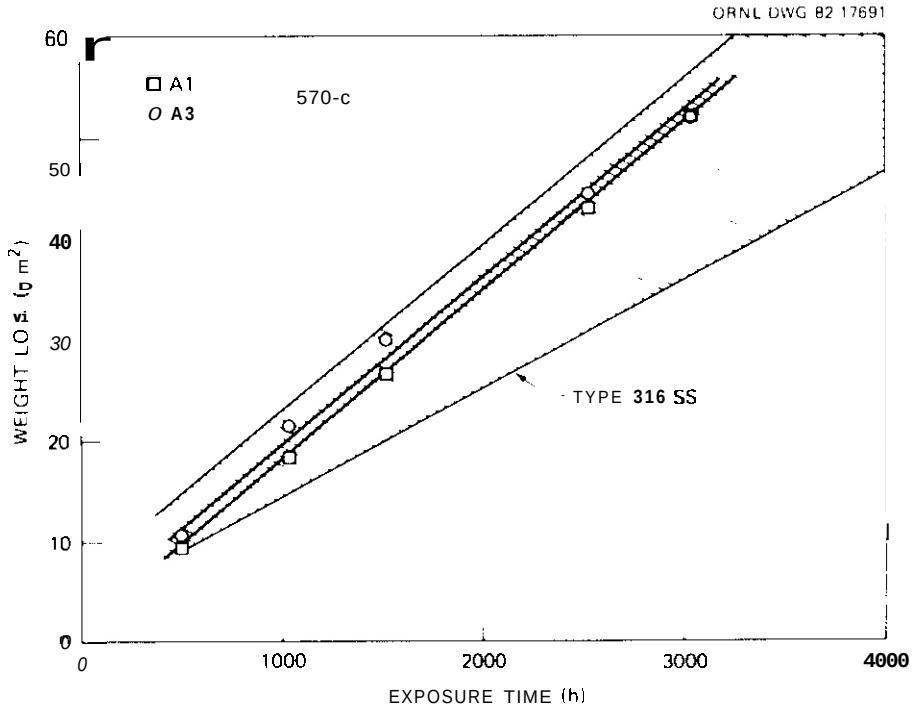

Fig. 9.1.2. Weight Loss Versus Exposure Time for Path A PCA A1 and A3 at 570°C in Thermally Convective Lithium. Shaded area represents envelope of similar data for type 316 stainless steel.

The above discussion of corrosion data has involved only cumulative weight-loss measurements. Of more importance, however, are the rates of weight loss. These rates are typically gotten from the slope of the weight loss versus exposure time curves after linear weight-loss kinetics has been established. Such a procedure has been used previously for the type 316 stainless steel data (see, for example, ref. 2). Normally weight losses become linear with exposure time after an initial transient period. If we attempt to gage this "steady-state" value by taking the slope of the least-squares fit line between 1000 and 3000 h, the slope gives dissolution rates at 600°C of 27 and 25 $g/(m^2 \cdot h)$ for A1 and A3, respectively. As with the cumulative weight losses, these rates are greater than those for type 316 stainless steel [lo—15 $g/(m^2 \cdot h)$]; however, this difference can be expected to decrease when longer term data for the PCA specimens become available.

A higher corrosion rate for PCA alloys compared with type 316 stainless steel for the first 3000 h was expected because the nickel

concentration of PCA is significantly greater than that of type 316 stainless steel (see above table). It has been shown[3] that corrosion of Fe–Cr–Ni alloys in thermally convective lithium increases with increasing nickel concentratton of the exposed alloy. It is also possible that microstructural variations (i.e., cold work and precipitate type and distribution) could affect the alloy's corrosion response in lithium. However, in the current tests there was no difference in the corrosion response of the two PCA alloys despite variations in the thermomechanical treatment (cold work) of these specimens. (Other path A PCA specimens with different processing histories will be eventually exposed under similar conditions to further check possible additional microstructural influences on corrosion by lithium.) Finally, a dissimilar–metal gradient between the PCA specimens and the type 316 stainless steel loop could contribute to a slightly higher corrosion rate for the PCA alloys compared with type 316 stainless steel.

In previous work,[4,5] the morphological and compositional changes of type 316 stainless steel surfaces exposed to thermally convective lithium have been reported. However, a complete scanning electron microscope/ energy–dispersive x–ray analysis examination of such surfaces, particularly at longer exposure ttmes, was lacking. Consequently, such work was initiated for type 316 stainless steel coupons exposed to lithium for 7488 h in a TCL test of the type described above. Examinatton of a series of hot–leg specimens (500–600°C) has now been completed, and a distinct change in surface topography was noted as a function of position (temperature) in the hot leg. The surface of the coupon at the maximum temperature position (600°C) was very porous (Fig. 9.1.3) and was found to be depleted in both nickel and chromium (Fig. 9.1.4). As such, these results are consistent with past observations of porosity and preferential leaching.[4,5] However, in the present studies we also observed on the corroded surfaces small areas (nodules) that were somewhat enrtched in molybdenum. The nodules appear to be areas of molybdenum–containing precipitates that recede only slowly relative to the remainder of the matrix.

M-16722

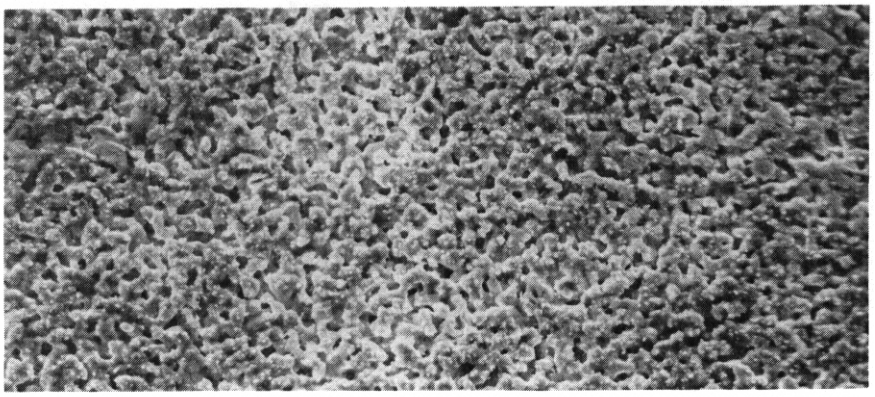

M-16718

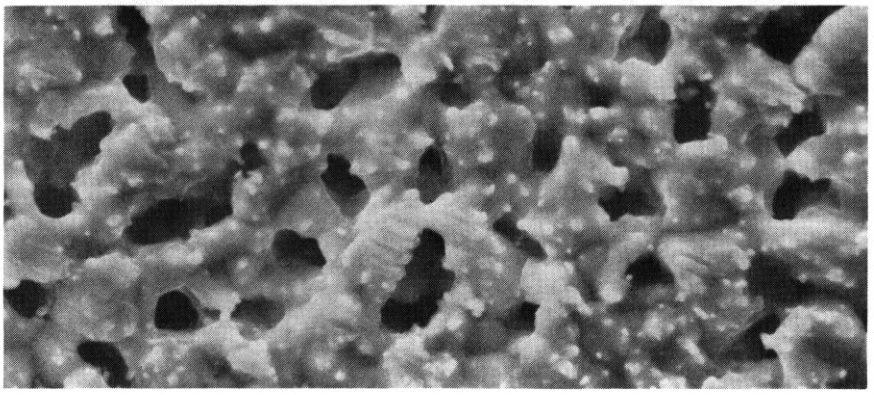

M-16723

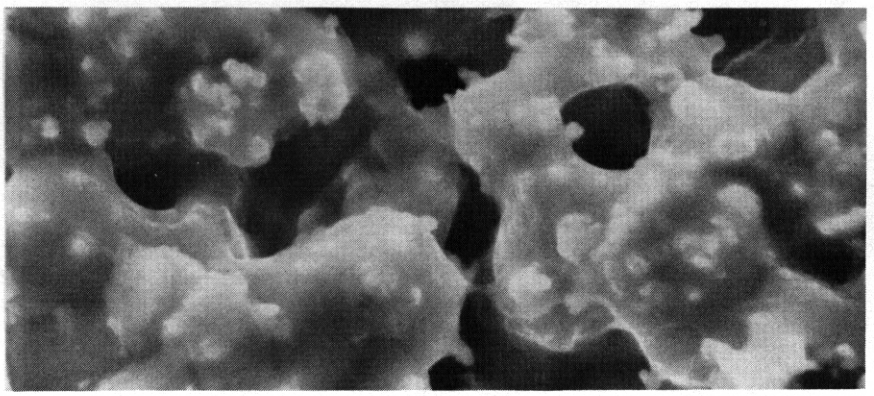

Fig. 9.1.3. Scanning Electron Micrographs of Type 316 Stainless Steel Exposed to Thermally Convective Lithium at 600°C for *7488* **h.**

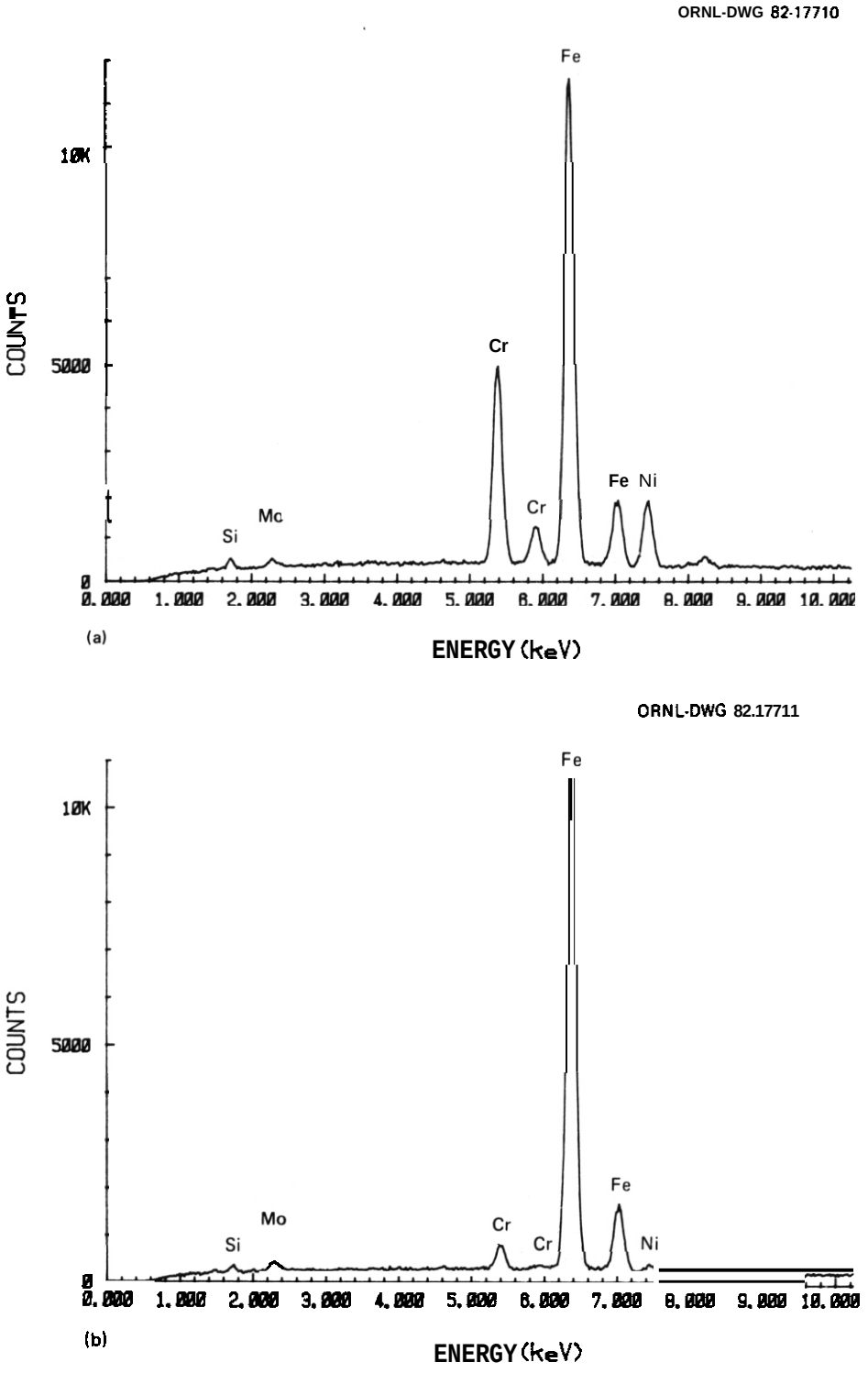

Fig. *9.1.4.* Comparison of Typical Energy-Dispersive X-Ray Spectra for (a) Unexposed Type 316 Stainless Steel and (b) Type 316 Stainless Steel Exposed to Thermally Convective Lithium at 600°C for *7488* h.

It is particularly interesting to note how the surface structure of the corroded specimens changed with loop position (exposure temperature). These results are shown in Fig. 9.1.5, which includes typical scanning electron micrographs of the respective specimens. Note how the size and distribution of the porosity decreased with decreasing temperature until, at and below 520°C, porosity is minimal, and deposits are the predominant surface feature. This change in surface topography was accompanied by significant changes in the surface compositions of the various specimens. As seen from the energy-dispersive x-ray analysis data in Table 9.1.1, the hotter specimen surfaces were depleted in nickel and chromium while the cooler ones were enriched. (The x-ray spectral data are necessarily qualitative because of the very rough specimen surfaces and the corresponding uncertainties in the extent of electron and x-ray absorption paths.) The surface enrichment at lower temperature, which is caused by

Table 9.1.1. Ratios of K_α Peak Intensities for Type 316 Stainless Steel Exposed to Thermally Convective Lithium for 7488 h

Exposure Temperature (°C)	K_α Peak Intensities[a]		
	Cr/Fe	Ni/Fe	Si/Fe
Unexposed	0.40	0.13	0.01[b]
600	0.05	0.01	0.01
575	0.08	0.01	0.01[b]
560	0.10	0.01	0.01
540	0.11	0.02	0.01[b]
520	0.58[d]	0.14	0.01
500	4.16	0.31	0.03

[a]Average taken from spectra over raster areas on surfaces; standard deviation less than ±15% unless otherwise noted.

'Standard deviation ±16%.

"Standard deviation ±28%.

[d]Standard deviation ±25%.

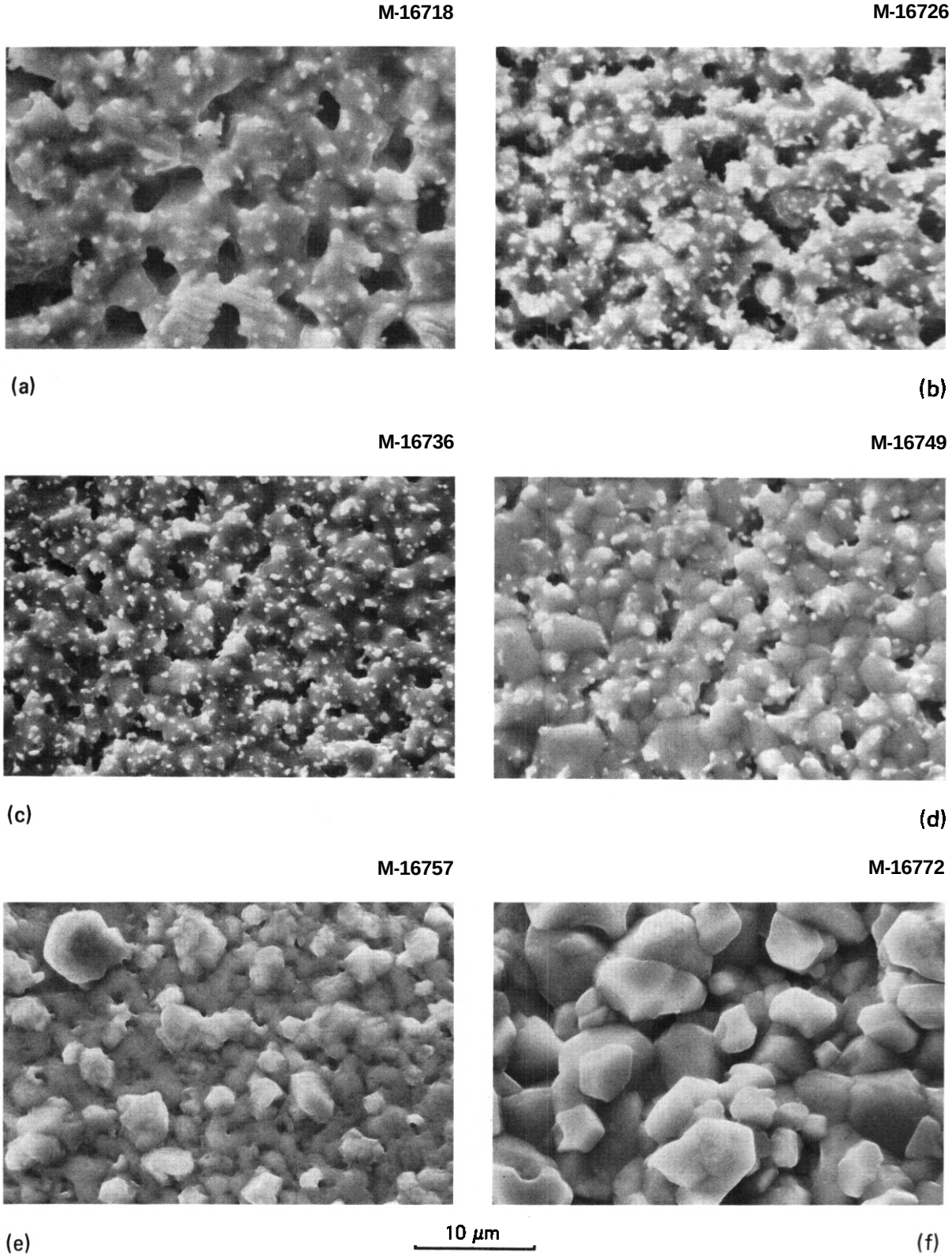

Fig. 9.1.5. Comparison of Topography of Surfaces of Type 316 Stainless Steel Exposed to Lithium in a Thermal–Convection Loop with a Maximum Temperature of 600°C and a ΔT of 150°C, for 7488 h: (a) 600°C; (b) 570°C; (c) 555°C; (d) 540°C; (e) 520°C; (f) 500°C.

deposition of dissolved species from the lithium, was not uniform. Spectra taken from different deposition zones on a surface varied significantly, particularly in their peak intensities for chromium. Detailed analyses of these surfaces indicated that some underlying deposits tended to be rich in chromium, while those resting on top were less so (Fig. 9.1.6). Such observations are consistent with findings from earlier work with lithium–type 316 stainless steel thermal-convection systems:' deposits of pure chromium formed during the initial stages of loop operation, while at later exposure times (greater than 5000 h) the deposits contained significant quantities of nickel and iron in addition to chromium. It is also interesting to note from Table 9.1.1 that, while the chromium concentration of the surface increased steadily with decreasing temperature between 600 and 540°C, the surface nickel concentration remained low throughout this temperature interval. This extended temperature range over which nickel remains depleted has also been observed with x-ray fluorescence on austenitic stainless steel specimens exposed to lithium in a different set of shorter term TCL experiments.[5] The present data from surface analysis of lithium-corroded type 316 stainless steel therefore confirms several of our findings from earlier work with thermal-convection systems while yielding new information about topographical differences among hot-leg specimens and about the disposition of molybdenum on the corroded surfaces.

In the preceding progress report,[2] initial data from a lithium-Fe-12 Cr-1 MoVW steel TCL of the type described above were reported for a maximum temeprature of 500°C and a AT of 150°C. More recent test results at longer operating times for the 500°C specimen are included in Fig. 9.1.7. Note that the dissolution rate at times greater than 1000 h, as gotten from the slope of the least-squares fit line between 1000 and 7340 h, has remained relatively small [0.4 mg/(m^2·h)] and compares closely with that measured at 500°C for type 316 stainless steel [0.4 mg/(m^2·h)] (ref. 2). As discussed previously,[2] this is not unexpected since, after a transient period, the surface compositions of exposed type 316 stainless steel approach the Fe-12 Cr-1 MoVW steel bulk composition.

One of the general characteristtcs of liquid metal corrosion test loops is that the weight loss is maximum at the point of the highest loop

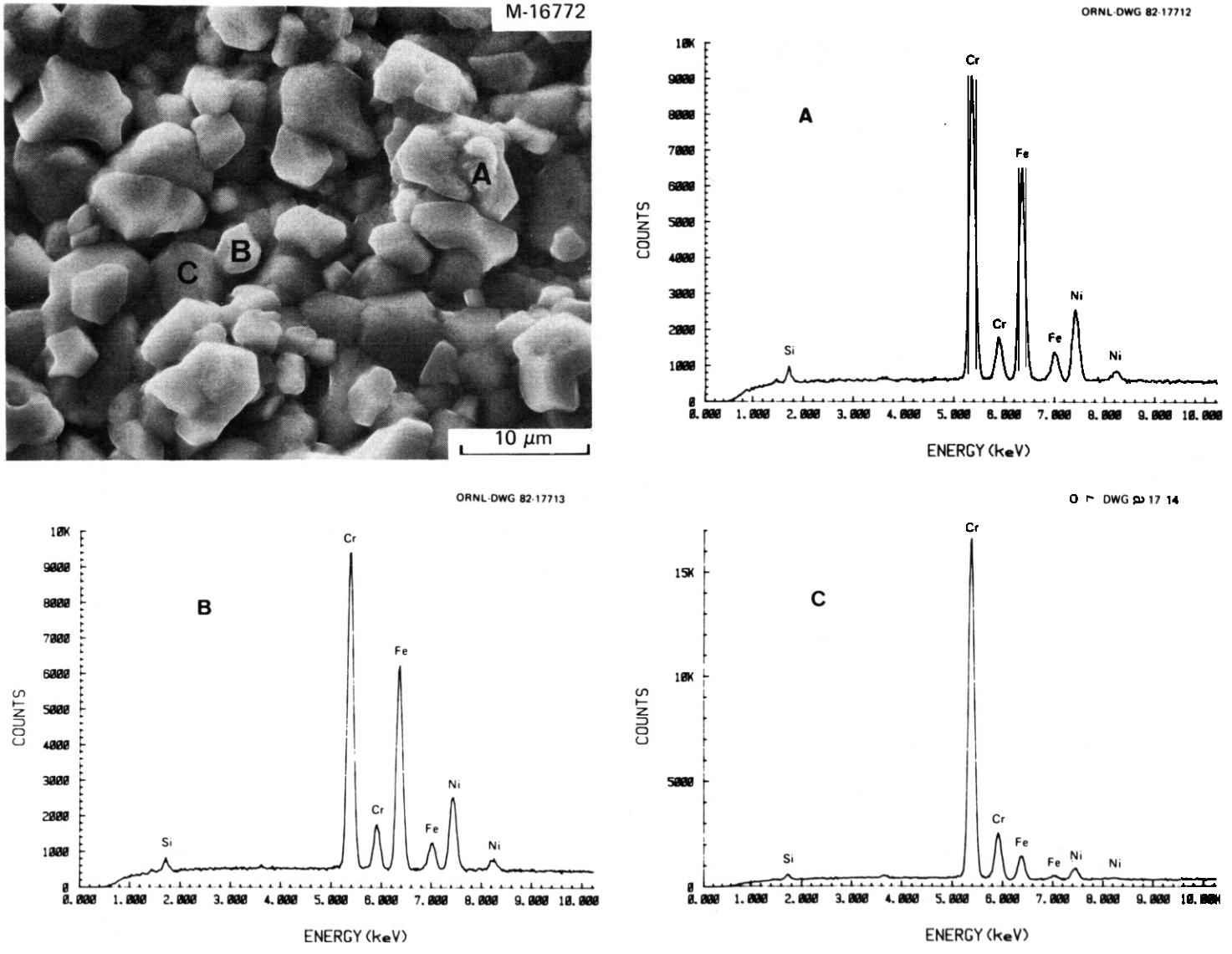

Fig. 9.1.6. Type 316 Stainless Steel Exposed at 500°C to Thermally Convective Lithium in a Loop with a Maximum Temperature of 600°C. Scanning electron micrograph of surface and associated energy-dispersive x-ray spectra of indicated areas that show underlying chromium-rich deposits.

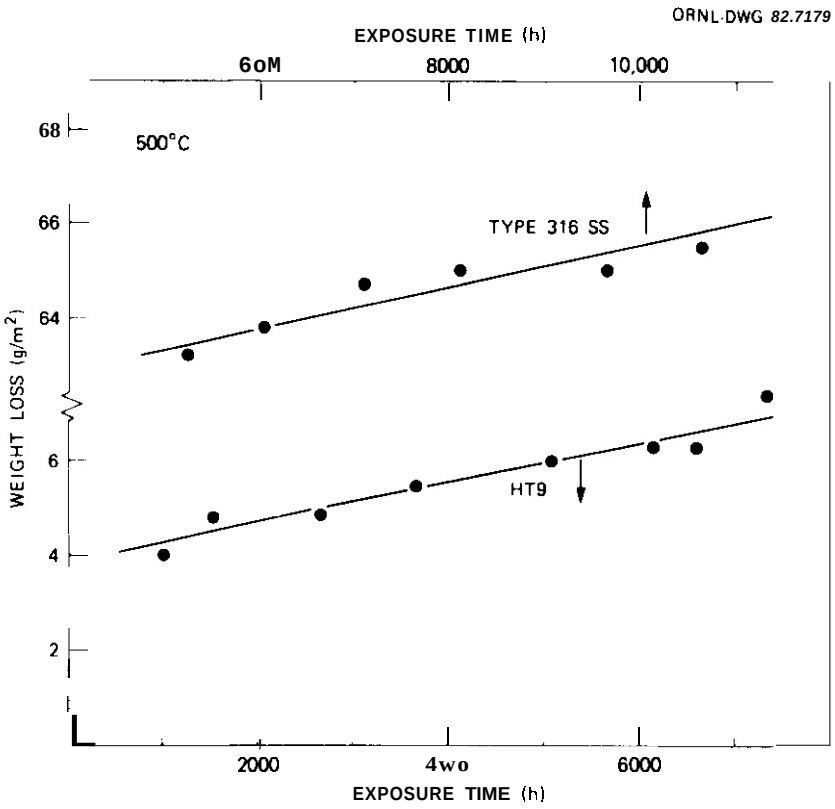

Fig. 9.1.7. Weight Loss Versus Exposure Time for Fe–12 Cr–1 MoVW Steel Exposed to Thermally Convective Lithium at 500°C (Maximum Loop Temperature).

temperature. However, in the Fe–12 Cr–1 MoVW steel loops, the coldest (350°C) specimen had the largest weight loss. Furthermore, in general, the cooler specimens had weight losses as great as or greater than the hotter specimens and were always at least partially covered with a rust-colored oxide scale after they were rinsed with water to remove residual lithium as per our standard operating procedure for lithium–exposed specimens. (The scale was removed prior to weighing.) This latter observation of rust on the cooler loop coupons indicates preferential chromium removal from the cooler specimens. In addition, metallographic examination of cross sections revealed greater attack of the 350°C specimen than of the one in the 500°C loop position. We do not yet know the relative contributions of chromium removal and of iron oxidation during cleaning to the total weight losses of the cold–leg specimens. Lithium removal with nonaqueous solvents will be attempted in future weighings to resolve the

major cause of the cold-leg weight losses. Also microprobe examinations of the specimens will be conducted to measure the chromium surface concentration.

9.1.5 Conclusions

1. The short-term weight losses of path A PCA in thermally convective lithium are slightly greater than those of type 316 stainless steel and may be attributed to the higher nickel concentration of PCA. Microstructural variations of the PCA (in terms of cold work) did not affect the weight losses in lithium.

2. Both the surface topography (amount of porosity and surface deposits) and composition of type 316 stainless steel changed significantly as a function of temperature in the hot leg of a lithium TCL. Earlier observations of preferential leaching of nickel and chromium (and its temperature dependeces) and of initial pure chromium deposition were confirmed. Localized molybdenum enrichment on the hotter surfaces was noted.

3. Further weight loss data as a function of time for Fe-12 Cr-1 MoVW steel exposed at 500°C yielded a dissolution rate that was similar to that gotten for nickel-depleted type 316 stainless steel.

9.1.6 References

1. J. H. DeVan and J. R. DiStefano, "Thermal-Convection Loop Tests of Type 316 Stainless Steel in Lithium," *ADIP Quart.* Prog. *Rep.* **Yur.** *31, 1978,* DOE/ET-0058/1, pp. 200–08.
2. P. F. Tortorelli, J. H. DeVan, and C. T. Liu, "Corrosion of Austenitic, Ferritic, and Long-Range-Ordered Alloys in Flowing Lithium," *ADIP Semiannu.* Prog. *Rep. Mar. 31, 1982,* DOE/ER-0045/8, pp. 482–90.
3. P. F. Tortorelli and J. H. DeVan, "Effect of Nickel Concentration on the **Mass** Transfer of Fe-Ni-Cr Alloys in Lithium," *J. Nucl. Mater.* 1036104: 633–38 (1981).
4. P. F. Tortorelli and J. H. DeVan, "Thermal Gradient **Mass** Transfer in Lithium-Stainless Steel Systems," *J. Nucl. Mater.* 85&86: 289–93 (1979).

5. P. F. Tortorelli, J. H. DeVan, and J. E. Selle, "Corrosion in Lithium Stainless Steel Thermal-Convection Systems," pp. 13-44—54 in *Proc. 2d Int. Conf. Liquid Metal Technology in Energy Production*, CONF-800401-P2, U.S. Department of Energy, 1980.

6. P. F. Tortorelli and J. H. DeVan, "Mass Transfer Deposits in Lithium-Type 316 Stainless Steel Thermal-Convection Loops," pp. 13-55—13-63 in *Proc. 2d Int. Conf. Liquid Metal Technology in Energy Production*, CONF-800401-P2, U.S. Department of Energy, 1980.

9.2 ENVIRONMENTAL EFFECTS ON PROPERTIES OF STRUCTURAL ALLOYS – O. K. Chopra and D. L. Smith (Argonne National Laboratory)

9.2.1 ADIP Task

ADIP tasks are not defined in the 1978 program plan.

9.2.2 Objective

The objective of this program is to investigate the influence of chemical environment on the corrosion and mechanical properties of structural alloys under conditions of interest for fusion reactors. Test environments to be investigated include lithium, lead–lithium, helium, and water. Emphasis will be placed on the combined effect of stress and chemical environment on corrosion and mechanical behavior of materials. Initial investigations are focused on the influence of flowing lithium and lead–lithium environments on corrosion and mechanical properties of structural materials.

9.2.3 Summary

Compatibility tests were conducted with several ferritic and austenitic steels at 700 and 755 K to study the corrosion behavior in flowing lithium, and fatigue tests were performed with Type 316 stainless steel in lithium at 755 K. The results indicate that an increase in the nitrogen content in lithium increases the dissolution rate, whereas the depth of internal penetration is not affected significantly. The dissolution rate of ferritic steels is an order of magnitude lower than for the austenitic stainless steel. The austenitic steels develop a very porous ferrite layer, whereas the ferritic steels exhibit little or no penetration. For the austenitic stainless steels, depth of internal penetration increases with time and the penetration rates at 755 K range from 50 to 180 μm/year. Preliminary data on Type 316 stainless steel yield similar penetration rates at 700 and 755 K. The fatigue life of annealed Type 316 stainless steel in lithium at 755 K is a factor of 3 to 8 greater than in air.

9.2.4 Progress and Status

9.2.4.1 Lithium Environment

The effects of a flowing lithium environment on the corrosion behavior and low-cycle fatigue properties of ferritic and austenitic steels are being investigated. Tests are conducted in a forced-circulation lithium loop equipped with a cold-trap purification system to control the concentration of nonmetallic elements, e.g., N, C, and H. The cold-trap temperature is maintained at 498 K (225°C). By hot trapping with Ti or Zr foils (or use of dissolved getters), the nitrogen level in lithium is reduced to ~50 wppm, which is considerably below that attainable by cold trapping alone. Data obtained from compatibility tests (with and without constant applied stress) and continuous-cycle fatigue tests in lithium at 755 K (482°C) were presented in earlier reports.[1,2] The results indicate that the corrosion rate of ferritic steels, e.g., HT-9 alloy and Fe-9Cr-1Mo steel, is an order of magnitude lower than for the austenitic Types 304L and 316 stainless steel. The corrosion rate for cold-worked Type 316 stainless steel is a factor of ~3 greater than that for the annealed steel. For Type 316 stainless steel, the dissolution rates in cold-trapped flowing lithium are a factor of 10 greater than those observed in static lithium or thermal convection loops with small temperature gradients (i.e., $\Delta T \simeq$ 150 K).[3,4] In flowing lithium with 50-100 ppm nitrogen, the corrosion behavior of HT-9 alloy and Type 304 stainless steel is independent of applied stress (stress values below the yield stress of the material).

The fatigue properties of HT-9 alloy and Type 304 stainless steel at 755 K are strongly influenced by the concentration of nitrogen in lithium. The fatigue life of the HT-9 alloy in lithium containing 100-200 ppm nitrogen is a factor of 2 to 10 greater than in lithium with 1000-1500 ppm nitrogen. In general, the fatigue life of these materials in low-nitrogen lithium is greater than in air. Furthermore, the fatigue life of the HT-9 alloy in low-nitrogen lithium at 755 K is

independent of strain rate and a 4.0-Ms (1100-h) preexposure of the alloy to lithium has no effect on fatigue life.

During the current reporting period, corrosion tests were conducted at 755 and 700 K with several ferritic and austenitic steels to study the corrosion behavior in flowing lithium, and fatigue tests were performed with solution-annealed Type 316 stainless steel in lithium at 755 K. Flat corrosion coupons, ~72 x 13 x 0.2-0.5 mm in size, were exposed to lithium for 4.0 Ms (1100 h) at 700 K (427°C) and 7.2 Ms (2000 h) at 755 K (482°C). The ferritic steels, HT-9 and Fe-9Cr-1Mo, were in the normalized and tempered condition; the Types 304 and 316 stainless steel were solution annealed. Specimens of 20% cold-worked Type 316 stainless steel were also exposed. During exposure, the concentration of nitrogen in lithium was ~200 ppm.

The corrosion behavior was evaluated from measurements of weight loss and depth of internal corrosive penetration. The depth of internal penetration was determined from the difference between the initial thickness of the specimen and the sound metal remaining (i.e., the unreacted metal) after exposure to lithium. At least 10 measurements were made to obtain an average value for penetration. The results are given in Table 9.2.1. Previous results for specimens exposed at 755 K in lithium containing 50-100 ppm nitrogen are also included in the table. Data on dissolution rate (expressed as the rate of weight loss per unit area of the specimen) and depth of internal penetration show the following features:

(a) For all specimens exposed at 755 K in lithium containing ~200 ppm nitrogen, the dissolution rates are a factor of 2 to 4 greater than in low-nitrogen (i.e., 50 ppm) lithium.

(b) For identical lithium purity, the dissolution rates for annealed or cold-worked Type 316 stainless steel are comparable at 700 and 755 K. These rates, however, are greater than those in low-nitrogen lithium at 755 K.

Table 9.2.1. Dissolution Rate and Depth of Internal Penetration for Alloys Exposed at 755 and 700 K to Flowing Lithium

Alloy	755 K (482°C) ~200 ppm N in Lithium 4.68 Ms (1300 h) Dissolution Rate, $mg/m^2 \cdot h$	755 K (482°C) ~200 ppm N in Lithium 4.68 Ms (1300 h) Average (Max.) Penetration, μm	755 K (482°C) ~200 ppm N in Lithium 10.80 Ms (3000 h) Dissolution Rate, $mg/m^2 \cdot h$	755 K (482°C) ~200 ppm N in Lithium 10.80 Ms (3000 h) Average (Max.) Penetration, μm	755 K (482°C) ~200 ppm N in Lithium 7.20 Ms (2000 h) Dissolution Rate, $mg/m^2 \cdot h$	755 K (482°C) ~200 ppm N in Lithium 7.20 Ms (2000 h) Average (Max.) Penetration, μm	700 K (427°C) ~200 ppm N in Lithium 3.96 Ms (1100 h) Dissolution Rate, $mg/m^2 \cdot h$	700 K (427°C) ~200 ppm N in Lithium 3.96 Ms (1100 h) Average (Max.) Penetration, μm
HT-9	0.23	3	0.45	3	1.5	4	0.2	5
9Cr-1Mo	0.25	4	0.33	4	1.0	5	0.38	4
304L	2.4	8 ± 1	1.5	7 ± 1 (30)[a]	9.4	14 ± 3	-	-
316 SS	5.1	13 ± 2 (37)[a]	5.4	34 ± 9 (60)[a]	10.5	25 ± 9	15.6	21 ± 2
316 CW	18.4	24 ± 3	-	-	23.3	47 ± 8	22.6	25 ± 3 (40)[a]

[a]The maximum values represent the edge or end sections of the specimens. These values were not included when calculating average values.

(c) Dissolution rates for ferritic steels at 700 K in lithium containing ~200 ppm nitrogen are similar to those in low-nitrogen lithium at 755 K but are lower than those at 755 K in lithium of the same purity.

(d) Data on depth of internal penetration for the austenitic stainless steels show a small effect of nitrogen content in lithium. Assuming a linear rate law, the data yield penetration rates of 184 ± 31, 99 ± 11, and 45 ± 22 μm/year for Types 316 CW, 316, and 304L stainless steel. For similar lithium chemistry (200 ppm N), the penetration rates for Type 316 stainless steel in lithium at 700 and 755 K are comparable.

(e) Ferritic steels show little or no internal penetration. The values of 3 to 5 μm of penetration for ferritic steels correspond to the limit of measurement for the method used in the study.

The results for dissolution rates show a strong dependence on nitrogen content in lithium. In general, the weight loss in lithium is due primarily to the loss of nickel from the material and, to a lesser extent, to the dissolution of chromium and iron. This accounts for the large difference in the dissolution rates between austenitic and ferritic steels. Metallographic examination of the exposed specimens reveals a porous corrosion layer for the austenitic stainless steels, whereas the ferritic steels show little or no corrosion. Micrographs of the corrosion layers formed on the austenitic stainless steels exposed at 755 K in lithium with ~200 ppm nitrogen are shown in Fig. 9.2.1. A typical energy dispersive x-ray analysis of the scale yields <1% nickel, ~12% chromium, and balance iron, i.e., a ferrite phase. Several studies on corrosion of austenitic stainless steels in flowing lithium indicate that an increase in nitrogen content in lithium increases the dissolution rate owing to preferential leaching of chromium from the steel.[5]

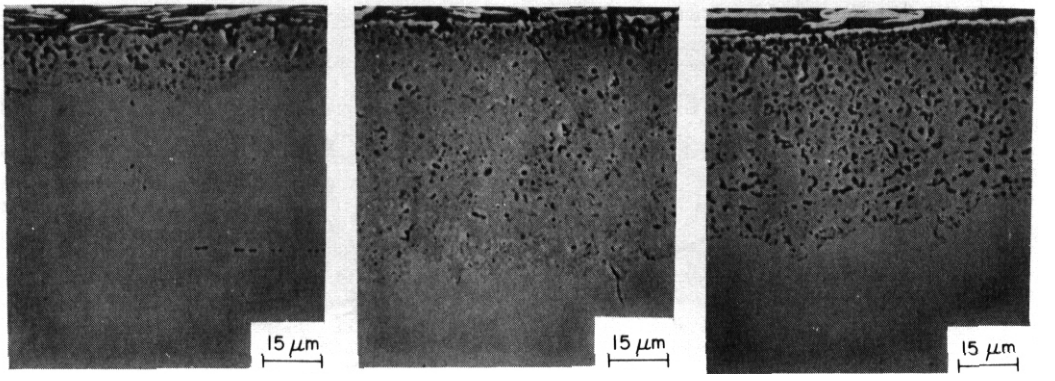

Fig. 9.2.1. Micrographs of the Corrosion Layers Formed on Austenitic Stainless Steels Exposed for 7.2 Ms at 755 K in Lithium Containing ~200 ppm Nitrogen.

However, such behavior will have less effect on the depth of internal penetration, which is basically controlled by dissolution of nickel from the material.

The influence of a lithium environment on the cyclic properties of annealed Type 316 stainless steel was investigated by conducting fatigue tests in flowing lithium at 755 K. The concentration of nitrogen in lithium was ~50 ppm. Figure 9.2.2 shows the total-strain/life behavior of Type 316 stainless steel tested in lithium and air at 755 K,[6] and in sodium at 823 K.[7] The results show that fatigue life in lithium is a factor of 3 to 8 greater than in air. Data in sodium at 755 K are not available, but fatigue life in lithium at 755 K is slightly greater than in sodium at 823 K. Fatigue specimens of Type 316 stainless steel are being exposed to flowing lithium at 755 K. Fatigue tests will be conducted with these specimens to determine the effect of preexposure on fatigue life.

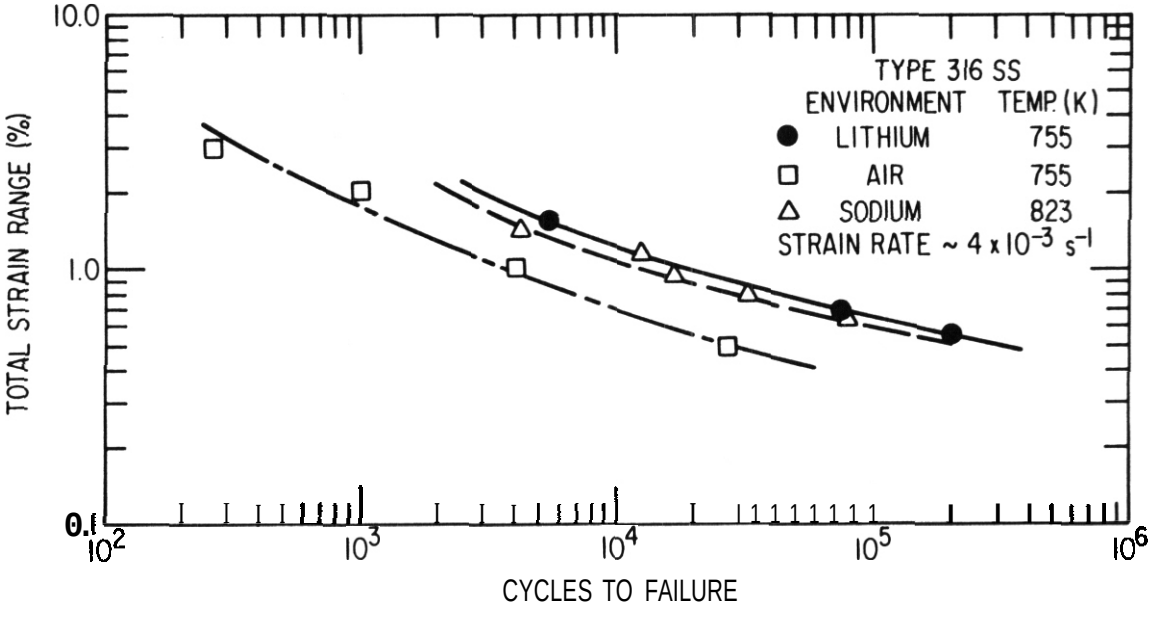

Fig. 9.2.2. Total Strain Range vs Cycles to Failure for Type 316 Stainless Steel Tested in Lithium and Air[5] at 755 K and in Sodium[6] at 823 K. The concentration of nitrogen in lithium was ~50 ppm.

9.2.4.2 Lead–Lithium Environment

A forced–flow loop for conducting corrosion and mechanical tests of structural materials in a well–characterized liquid 17Li-83Pb environment is nearly complete. A schematic of the loop is shown in Fig. 9.2.3. The loop consists of a high–temperature test vessel and a cold leg. The total volume of the loop is ~2 liters. The test vessel is designed to accommodate a mechanical fixture for conducting either constant stress or constant extension rate tests. Approximately 6 liters of the eutectic 17Li-83Pb alloy were prepared by melting lead in the mixing vessel under a purified argon environment and adding small amounts of liquid lithium (~10 cm^3 per addition). The liquid lead/alloy was maintained at ~740 K with constant stirring during the lithium additions. The increase in temperature of the liquid lead/alloy after each lithium addition was <1 K. The reactions between liquid lithium and lead were observed through the two ports in the cover of the mixing vessel. Initially. the surface of the liquid lead was covered with a grayish–black layer of lead oxide, which prevented proper wetting

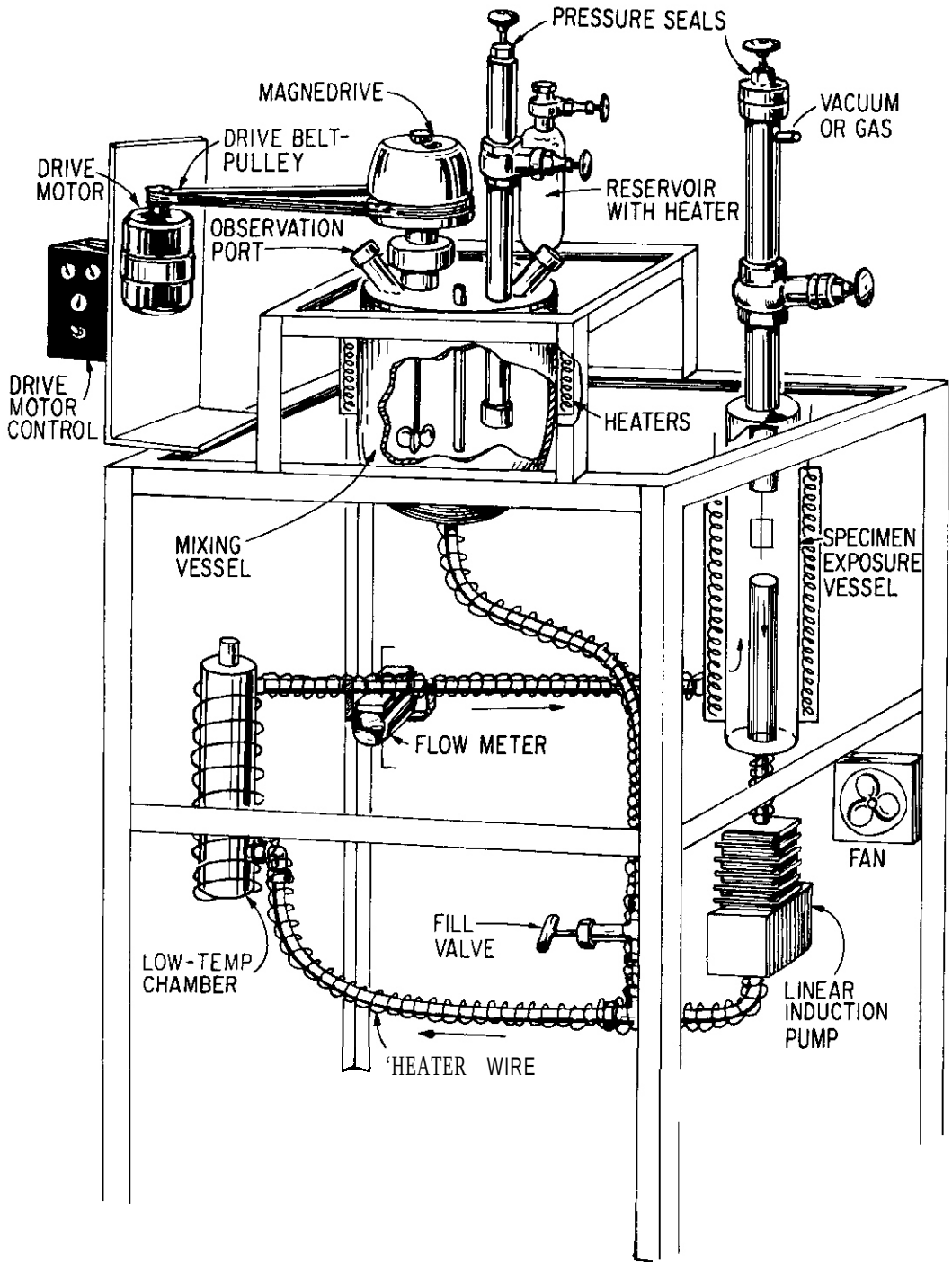

Fig. 9.2.3. Schematic of the Lead-Lithium Test Loop.

between liquid lithium and lead. The reaction between lithium and lead for each Li addition proceeded as follows: Upon contact with the lead, the lithium drops displaced the oxide film and formed a pool on the surface. For the next 20 to 40 s, the layer of lithium in contact with lead solidified, possibly owing to the formation of a lithium-rich lead compound. Then this solid dissolved rapidly in the lead, releasing intense heat in the process. The reaction produced an orange-red flame-like color at the solid-liquid interface. A grayish solid remained floating on the surface; on stirring, this gradually dissolved in the lead.

The eutectic alloy will be bottom poured into the loop after it is analyzed to check the composition and determine the concentration of interstitial elements such as C, N, and H.

9.2.5 Conclusions

The corrosion rates of ferritic steels in cold-trapped flowing lithium at 700 and 755 K are a factor of ~10 lower than for the austenitic stainless steels, and the rate for cold-worked Type 316 stainless steel is a factor of ~2 to 3 greater than for the annealed material. After exposure to lithium, the austenitic steels develop a very porous ferrite layer, whereas the ferritic steels show little or no corrosive penetration. Data on dissolution rates indicate a strong dependence on nitrogen content in lithium in the range 50-200 ppm. Measurements of the depth of internal penetration show less dependence on nitrogen content in lithium and yield values of 184, 99, and 45 μm/year as the penetration rates in lithium at 755 K for Type 316 CW, 316, and 304L stainless steels. The ferritic steels show no measurable penetration. The penetration rates obtained from short-term data for Type 316 stainless steel are comparable at 700 and 755 K.

The fatigue life of annealed Type 316 stainless steel in flowing lithium at 755 K is a factor of 3 to 8 greater than in air. In a low-nitrogen lithium environment, the fatigue life of this steel is comparable to that in sodium. Fatigue tests will be conducted on lithium-exposed specimens to evaluate the long-term effects of lithium on the cyclic properties of Type 316 stainless steel.

9.2.6 References

1. O. K. Chopra and D. L. Smith, "Environmental Effects on Properties of Structural Alloys," pp. 321-347 in Alloy Development for Irradiation Performance: Semiannual Progress Report for Period Ending September 30, 1981, Oak Ridge National Laboratory, DOE/ER-0045/7.
2. O. K. Chopra, D. L. Smith, and W. E. Ruther, "Environmental Effects on Properties of Structural Alloys," pp. 491-499 in Alloy Development for Irradiation Performance: Semiannual Progress Report for Period Ending March 31, 1982, Oak Ridge National Laboratory, DOE/ER-0045/8.
3. P. F. Tortorelli, J. H. Devan, and C. T. Liu, "Corrosion of Iron-Base Alloys in Flowing Lithium," ibid., pp. 312-320.
4. P. F. Tortorelli, J. H. Devan, and R. M. Yonco, "Compatibility of Fe-Cr-Mo Alloys with Static Lithium," paper presented at Corrosion/81 T-2-1 Meeting, Toronto, Canada, 1981.
5. P. F. Tortorelli and O. K. Chopra, J. Nucl. Mater. 103 & 104, 621-632 (1981).
6. D. R. Diercks, A Compilation of Elevated-Temperature, Strain Controlled Fatigue Data on Type 316 Stainless Steel, Argonne National Laboratory, ANL/MSD-77-8. 1977.
7. G. J. Zeman and D. L. Smith, Nucl. Technol. 42(1): 82-89 (1979).

9.3 CORROSION OF FERROUS ALLOYS IN STATIC Pb AND Pb–17 at. % Li

P. F. Tortorelli and J. H. DeVan (Oak Ridge National Laboratory)

9.3.1 ADIP Task

ADIP Task I.A.3, Perform Chemical and Metallurgical Compatibility Analyses.

9.3.2 Objective

The purpose of this program is to determine the chemical compatibility of fusion reactor candidate material with possible coolants and tritium-breeding materials. Specimens are exposed to static lithium, lead-lithium, and lead melts to identify the kinetics and mechanisms that govern corrosion. Other program objectives include (1) to determine the effects of N, C, H, and O on apparent solubilities of metals in lithium and lead-lithium; (2) to determine the carbon and nitrogen partitioning coefficients between alloys and these melts; (3) to determine the effects of soluble (Ca, Al) and solid (Y, Zr, Ti) active metal additions on corrosion by lithium and lead-lithium; and (4) to determine the tendencies for mass transfer between dissimilar metals.

9.3.3 Summary

Specimens of type 316 stainless steel were exposed to static pure lead for 1000 and 3000 h at 400, 500, and 600°C, respectively. Weight losses measured in these tests were compared with those measured in similar tests with Pb–17 at. % Li. The data showed that the addition of 17 at. % Li to lead has some effect on its dissolution behavior relative to type 316 stainless steel; however, the weight losses in both the lead-lithium and pure lead melts were much larger than in pure lithium. Preliminary results from compositional analyses of type 316 stainless steel exposed to static Pb–17 at. % Li showed surface depletion of nickel at 500°C.

9.3.4 Progress and Status

A molten lead-lithium alloy is being considered as a possible tritium-breeding medium for fusion reactors.[1] We are therefore studying

the compatibility of candidate structural alloys with molten lead–lithium by exposing tensile specimens of type 316 stainless steel and Sandvik HT9 to the low-melting-point (235°C) eutectic composition of Pb–17 at. % Li. Some results from capsule tests with Pb-17 at. % Li have been reported previously.[2,3] Recently, we have completed experiments in which type 316 stainless steel tensile specimens were exposed to pure, static, molten lead in order to directly compare corrosion weight losses and processes in lead and Pb–17 at. % Li. In this way, we could evaluate whether the 17% Li addition has a significant effect on the corrosivity of liquid lead. The experimental conditions for the lead tests were similar to those used previously for pure lithium and Pb-17 at. % Li static tests. The specific procedures for preparing the lead and cleaning the test specimens were the same as those used with Pb–17 at. % Li and are fully described in a previous progress report.[2] Following exposure of tensile specimens in the lead-containing capsules, the specimens were cleaned by immersion in pure lithium, followed by a water rinse. We previously showed that using lithium for this purpose did not affect the specimen weight change at temperatures near the melting point of lithium. The cleaning procedure was repeated until specimen weights became approximately constant, which then indicated that most of the residual lead had been removed. The lead used in all the experiments was as-received high-purity (99.99%) metal. Neutron activation analysis revealed an oxygen concentration in the as-received lead of less than 3 wt ppm, while post-test analyses of lead from selected capsules yielded oxygen concentrations of 10 wt ppm and less.

Weight changes have now been determined for type 316 stainless steel in static lead at 400, 500, and 600°C following 1000- and 3000-h exposures, respectively. (Exposures of 5000 h have not yet been completed.) The weight change data from these experiments are shown in Figs. 9.3.1 through 9.3.3, which also contain previously reported[3] data for exposures of type 316 stainless steel to pure lithium and Pb–17 at. % Li. Note that the weight losses of type 316 stainless steel specimens exposed to lead increased with increasing exposure time and temperature and were significantly higher at all temperatures than the losses in pure lithium. The

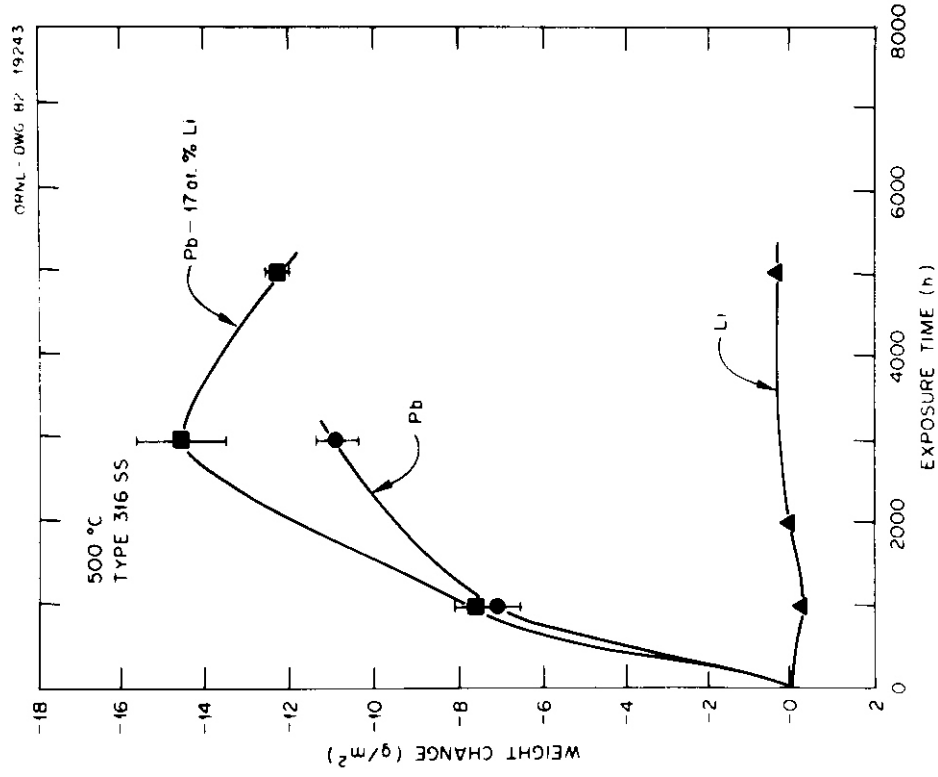

Fig. 9.3.2. Weight Change Versus Exposure Time for Type 316 Stainless Steel Exposed to Static Li, Pb, and Pb–17 at. % Li at 500°C.

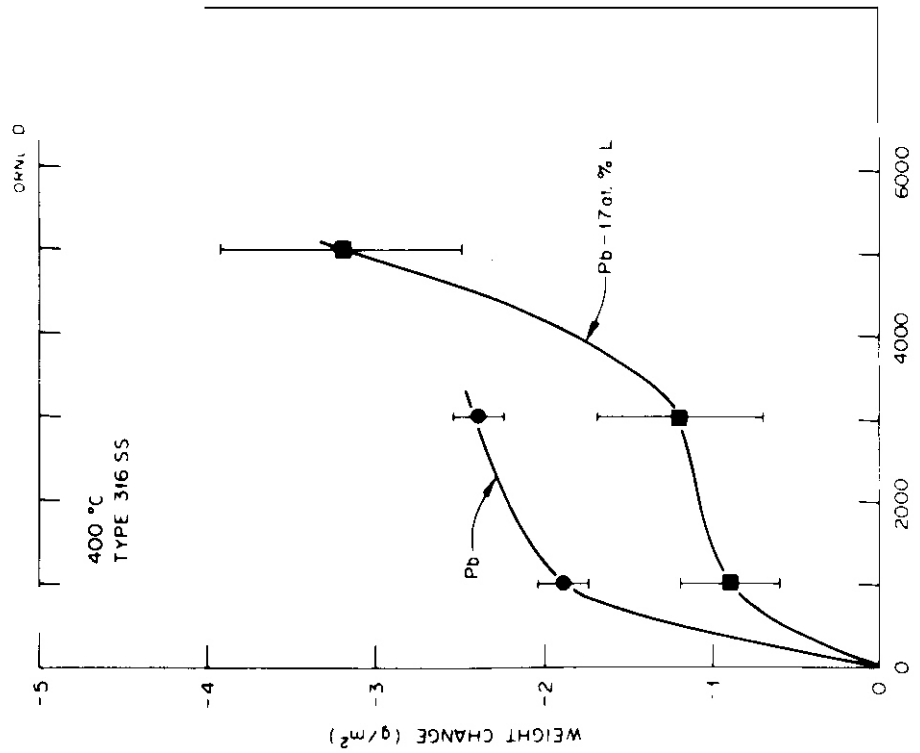

Fig. 9.3.1. Weight Change Versus Time for Type 316 Stainless Steel Exposed to Static Pb and Pb–17 at. % Li at 400°C.

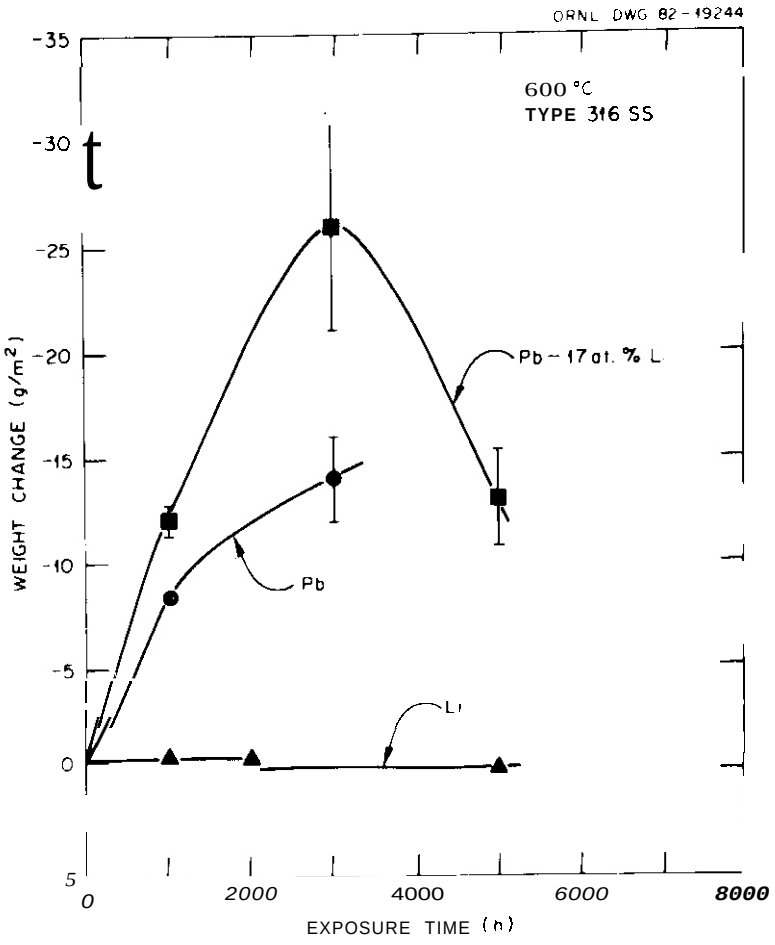

Fig. 9.3.3. Weight Change Versus Exposure Time for Type 316 Stainless Steel Exposed to Static Li, Pb, and Pb–17 at. % Li at 600°C.

weight losses in pure lead were slightly higher at 400°C and lower at 500 and 600°C than those in the lead–lithium melt. However, the standard deviation of the 3000-h data for Pb–17 at. % Li is relatively large, particulary at 600°C, and comparisons after 5000 h are needed to amplify these observations.

The higher weight losses in lead compared with lithium are in accord with data previously published for lead.[4] The present data show that these higher weight losses are not significantly reduced by the addition of 17 at. % Li to the lead; in fact, there is a preliminary indication that the corrosivity of the Pb-17 at. % Li alloy may possibly be greater than that of pure lead at 500 and 600°C. Because of the relatively high corrosivity of Pb–17 at. % Li toward ferrous alloys, we plan to initiate

further capsule tests to investigate the effectiveness of corrosion inhibition elemental additions, such as titanium, to the melt. Such additions reduced the corrosivity of pure lead.[5]

The weight losses in Figs. 9.3.1 through 9.3.3 are indicative of corrosion under static conditions and are not truly indicative of the magnitude of corrosion rates in flowing Pb–17 at. % Li, particularly when a temperature gradient is imposed on the flowing system. Because of this we are planning to conduct a thermal-convection loop test with Pb–17 at. % Li, using procedures previously described[6] for our lithium loop experiments. In this way, we can obtain kinetic data for dissolution in slowly flowing Pb–17 at. % Li under an impressed temperature gradient that would be applicable for use of the liquid metal as a semistagnant tritium-breeding fluid.

Scanning electron microscopy and energy-dispersive x-ray analysis have been used to determine the effects of exposure to static Pb–17 at. % Li on surface topography and composition. Figure 9.3.4 includes scanning electron micrographs of type 316 stainless steel exposed to Pb–17 at. % Li for 5000 h at 300, 400, and 500°C. A micrograph of the surface of a type 316 stainless steel control specimen exposed to argon for 5000 h at 500°C is also included in the figure. Note that corrosion-induced surface changes are not significant below 500°C. This observation is consistent with our metallographic examination of polished cross sections.[2] The energy-dispersive x-ray analysis of these surfaces is not complete, but some results for a type 316 stainless steel specimen exposed at 500°C are shown in Figs. 9.3.5 and 9.3.6 and Table 9.3.1. In Fig. 9.3.5, the characteristic x-ray spectrum for a typical area on the exposed specimen surface is shown along with a spectrum from as-received type 316 stainless steel. The relative intensity of the nickel K_α peak is significantly less for the type 316 stainless steel exposed to Pb–17 at. % Li, and it is evident that nickel has been preferentially leached from the steel. A similar effect is obvious from the results shown in Fig. 9.3.6 and Table 9.3.1. Underlying areas of the surface have higher ratios of nickel to iron K_α intensities than those areas right on the surface. Although nickel depletion does not commonly occur for

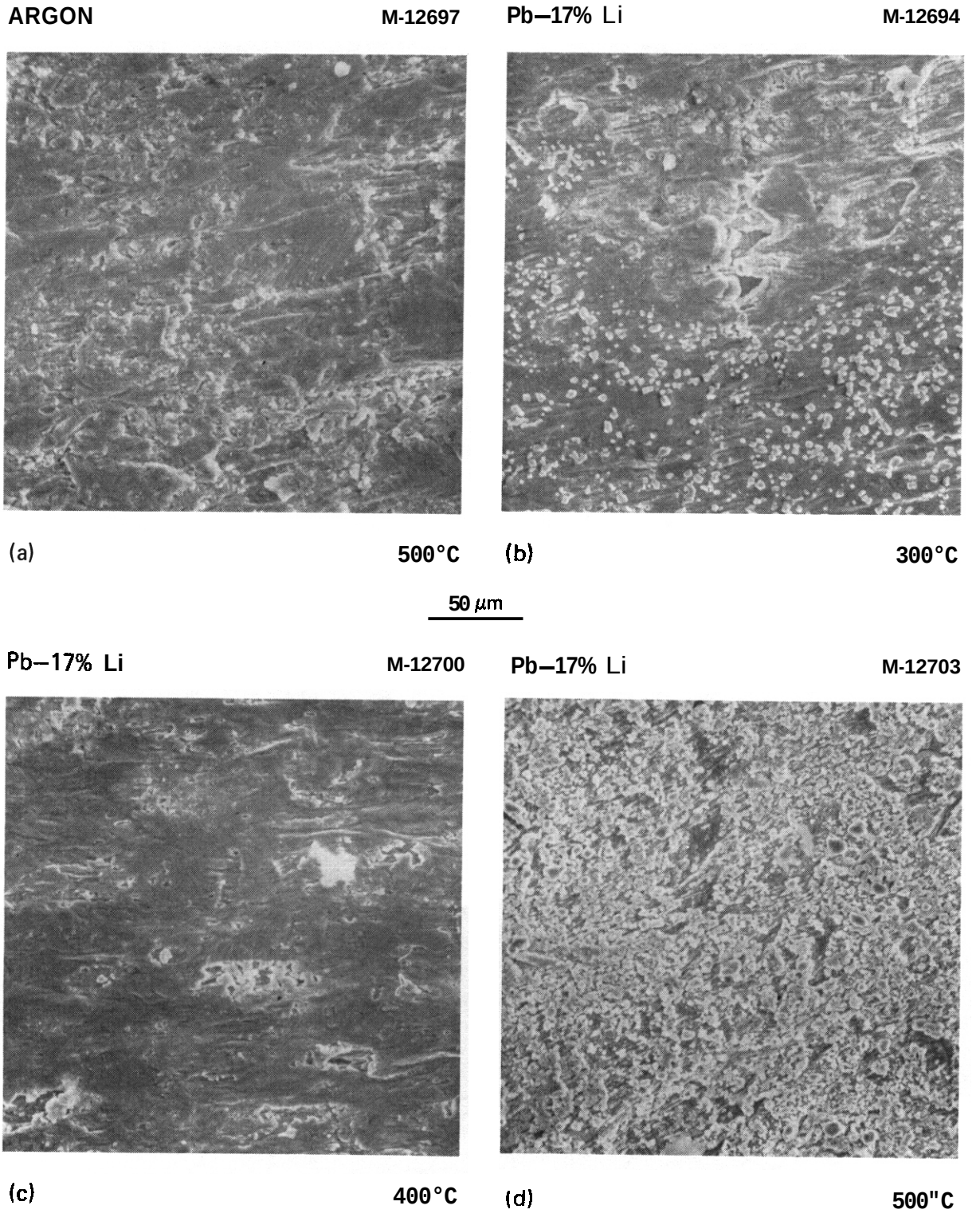

Fig. 9.3.4. Scanning Electron Micrographs of Type 316 Stainless Steel Exposed to Static Argon and Pb–17 at. % Li.

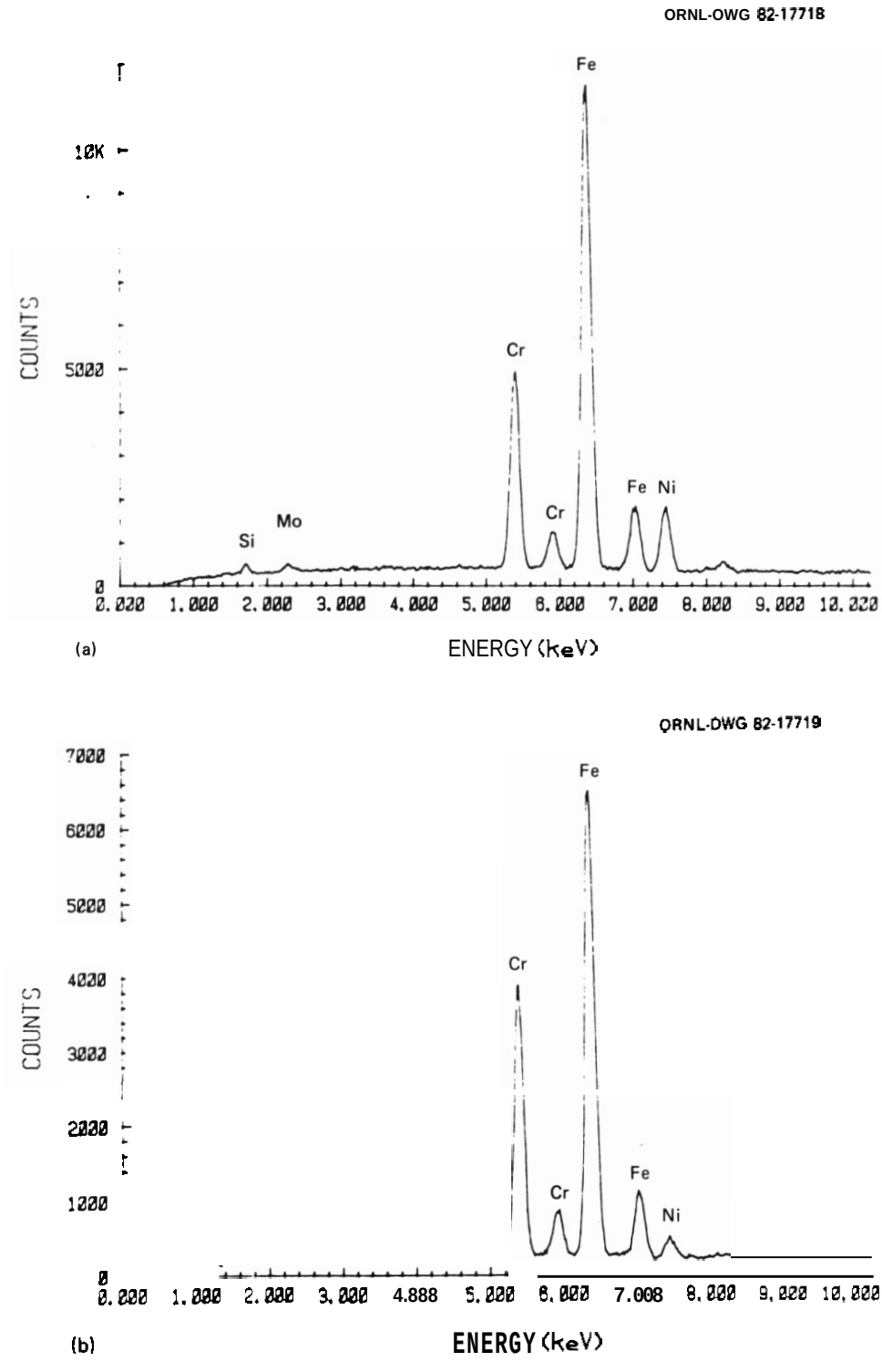

Fig. 9.3.5. Energy-Dispersive X-Ray Spectra for Type 316 Stainless Steel: (a) Unexposed Standard; (b) Exposed to Static Pb–17 at. % Li for 5000 h at 500°C.

M-16779

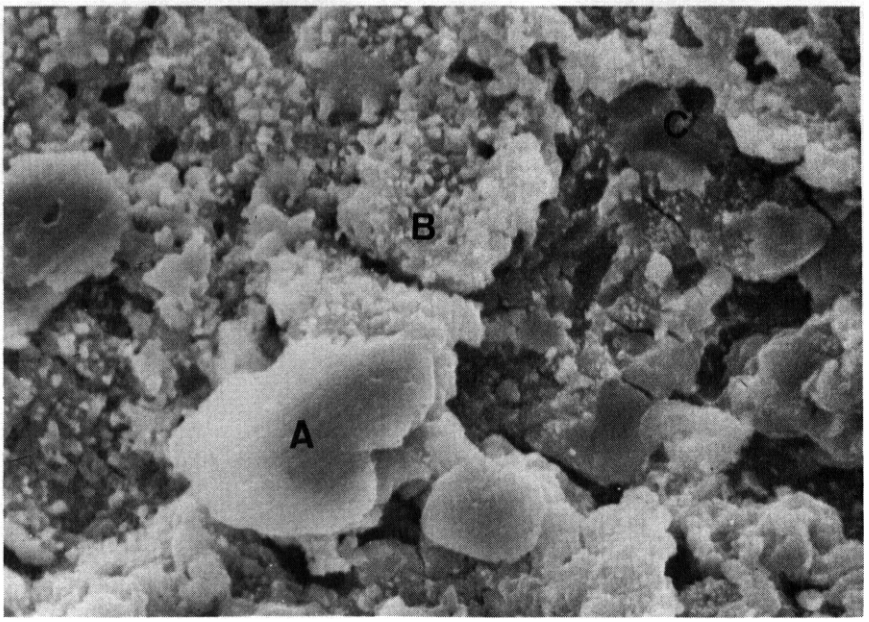

Fig. 9.3.6. Scanning Electron Micrograph of Type 316 Stainless Steel Exposed to Static Pb–17 at. % Li for **5000** h at 500°C; Near Shoulder of Tensile Specimen; Letters Refer to Energy–Dispersive X–Ray Spectra Taken at Those Areas (see Table 9.3.1).

Table 9.3.1. K_α Peak Ratios for Selected Areas on a Type 316 Stainless Steel Surface Exposed to Pb–17 at. % Li for *500* h at 500°C

Area[a]	K_α Peak Ratios	
	Cr/Fe	Ni/Fe
A	***0.24***	0.01
B	0.64	0.03
C	0.71	0.06
Standard	***0.40***	**0.13**

[a]Areas defined by Fig. 9.3.6.

nickel-containing alloys in static lithium, it characteristically is observed in flowing lithium systems.[4] Data from x-ray diffraction of specimens exposed to Pb-17 at. % Li confirmed that nickel depletion did indeed occur: both austenitic and ferritic phases were detected on these surfaces. The presence of a ferritic phase typically indicates that depletion of nickel has occurred such that the austenite becomes unstable and transforms to ferrite. The ferritic phase was detected on specimen6 exposed at all three test temperatures (300, 400, and 500°C).

9.3.5 Conclusions

1. Weight losses of type 316 stainless steel exposed to static pure lead are no worse than those of specimens exposed to static Pb-17 at. % Li. Such weight losses in both lead and Pb-17 at. % Li are much greater than the weight changes measured in static pure lithium under similar conditions.

2. The surfaces of type 316 stainless steel specimens exposed to static Pb-17 at. % Li at 300, 400, and 500°C were depleted in nickel.

9.3.6 References

1. D. K. Sze, R. Clemmer, and E. T. Cheng, *LiPb, A Novel Material for Fusion Applications,* UWFDM-378, University of Wisconsin, Madison, October 1980.
2. P. F. Tortorelli and J. H. DeVan, "Compatibility of Austenitic and Ferritic Steels with Pb-17 at. % Li," *ADIP Semiannu. Prog. Rep. Sept. 30, 1981,* DOE/ER-0045/7, pp. 300-11.
3. P. F. Tortorelli and J. H. DeVan, "Corrosion of Austenitic and Ferritic Steels in Static Pb-17 at. % Li," *ADIP Semiannu. Prog. Rep. Mar. 31, 2,982,* DOE/ER-0045/8, pp. 500-06.
4. P. F. Tortorelli and O. K. Chopra, "Corrosion and Compatibility Considerations of Liquid Metals for Fusion Reactor Applications," *J. Nucl. Mater.* 103&104: 621-32 (1981).
5. R. C. Asher, D. Davies, and S. A. Reetham, "Some Observations on the Compatibility of Structural Materials with Molten Lead," *Corros. Sci.* 17: 545-57 (1977).

9.4 COMPATIBILITY STUDIES OF STRUCTURAL ALLOYS WITH SOLID BREEDER MATERIALS - O. K. Chopra and D. L. Smith (Argonne National Laboratory)

9.4.1 ADIP Task

ADIP tasks are not defined in the 1978 program plan.

9.4.2 Objective

The objective of this task is to evaluate the compatibility of solid breeder materials with structural alloys. The interactions between breeder materials and alloys are investigated as a function of temperature, time, and environmental parameters (i.e., flowing helium environments with different moisture contents). Reaction rates are determined by measuring the weight change, depth of internal penetration, and thickness of corrosion scales. These measurements, coupled with metallographic evaluation of the alloy surfaces, are used to establish the mechanisms and rate-controlling processes for the corrosion reactions. Breeder materials to be investigated include Li_2O, $LiAlO_2$, Li_2SiO_3, Li_2TiO_3, and Li_2ZrO_3.

9.4.3 Summary

The compatibility of ferritic and austenitic steels with Li_2O pellets has been investigated at 823 K (550°C) in flowing helium containing 93 ppm H_2O and 1 ppm H_2. The results indicate that both steels develop an iron-rich outer scale and a chromium-rich subscale. The reaction rates for ferritic and austenitic steels are comparable and yield a value of ~85 μm/year for penetration rate. The Li_2O pellets exposed with the various alloys lose weight. The weight loss follows a parabolic law, predicting a value of ~4.8%/year.

9.4.4 Progress and Status

A comparative evaluation of the reactivity of the HT-9 alloy and annealed Type 316 stainless steel with solid Li_2O, $LiAlO_2$, and Li_2SiO_3 at 973 and 773 K (700 and 500°C) was presented in earlier reports.'"

For these tests, tube specimens packed with the ceramic material were sealed under vacuum, enclosed in a quartz tube, and annealed for 3.6 and 7.2 Ms (1000 and 2000 h). The results indicate that Li_2O is the most reactive of the three breeding materials. Reactivity of the **HT-9** alloy is comparable to that of Type 316 stainless steel. Specimens exposed with Li_2O developed a layer of internal penetration and a thicker outer scale that consisted of ceramic material emhedded with iron-rich reaction products. Three reaction products, Li_5FeO_4, $LiFe_2CrO_4$, and $LiCrO_2$, were detected in the reaction scales on RT-9 and Type 316 stainless steel. Li_5FeO_4 was predominant in the outer scale whereas $LiFe_2CrO_4$ and $LiCrO_2$ were present in the layer of internal corrosive penetration. The values ***of*** the total scale thickness and internal penetration at 773 K were lower by a factor of ~3 and 4, respectively, than those at 973 K.

A significant result from the capsule compatibility tests is that the thickness of the reaction scale or depth of internal penetration is the **same** after 3.6 and 7.2 Ms. This behavior suggests that the interactions between alloy and ceramic stop after a short time. It is probable that in a closed system, such as sealed capsules, the chemical activity of the reactive species decreases with time, i.e., the reaction is starved of the reactive species. A better understanding of the nature of the corrosive interactions can be gained by conducting compatibility tests in a flowing helium environment with controlled partial pressures of oxygen and hydrogen. Such experiments simulate the conditions projected for blanket structures during reactor operation.

During the current reporting period, tests were conducted with Li_2O at 823 K (550°C) in a flowing helium environment containing ~93 ppm H_2O and ~1 ppm H_2. A detailed description of the compatibility test facility has been given earlier.' A schematic of the specimen exposure tube is shown in Fig. 9.4.1. Alloy specimens, approximately 10 x 10 x 0.4 mm in size, were sandwiched between trio ~12-mm-diameter and ~2.4-mm-thick pellets of Li_2O and mounted in a specimen holder such that the

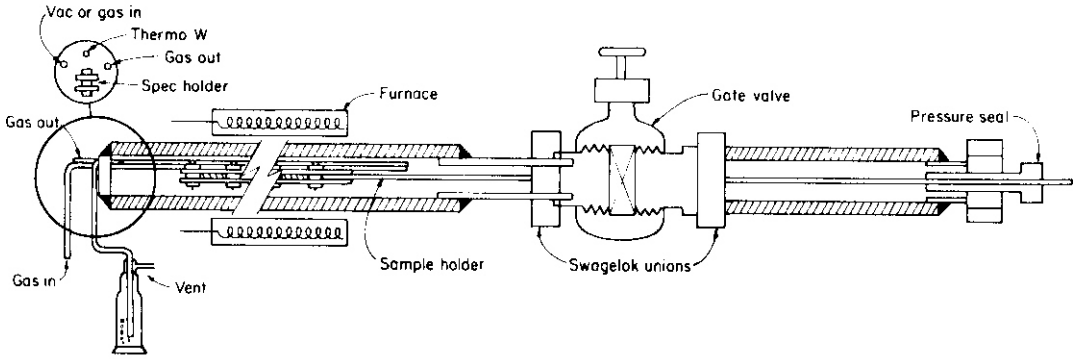

Fig. 9.4.1. Schematic of the Specimen Exposure Tube.

surface of the ceramic specimens was exposed to the flowing gas environment. The alloy–ceramic couples were assembled inside a glove box and transferred to the furnace in a specimen transfer tube filled with a vacuum–tight gate valve. The specimen exposure tubes were evacuated and flushed with pure helium before the specimens were introduced into the furnace. The alloy–ceramic couples were exposed for 1.8, 3.6, and 7.2 Ms (500, 1000, and 2000 h). Four reaction couples consisting of HT–9 alloy, Fe-9Cr-1Mo steel, 20% cold–worked Type 316 stainless steel, and either pure nickel or annealed Type 316 stainless steel were included in each compatibility test. In addition, a nickel foil (without the Li_2O pellets) was placed downstream from the reaction couples to study the deposition behavior.

A second compatihility test with Li_2O has been initiated at 823 K in flowing helium containing ~1 ppm H_2O and ~1 ppm H_2. The specimens will he exposed for 3.6, 9.0, and 14.4 Ms (1000, 2500, and 4000 h). The 3.6–Ms test has been completed. These compatibility tests are being conducted as part of the cooperative US/Japan exchange with Dr. Kurasawa of the Japan Atomic Energy Research Institute.

The alloy and ceramic specimens were weighed before and after the compatihility tests. In addition, the alloy specimens were examined metallographically to determine the thickness of the reaction scale and depth of internal corrosive penetration. Tho total thickness of the reaction scale was determined from the difference between the specimen

thickness after the test and the sound metal remaining (i.e., the unreacted material). Depth of internal penetration was obtained from the difference between the initial thickness of the specimen and the sound metal remaining after the test. Electron microprobe and x-ray diffraction analyses were carried out to identify the phases in the reaction scale.

The weight changes for alloys exposed with Li_2O at 823 K in flowing helium environments are given in Table 9.4.1. The results indicate that all alloys gained weight after exposure and the weight gains for austenitic and Eerritic steels were comparable. The weight gains after 1.8 and 3.6 **Ms** were approximately the same; a significant increase was observed after the **7.2-Ms** exposure. However, after exposure, the alloy-ceramic interface was not always well defined, and in some instances, sections of the reaction scale on the alloys came off with the ceramic pellet when the reaction couples were separated. Consequently, measurements of weight gain are subject to error, particularly for specimens exposed for short times.

Table 9.4.1. Weight Change for Alloys Exposed with Li_2O at 823 K in a Flowing Helium Environment Containing 33 or 1 ppm H_2O and 1 ppm H_2

Exposure Time, Ms (h)	Weight Gain, mg					
	IT-9 Alloy	Fe-9Cr-1Mo	316 CW	316 SS	Pure Ni	Ni Foil[a]
	Helium with 93 ppm H_2O and 1 ppm H_2					
1.8 (500)	2.7	3.6	6.3	b	0.1	b
3.6 (1000)	2.3	3.5	6.2	4.6	b	0.6
7.2 (2000)	17.6	c	19.2	b	6.0	0.4
	Helium with 1 ppm H_2O and 1 ppm H_2					
7.6 (1000)	3.2	5.5	5.5	b	1.0	0.1

[a]Exposed without the Li_2O pellets and located downstream from the reaction couples.
[b]Not tested.
[c]Weight change could not be determined because the scale spalled off.

The change in weight for Li_2O pellets exposed with various alloys at 823 K in a flowing helium environment is given in Table 9.4.2. The Li_2O pellets from all reaction couples lost weight after exposure and the weight loss in helium containing 93 ppm H_2O was greater than in helium containing 1 ppm H_2O. Figure 9.4.2 shows the weight loss of the Li_2O pellets expressed by a parabolic rate law. The results predict a weight loss of ~4.8%/year for Li_2O exposed to helium with 93 ppm H_2O and ~1.5%/year in helium containing 1 ppm H_2O. However, two separate interactions, viz., alloy–pellet and gas–pellet interactions, contribute to the weight loss shown in Fig. 9.4.2. The reaction products from the alloy–pellet interactions form an adherent corrosion scale on the alloy surface and lead to a weight loss for the Li_2O pellets and a gain in weight of the alloy specimen, whereas moisture in the helium environment reacts with Li_2O to form LiOH gas which is carried away by the flowing gas stream. This reaction leads to a net weight loss for the total reaction couple, i.e., a decrease in the combined weight of alloy and Li_2O pellets. Data on weight change indicate a net 5 to 9-mg loss in weight for all the reaction couples exposed for 1.8 and 3.6 Ms in flowing helium containing 93 ppm H_2O. Reaction couples exposed for 7.2 Ms show a net weight gain or insignificant weight loss because of other alloy–pellet–gas reactions. For example, liquid Li may form from certain Li_2O–metal oxide reactions. Lithium would then react with H_2O to form solid Li_2O. These reactions will result in a weight gain for the alloys without a significant change in the weight of Li_2O. The alloy–pellet interactions would dominate at long exposure times and cause a net weight gain for the reaction couple. The individual contributions of alloy–pellet and gas–pellet tnteractions can be determined from an understanding of the various alloy–pellet–gas interactions.

The loss of weight for Li_2O from gas–pellet interactions is reflected in the weight change of the Ni foils located downstream from the reaction couples. In all compatibility tests, the Ni foils gained weight. The surface of the Ni foil exposed for 3.6 Ms in helium containing 93 ppm H_2O is shown in Fig. 9.4.3. The reaction product on the surface was identified by x–ray diffraction to he $Li_2Ni_8O_{10}$. Nickel oxide was not

Table 9.4.2. Weight Change for Li_2O Exposed with Various Alloys at 823 K in a Flowing Helium Environment Containing 93 or 1 ppm H_2O and 1 ppm H_2

Exposure Time, Ms (h)	Weight Loss in mg (%) of Li_2O Pellets[a] Exposed with				
	HT-9	9Cr-1Mo	316 CW	316 SS	Pure Ni
		Helium with 93 ppm H_2O and 1 ppm H_2			
1.8 (500)	11 ▪ (▪ ≈○)	11.9 (1.25)	11.1 (1.16)	b	c
3.6 (1000)	c	11.4 (1.19)	11.6 (1.24)	13.5 (1.41)	b
7.2 (2000)	13 ▪ (▫ 4▪)	22.7 (2.46)	22.2 (2.39)	b	32.0 (3.51)
		Helium with 1 ppm H_2O and 1 ppm H_2			
3 6 (1000)	▪ ▪ (○ 40)	6.8 (0.69)	6.6 (0.65)	b	2.4 (0.26)

[a]Average weight of the Li_2O pellets was 0.76 ± 0.019 grams. Surface areas ▫ x▫os▫d to gas and to alloy specimens were ~200 and ~115 mm^2, respectively.

[b]Not tested.

[c]Weight change could not be determined because pieces of the pellet chip▫▪▫ off

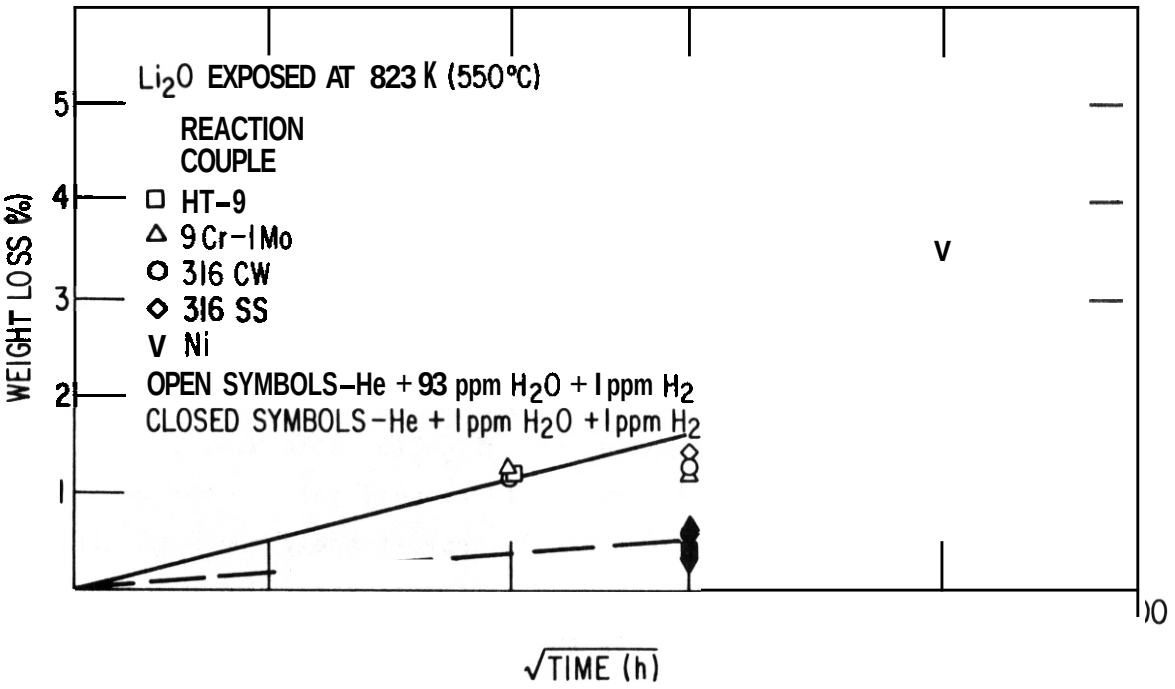

Fig. 9.4.2. Weight Loss vs Exposure Time for Li_2O Pellets Exposed with Various Alloys at 823 K in a Flowing Helium Environment Containing Small Amounts of H_2O and H_2.

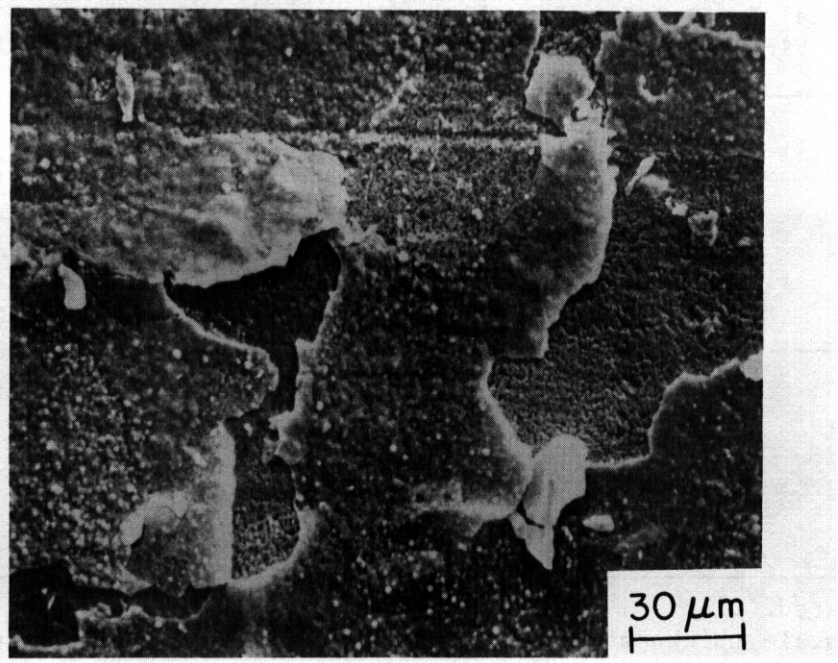

Fig. 9.4.3. Micrograph of the Surface of the Nickel Foil Located Downstream from the Li_2O–Alloy Reaction Couples after 3.6–Ms Exposure at 823 K in Helium Containing 93 ppm H_2O and 1 ppm H_2.

observed. These results indicate that Li is transferred from Li_2O, probably as LiOH, and deposited on the foil to form $Li_2Ni_8O_{10}$.

Metallographic examination of the alloy specimens revealed that the reaction scale on the specimen surface consisted of a very uniform and dense layer of outer scale and a porous layer of subscale. For most specimens, the original alloy surface could be easily resolved. The depth of internal penetration included portions of the outer scale and the subscale. Average values of total scale thickness and depth of internal penetration for alloys exposed with Li_2O at 823 K in flowing helium containing 93 ppm H_2O and 1 ppm H_2 are given in Table 9.4.3. For all alloys, the thickness of the total scale closely follows the weight gain of the alloys, i.e., scale thickness is approximately the same after 1.8- and 3.6-Ms exposure and increases significantly after 7.2 Ms. The depth of internal penetration, however, increases gradually with time. As mentioned earlier, the measurements of total scale thickness are subject to error because of the uncertainty in locating the final interface between the reaction scale and Li_2O pellet. In contrast, the depth of

Table 9.4.3. Average Values of Total Scale Thickness and Depth of Internal Penetration for Alloys Exposed with Li_2O at 823 K in Flowing Helium Containing 93 ppm H_2O and 1 ppm H_2

	Exposure Time					
	1.8 Ms (500 h)		3.6 Ms (1000 h)		7.2 Ms (2000 h)	
Alloy	Total Scale, μm	Penetration Depth, μm	Total Scale, μm	Penetration Depth, μm	Total Scale, μm	Penetration Depth, μm
HT-9	14	3	b	8	52	22
Fe-9Cr-1Mo	17	7	27	12	b	15
316 CW	23	6	20	14	56	21
316 SS	a	a	27	7	a	a
Pure Ni	0	0	a	a	15	9

[a]Not tested.
[b]Total scale thickness could not be measured because the scale spalled off.

internal penetration can be determined accurately. Figure 9.4.4 shows the increase in penetration depth and total scale thickness with time. Depth of internal penetration can be represented by a linear rate of increase and yields a value of ~85 μm/year for penetration. Data for internal penetration may also be expressed by a parabolic rate law and yield a 0.7-Ms (195-h) incubation period and ~50 μm/year penetration rate.

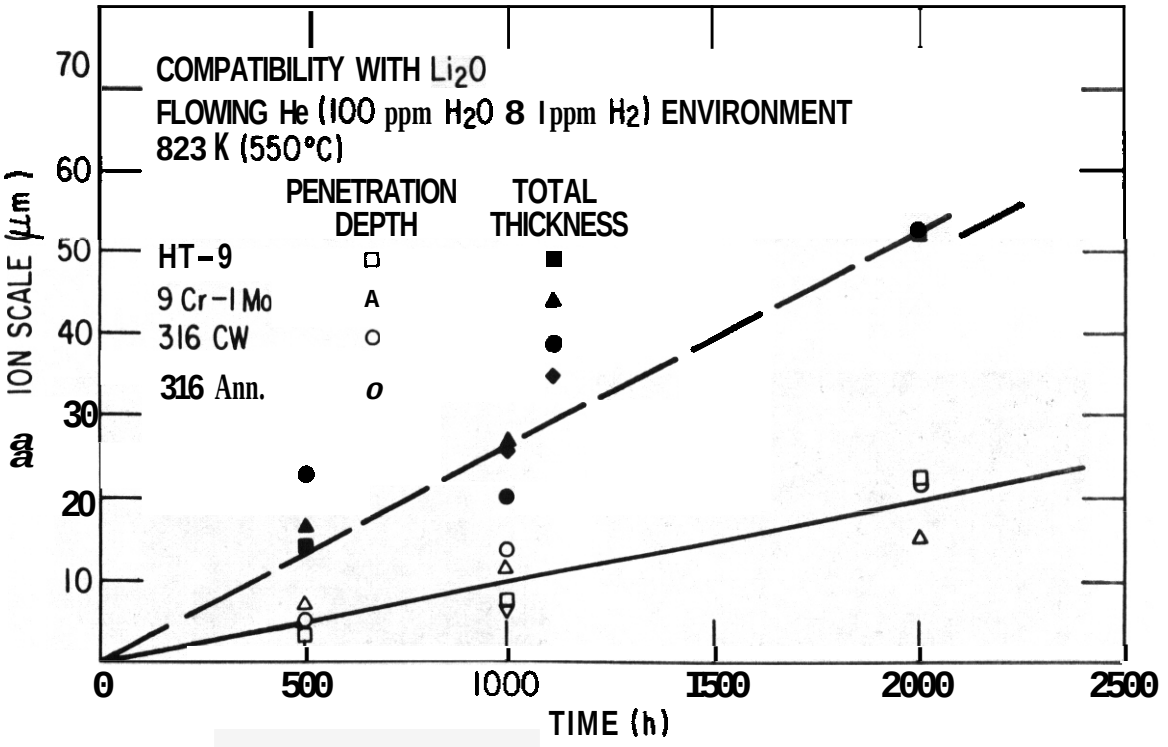

Fig. 9.4.4. The Change in Total Thickness of the Reaction Scale and Penetration Depth for Alloys Exposed with Li_2O at 823 K in Flowing Helium Containing 93 ppm H_2O and 1 ppm H_2.

Micrographs of the reaction scales on the various alloy specimens exposed with Li_2O at 823 K in helium containing 93 ppm H_2O and 1 ppm H_2 are shown in Figs. 9.4.5 and 9.4.6 for 3.6 and 7.2-Ms exposures, respectively. The specimens of ferritic and austenitic steels show identical Eeatures, viz., a very uniform and dense outer scale and a porous

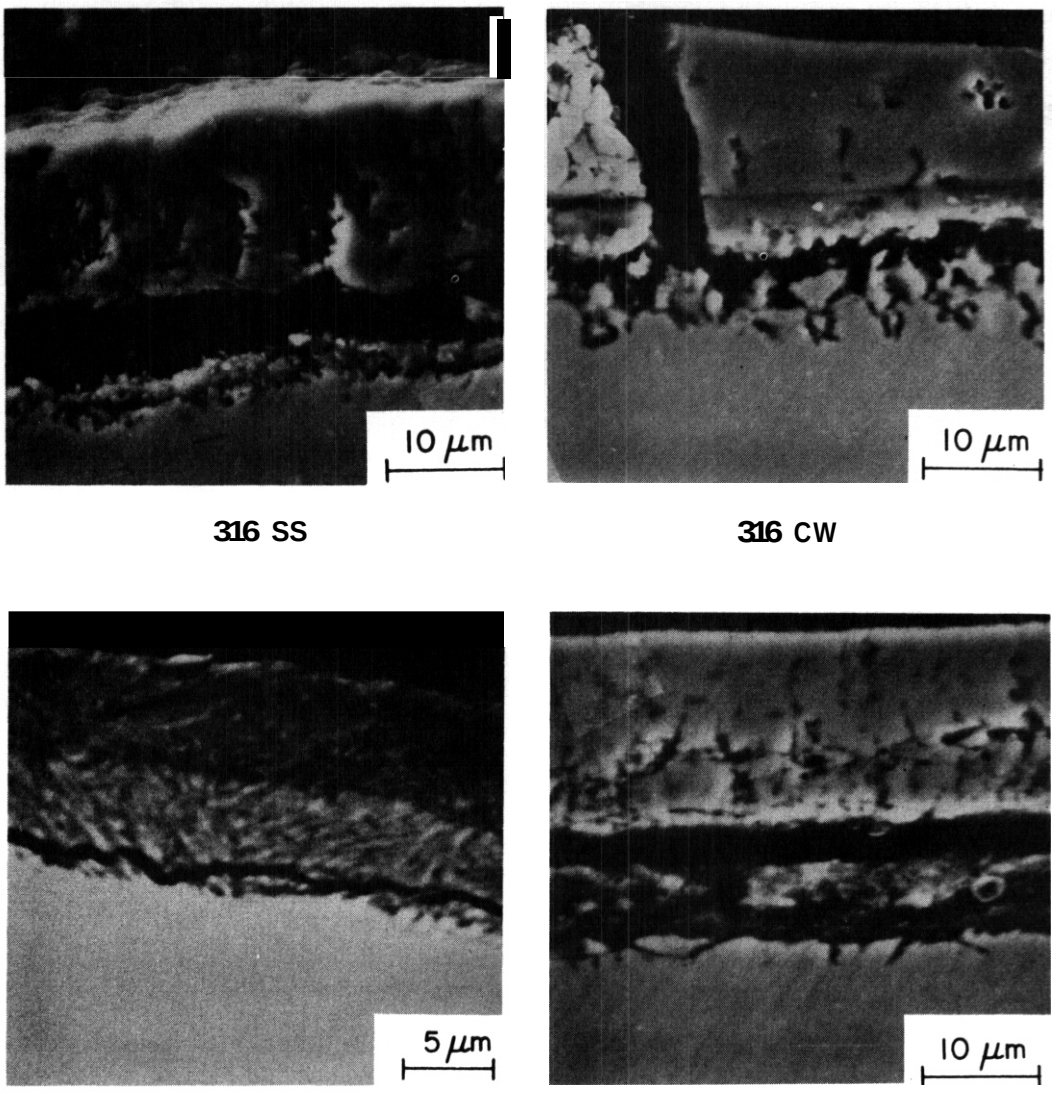

Fig. *9.4.5.* Micrographs of the Reaction Scales on Alloys Exposed with Li_2O at 823 K for 3.6 Ms in Flowing Helium Containing 93 ppm H20 and 1 ppm H_2.

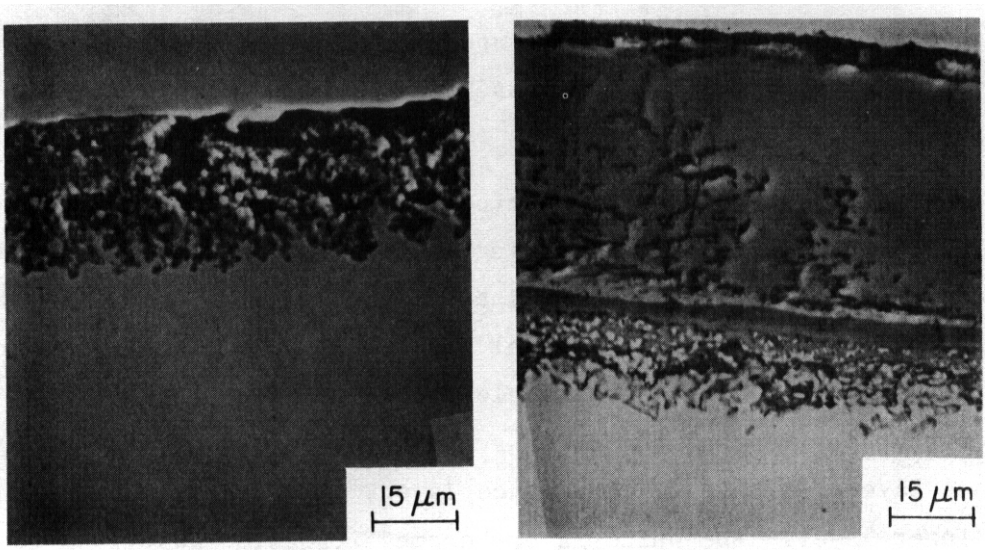

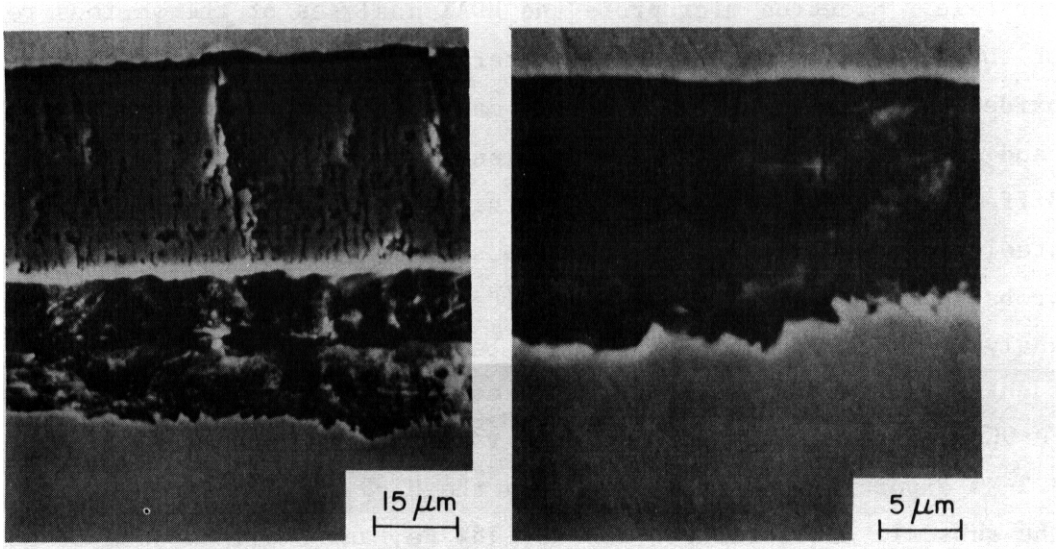

Fig. 9.4.6. Micrographs of the Reaction Scales on Alloys Exposed with Li_2O at 823 K for 7.2 Ms in Flowing Helium Containing 93 ppm H_2O and 1 ppm H_2.

subscale. In addition, stringers of corrosion products are observed extending into the matrix for cold-worked Type 316 stainless steel. The outer scales on HT-9 alloy exposed for 3.6 Ms and Fe-9Cr-1Mo steel exposed for 7.2 Ms had spalled off and are, therefore, not observed in the micrographs. The pure nickel specimen also shows considerable corrosive attack.

The reaction scales on the various alloys showed some differences in thickness and morphology depending on the location. Micrographs of the scale formed near the center, intermediate section, and edge of the cold-worked Type 316 stainless steel specimen exposed for 7.2 Ms are shown in Fig. 9.4.7. The total scale thickness is smaller towards the edge of the specimen and the outer scale near the edge consists of three distinct layers; a thin black surface layer, a wide gray region, and a white inner layer. The white layer becomes irregular away from the edge and at the center of the specimen it forms a thin band next to the subscale. Electron microprobe and EDAX analyses of the various regions of the scale indicated that the outer scale is primarily lithium-iron oxide. The black surface layer is manganese-rich, and the inner white band is nickel-rich. The compositions and the possible phases of the different regions of the scale on the cold-worked Type 316 stainless steel are shown in Fig. 9.4.8. The subscale is rich in chromium and probably consists of $LiCrO_2$ and $Li(Fe_2Cr)O_4$ phases. X-ray diffraction analyses of the reaction scale are being conducted to positively identify the various phases. The reaction scales on HT-9 alloy and Fe-9Cr-1Mo steel did not show much variation in composition. After a 7.2-Ms exposure, the outer scale on the HT-9 alloy contained ~66% Fe and the subscale consisted of ~30%Cr, 18%Fe, and small amounts of Mo, V, and Si. Micrographs and typical compositions of the reaction scales developed on Fe-9Cr-1Mo steel and cold-worked Type 316 steel exposed for 3.6 Ms are shown in Fig. 9.4.9.

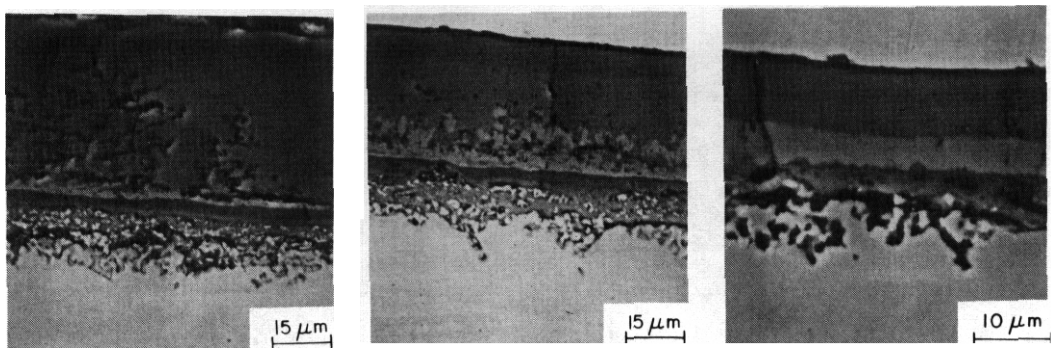

Fig. 9.4.7. Micrographs of the Reaction Scales Near the (a) Center, (b) Intermediate Region, and (c) Edges of the Cold-worked Type 316 Stainless Steel Specimen Exposed at 823 K for 72 Ms in Helium Containing 93 ppm H_2O and 1 ppm H_2.

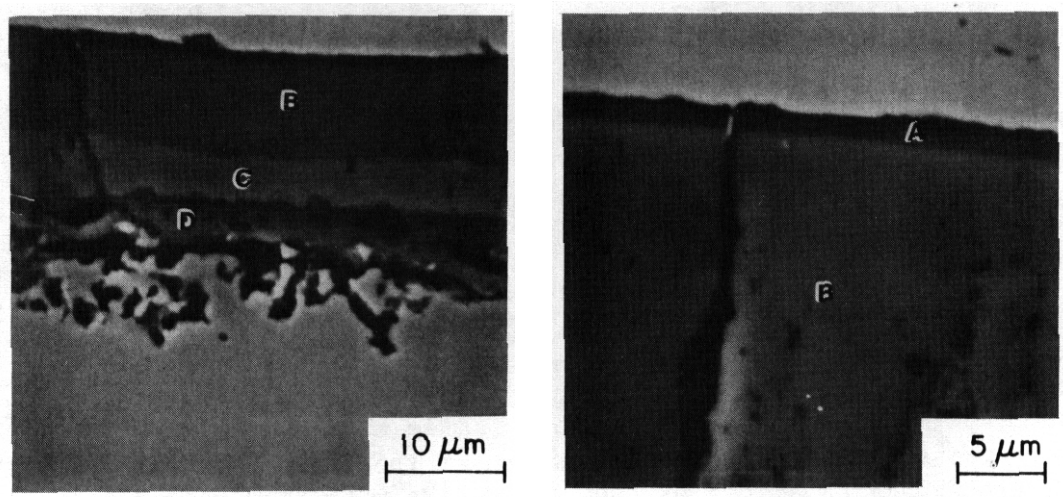

Location	Composition, wt % O	Fe	Cr	Ni	Mn	Li[a]	Possible Phase
A	30	31	1	-	24	13	$Li(Fe,Mn)O_2$
B	29	57	1	0	0	10	$LiFeO_2$
C	26	53	4	12	-	5	-
D		14	46	1	-	2	$Li(Fe_2Cr)O_4$
		4	50	-	-	8	$LiCrO_2$

[a]Estimated from difference.

Fig. 9.4.8. Chemical Composition and Possible Phases of the Different Regions of the Reaction Scale Shown in Fig. 9.4.7(c). Two different compositions for region D correspond to typical analyses of different regions of the inner scale.

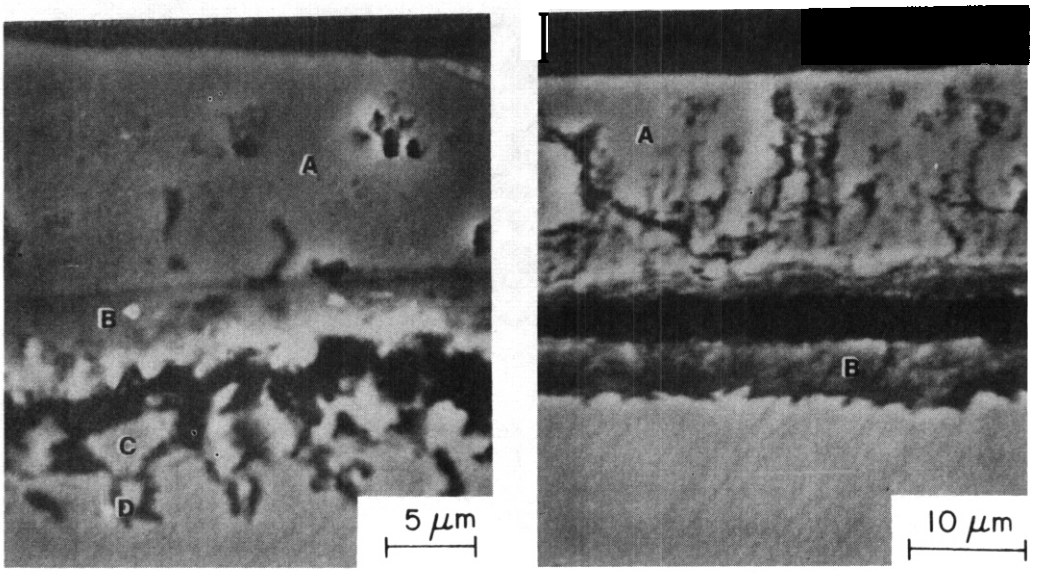

316 CW

Location	Composition, wt % O	Fe	Cr	Ni	Li[a]
A	30	61	1	-	9
B	26	9	47	4	2
C	5	40	a	42	-
D	16	42	24	17	-

Fe-9Cr-1Mo

Location	Composition, wt % Fe	Cr
A	66	1
B	37	19

[a]Estimated from difference.

Fig. 9.4.9. Chemical Composition of the Different Regions of the Reaction Scale on Alloys Exposed for 3.6 Ms with Li_2O at 823 K in Flowing Helium Containing 93 ppm H_2O and 1 ppm H_2.

Micrographs of the specimen edges that were not in contact with Li_2O and thus were exposed to the gas environment alone are shown in Fig. 9.4.10. Both Eerritic and austenitic steels show a 10 to 25-μm-thick reaction scale. EDAX analyses indicate that these scales are rich in chromium and the compositions are similar to those for the subscales formed in contact with Li_2O. These results indicate that lithium is transferred via the vapor phase or by surface diffusion to react with surfaces that are not in contact with Li_2O.

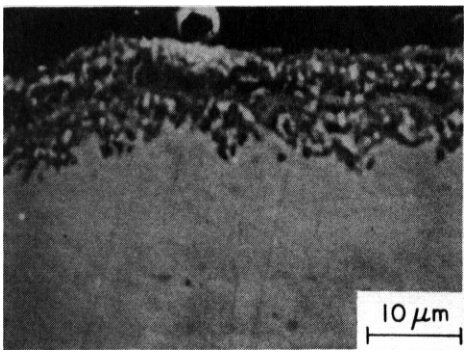

316 CW

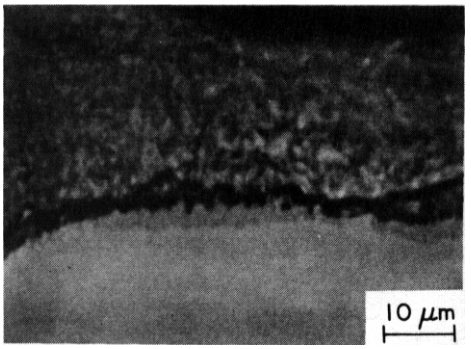

HT-9

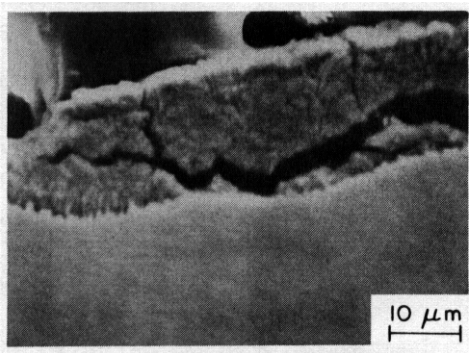

Fe-9 Cr-1 Mo

Fig. 9.4.10. Micrographs of Specimen Edges Exposed to the Gas Environment Only.

9.4.5 Conclusions

Data from the compatibility tests with Li_2O at 823 K for up to 7.2 Ms (2000 h) in a flowing helium environment containing 93 ppm H20 and 1 ppm H_2 indicate that both ferritic and austenitic steels develop a

reaction scale which consists of an iron-rich outer layer and a chromium-rich subscale. The total thickness of the scale and the depth of internal penetration increase with time. The reaction rates for ferritic and austenitic steels are comparable and yield a value of 85 μm/year for penetration. Pure nickel also reacts with Li_2O in flowing helium containing 93 ppm H_2O.

The Li_2O pellets exposed with the various reaction couples lost weight. The weight loss follows a parabolic law and yields a value of ~4.8%/year. The weight loss in helium with 1 ppm H_2O is lower than that in helium containing 93 ppm H_2O. However, for the present study, the weight loss results from gas-pellet and alloy-pellet interactions. The various alloy-pellet-gas interactions need to be established to determine the weight loss from the gas-pellet reaction.

9.4.6 References

1. O. K. Chopra and D. L. Smith, "Environmental Effects on Properties of Structural Alloys," pp. 321-327 in Alloy Development for Irradiation Performance: Semiannual Progress Report for Period Ending September 30, 1981, Oak Ridge National Laboratory. DOE/ER-0045/7.
2. O. K. Chopra and D. L. Smith, "Compatibility Studies of Structural Alloys with Solid Breeder Materials," pp. 507-513 in Alloy Development for Irradiation Performance: Semiannual Progress Report for Period Ending March 31, 1982, Oak Ridge National Laboratory, DOE/ER-0045/8.

DOE/ER-0045/9
Distribution
Category
uc-20, 20c

DISTRIBUTION

1. Ames Laboratory, Ames, IA 50011

   F. V. Nolfi

2–7. Argonne National Laboratory, 9700 South Cass Avenue, Argonne, IL 60439

   L. Greenwood
   V. Maroni
   R. F. Mattas
   R. E. Nygren
   D. L. Smith
   H. Wiedersich

8–9. Battelle-Pacific Northwest Laboratory, P.O. Box 999, Richland, WA 99352

   J. L. Brimhall
   D. Dingee

10. Brookhaven National Laboratory, Upton, NY 11973

   C. L. Snead, Jr.

11–194. Department of Energy, Technical Information Center, Office of Information Services, P.O. Box 62, Oak Ridge, TN 37830

   For distribution as shown in TID-4500 Distribution Category, UC-20 (Magnetic Fusion Energy), and UC-20c (Reactor Materials)

195–201. Department of Energy, Office of Fusion Energy, Washington, DC 20545

   M. M. Cohen
   G. M. Haas
   T. C. Reuther, Jr. (5 copies)

202. Department of Energy, Oak Ridge Operations Office, P.O. Box E, Oak Ridge, TN 37830

   Office of Assistant Manager for Energy Research and Development

203. Energy Technology Engineering Center, P.O. Box 1449, Canoga Park, CA 91304

   ETEC Library

204. General Atomic Company, P.O. Box 81608, San Diego, CA 92138

D. I. Roberts

205–207. Lawrence Livermore Laboratory, P.O. Box 808, Livermore, CA 94550

E.N.C. Dalder
M. Guinan
C. M. Logan

208. Massachusetts Institute of Technology, 138 Albany Street, Cambridge, MA 02139

O. K. Harling

209–210. Massachusetts Institute of Technology, 77 Massachusetts Ave., Cambridge, MA 02139

N. J. Grant
J. B. Vander Sande

211–212. McDonnell Douglas Astronautics Company, East, P.O. Box 516, St. Louis, MO 63166

J. W. Davis
D. L. Kummer

213. Mellon Institute, Schenley Park, Pittsburgh, PA 15213

J. C. Williams

214. National Materials Advisory Board, 2101 Constitution Ave., Washington, DC 20418

K. M. Zwilsky

215–216. Naval Research Laboratory, Washington, DC 20375

Superintendent, Materials Science and Technology Division
J. A. Sprague

217–253. Oak Ridge National Laboratory, P.O. Box X, Oak Ridge, TN 37830

Central Research Library (2 copies)
Document Reference Section
Lahoratory Records Department (2 copies)
Laboratory Records Department, RC
ORNL Patent Section
E. E. Bloom (10 copies)
D. N. Braski
F. R. Cox (3 copies)
J. H. DeVan
I. T. Dudley
M. L. Grossbeck

R. L. Klueh
R. A. Lillie
C. T. Liu
K. C. Liu
L. K. Mansur
P. J. Maziasz
C. J. McHargue
T. K. Roche
A. F. Rowcliffe
J. L. Scott
P. F. Tortorelli
J. M. Vitek
F. W. Wiffen

254–255. Rensselaer Polytechnic Institute, Troy, NY 12181

D. Steiner
N. Stoloff

256–257. Sandia National Laboratories, Livermore Division 8316, Livermore, CA 94550

W. Bauer
J. Swearengen

258. Science Applications, Inc., 1200 Prospect, La Jolla, CA 92037

H. Gurol

259–260. University of California, Department of Chemical, Nuclear, and Thermal Engineering, Los Angeles, CA 90024

R. W. Conn
N. M. Ghoniem

261. University of California, Santa Barbara, CA 93106

G. R. Odette

262. University of Missouri, Department of Mechanical and Aerospace Engineering, Columbia, MO 65211

M. Jolles

263. University of Virginia, Department of Materials Science, Charlottesville, VA 22901

W. A. Jesser

264. University of Wisconsin, 1500 Johnson Drive, Madison, WI 53706

W. G. Wolfer

265–266. Westinghouse Electric Company, Advanced Reactors Division, P.O. Box 158, Madison, PA 15663

W. A. Boltax
R. E. Cold

267–274. Westinghouse Hanford Company, P.O. Box 1970, Richland, WA 99352

H. R. Brager
D. G. Doran
A. M. Ermi
F. A. Garner
D. S. Gelles
E. C. Opperman
R. W. Powell
J. L. Straalsund

☆ U S GOVERNMENT PRINTING OFFICE 1983 646 055 172